ORNL-3908
UC-20 – Controlled Thermonuclear Processes

THERMONUCLEAR DIVISION

SEMIANNUAL PROGRESS REPORT

FOR PERIOD ENDING OCTOBER 31, 1965

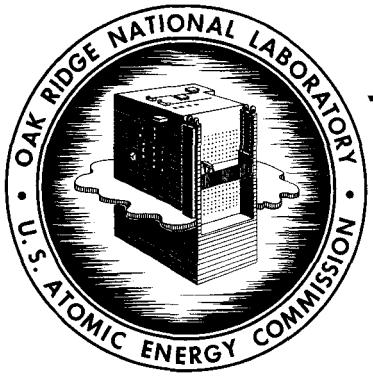

OAK RIDGE NATIONAL LABORATORY
operated by
UNION CARBIDE CORPORATION
for the
U.S. ATOMIC ENERGY COMMISSION

Printed in USA. Price $5.00. Available from the Clearinghouse for Federal Scientific and Technical Information, National Bureau of Standards, U.S. Department of Commerce, Springfield, Virginia

ORNL-3908

Contract No. W-7405-eng-26

THERMONUCLEAR DIVISION

SEMIANNUAL PROGRESS REPORT

For Period Ending October 31, 1965

MARCH 1966

OAK RIDGE NATIONAL LABORATORY
Oak Ridge, Tennessee
operated by
UNION CARBIDE CORPORATION
for the
U. S. ATOMIC ENERGY COMMISSION

Contents

Introduction

A. H. Snell

In the last of these reports we enthused over a theoretical guideline that suggested how injection-accumulation experiments might be directed with a possibility of simultaneous hydromagnetic and microstability. The indications appeared to us to be more clear-cut than have been usual in the field of controlled fusion. The recipe (T. K. Fowler), succinctly stated, is:

1. Use a magnetic well.
2. End and wall mirror ratios should be 3 for a β of 0.3, but this can be reduced for lower β.
3. Inject with an energy spread of at least 60% of the mean energy.
4. $T_e \leq 0.3\ T_i$.
5. $T_{\perp i} \leq 2\ T_{\parallel i}$.
6. Radial size of plasma is determined by desired density: $R/\rho_i > (\omega_{pi}/\omega_{ci})^{4/3}$; thus for $n_i = 10^{13}$, $\omega_{pi}/\omega_{ci} = 30$, and plasma "diameter" should exceed about 100 Larmor diameters.
7. Length of plasma is determined by desired density; for example, for $n_i = 10^{13}$, length should be less than 100 Larmor radii.

In our last report, a fusion reactor based upon 600-kev injection, and calculated as an example, turned out to be a gigantic thing, and one looked for laboratory-scale experiments that could test the recipe (or some features of it) in a modest and controllable way. We have found such a regime in low-energy neutral injection (well below 10 kev) in apparatus of approachable size, and doubtless experimentation of this kind will also be started in other laboratories – laboratories which indeed are of themselves aware of the interest in this regime.

Meanwhile, from our own group, an added impetus has arisen because the DCX-1 experimenters have diagnosed the microinstability that causes the loss of 90% of their trapped 300-kev protons under steady-state conditions as the *negative mass instability*. Details of this diagnosis are given *in extenso* in Sect. 1 of this report, and we announced the finding at the Culham Conference last September. The added interest arises because the magnetic wells, already widely recognized as successful hydromagnetic stabilizers, should also be effective in controlling the negative mass micro-instability, particularly if the field gradients extend in to the center. Indeed, the Culham Conference reports from the ALICE and PHOENIX II experiments showed radio-frequency signals in many respects like those of DCX-1, and the application of the magnetic wells appeared to cause at least a *modification* of the signals. It is certainly too early to draw broad conclusions from the comparisons; perhaps, indeed, one needs to consider further the nature of the negative mass instability in configurations in which the gyro-frequency loses its unique value, as it does in magnetic wells. In ALICE and PHOENIX II, the radio-frequency signals did not, after all, disappear completely.[1]

The proposal of a low-energy injection experiment to test the Fowler recipe requires at least three phases of development work. One is the development of the low-energy H^{0*} beams under good control as to current and divergence; for our success in this direction, see Sect. 6. A second is the introduction of energy spread; one method for doing this has been evolved at low beam currents and is described in Sect. 5.2 (see especially Fig. 5.3). The third is the development of detectors that can register H^0 particles in the difficult

[1] I endeavor here to present the situation as it appeared at the closing date of this report. The disclosure that ALICE may also exhibit the negative mass instability in the octupole Ioffe field did not come until a few days later. Much remains to be clarified, but the interplay between DCX-1, ALICE, and PHOENIX II is gratifying and can hardly fail to be illuminating.

energy range of a very few kilovolts; we have started on this and describe preliminary results in Sect. 5.4.

The further question arises: what about trapping and stability in the flat-field case, such as we have in DCX-2? Present feeling in the DCX-2 group is that the DCX-2 phenomena have yet to be related to those of DCX-1. The work of the past six months has added to our knowledge of the performance of DCX-2 under the conditions of trapping by dissociation on the background gas and trapping by hydrogen arc dissociation; these experimental results can now be compared with the older data on lithium-arc trapping. Although DCX-2 has undergone a period of unusually severe operational troubles, the new results that appear in Sect. 2 include: (1) an observation that because of the interplay between rate of energy spread and charge-exchange cross sections, a regime exists around a pressure of 7×10^{-5} torr that gives a somewhat higher fast-proton density than results at lower pressures (10^{-6} torr); (2) the directional (pitch-angle) distribution of the emerging charge-exchange neutrals obtained with gas dissociation lacks the central peak that indicates, when the lithium arc is used, that under magnetic field adjustment for maximum density the majority of the fast ions, and simultaneously the more energetic ions, have essentially no longitudinal velocity (in fact, the whole pitch-angle situation requires more study); (3) the radio-frequency spectrum emitted by the trapped protons can contain a multitude of harmonics (up to the 100th) of the proton cyclotron frequency, thus providing a complement in the ions to the rich harmonic spectra that have been known for several years in the electrons of magnetically confined plasma. The peak electric radiation fields can amount to 100 v/cm or more. Another accomplishment closely related to DCX-2 is the production of H_2^+ beams of greater intensity than we had previously achieved (Sect. 6); we should soon be able to double or triple the input to DCX-2.

Our experience in the stability of the electron-cyclotron plasmas in simple mirror configurations has for some time directed our attention to the matter of stabilization by cold plasma, or "line tying." We feel that more should be known about this: for example, how much cold plasma is needed, to what beta-values can it be exploited, and to what extent can it be combined with other stabilization schemes? Section 7.2 contains a short theoretical discussion, and in Sect. 7.3 we describe how the old EPA apparatus has been modified into an experiment somewhat bafflingly called INTEREM, where three mirror regions are used in line, the outer two serving as regions for the generation of cold plasma which is used to stabilize the plasma in the central region, thus permitting a much lower neutral pressure in the central region. So far, the central-region pressure has been forced down to a tenth of that previously required for stable electron-cyclotron plasmas; we hope to go further. The injection of 20-kev H^0 atoms, originally started for diagnostic purposes, has yielded trapped fast-ion densities of over 3×10^7 cm^{-3} within the hot-electron medium, so INTEREM may quickly develop into a competitive injection-accumulation experiment. The fast-ion decay curves show both a rapid and a slow component; these must be studied further. Meanwhile, other electron-cyclotron plasma work includes a study of the energy groups in the 8-mm heating experiment ELMO (with the observation that electrons can be heated to the limit set by their radiation cooling rate), and the observation in the old PTF apparatus that two types of instabilities can be instigated: the flute and the mirror. Pressure and magnetic field manipulations can favor either the one or the other, or neither. This may be the first experimental recognition of the mirror instability.

In the matter of turbulent heating by beam-plasma interaction, we describe in Sect. 4.1 probe and power measurements that indicate the following situation in Burnout V: (1) as much as 10% of the input power can go into heating the ions; (2) the ions are mostly in a population with a temperature (lab system) of 550 ev and a density in the 10^{11} to 10^{12} cm^{-3} range; (3) the electron temperature is low; (4) a few of the ions (equivalent density about 10^6 cm^{-3}) are heated to temperatures above 100 kev; (5) the core of the discharge is strongly negative in potential, so there is fierce $E \times H$ rotation; (6) with deuterium there is a neutron source of about 10^5 sec^{-1} in the region of the midplane between mirror coils. In Sect. 4.2 we show that in the hot-electron version of the "mode II" reflex discharge, with one or two sources set off axis in a large mirror configuration, the electron density in the annular "blanket" about 18 in. in diameter and 3 or 4 ft long has been increased by the methods of laboratory black art to about 10^{12} electrons/cm^3. This is becoming interesting,

and attempts will be made to increase the density still further.

Two continuing studies of radial loss of plasma from the hydrogen vacuum arcs show that (1) when the field shape is changed so as to provide a radial minimum B the loss is reduced but not eliminated (Sect. 4.7), and (2) in the uniform field of the Long Solenoid, the "fluting" is of such fine structure as to be better described as a surface turbulence of random nature (Sect. 4.8).

In the field of magnetics we note refinements in magnetic field calculations and coil arrangements (Sects. 8.1 and 8.2), the development of small, high-power-density "expendable" coils (Sect. 8.3), and an iron magnet that inexpensively gives a magnetic well of the "baseball seam" type (Sect. 8.4). The study of wavelike flux penetration into superconducting cylinders and the flux jumps that result from the penetration is pursued theoretically and experimentally in Sect. 8.5. In other experiments the miniature Hall probes that we have developed have been invaluable in revealing the flux distribution through the superconducting material; their resolving power is illustrated in Figs. 8.24 and 8.25, where ripple shows, arising from individual layers or windings in a small superconducting coil wound with 10-mil Nb-Zr. An attempt is made in Sect. 8.5.4 to develop a macroscopic theory for the behavior of type III superconductors on the basis of the "pinning" of flux lines, but the results so far are regarded by the author as somewhat inconclusive.

The matter of tritium penetration and inventory in the walls of a hypothetical fusion reactor is discussed further in Sect. 9. The conclusions of both a literature survey and some experimental work are that there will probably be no serious problem here. Vacuum notes discussed the periodic pressure "blips" that come from dry elastomer O-rings in vacuum systems (Sect. 9.3), and the control by cooling of the vapor streaming that can falsify absolute pressure measurements made with conventional McLeod gages (Sect. 9.6). The research contributions of this progress report conclude with some sputtering yields for 30-kev D^+ ions (Sect. 9.7) that suggest that copper may sometimes be an unfavorable choice for a surface to be subjected to bombardment.

Abstracts

1. INJECTION AND ACCUMULATION: SINGLE-PASS EXPERIMENTS (DCX-1)

The axial oscillation amplitudes and the energy spread of trapped protons were deliberately increased in attempts to stabilize the instability driving proton losses to permit the accumulation of higher densities. The threshold density for this instability could be increased by nearly two orders of magnitude by these techniques. However, the maximum thresholds remained below the density at which proton losses occur, and the limiting plasma density, 1 to 2×10^8 cm^{-3}, was not increased significantly. A number of experiments relating directly to the problem of mode assignment for the instability were performed. These experiments included studies of threshold variations with energy spread, with changes in the distribution of trapped protons in radial oscillation amplitude, and with changes in the shape of the magnetic field. Some instability growth-time measurements were also made. The results of the experiments are in agreement with the theory of the negative mass instability. Progress in analytic calculation of orbits and orbit frequencies and results of injecting into mode I and mode II discharges are also reported.

2. INJECTION AND ACCUMULATION: MULTIPLE-PASS EXPERIMENTS (DCX-2)

Experiments have been carried out in which we studied the plasma properties with hydrogen arc dissociation and hydrogen and nitrogen gas dissociation. The densities obtained vary, depending on the conditions, from 1×10^8 ions/cm^3 to several times 10^9 ions/cm^3, somewhat lower than those obtained with the lithium arc dissociation. The highest densities are obtained with the hydrogen arc used as a dissociator despite the fact that the pressure could not be reduced in these experiments below $\sim 5 \times 10^{-6}$ torr. In the case of gas dissociation, a quantitative use of the energy analyzer data has been made to determine directly the trapped proton density, and the results agree with the usual measurements using the integral of the charge-exchange flux following beam turnoff. It appears that in the case of gas dissociation, the evidence suggests fairly good accountability of the injected beam from the charge-exchange flux at equilibrium. Surprisingly, the trapped density is observed to rise to a peak as the pressure is increased and then falls at pressures above 2×10^{-5} torr. This behavior is shown to be due to variations in the energy spread as a result of the presence of the microinstability. The intensification of the instability causes, in some cases, actually a significant improvement of containment time as a result of the average energy increase. This is not to say that the instability is desirable, but merely indicates its presence is not catastrophic.

Studies of the pitch-angle distribution in gas breakup were made. In certain instances no central peak was observed. The interpretation of these results in terms of what limitations for the density may be expected is still ambiguous. Radio-frequency measurements were made with improved calibrated probes which show electric fields at the probes in excess of 100 v/cm for some of the harmonics. The variation of the behavior of the harmonic spectra as a function of gas pressure and energetic particle density is also described.

3. ELECTRON-CYCLOTRON HEATING

The EPA Facility, as discussed in Sect. 3.1, has been modified extensively and will henceforth be called INTEREM for Injection of Neutrals and Trapping on an Electron Resonance Environmental Medium. The injected 20-kev neutral beam current has increased in magnitude. As a result of these improvements, the density of 20-kev ions trapped in the electron-cyclotron plasma has increased to

$\sim 3 \times 10^7$ ions/cm^3. Hot-ion instabilities have not been yet observed in the presence of the environmental plasma medium. The neutral beam has also been used to measure the cold-ion density in the environmental plasma.

A description of the 2-kw, 8-mm continuous-wave microwave source used to form the electron-cyclotron plasma in the ELMO Facility is given in Sect. 3.2. Experimental results show that the multicomponent plasma might have as many as four rather distinct energy groups. The results of some density and temperature measurements using bremsstrahlung diagnostics, neutron intensities, diamagnetic measurements, and axial currents are presented.

As described in Sect. 3.3, two types of instabilities can be induced in a hot-electron plasma produced by electron-cyclotron heating in a magnetic mirror. One type results in radial loss of particles across magnetic field lines and appears to be due to the growth of flutes. The other results primarily in loss along magnetic field lines and appears to be due to the mirror instability. Both types are accompanied by radio-frequency oscillations and result in the loss, per event, of $\sim 10\%$ of the energy stored in the plasma.

4. PLASMA PHYSICS

Ion and electron temperatures and densities are being measured in the burnout experiments. The power density of Burnout V has been increased. Deuterons up to 170 kev have been analyzed, and corresponding neutron fluxes from wall reactions have been observed. Probe measurements of the plasma in Burnout V suggest that the ion temperature is about 0.5 kev, that the ion density is greater than 10^{11} cm^{-3} and is probably about 3×10^{12} cm^{-3}, that the electron temperature is about 100 ev, and that strong radial electric fields exist in the device.

A wide-angle optical system has been used to study the light emitted from the plasma of Burnout V. As expected, in mode II operation, the central arc is observed to fade and is replaced by a dim glow throughout the entire plasma container. In Burnout IV detailed investigation of the spectral light distribution using both spectrographs and filters is being made.

Development of hot-electron plasmas continues. In an annular shell trapped between magnetic mirrors, two feed arcs operating simultaneously contribute to an electron density of 10^{12} cm^{-3} and temperature of 100 ev. Electrons of 100 kev at 5×10^8 cm^{-3} density are found on both the inside and outside of the shell.

Ionic sound wave studies have been continued, and have verified that γ, the adiabatic compression coefficient for the plasma electrons, is unity, as is expected on theoretical grounds. An electron-emitting hot probe has been found to be a supersensitive ion-wave detector, apparently because the ion wave perturbs a space-charge sheath surrounding the probe.

A simple model has been used to predict which gases in cylindrical discharge tubes tend to produce moving striations and which do not. Those that tend to produce moving striations have electron-atom scattering cross sections increasing with increasing electron energy, and conversely. A study of Langmuir probes shows that in small, quiescent plasma systems of low density, Langmuir probes are not always satisfactory. In these systems, Langmuir probes can be supplemented by a simple "decay" technique for density measurements. Calculations for the momentum probe (magnetic analyzer) for plasma studies have been extended to include the effects of electric potentials placed on the probe.

Studies of the macroscopic cross-field mass motion (fluting) from the hydrogen arc have continued in a modified magnetic field geometry. The addition of a pair of coils inside the main mirror coil pair enables us to produce a field with a radial minimum on the axis. For the largest depth of this magnetic well, correlated signals which may be identified as flutes still appear, although their radial velocity is reduced, perhaps by an order of magnitude. The radial density profile is also narrowed.

Flutes have also been observed in the plasma, produced apparently by a streaming interaction (turbulent heating), in the uniform field of beta tank D, using the PIG-configuration plasma source. The observed flute velocities, of the order of $\sim 2 \times 10^6$ cm/sec, are somewhat higher than are observed in the gas arc facility. At large radii these flutes cannot be observed, but fluctuations in the ion current appear which may be interpreted as a rigid rotation of the plasma body at a frequency with a period of 2 μsec.

Axially correlated irregularities at least 40 in. long were found on the hydrogen arc column in

the long solenoid. The number of fluctuations registered per second increases sharply with arc current. Inasmuch as the correlated structure is small in radial and azimuthal extent, the behavior is thought to resemble a turbulence rather than gross hydromagnetic flutes in the usual usage of the term.

In calutron beam work during this period, the Ca^+ beam passing through a homogeneous magnetic field has been studied. The disturbance which perturbs the beam and gives rise to a large beam imperfection appears to be associated with the depth of the positive potential well.

Further spectroscopic studies of the energetic carbon arc suggest for the first time a possible leveling off of the heating mechanism in very long, magnetically confined carbon arcs. The heating process appears also to depend on the concentration of C^{2+}. The excitation-heating mechanism is substantiated further by a quasi-resonance intermediate step, which predicts a fairly low collisional energy for the maximum in the cross section of the heating step. A firmer understanding of the line intensity anomalies has been obtained. A crude estimate of 1.0 for "ln λ" has been made in terms of the arc resistivity and may be compared with the conventional theoretical value of 8.6 vs the revised theoretical value of 1.4. The concepts of "ignition" and "burning temperature" are discussed briefly.

5. ATOMIC AND MOLECULAR CROSS SECTIONS

Measurements have been made to confirm the existence of stable electronic excited states of H_3, similar to those found in H and H_2. Capture into repulsive levels of H_3 dominates the electron capture process, but the capture into all levels is an order of magnitude less than expected.

The parameters influencing the charge-transfer conversion of monoenergetic protons into energy-dispersed neutral particle beams have been investigated. A 50-kev proton beam was passed through an argon gas cell composed of 11 insulated electrodes arranged to provide a linear decelerating field. Application of a 40-kv retarding field resulted in a nearly flat energy distribution with a 40% conversion efficiency of incident protons to neutrals. Fifty-kiloelectron-volt H_2^+ particles incident on the gas cell exhibited 45% conversion.

Engineering modifications have decreased the measured noise width of the silicon surface barrier for measuring low-energy protons. A minimum noise width of 2.75 kev has been obtained. The pulse spectrum of 6-kev protons was resolvable with the present geometry. Resolvable pulse spectra were also obtained for 10-kev He^+ and 15-kev N^+ ions.

The fast time response of a barium titanate crystal has been determined for a pulsed 300-kev H^0 beam. At low power levels (10^{-4} w/cm) the shape of the output signal pulse from the crystal was differentiated; however, as the input power increased, the time response of the crystal was the same as that of the beam.

6. HIGH-CURRENT ION-BEAM PRODUCTION AND INJECTION

Development of ion sources and facilities for extracting, focusing, and handling ion beams for direct application into present thermonuclear devices and potential application into future devices has continued to be our major effort. Intense direct-current hydrogen ion beams, either atomic or molecular, are now available over an energy range of 4 to 600 kev with total beams of from 200 ma to 1 amp. The fraction of the total beam usable for various experiments is indicated by imposing various degrees of collimation.

7. PLASMA THEORY AND COMPUTATION

A concentrated effort has been made to obtain a comparison between theory and experiment in two important instances: the low-density instability in DCX-1 and the flutelike instabilities which can be excited in the PTF machine. The importance of these particular cases stems from the general questions they bear upon: the domain of relevance of negative-mass instability theory, and the broad question of finite length and cold-plasma effects respectively.

In a quite separate area, the long-range program to obtain a complete theoretical description of plasma transport phenomena has progressed to a most important point. The formulas derived earlier to describe "anomalous" diffusion rates due to specified fluctuation spectra have been

studied from several viewpoints. Work now in progress is aimed at predicting the fluctuation spectrum to be expected on the basis of the nonlinear development of plasma instabilities. This information would then permit a general diffusion calculation, which might give answers to the question of what levels of instability are tolerable in a fusion plasma.

8. MAGNETICS AND SUPERCONDUCTIVITY

For various plasma physics experiments the generation of magnetic fields with extended zones of high homogeneity is of great interest. In other cases the uniformity of the axial field gradient may be important. In all these cases coil systems with good Fabry factors and small volume factors are, of course, desirable. Because of the great number of independent variables (coil dimensions, distances between coils, etc.), it is very difficult to find optimum solutions. Calculation methods recently developed here have been refined and adapted for this purpose. The results are surprisingly good and prove that the probability of finding, at random, favorable solutions is very small.

An appropriate way to represent these fields graphically is to trace constant-vector-magnitude curves. It is more effective to use the new concept of "total vector error contours." These two graphical methods are applied to a study of the field configurations of the new large-volume magnet coil systems "C" and "D," which are being built for our magnet laboratory.

Other tasks of magnetic field production for thermonuclear research encounter considerable technological difficulties: first, the generation of high fields in small volumes (for instance in the bores of mirror coils) with the additional condition of disturbing by mechanical construction parts the surrounding plasma as little as possible. Two different new designs which try to solve this problem are described. Both showed promising preliminary test results.

A second problem is the generation of "magnetic wells" with nonzero field minima. Air-core coil designs are difficult because of the necessary high current densities in the windings. Recently, for this purpose an iron-core design was developed here which needs only low power densities in the coils, allows simple changing of the mirror ratio, and permits ample access to the plasma volume.

The work on superconductivity at the Thermonuclear Division is guided by our opinion that for the successful development of superconducting, large-volume, high-field magnets of various shapes (coils, Ioffe bars, etc.), a better understanding of the relevant physical properties of the high-field superconductors is necessary.

Thus a program was initiated a few years ago which tries to reach this goal by following simultaneously several experimental approaches: magnetic moment measurements, field scanning with micro Hall probes, flux jump and flux creep investigations, and the measurement of critical currents under greatly diversified experimental conditions.

This report describes recent results on micro Hall probe measurements on Nb–25% Zr cylinders and coils, and investigations on the field distributions in hard-superconducting cylinders with adiabatic field change. A note on the macroscopic theory of superconductors of the second and third kind tries to clarify the basic theoretical concepts.

9. VACUUM STUDIES, SPUTTERING, ADSORPTION, AND DIFFUSION OF GASES IN METALS

Further consideration of tritium inventory problems in a thermonuclear reactor has been made. The data found in the literature have been analyzed and show that tritium inventory control is associated with the primary factors, temperature, metal cleanliness and purity, and bombarding flux of energetic atoms or ions. An experimental study was conducted using low-energy bombardment in a glow discharge; the study yielded results in agreement with the detailed literature study.

Part of the continuing studies of vacuum systems and components included a study of the periodic pressure bursts frequently observed in vacuum systems. In the particular system used for this study, the gases were identified with water and carbon dioxide effusing from the pump flange elastomer gasket and not air or background gases in the vacuum system. Oil transport in vacuum systems was previously found to be by a surface transport process for a mixed hydrocarbon oil. The results of a study using

a high-mass-resolution mass analyzer on the mobility of a trisiloxane oil could be interpreted most simply by assuming a vapor-phase transport mechanism. The subject of transport mechanisms of high-molecular-weight materials is still moot.

Measurements with a refrigerated McLeod gage indicate that the "Hg vapor pumping effect" can be eliminated by immersing the gage in a region where the ambient temperature is $-15^{\circ}C$. Calibration of a commercial capacitive differential manometer was made to determine the usefulness of such a gage for a pressure standard in measuring condensable vapors.

Sputtering ratios have been measured for 30-kev D^{+} ions on tungsten, molybdenum, copper, and 316 stainless steel. Sputtering ratios range from 0.03 for copper to 0.007 for the stainless steel.

1. Injection and Accumulation: Single-Pass Experiments (DCX-1)

J. L. Dunlap
R. S. Edwards
G. R. Haste[1]
L. A. Massengill
C. E. Nielsen[2]
H. Postma
R. G. Reinhardt
W. J. Schill
E. R. Wells
R. A. Young[3]

1.1 INTRODUCTION

The previous report[4] reviewed the information accumulated concerning microinstability-driven proton losses and microinstability-generated rf signals from the DCX-1 plasma. It also described the results achieved by applying two different techniques aimed at stabilization by deliberately decreasing the anisotropy of the trapped proton distribution.

Work during the present report period has been almost equally divided between experiments with other stabilization techniques and studies directly relating to the problem of mode assignment for the principal proton-loss instability. In the first category are the deliberate introductions of increased proton axial oscillation amplitudes (Sect. 1.2) and of proton energy spread induced by stochastically driven cyclotron dee structures and by modulation of the molecular-beam energy (Sect. 1.3). The density threshold for observation of the instability was quite insensitive to the deliberate introduction of axial oscillations, but it could be increased from 3×10^5 cm^{-3} to 3×10^7 cm^{-3} by energy spread. Energy spreads introduced by these techniques were not particularly effective in increasing the limiting plasma density of 1 to 2×10^8 cm^{-3}. Spreading by the cyclotron drives decreased this density, and use of beam energy modulation increased the density by only a factor of 2.

Experiments directly relating to mode assignment are described in Sect. 1.4 in which are introduced measurements of growth times for the instability, threshold measurements for different proton distributions in radial oscillation amplitude, measurements of the frequency of the $l = 1$ unstable mode as a function of the minimum radial oscillation amplitude of the injected proton distribution, and studies of threshold changes with energy spread for different magnetic field gradients. That the results of these experiments and others examining the response of threshold to energy spread are in good quantitative agreement with theoretical predictions of negative mass instability is demonstrated in Sect. 1.5.

Some attempts have been undertaken to generalize negative mass theory to treat particles stored in decidedly nonuniform magnetic fields. One difficulty encountered was that gyrofrequency is not well defined in such fields. Section 1.6 defines some frequencies by which orbits in general can be characterized and reports recent progress in analytic calculation of orbits and orbit frequencies.

Section 1.7 describes injection into mode I and mode II discharges operated in DCX-1. The results indicated that any burned-out volume associated with mode II was too small to provide significant shielding of the 300-kev proton plasma formed by injection.

---

[1]Present address, Physics Department, University of Tennessee.

[2]Consultant from Ohio State University.

[3]Summer employee. Present address, Physics Department, University of Chicago.

[4]*Thermonuclear Div. Semiann. Progr. Rept. Apr. 30, 1965*, ORNL-3836, pp. 1–13.

Finally, Sect. 1.8 is an appendix which gives principal features of a negative mass theory useful in interpreting some of the experimental results.

1.2 DELIBERATE INTRODUCTION OF PROTON AXIAL OSCILLATION AMPLITUDES

With the standard injection trajectory, the H_2^+ beam is in the median plane, and the ratio of $T_\perp/T_{||}$ for initially trapped protons is approximately 100, so the axial oscillation amplitude of injected protons is quite small ($\frac{1}{2}$ to $\frac{3}{4}$ in.). A convenient way to increase this amplitude is to employ electrostatic deflection of the molecular beam just prior to its entrance into the main vacuum vessel to deflect the beam from the median plane.

Thresholds for onset of the proton-loss instability (the gyrofrequency mode of earlier reports[4]) were measured for various displacements of the molecular beam from the median plane. The maximum displacement reduced the anisotropy ratio to about 4, and gave average proton axial oscillation amplitudes of 4 to 5 in. Threshold was determined from the appearance of rf signals during plasma accumulation, and the central density at threshold was measured in the usual way from charge-exchange loss signals.

The threshold density was quite insensitive to the variations of trapped proton distribution. Since the charge-exchange detectors were not collimated and no attempt was made to correct the central density estimate for changes in the axial distribution of the trapped plasma, threshold changes by small factors (2 or 3) may have been present. However, the stabilizing effects of the axial oscillations introduced are still small in comparison with the effects of radial oscillations.[5,6]

Since no significant degree of stabilization was obtained for the available range of trajectory shifts from the median plane, such trajectory variations were not further examined.

[5] *Thermonuclear Div. Semiann. Progr. Rept. Apr. 30, 1965*, ORNL-3836, p. 8.

[6] This report, sect. 1.4.2.

1.3 DELIBERATE INTRODUCTION OF PROTON ENERGY SPREAD

1.3.1 Cyclotron Drives

Cyclotron structures mounted within the plasma chamber have been used to increase the energy spread of the trapped protons. Two such structures were employed, one suited for operation at the third harmonic of the proton cyclotron frequency and one for operation at the fundamental. Both structures permitted a plasma radius of 9 in. Approximately stochastic accelerations were desired. For this reason, in each case the driving potentials were obtained by amplifying the output of noise generators filtered for a pass band of 1 to 2 Mc about the appropriate harmonic, which was that for 300-kev protons on the equilibrium (circular) orbit.

A diagram of the third-harmonic dee structure is given as Fig. 1.1. At this frequency both driven and passive elements were necessary. As shown in Fig. 1.2, only the driven element was required for the fundamental structure since the grounded walls of the plasma chamber then served as a dummy dee. The side walls of the third-harmonic structure restricted the axial extent of the plasma to $Z = \pm 1\frac{1}{2}$ in. The fundamental structure allowed the normal axial extent, $Z = \pm 6\frac{1}{2}$ in.

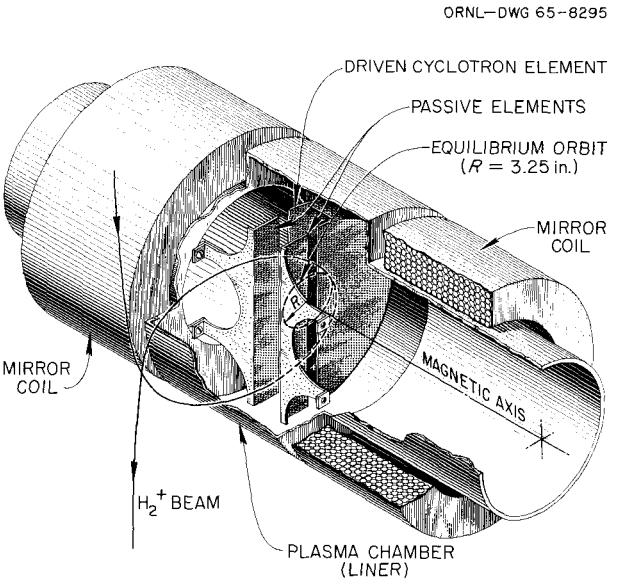

Fig. 1.1. Third-Harmonic Cyclotron Dee Structure Used in Energy Spreading Experiments.

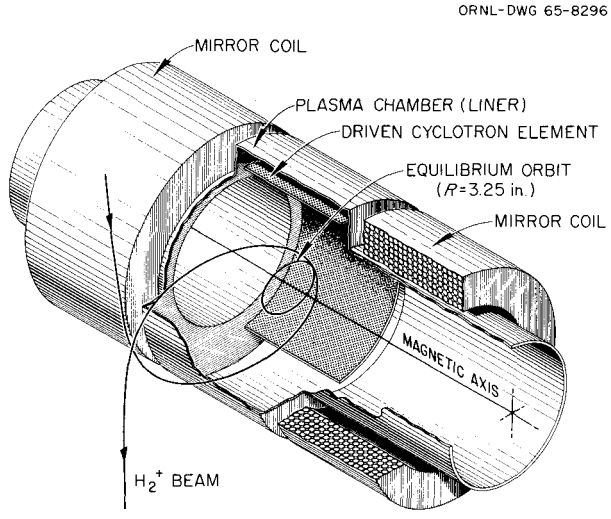

Fig. 1.2. Fundamental Cyclotron Dee Structure Used in Energy Spreading Experiments.

The experiments involved measurements of the instability rf signals (their absence denoted stability), the charge-exchange loss currents (to determine the total number and density of trapped protons), and the energy distribution of trapped protons (to determine the energy spread). An electrostatic probe was usually used. With the third-harmonic drive, a low-pass filter in the signal lead from the rf probe allowed detection of instability signals from the first and second harmonics even with dee voltage applied. With the fundamental drive, observation of the rf signal was somewhat more difficult. A gating circuit was arranged to very quickly reduce the dee voltage to a low level, and the second harmonic instability signal was examined through a band-pass filter immediately after the gate was applied. The absence of the instability signal at that time was taken as evidence of stabilization.

The energy distributions were determined in steady state by the usual technique, measuring the distribution of escaping charge-exchange neutrals with a surface-barrier detector in the median plane and then, when required, correcting for the energy dependence of the electron-capture cross section in order to obtain the proton distribution. The resolutions of the several detectors employed in this work varied from 12 to 18 kev full width at half maximum (at 300 kev), and the measured distributions sometimes were only slightly broader than this. As a result, only ΔE values above about 10 to 15 kev full width at half maximum were determined by direct measurement. Lower values were determined by extrapolation of measured ΔE vs dee voltage curves to lower dee voltages.

With first-harmonic drive, threshold was determined by appearance of rf signals during the period of plasma accumulation, and in steady state by adjusting the injected beam current and cyclotron drive to define the stable-unstable boundary. Results were identical. With third-harmonic drive, the determinations were limited to steady state.

This work was done with the standard molecular-beam trajectory. It involved studies of two distinctly different plasma situations. We consider first those studies of plasmas established by Lorentz dissociation and initially instability-limited to densities of 1 to 2×10^8 cm^{-3} for the fundamental structure and to somewhat lower densities for the third-harmonic structure (because of axial expansion and loss to the side walls). The application of dee voltage in this situation resulted in decrease of plasma density. The additional plasma losses are apparently radial, driven by the cyclotron fields.

Despite the failure of this technique to relax the density limitation imposed by the microinstabilities, useful information was gained when the technique was applied to lower-density plasmas established by gas dissociation. Charge exchange is the only proton loss mechanism for these plasmas. They could be stabilized by the energy spread without introducing other losses. Figure 1.3 gives typical results in the form of the total number of protons trapped at threshold as a function of the proton energy spread. The data points for fundamental and third-harmonic dee structures are essentially identical. The line fit shows that the threshold varies approximately as the square of the energy spread. That the results are in quantitative agreement with theory for the negative mass instability will be demonstrated in Sect. 1.5.

The maximum ordinate value for the data of Fig. 1.3 corresponds to a central fast-proton density of 3×10^7 cm^{-3}. An extrapolation of the data to a density of 3×10^9 indicates that an energy spread equal to the injected energy (300 kev) would be required for stabilization. Since the orbit changes associated with the cyclotron

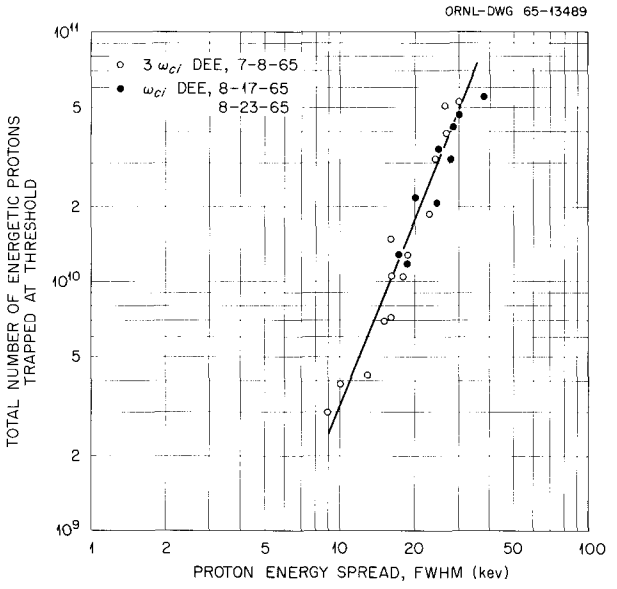

Fig. 1.3. Threshold Population as a Function of Proton Energy Spread Introduced by Use of Cyclotron Structures. Standard beam trajectory and field, 8-in. plasma radius, and charge-exchange decay time (τ) of 50 msec. The maximum threshold density is 3×10^7 cm^{-3}.

fields resulted in proton losses to the radial walls at values of dee voltage not much higher than those required to stabilize 3×10^7 cm^{-3}, such spreads, in practice, could not be approached by this technique.

Other features of this experiment are of interest. The indications of stabilization from the rf signals were sharply defined, and the dee voltages required for stabilization could therefore be accurately fixed (to within ±10%). For a given set of operating conditions, the critical voltage was the same whether the stable-unstable boundary was approached from the unstable region (gradually increasing the dee voltage) or from the stable region (decreasing the dee voltage). In each case, the energy spread required for stabilization was somewhat larger than that characteristic of the unstable plasma.

The data of Fig. 1.3 were obtained with a plasma lifetime of 50 msec. One logical question is whether the energy spread required to stabilize a particular density is independent of τ. We have examined the measured energy spreads and the dee voltages required to stabilize a density of 1×10^7 cm^{-3} for τ values over the range 0.25 to 0.001 sec. The energy resolution problem and difficulties with high counting rates confined meaningful direct measurements of the energy spread to about one-half this range, that at longer lifetimes. The results were consistent with a constant energy spread, but they did not exclude some slight τ dependence. Such a dependence is suggested by the variation of critical dee voltage with τ (Fig. 1.4), for V varies less rapidly than the $\tau^{-1/2}$ dependence anticipated for spreading by stochastic collisions.

1.3.2 Modulation of the Molecular-Beam Energy

A 60-cycle modulation of the energy (normally 600 kev) of the molecular-ion beam was introduced by adding a transformer secondary in series with the high-voltage connection to the accelerator tube. In these experiments the unperturbed 600-kev trajectory was the standard trajectory, which is in the median plane. The beam channel is not magnetically shielded, and modulation of beam energy results in an oscillating displacement of the beam trajectory. The beam remains in the median plane, but beam turnaround (the point of closest approach of beam to magnetic axis) oscillates about the usual 3.25-in. value. The requirement that the beam pass through the plasma chamber restricted the modulation to ±30 kev.

With the maximum modulation, the microinstability-limited density was increased by a factor of 2, but plasma of this density was not stabilized.

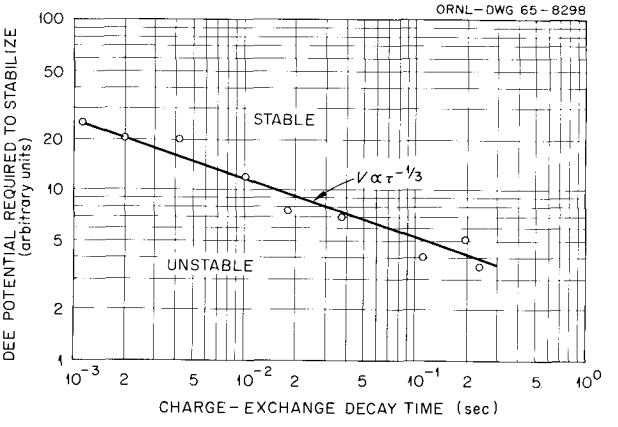

Fig. 1.4. Dee Potential Required to Stabilize Fixed Density Plasma as a Function of Charge-Exchange Decay Time. Standard beam trajectory and field, third-harmonic dee structure, and central fast-proton density of approximately 1×10^7 cm^{-3}.

Threshold studies with gas dissociation and a τ of 50 msec (chosen for comparison with the data of Fig. 1.3) showed that the maximum modulation would stabilize to densities of 1×10^7 cm^{-3}. Threshold density again varied as the square of the measured energy spread, as in the cyclotron experiments. There was, however, considerably more scatter in these data points, and the threshold vs energy spread curve was shifted about a factor of 2 to higher ΔE.

The results of the energy modulation experiments are not directly comparable with results of the cyclotron experiments. Interpretation of the former is considerably complicated by the fact that the technique combines, in a complex fashion, energy spread and orbit displacement. That the variation of threshold with $(\Delta E)^2$ is common to both techniques is regarded as significant. That higher energy spreads are required to stabilize by energy modulation is regarded to be an indication that the portion of the proton distribution determining stability does not require, and does not have, the total measured spread. This interpretation is quite reasonable in terms of the negative mass instability (Sect. 1.5), for properties of the more ordered portion of the trapped proton distribution then determine stability, and with the orbit and energy coupling provided by modulation, this portion could have significantly less energy spread than that measured for the total plasma.

1.4 OTHER EXPERIMENTS RELATING TO INSTABILITY MODE ASSIGNMENT

We have already presented considerable data relating directly to the problem of theoretical mode assignment for the principal proton-loss instability: the gyrofrequency mode[4] of instability described in earlier reports. Some features of the rf spectra, the fact that threshold hot-ion densities are as low as 3×10^5 cm^{-3}, and the pronounced stabilizing effect of increasing proton radial oscillation amplitudes were all reviewed in the previous report.[4] In the present report we have already described the lack of threshold sensitivity to some changes in proton axial oscillation amplitudes (Sect. 1.2) and threshold sensitivity to energy spread (Sect. 1.3).

In this section we introduce additional experimental data which were obtained specifically for comparison with theory. Section 1.4.1 describes measurements of growth times for the instability; Sect. 1.4.2 gives threshold measurements for a number of proton distributions in radial oscillation amplitude; and Sect. 1.4.3 discusses measurements of the frequency of rf signals from the $l = 1$ mode as a function of the minimum radial oscillation amplitude of the injected proton distribution. These experiments were all performed in the standard two-coil magnetic field. Section 1.4.4 describes stabilization by energy spread in two other field configurations.

1.4.1 Measurements of Instability Growth Times

The ideal plasma for these measurements would be one which could be established instantaneously at $t = 0$ with a known, controllable plasma density that remains constant during the initial phases of the instability buildup. In practice the ideal was approximated by injecting a molecular-beam pulse of controllable duration. This duration was made as short as would allow appearance of rf signals from the instability. The experiments were conducted with gas dissociation and the standard molecular-beam trajectory. Radio-frequency signals at the first and second harmonics were detected by using an electrostatic probe and band-pass filters.

Figure 1.5 is an example of rf signals with the shortest beam pulse that would consistently allow observation of an instability signal. Only the $l = 1$ mode appeared, and it developed above noise level after the H_2^+ beam had been shut off. The time scale for growth of the instability to maximum amplitude was very short compared with the exponential decay time (7 msec) for charge-exchange loss of the trapped proton density; for the time duration of interest, the density was essentially constant.

The beam pulse was gradually lengthened until the $l = 2$ mode appeared (Fig. 1.6). The density threshold for $l = 2$ is obviously the greater, and since $l = 2$ was observed before $l = 1$, the growth time for $l = 2$ is the shorter.

The total numbers of protons trapped under these conditions were determined from measurements of the charge-exchange neutrals. The average values from repeated measurements were 1.45×10^9 for $l = 1$ only and 1.85×10^9 for $l = 1$ and $l = 2$ modes. Individual measurements registered $\pm 15\%$ fluctuations about the average, in part due to ripple on the incoming beam current.

Measurements of the growth times were facilitated by simultaneously recording the rf signals on a second oscilloscope operated with higher sensitivity and faster sweep speed than that employed for Figs. 1.5 and 1.6. The four cleanest growths for each set of operating conditions were selected for detailed analysis. Semilog plots of the amplitude buildup above noise were usually reasonably linear (Figs. 1.7 and 1.8). The average growth time for $l = 1$ only was 40 μsec. The average times with both $l = 1$ and $l = 2$ observed were 50 μsec for $l = 1$ and 13 μsec for $l = 2$. Fluctuations of roughly 50% about these averages are believed to be primarily the result of fluctuations in beam current and some high-frequency ripple of the 600-kev accelerator power supply.

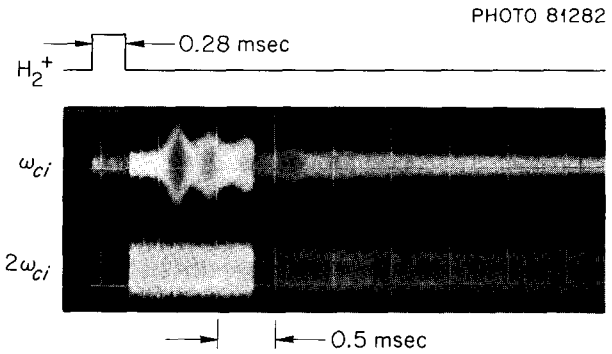

Fig. 1.5. Instability rf Signals for an Injected Beam Pulse of 0.28 msec. 1.45-ma H_2^+, $\tau \approx 7$ msec, standard trajectory and field.

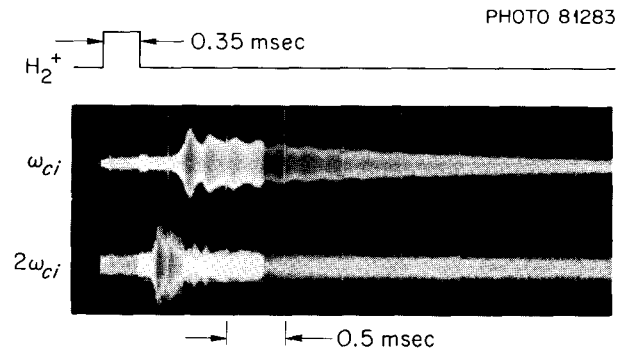

Fig. 1.6. Instability rf Signals for an Injected Beam Pulse of 0.35 msec. 1.45-ma H_2^+, $\tau \approx 7$ msec, standard trajectory and field.

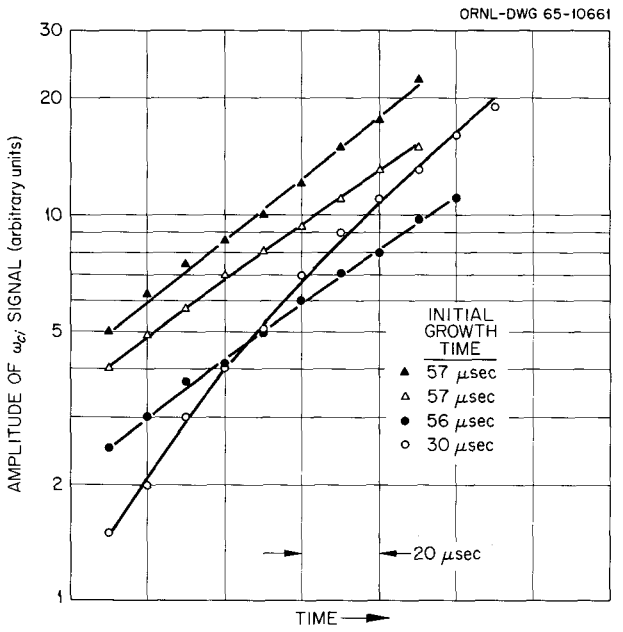

Fig. 1.7. Initial Growth of rf Signal Amplitude from $l = 1$ Instability Mode. Each curve represents an exposure like Fig. 1.6.

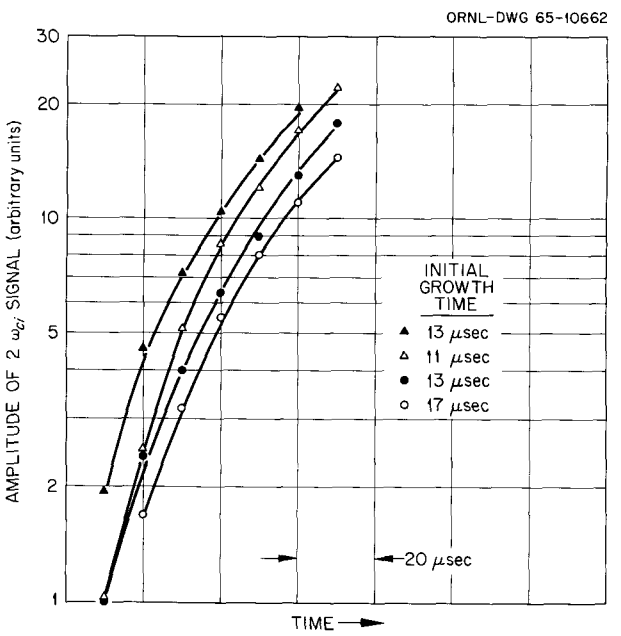

Fig. 1.8. Initial Growth of rf Signal Amplitude for $l = 2$ Instability Mode. Each curve represents an exposure like Fig. 1.6.

1.4.2 Threshold Measurements for Different Distributions in Radial Oscillation Amplitude

We first want to make clear how we are able to control the distribution in radial oscillation amplitude. Figure 1.9 will remind the reader of the standard molecular-beam trajectory. The point of closest approach of beam to axis is called beam turnaround. With this standard trajectory, the turnaround radius is equal to the proton equilibrium orbit radius. This trajectory produces the most ordered initial proton distribution, that is, the one characterized by the largest fraction of protons with very small radial oscillation amplitudes. One control on the proton distribution is the beam trajectory itself. Shifting the turnaround radius either inside or outside of the equilibrium orbit increases the *minimum* value of radial oscillation amplitude. In some experiments we have used a second control in the form of a 0.1-in.-diam rod perpendicular to the median plane and movable in radius. The plasma radius, and therefore the *maximum* permitted radial oscillation amplitude, is controlled by the position of this obstruction.

Figure 1.10 shows, as a function of canonical angular momentum, some general features of radial motion of 300-kev protons in the median plane. The effects of the two available controls can be described in a more quantitative fashion by reference to this figure.

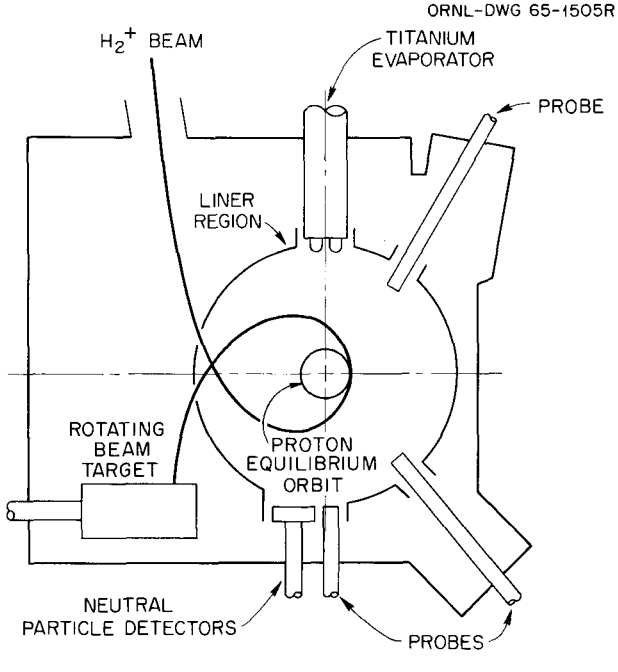

Fig. 1.9. Median Plane Section of the Experimental Facility, Showing the Standard Beam Trajectory with Turnaround at the Proton Equilibrium Orbit.

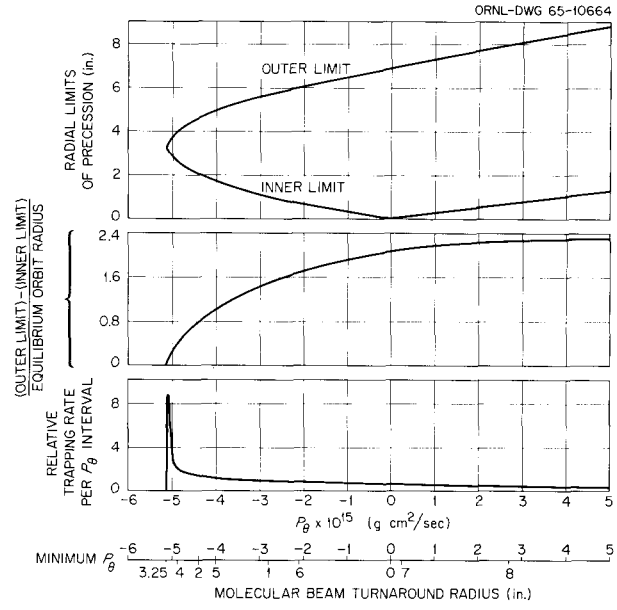

Fig. 1.10. Properties of Proton Orbits as Functions of Proton Canonical Angular Momentum and Molecular Beam Trajectory. For 600-kev H_2^+ injection, standard trajectory and field, gas dissociation.

The uppermost curve shows the radial limits of the proton orbits. For negative values of momentum the orbits link the magnetic axis; for positive values they do not. For the most negative value of momentum, the orbit is the equilibrium orbit, a circle of 3.25 in. radius which appears as a point on the curve. As momentum is increased, the protons precess with increasing radial oscillation amplitude. The limits of radial oscillation are given by the two branches of the uppermost curve, and the normalized amplitude of radial oscillation is given by the second curve.

The injected distribution depends on the molecular-beam trajectory. In particular the minimum momentum of the distribution is that of protons formed at beam turnaround. The relation between the values of minimum momentum and turnaround radius is given by the scale at the bottom of the figure.

The lowest curve shows the injected proton momentum distribution calculated for the standard 600-kev H_2^+ trajectory (turnaround at 3.25 in.

with beam linking the axis). A line trajectory and gas dissociation were assumed.

In the context of Fig. 1.10, we now state more precisely the effects of the two controls on the initially trapped proton distribution. Shifting the beam turnaround from the usual location shifts the minimum momentum of the distribution to higher values and therefore increases the minimum value of radial oscillation amplitude. Reducing the plasma radius (normally 8 to 9 in.) acts as a similar control on the other end of the momentum distribution and reduces the maximum radial oscillation amplitude. Use of these controls allows one to measure threshold properties of various distributions in radial oscillation amplitude. We now proceed to discussions of such measurements, which have been of three general types.

1. *Normal beam turnaround and plasma radius varied.* These experiments, like those to follow, were conducted with gas dissociation. The basic procedure was to adjust the beam trajectory and then to measure the total number of protons trapped at threshold as a function of the position of the radial obstruction. Threshold was determined by cutting on the H_2^+ beam and recording the rf probe signal and the charge-exchange loss current from the plasma. The instability signal appeared above noise at a time interval Δt after injection was started. The trapped population at threshold was evaluated from Δt, the magnitude of the steady-state charge-exchange current, and the charge-exchange decay time, or, alternatively, from the decay time and the magnitude of the charge-exchange current at Δt.

Results typical of these experiments are shown in Fig. 1.11. The symmetry about $R = 0$ and the near symmetry about the $R = 3.25$ in. values are readily understood. The locations of the minimum threshold values are the points nearest $R = 3.25$ in. These points are threshold values for proton distributions with very small radial oscillations about the circular equilibrium orbit. The maximum threshold values occur for the most unrestricted proton distribution, that which is obtained with the normal plasma radius.

One experimental observation, that the value of Δt does not vary with the position of the radial obstruction, is of particular significance. For this observation indicates that the small group of protons near equilibrium orbit, common to all of the unstable distributions, determines threshold even in the presence of a much larger population of protons with less ordered orbits.

We define the standard plasma distribution as that distribution established using the normal plasma radius (8 in.) and the standard beam trajectory. The stability properties of this standard distribution are therefore those of a toroidal distribution at its core. This toroidal distribution is isolated when the plasma radius is as close to the H^+ equilibrium orbit radius (3.25 in.) as will allow the instability to develop.

The toroidal distribution has a major diameter equal to the H^+ equilibrium orbit diameter and a minor diameter of approximately 1 cm. From extrapolation of energy spread data obtained as described in Sect. 1.3.1, the energy spread of protons within this torus is 4 kev, which is also one-half the estimated ripple of the 600-kev molecular beam supply. Experimental determinations of threshold line density for the toroidal distribution produce values of 6 to 16×10^5 energetic protons/cm. The threshold population of the toroidal distribution relative to that of the standard distribution is the ratio of the minimum to maximum ordinate values of curves like Fig. 1.11. Careful determinations of this ratio show that the toroidal distribution contains 2 to 3% of the population of the standard distribution.

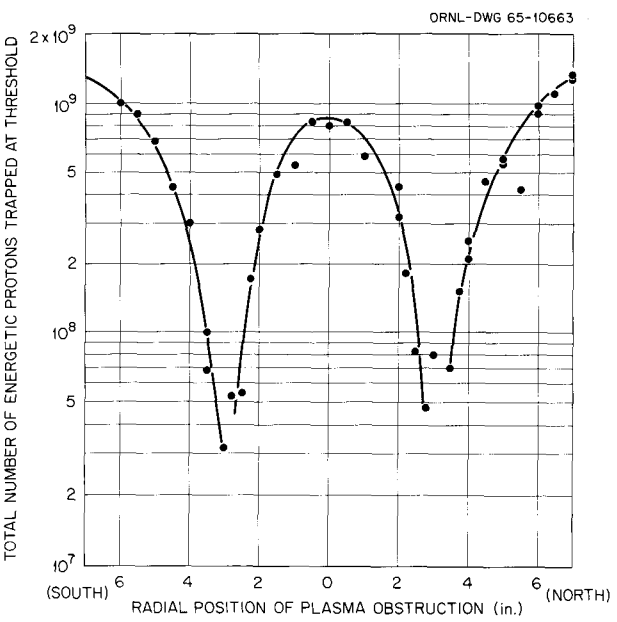

Fig. 1.11. Threshold Population as a Function of Radial Position of a Plasma Obstruction. Standard trajectory and field, 1.5-ma H_2^+, $\tau \approx 75$ msec. No plasma is trapped with the obstruction at 3.25 in.

2. *Normal plasma radius and beam turnaround varied.* In these experiments the normal plasma radius of 8 in. was maintained, so the positive cutoff of the injected canonical angular momentum distribution was constant. The quantity varied was the minimum momentum of the distribution – hence the minimum value of radial oscillation amplitude.

The stabilizing effects of increasing the minimum value of radial oscillation amplitude were described in the previous report.[5] There threshold was given as a function of turnaround radius, which was located by use of a movable target for the molecular-ion beam.

We have repeated these experiments with the more precise determinations of the minimum momentum of the injected distribution that were permitted by use of the movable radial obstruction. The beam was first adjusted, and then the obstruction was gradually inserted into the plasma while the charge-exchange current from the plasma was being observed. Disappearance of detectable charge-exchange current defined the outer radial limit of oscillation for the minimum momentum group (see Fig. 1.10). The obstruction was advanced further toward the axis until charge-exchange current was again detected, thus also defining the inner radial limit. When interpreted in terms of the proton orbit properties of Fig. 1.10, the two limits gave identical values of momentum.

Figure 1.12 shows the variation of threshold with minimum momentum value of the injected proton distribution as obtained in two different runs. Both runs involved determining the momentum value by the technique just described. The solid-line curve of Fig. 1.13 is the line fitted to the data of Fig. 1.12, but here threshold is given as a function of radial oscillation amplitude of the protons with minimum momentum.

3. *Both plasma radius and beam turnaround varied.* We realized that the injected distributions involved in the studies just described were not the best available for direct comparison with theory. For this reason we performed another series of experiments using both controls on the trapped distribution. The results are shown by the broken-line curve of Fig. 1.13. For each point the beam turnaround was changed to set the minimum value of oscillation amplitude, and then the plasma radius was reduced to give the smallest maximum value of oscillation amplitude that would permit the instability. This adjustment was such that the spread in radial oscillation amplitude of the trapped distribution at each point was typically one-third to one-half of an X axis division. The dotted-line curve therefore gives thresholds for narrow distributions in radial oscillation amplitude.

In paragraph 1 above, we reported that the threshold properties of the standard distribution were those of the toroidal core; that is, that Δt remains constant with increasing plasma radius. Similar measurements of Δt as a function of plasma radius have been made with beam trajectories corresponding to values of about 0.3 and 0.6 on the abscissa of Fig. 1.13. For these trajectories the addition of less-ordered protons exerts a stabilizing influence, and Δt increases as the radius is increased to the normal value. The change of Δt is responsible for the difference in shapes of the curves of Fig. 1.13.

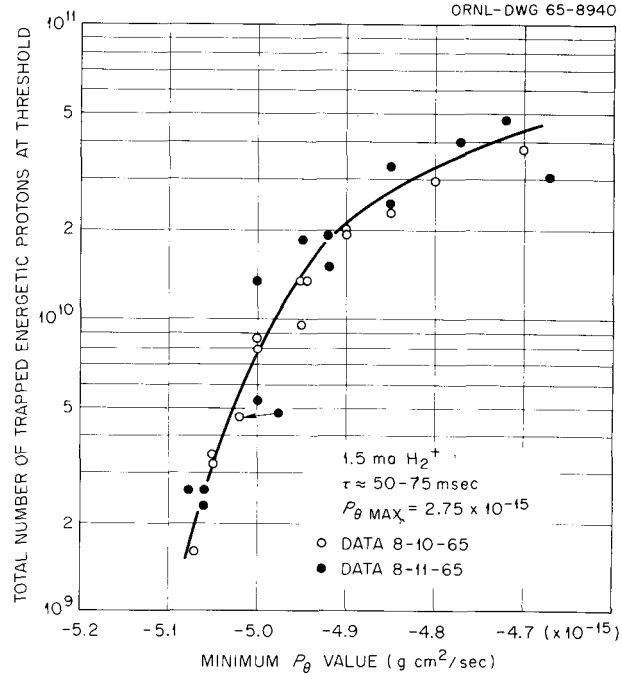

Fig. 1.12. Threshold Population as a Function of the Minimum Canonical Angular Momentum (P_θ) of the Injected Proton Distribution. Minimum P_θ controlled by changing beam turnaround radius. Standard field, fixed plasma radius of 8 in.

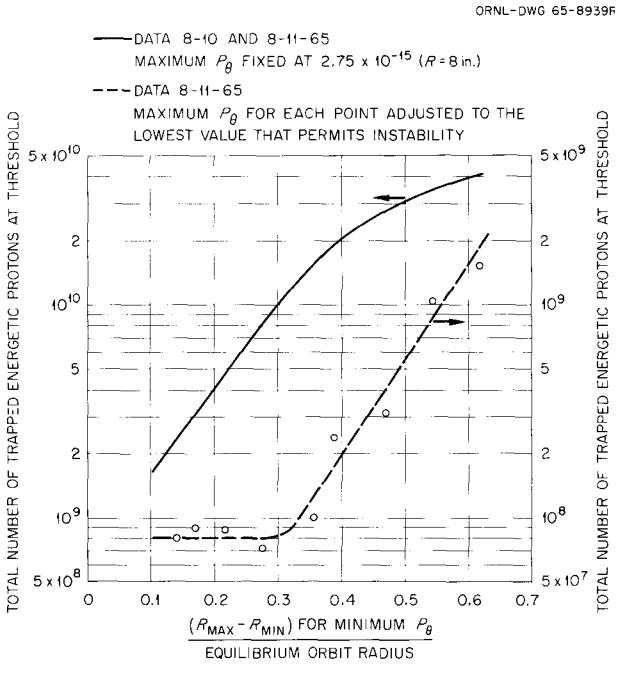

Fig. 1.13. Threshold Population as a Function of Minimum Radial Oscillation Amplitude of the Injected Proton Distribution. Minimum oscillation amplitude controlled by changing beam turnaround radius. Solid-line curve is data of Fig. 1.12. For dotted-line curve, maximum oscillation amplitude was reduced by control of plasma radius.

1.4.3 Measurements of $l = 1$ Mode Frequency

We have investigated the sensitivity of the $l = 1$ mode frequency to changes in beam turnaround radius when operating with a plasma radius of 8 in. High-pressure gas dissociation was used in order to eliminate the upward excursions of mode frequency previously described.[7] The frequency range from 14 to 15 Mc was examined with a spectrum analyzer. The resolution was such that changes of 0.05 Mc could be detected.

The gyrofrequency for protons on equilibrium orbit is 14.6 Mc. This was the mode frequency for the standard beam trajectory. As the trajectory was altered, the only frequency change noted was a shift to 14.55 Mc for the most displaced trajectory (0.6 on the abscissa of Fig. 1.13).

[7] *Thermonuclear Div. Semiann. Progr. Rept. Oct. 31, 1964*, ORNL-3760, sect. 1.2, p. 4.

1.4.4 Threshold Changes with Energy Spread in Other Field Configurations

The negative mass instability is sensitive to variation of the magnetic field index n, where

$$n = -\frac{r}{B_z}\frac{dB_z}{dr},$$

and the parameters are evaluated at the equilibrium orbit. For this reason some experiments were performed to investigate threshold sensitivity to changes in n. The arrangement of magnetic field coils was altered by spacing the mirror coils further apart (coil centers at $Z = 19\frac{1}{4}$ in. rather than the usual $15\frac{1}{4}$ in.) and adding additional mirror coils close to the median plane (coil centers at $Z = 3$ in.). The two sets of mirror coils were powered by separate generators. The exit H_2^+ beam target and diagnostic probes were also relocated.

Two values of field index have been used in this revised geometry, $n = 0.019$ and 0.060. The corresponding mirror ratios were 1.7 and 2.6. In each case the field magnitude was adjusted for the usual 3.25-in. equilibrium orbit radius. By way of comparison, the standard field index and mirror ratio are 0.09 and 2.0 respectively.

Difficulties with H_2^+ beam control allowed meaningful comparisons only for H_2^+ beam trajectories which approached the axis to a point of tangency at the equilibrium orbit radius. The effects of changing the molecular trajectory therefore were not investigated, and the studies were confined to measurements of threshold changes with energy spread and with plasma radius for the two values of field index.

Energy spread was controlled by use of the third-harmonic dee structure described in Sect. 1.3.1. The observed variations of threshold are shown in Fig. 1.14. The change of field index has a definite effect on threshold, with the lower field index producing the lower thresholds. Both curves show threshold varying approximately as $(\Delta E)^2$, as was the case in the similar experiments described in Sects. 1.3.1 and 1.3.2.

Figure 1.15 shows the response of threshold to plasma radius for the two values of field index. The experiment was equivalent to that described in Sect. 1.4.2 (paragraph 1), and the parameter Δt defined there is again of interest. For each value of field index, Δt was nearly constant, and

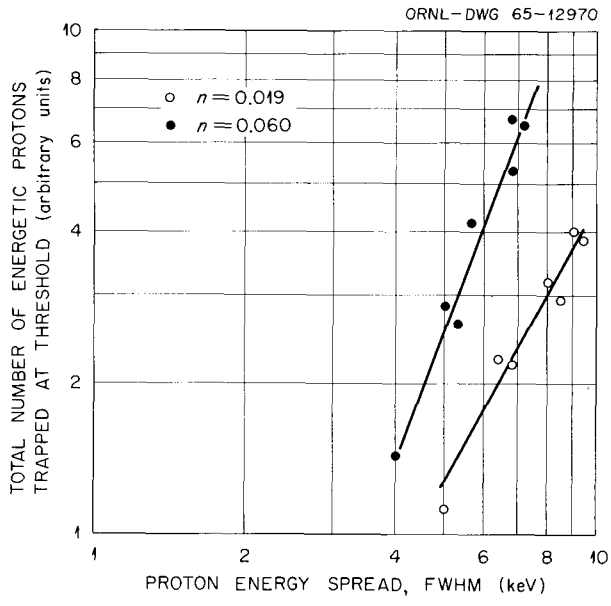

Fig. 1.14. Threshold Population as a Function of Proton Energy Spread for Different Values of Field Index. Standard trajectories, third-harmonic dee structure, $\tau \approx 50$ msec.

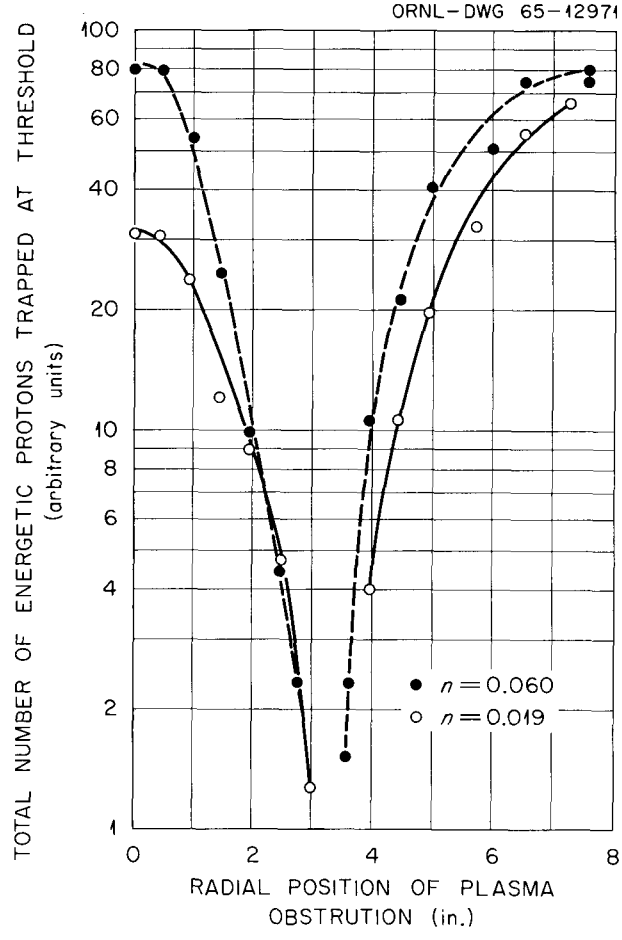

Fig. 1.15. Threshold Population as a Function of Radial Position of a Plasma Obstruction for Different Values of Field Index. Standard trajectories, $\tau \approx 50$ msec. No plasma is trapped with the obstruction at 3.25 in.

so we again conclude that a toroidal distribution of protons near equilibrium orbit determines threshold. For each value of field index, the population of the toroidal distribution was 2% of the population of the appropriate "standard" plasma distribution. Over most of the range of plasma radius, a comparison of the two curves of Fig. 1.15 indicates thresholds lower by about a factor of 2 in the case of the lower field index. We feel that the coincidence of the curves for R = 2 to 3 in. is the result of some experimental difficulties that arose as data were being obtained in this region with n = 0.019. We believe that more accurate data would show a constant displacement of the two curves.

1.5 COMPARISONS OF EXPERIMENTAL DATA AND NEGATIVE MASS THEORY

The general question of theoretical mode assignment for the gyrofrequency mode of instability was considered in some detail in the previous report.[4] Primarily on the basis of the low density threshold obtained with normal operation of the facility, it was judged that the instability was probably negative mass, although drift cyclotron with $k_{\parallel} \neq 0$ also seemed a possibility. Here we make quantitative comparisons of experimental data with predictions of negative mass theory and again examine the possibility of drift-cyclotron instability. The results strengthen our conclusion that the correct mode assignment is indeed negative mass.

A theory of negative mass instability in DCX-1 is presented in Sect. 7.1 of this report. There it is shown that energy spread, radial oscillations, and axial oscillations exert stabilizing influences. The relative importance of these stabilizing terms can be evaluated from the stability criterion of Sect. 7.1.

We first consider experiments in which we can ascribe the instability threshold to the toroidal

distribution that consists of protons on near-equilibrium orbits. These experiments are those which involve injecting with the standard beam trajectory. For the standard field index, the experiments include measurements of the threshold population and growth times of the unperturbed distribution, and measurements of threshold population as a function of energy spread. For the two other values of field index, they include measurements of relative threshold population as a function of energy spread.

Using the negative mass stability criterion of Sect. 7.1 and substituting suitable parameters for the toroidal distribution ($\Delta E \geqq 4$ kev, $\Delta d \approx \Delta\delta \sim 0.5$ cm) shows that energy spread dominates by significant factors (5 to 10 for $\Delta E = 4$ kev). The results of Sect. 7.1 then reduce to those obtained earlier by T. K. Fowler,[8] who considered an accelerator-like version of negative mass theory with stabilization by energy spread. The calculation was not given external distribution, and for this reason the essential features are presented in Sect. 1.8.

We consider now the threshold density of the unperturbed toroidal distribution and compare the value from the stability criterion, Eq. (1.11), with the experimental values (6 to 16×10^5 cm^{-1} from Sect. 1.4.2, paragraph 1). The appropriate parameters for use in the equation are $n = 0.09$, $\Delta E = 4$ kev, $\gamma_1 \approx 6.5$, and $E_0 = 300$ kev. From theory the threshold line density is 7×10^5 cm^{-1} for this distribution, in reasonable agreement with the experimental values. This line density corresponds to a volume density of about 4×10^5 cm^{-3}.

We next treat the growth rate measurements, using Eq. (1.12). For τ_1 we take 40 μsec, the average value from experiment (Sect. 1.4.1), and for N_{01} we take 7×10^5 cm^{-1}, the value from the preceding calculation. Treating N as the unknown yields $N = 1.2 \times 10^6$ cm^{-1}, corresponding to a toroidal distribution population of 6.3×10^7 fast protons. Comparison with experiment is made by noting that the ratio of the toroidal population to the population of the standard distribution (1.45×10^9 from Sect. 1.4.1) is 4.4%. This value lies somewhat outside the experimentally determined range for this population ratio, 2 to 3%, but in view of the uncertainties in assigning and using distribution function parameters, the agreement of experiment and theory is good. Some features of the experiment (τ_1 values vary over a 2:1 range, $\langle \tau_1 \rangle$ did not decrease as expected in going from 0.28- to 0.35-msec beam hold-on times, and the ratio τ_2/τ_1 is only half the expected) probably reflect fluctuations in the values of N and N_{01}.

The results of the energy spread experiments (Fig. 1.3) are in close quantitative agreement with the stability criterion for negative mass if we use the measured full-width-at-half-maximum energy spread for ΔE and 6% of the total population for the population of the unstable core. The 6% value also lies somewhat outside the experimentally determined range, but the agreement of experiment and theory is still considered good.

The variations of field index produced results (Fig. 1.14) that are also in agreement with negative mass theory. The experiment (Sect. 1.4.4) showed that the threshold populations of the toroidal distributions relative to those of the "standard" distributions were the same (2%) for field index values of 0.019 and 0.060. From the stability criterion it then follows that the observed thresholds for the "standard" distributions should, for negative mass, vary as the product (field index) $(\Delta E)^2$. Figure 1.16 shows that the experimental data behave nearly in this fashion. Somewhat

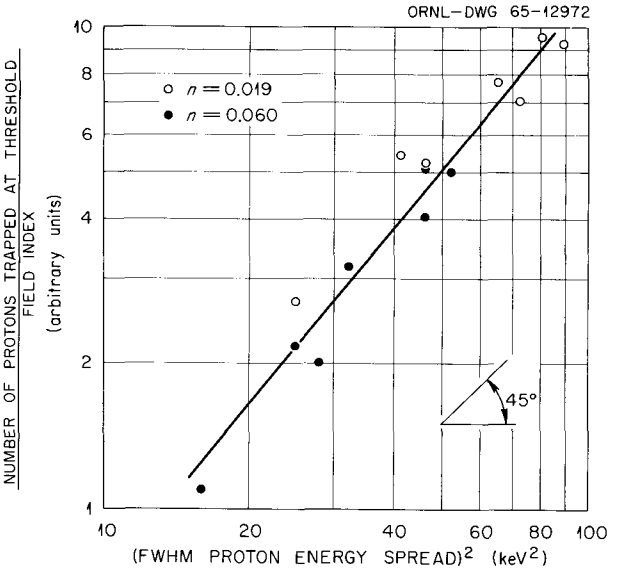

Fig. 1.16. Ratio of Threshold Population to Field Index as a Function of Proton Energy Spread Squared for Different Values of Field Index. Experimental data are those of Fig. 1.14. Agreement with theory is indicated by the fit to a single line with 45° slope.

[8] Present address: General Atomic, La Jolla, Calif.

better data, like Fig. 1.15, are desirable, for the two curves should have been displaced by a factor of 3, the ratio of the field index values.

We now turn to those experiments which involved displacement of the molecular ion trajectory so as to increase axial or radial oscillation amplitudes. The observation that threshold is relatively insensitive to increasing average axial oscillation amplitude cannot be subjected to critical theoretical comparison. Such a comparison requires knowledge of the proton distributions in both axial and radial oscillation amplitudes, and these distributions are not well defined in the experiment. However, the observation does not appear to be inconsistent with negative mass theory. The work involving radial oscillations alone is more definitive. Section 7.1 shows that the stabilizing effect of radial oscillations and the variation of mode frequency with these oscillations are in reasonable agreement with negative mass theory.

Having shown that the observed threshold properties of this instability are very similar to those indicated by negative mass theory, we wish to examine further the possibility that some instability other than negative mass might actually be involved. An earlier discussion[4] led to the conclusion that the low observed threshold density for the standard plasma distribution (about 4×10^5 cm^{-3}) was consistent with negative mass and possibly some $k_{||} \neq 0$ modes of drift-cyclotron instability. The latter possibility could not positively be ruled out on general grounds, such as theoretical threshold density higher than the observed (with cold but not zero-temperature electrons the growth rate does not vanish for $\omega_{pe} < \omega_{ci}$ but only decreases rapidly),[9] or axial wavelengths of growing waves too large to exist within the plasma chamber. However, the results of Harris[9] indicate that the threshold can be reduced to the low experimentally observed values ($\omega_{pe} \approx \frac{1}{2}\omega_{ci}$) only in the presence of large shift of unstable mode frequency away from ω_{ci}. No such shift is observed in these experiments. From this consideration and the demonstrated agreement with negative mass theory, we conclude that negative mass is the correct mode assignment.

Since the experimental data justifying mode assignment were obtained for specific operating conditions and a limited density range, we next anticipate and attempt to answer two basic questions regarding the generality of the assignment.

Question 1: The experiments relating directly to mode assignment concern properties of the instability at or near threshold. Granted that these properties are those of negative mass, what are the grounds for assuming that the instability is still negative mass at higher densities in steady state? The experiments demonstrated control of threshold to densities of 2 to 3×10^7 cm^{-3}, in agreement with negative mass theory. The question therefore concerns the nonlinear development of the instability at densities up to the limiting value, 1 to 2×10^8 cm^{-3}. Since the theory is a linear approximation and accurate only for initial development of the instability, our argument is necessarily qualitative. Essentially, it is that once threshold is exceeded, the measurable properties of the instability do not appear to change in any basic fashion as the density is increased. The rf signals increase in amplitude but are otherwise relatively unchanged. Furthermore even at the highest available densities, during plasma decay following cessation of injection, the signals disappear in a small fraction of a charge-exchange decay time. Despite the stability of such decaying plasmas, for several decay times the density can remain above the value initially required for instability growth. The steady-state instability is therefore not to be attributed to a simple density threshold in terms of either ions or electrons. Instead it is due to specific features of the anisotropic ion distribution, such as is the case for negative mass.

Question 2: The mode assignment experiments were performed with gas dissociation, but instability-driven losses are observed only with Lorentz dissociation. How does one justify the position that the threshold studies were studies of the "proton-loss instability"? In our previous detailed studies we have observed no basic differences in properties of the gyrofrequency mode with Lorentz dissociation as compared with gas dissociation. The latter was chosen for these experiments purely as a matter of convenience.

1.6 ORBITS AND ORBIT FREQUENCIES

C. E. Nielsen

In nonuniform magnetic fields, such as the mirror field, or mirror plus multipole, gyrofrequency is

[9] E. G. Harris, CLM-R32 (1963).

not well defined. It is nevertheless desirable, both for understanding of experimentally observed frequencies and for use in theoretical stability analysis, to define, if possible, frequencies by which orbits in general can be characterized, and to determine the values of these frequencies. We here attempt such definitions and report recent progress in analytic calculation of orbits and orbit frequencies. Since nearly centered orbits in the mirror field are fairly well described by betatron orbit theory, we discuss eccentric orbits, about which betatron theory gives no information.

The simplest eccentric orbit in an axisymmetric mirror is the one traversed by a particle confined to the median plane. The particle in this orbit oscillates radially and drifts on the average in azimuth. Its radial motion is perfectly periodic and is therefore characterized by a well-defined radial frequency. Its azimuthal motion is not in general periodic, since most median-plane orbits do not close after drift through 2π in azimuthal angle ϕ, but it may be characterized by a mean drift rate.

When we consider the more general orbit with oscillation in the z direction superimposed on radial and azimuthal motion, we see that none of the three components of motion is periodic. We then characterize the motion by the three *mean* frequencies of radial oscillation, axial oscillation, and azimuthal drift, defined in each case by averages over a sufficiently long time. The same description may be applied also to orbits in the mirror plus multipole field, providing the averaging time is chosen appropriately.

The procedure for calculating orbits and frequencies will be illustrated by analysis of a median-plane eccentric orbit in an axisymmetric mirror. Since a curve is everywhere characterized by a local radius of curvature, the orbit followed by a particle starting with given initial conditions may be traced out by assigning to it the radius of curvature appropriate to each point.

Let a be the local radius of curvature; it is a function only of r in an axisymmetric field. Let r and ϕ be polar coordinates and define angles α and γ as shown in Fig. 1.17. From the figure we see that the following relations hold:

$$\alpha = \gamma + \phi \,, \tag{1.1}$$

$$d\alpha = \frac{ds}{a(r)} \,, \tag{1.2}$$

$$dr = ds \cos \gamma \,, \tag{1.3}$$

$$d\phi = \frac{ds}{r} \sin \gamma \,. \tag{1.4}$$

It is convenient to develop a description in terms of the parameter γ partly because γ is known to increase by 2π during one radial oscillation period whereas the more usual variables r, ϕ, and t change by amounts unknown in advance. Elimination of $d\phi$, ds, and $d\alpha$ from Eqs. (1.1) through (1.4) leaves the relation

$$\frac{dr}{r} \sin \gamma + d\gamma \cos \gamma = \frac{dr}{a} \,,$$

which integrates to

$$r \sin \gamma \Big]_{r_1}^{r_2} = \int_{r_1}^{r_2} \frac{r\, dr}{a(r)} \,. \tag{1.5}$$

This equation expresses the equivalent of conservation of canonical angular momentum in an axisymmetric field.

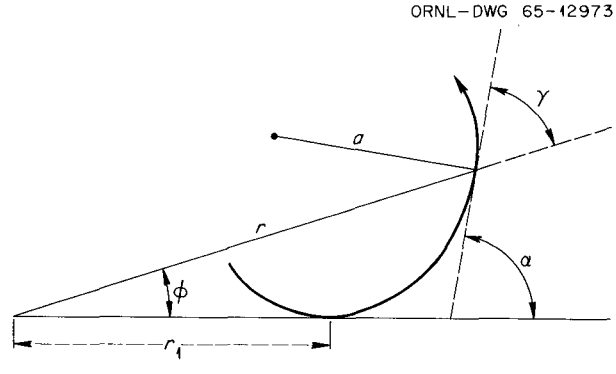

Fig. 1.17. Orbit Curve of Charged Particle in Magnetic Field, Showing Definitions of Several Parameters.

Dynamical laws and the characteristics of the field are added to the preceding purely geometrical relations in the evaluation of $a(r)$:

$$\frac{mv^2}{a(r)} = \frac{qv\,B(r)}{c} .$$

Let $B(r)$ be of the form

$$B(r) = B_0\left(1 - \epsilon\,\frac{r^2}{a_0^2}\right) ,$$

in which a_0 is the radius of the orbit of a particle of speed v_0 in field B_0, $1/a_0 \equiv qB_0/mcv_0$, and write

$$\frac{v}{a(r)} = \frac{v_0}{a_0}\left(1 - \epsilon\,\frac{r^2}{a_0^2}\right). \tag{1.6}$$

The dimensionless variable r/a_0 is of order unity for orbits to be considered, and $\epsilon r^2/a_0^2 \ll 1$, so that a solution to first order in ϵ will be adequate.

It is convenient to choose r_1 in Eq. (1.5) as the radius where $\gamma = 0$ and $d\phi/ds = 0$. The lower limit of the integral, which corresponds to the canonical angular momentum, is then denoted by p. With this choice, Eqs. (1.5) and (1.6) combine to give

$$\frac{v_0}{v}\cdot\frac{r^2}{2a_0^2}\left(1 - \epsilon\,\frac{r^2}{2a_0^2}\right) - \frac{r}{a_0}\sin\gamma - \frac{p}{a_0 v} = 0 . \tag{1.7}$$

The ϵ term in this equation is small, so that the equation can be solved for r by a successive approximation procedure. For the zero-order approximation, set $\epsilon = 0$:

$$\left(\frac{r}{a_0}\right)^{(0)} = \frac{v}{v_0}\left(\sin\gamma + \sqrt{\sin^2\gamma + 2pv_0/a_0v^2}\right)$$

$$\equiv g_0(\gamma) .$$

This solution describes a circle, of radius a_0 when $v = v_0$, tangent to r at r_1.

To obtain a result to first order in ϵ, put the zero-order g_0 into the equation as the coefficient of ϵ. The first-order result is

$$\left(\frac{r}{a_0}\right)^{(1)} = \frac{v}{v_0}\,\frac{\sin\gamma + \sqrt{\sin^2\gamma + b(1 - \frac{1}{2}\epsilon g_0^2)}}{1 - \frac{1}{2}\epsilon g_0^2} \tag{1.8}$$

$$\equiv g_1(\gamma) , \qquad b \equiv \frac{2pv_0}{a_0v^2} .$$

This describes the radial dependence $r^{(1)}(\gamma)$ of the orbit, on the approximation that radius of curvature has the value derived from the field at the same γ on the circular orbit $r^{(0)}(\gamma)$ having the same canonical momentum.

Radial period is obtained by using $r(\gamma)$ from Eq. (1.8) to evaluate dr in Eq. (1.3) in terms of γ. As already noted, γ increases by 2π in one radial cycle, and the corresponding time is $\tau = 1/v\int ds$. Correct to first order in ϵ, Eq. (1.8) may be simplified by expansion to give

$$\left(\frac{r}{a_0}\right)^{(1)} = \left(g_0 - \frac{\epsilon}{4}\frac{v}{v_0}\,b\,\frac{g_0^2}{\sqrt{\sin^2\gamma + b}}\right)\left(1 + \frac{\epsilon}{2}g_0^2\right)$$

$$= g_0 + \frac{\epsilon}{2}g_0^3 - \frac{\epsilon}{4}\frac{vb}{v_0}\,\frac{g_0^2}{\sqrt{\sin^2\gamma + b}} .$$

When this expression is differentiated, divided by $v\cos\gamma$, simplified by consideration of the fact that terms with value antisymmetric about π will contribute nothing to the integral, and integrated from 0 to 2π the result is:

$$\tau_r = \frac{2\pi}{\omega_0}\left(1 + 3\epsilon\,\frac{v^2}{v_0^2} + \epsilon\,\frac{2p}{a_0v_0}\right), \tag{1.9}$$

$$\omega_0 \equiv \frac{v_0}{a_0} .$$

To check this result it may be seen that as $v \to 0$ the orbit frequency reduces to just the value appropriate to the field at $r = r_1$. According to this first-order calculation, orbit radial frequency decreases linearly both with energy and with canonical momentum.

In a similar fashion azimuthal drift is obtained by using ds and r in terms of γ in Eq. (1.4). The

calculation gives for drift angle $\Delta\phi$ per radial oscillation cycle

$$\Delta\phi = 2\pi\epsilon\left(\frac{v}{v_0}\right)^2 . \qquad (1.10)$$

Thus, to first order in ϵ, drift angle per radial cycle depends only upon energy and is independent of canonical momentum. It follows that at a given energy, drift frequency changes in the same way as radial frequency with change in canonical momentum.

It is possible to generalize this method of orbit analysis in terms of differential geometry to problems involving electrostatic or gravitational potentials and to some three-dimensional orbits. As one example of a three-dimensional problem, the form and frequency of a centered periodic orbit in a mirror plus quadrupole field have been calculated. It may perhaps be feasible to deal also with eccentric orbits in multipole fields and with orbits characterized by axial oscillations.

1.7 INJECTION INTO MODE I AND MODE II DISCHARGES[10]

We have studied the charge-exchange signals from plasmas established by high-energy molecular ion injection into mode I and mode II discharges operated along the axis of the DCX-1 facility. The arc reflectors were mounted outside the mirror coils. The pressure differential required for mode II was established by bleeding deuterium gas into the plasma chamber and isolating this chamber from the reflectors by restricting orifices at the coil throats. The input power for mode II operation was from 20 to 50 kw and the neutral gas pressures were typically 2 to 5×10^{-4} torr (plasma chamber) and 1 to 2×10^{-5} torr (reflector region). For mode I the values were approximately 5 kw and 5×10^{-4} torr. The injected beams employed were 600-kev H_2^+ and 400-kev H_3^+ on the standard beam trajectory (turnaround at $R = 3.25$ in.), and 600-kev H_2^+ with turnaround at the magnetic axis.

The experimental observations differ in detail, but both arcs appeared to contribute to dissociation. In comparison with gas dissociation at the same indicated ion gage pressure in the plasma chamber, operation with the arcs yielded increased trapping fractions. The evidence was most clear with the beam trajectory displaced to the center of the arc column (displaced to axis); the trapping enhancement then ranged from 10 to 100%. No definite conclusion was reached as to the size of the "burned-out" region possibly associated with mode II. It was not possible to isolate the effects of burnout on fast proton lifetime from the effects of the gross pumping action displayed by both discharges. If present, the burned-out region was small compared with the orbits of the trapped energetic protons (orbit diameter of 6 in.).

Additional experiments of this nature are planned.

1.8 CALCULATION OF THE NEGATIVE MASS INSTABILITY FOR DCX-1

We outline the essential features of a negative mass theory[11] which is concerned with stabilizing effects of energy spread on instability arising in the accelerator-like portion of the proton distribution formed in DCX-1 during operation with the standard beam trajectory. The theory ignores possible stabilizing effects of axial and of radial oscillation amplitudes.

The work of an original paper[12] on negative mass instability in accelerators is closely followed. A torus of charged particles of major radius R and minor radius a is considered. The ratio a/R is taken to be small, so the ions approximately execute closed circular orbits of radius R. The ion ring is neutralized in equilibrium by a uniform negative background of cold electrons. Being unable to move across the field, these electrons have no azimuthal motion and are treated as fixed. The ion charge is distributed uniformly in cross section. The equilibrium phase space distribution is assumed to be symmetric in ϕ, the azimuthal angle, and square in p, the azimuthal momentum. The distribution in p has width $2W_0$ and is centered at p_0, the momentum of an ion with equilibrium orbit radius equal to the major

[10] With I. Alexeff and R. V. Neidigh.

[11] By T. K. Fowler. A complete description of the calculation was given in an internal report, July 1961.

[12] C. E. Nielsen, A. M. Sessler, and K. R. Symon, "Longitudinal Instabilities in Intense Relativistic Beams," International Conference on High Energy Accelerators and Instrumentation, CERN, 1959.

radius R. The stability of the distribution for small perturbations in azimuth is examined by the usual techniques. The fact that the torus of charge is not shielded from itself is taken into account, and in this way the calculation of the space-charge electric field departs from the method of ref. 12.

Use of the above assumptions results in a stability criterion,

$$\frac{Nq^2\gamma_l}{n} < \frac{(\Delta E)^2}{8E_0}, \tag{1.11}$$

where

$2\pi RN$ = total number of ions in the torus (N is a line density),

q = elementary charge,

n = field index = $-r/B(dB/dr)$ evaluated at equilibrium orbit radius R,

E_0 = energy of ions with equilibrium orbit radius R,

ΔE = energy spread of ions in the torus,

$$\gamma_l = \frac{1}{l}\int_0^{2\pi} \frac{\sin\phi \sin l\phi \, d\phi}{\left[4 \sin^2 \tfrac{1}{2}\phi + (a/R)^2\right]^{3/2}},$$

l = harmonic number,

and cgs units are employed.

The instability growth time is given by

$$\tau_l = \frac{MR}{lq(nM\gamma_l)^{1/2}(N - N_{0l})^{1/2}}, \tag{1.12}$$

where

R = equilibrium orbit radius of ions with energy E_0,

M = mass of ion,

$N_{0l} = \dfrac{n(\Delta E)^2}{8q^2\gamma_l E_0}$ = threshold line density for lth mode.

For DCX-1, the appropriate values of γ_l are $\gamma_1 \approx 6.5$ (at ΔE = 4 kev), $\gamma_1 \approx 6.0$ (20 kev), $\gamma_2 \approx 5.6$ (4 kev), and $\gamma_2 \approx 4.6$ (20 kev).

2. Injection and Accumulation: Multiple-Pass Experiments (DCX-2)

P. R. Bell, J. S. Culver, R. C. Davis, S. M. DeCamp, J. C. Ezell, G. G. Kelley, N. H. Lazar, J. F. Lyon, O. B. Morgan, T. F. Rayburn, R. F. Stratton, C. W. Wright, A. J. Wyrick

2.1 TRAPPED PLASMA DENSITY AND ENERGY

During a considerable portion of this report period, DCX-2 was shut down for major repairs of two types: replacement of a mirror coil and major cleaning of the vacuum system. One of the major difficulties associated with attempting to improve the vacuum system has been the observation of a large peak in the mass spectrometer at mass 18, interpreted as water. This peak, in general, represents 50 to 80% of the total residual gas of the machine at base pressures. Effort has been expended in leak checking water lines, etc., to ensure that this water peak is not due to small leaks. In addition, we initiated some experiments using liquid-nitrogen cooling on large surfaces of the connecting cones between the main liner and the mirror coil liner sections. This resulted in a significant pressure reduction. We have, therefore, made modifications in the liner to enable us to apply liquid nitrogen to the entire liner, if it appears desirable after cleaning.

The data obtained with gas dissociation have been analyzed in greater detail, and as a result certain aspects of the plasma behavior have become clearer. We have used both the integral of the charge-exchange flux after the beam is turned off and the counting rate as a function of energy in the silicon barrier detector with the beam on to determine the density of the plasma in the midplane. In both cases one must make a correction for the fact that the detector samples only a small fraction of the total neutral current emitted from the plasma. The relation for ion density, using the geometrical correction for the foil neutral detector, has been given previously[1,2] and is

$$n_+ = \left(\frac{2\pi R_D L}{A_{\mathrm{eff}}\epsilon}\,\frac{1}{\pi r_p^2 L}\right)\int I_{cx}\,dt\,,$$

where $\int I_{cx}\,dt$ is measured, R_D is the distance from the detector to the axis of DCX-2, L is the plasma length, and A_{eff} (the effective detector area) is two-thirds of the foil area because of the attenuation of the neutrals in the copper support grid. The term ϵ is the effective transmission of the foil and is approximately $\frac{1}{2}$ for typical energy distributions, and r_p is the mean plasma radius. In general we take r_p as 15 cm, although we recognize that the average plasma radius probably varies to some extent with plasma behavior. In using this equation we assume azimuthal symmetry in the emission of the charge-exchange current and also assume that the plasma is effectively long compared to the length of the detector. It must further be remembered that this method of determining density is independent of any estimate of the lifetime of the plasma; it relies instead on a direct measurement of the collection of all particles that were present at the instant of beam

[1] *Thermonuclear Div. Semiann. Progr. Rept. Apr. 30, 1964*, ORNL-3652, p. 28.

[2] *Conference on Plasma Physics and Controlled Nuclear Fusion Research, Culham*, CN-21/112 (1965).

turnoff. To the extent that some of the particles in the plasma are not lost by charge exchange, this method is an underestimate of the density. The time dependence of the current following beam turnoff may not be directly related to the charge-exchange lifetime with the beam on, since the properties of the plasma with the beam on and the beam off may, in fact, be quite dissimilar.

From the value of the charge-exchange neutral flux to the energy analyzer, we can similarly determine the density from a geometrical correction, although in this case the charge-exchange cross section also enters. In our more recent experiments we have been using 5-μ-wide slits with 20-μ pinholes. Before the detector is assembled, the slits and pinholes are carefully examined using a high-power traveling microscope; the edges of the pinholes are seen to be quite sharp, and the slit edges are quite parallel. Other errors in dimensions and alignment can be shown to introduce only small uncertainties in the measurements. The density may be shown to be given by

$$n_+ = \left(\frac{8R_D L}{w}\,\frac{\delta s}{d^2}\,\frac{1}{\pi r_p^2 L}\right)\int \frac{I_{cx}(E)}{n_0 \sigma_{cx} v}\,dE\ ,$$

where w is the slit width, d is the hole diameter, δ is the total scanned angle, s is the spacing between the slit and hole, $1/n_0\sigma_{cx}v$ is the charge-exchange lifetime for given energy particles, and n_0 is the density of charge-exchange centers. As we have mentioned in the past, σ_{cx} is a strongly energy-dependent function which is quite different in both its energy dependence and absolute magnitude for hydrogen and nitrogen. In order to make use of the energy-analyzer information, it is necessary to know both the absolute number of charge-exchange centers and the ratio of hydrogen to other gases inside the liner. In the past[2] we have found that with lithium-arc dissociation the density of charge-exchange centers in the cold plasma may exceed the neutral-particle density determined from the ion gage reading by as much as an order of magnitude, presumably because of the presence of unstripped ions. Nevertheless, in these experiments with gas dissociation we have assumed that the neutral-particle density contributes all the charge-exchange centers. We have used a mass analyzer to determine the ratio of hydrogen to other gases. In calculating the density from the energy-analyzer information, we have separated out the hydrogen fraction and lumped all the other gases with nitrogen and used the nitrogen cross section. The assumption that n_0 is determined by the pressure was shown to be justified by the dissociation current to the detector. This current is related to the beam current and the dissociation mean free path, $1/n_0\sigma_d$, by a geometric factor. The currents observed with gas dissociation agree very well with the assumption that n_0 is given by the neutral-particle density.

The results of the experiment to determine density as a function of total neutral-particle density are shown in Fig. 2.1. At these relatively low plasma densities, if n_0 were of constant species, then from particle balance the density would be independent of pressure. That is, the breakup fraction for small breakup percentages is given by $n_0\sigma_d\,\mathfrak{L}$, where σ_d is the dissociation cross section and $\mathfrak{L}$ is the path length of the beam through the plasma region. Assuming that losses are all by charge exchange, the loss rate is also proportional to n_0. The density, which is given by

$$n_+ = \frac{I_{inj} n_0 \sigma_d\,\mathfrak{L}}{\pi r_p^2 L}\,\frac{1}{n_0 \sigma_{cx} v}\ ,$$

would be expected to be independent of n_0. The peak observed at high pressures is most likely

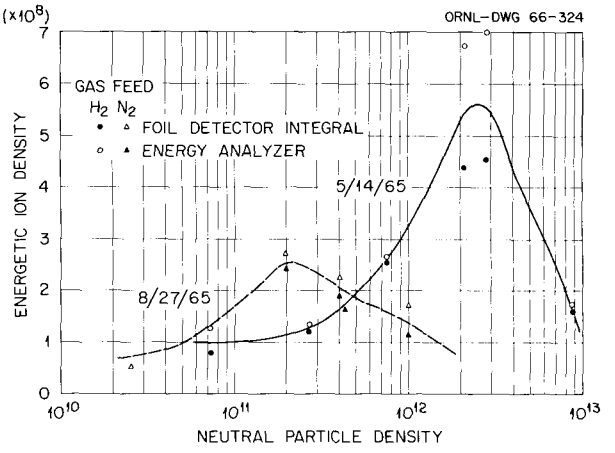

Fig. 2.1. Average Energetic-Ion Density as a Function of Neutral-Particle Density for Pressure Raised with Hydrogen Gas (Solid Curve) and Nitrogen Gas (Dashed Curve). Data are for density determined by both the total charge collected after beam turnoff and the analysis of the energy spectra.

caused by one of two phenomena: either the energetic ions have a lower loss rate per neutral particle at the higher pressures or there are enhanced losses at the lower pressures. A third possibility is that the injection rate per neutral particle is increased at higher pressures, but there is no evidence for this possibility.

It appears that the first possibility is the case. The total charge-exchange flux to the walls with the beam on may be obtained most easily by integrating the energy spectrum of the neutral flux. When this value is compared with the dissociated current given by

$$\left(1 - e^{n_0 \sigma_d \int}\right) I_{H_2^+},$$

the result shown in Fig. 2.2 is obtained, the variation being accomplished by changing n_0. The linearity of the curve indicates that if extraneous losses exist, they are proportionately the same at low and high pressures. The values of n_0 and σ_d were suitably chosen from the ratios of hydrogen to other gases in the same way as for the density determinations shown in Fig. 2.1.

The increased density at the higher pressures arises as a result of the effectively lower charge-exchange cross section at these pressures due to the change in the energy spectrum and the relative increase of hydrogen in the gas. This is shown in Table 2.1 and in Fig. 2.3. The values $\left\langle 1/\sigma_{cx} v \right\rangle$ are given for the points in Figs. 2.1 and 2.2 at the various pressures. It must be noted that the values given for $\left\langle 1/\sigma_{cx} v \right\rangle$ and $\overline{\tau}$ are optimistic, that is to say, too large. It may be remembered that the average is obtained from the energy-analyzer data and is defined by

$$\left\langle \frac{1}{\sigma_{cx} v} \right\rangle = \frac{\int_{E_{min}}^{\infty} (I_{cx}/\sigma_{cx} v)\, dE}{\int_{E_{min}}^{\infty} I_{cx}\, dE}.$$

The integral of the current from the lowest significant energy, say 10 kev, to the minimum energy measured, E_{min}, is not negligible and may amount to more than half the total current, while there is not expected to be a large contribution to the numerator in this range. Improvements in the energy analyzer are needed to properly establish the magnitude of these integrals. The energy spreads which are shown in Table 2.1 are clearly related to the microinstability which is obviously present. The radio-frequency spectrum as a function of pressure observed on electrostatic probes will be described below. The energy spread observed even at the lowest pressures is about twice the spectrum width typically observed in DCX-1, when the microinstability is intense. It may be fair to say, therefore, that the presence of a microinstability does not necessarily result in enhanced losses of particles contained in a mirror geometry. It must be pointed out, however, that had the particles remained at 300 kev, that is, had the microinstability not been present, the loss rate per particle would, in fact, have been lower for all these cases. We see no a priori necessity, however, that the average cross section be raised by the microinstability. The values of $1/\sigma_{cx} v$ for

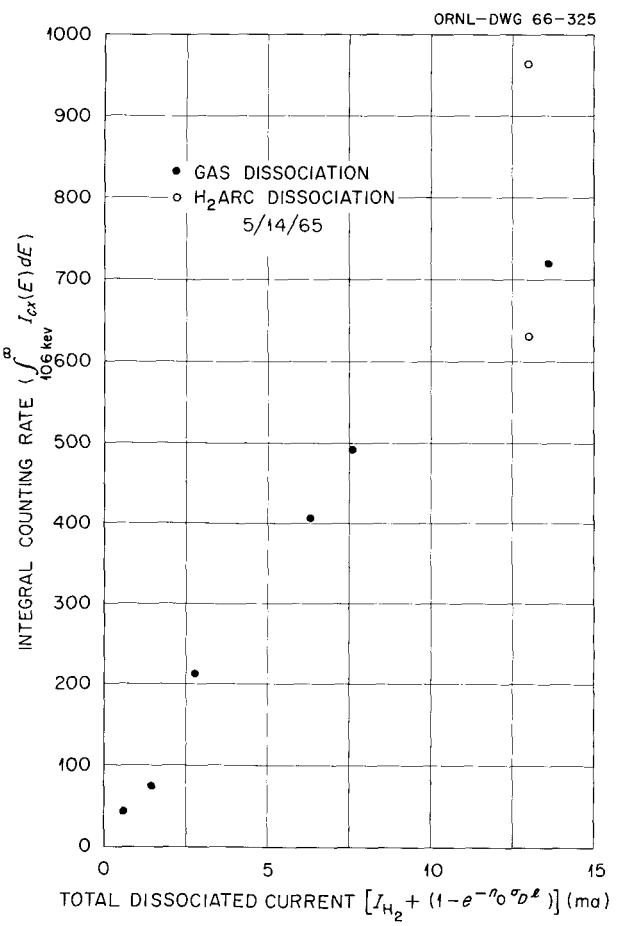

Fig. 2.2. Total Counting Rate Integrated over Energy Above 106 kev in the Energy Analyzer as a Function of Total Dissociated Current. L is taken as 50 m, and the value of $n_0 \sigma_D$ is corrected for the appropriate percentages of hydrogen and nitrogen.

Table 2.1. Results of Analysis of Energy-Analyzer Data for Gas Dissociation and for Hydrogen-Arc Dissociation Observed on 5-14-65

Picture No.	Ion Gage Pressure, p (torrs)	Total Neutral Particle Density, n_0 (cm^{-3})	Average Energy of Trapped Plasma, $\bar{E}$ (kev)	Inverse Mean Loss Rate per Neutral Particle, $\left\langle \frac{1}{\sigma_{cx} v} \right\rangle$ $(cm^3/sec)^{-1}$	Inverse Loss Rate per Neutral Particle of Ions of 300 kev, $\left(\frac{1}{\sigma_{cx} v} \right)_{300\ kev}$ $(cm^3/sec)^{-1}$	Integral of Counting Rate Above 106 kev, $\int_{106\ kev}^{\infty} I_{cx}\, dE$	Mean Lifetime of Ions Above 106 kev, $\bar{\tau}_{cx}$ (msec)
B-11	8.6×10^{-7}	0.73×10^{11}	334	6.0×10^{8}	1.39×10^{9}	46.2	8.3
B-9	1.9×10^{-6}	2.04×10^{11}	365	9.9×10^{8}	2.47×10^{9}		8.8
B-12	2.3×10^{-6}	2.68×10^{11}	330	1.4×10^{9}	2.9×10^{9}	76.5	5.3
B-13	5.15×10^{-6}	7.15×10^{11}	434	2.8×10^{9}	5.7×10^{9}	215	3.4
B-9	5.3×10^{-6}	7.41×10^{11}	380	2.9×10^{9}	6.0×10^{9}	267	3.9
B-14	1.3×10^{-5}	1.97×10^{12}	950	1.1×10^{10}	1.0×10^{10}	408	5.3
B-16	1.7×10^{-5}	2.61×10^{12}	988	1.2×10^{10}	1.0×10^{10}	492	4.6
B-15	4.6×10^{-5}	7.25×10^{12}	585	6.3×10^{9}	1.3×10^{10}	719	0.87
B-2[a]	5.3×10^{-6}	7.4×10^{11}	539	2.39×10^{9}	6.0×10^{9}	631	3.2
B-3[a]	8.2×10^{-6}	11.7×10^{11}	618	2.98×10^{9}	6.0×10^{9}	965	2.6

[a]Hydrogen-arc dissociation.

300-kev particles, taking into account properly the ratio of hydrogen to other gases, are also shown for the various cases in Table 2.1.

It is perhaps somewhat illuminating to examine the change in energy spectrum of the contained particles as the pressure is increased. Figure 2.4 shows the spectra at four different pressures, each curve determined by a suitable charge-exchange cross section using the appropriate percentage of hydrogen and other gases. It is interesting that a group of particles above 300 kev may be identified which appears to spread drastically with energy and that the group at 300 kev has a somewhat smaller and independent spread. In the past with arc dissociation this behavior was associated with two groups of particles, one with pitch angles close to zero degrees and the other with pitch angles close to the injected beam angle. A perpendicular-slit scan taken near the highest density of particles, however, does not show a large central peak under these conditions. This spectrum, however, is weighted very heavily by the current of low-energy particles. Scans taken under other conditions of gas dissociation, but with selected energy intervals, showed that the higher-energy groups show a tendency to peak at lower

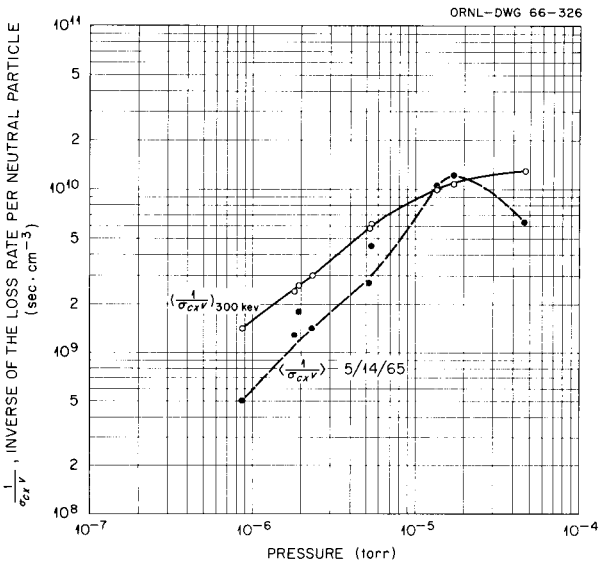

Fig. 2.3. Inverse of the Loss Rate per Neutral Particle Averaged over the Energy Spectrum of Emitted Particles, $\langle 1/\sigma_{cx} v \rangle$, as a Function of Pressure. Also shown is the value for $1/\sigma_{cx} v$ for particles of 300 kev for the appropriate mixture of hydrogen and nitrogen at these pressures. The variation with pressure is attributed to changes in composition and to changes in the energy spectrum of the contained protons.

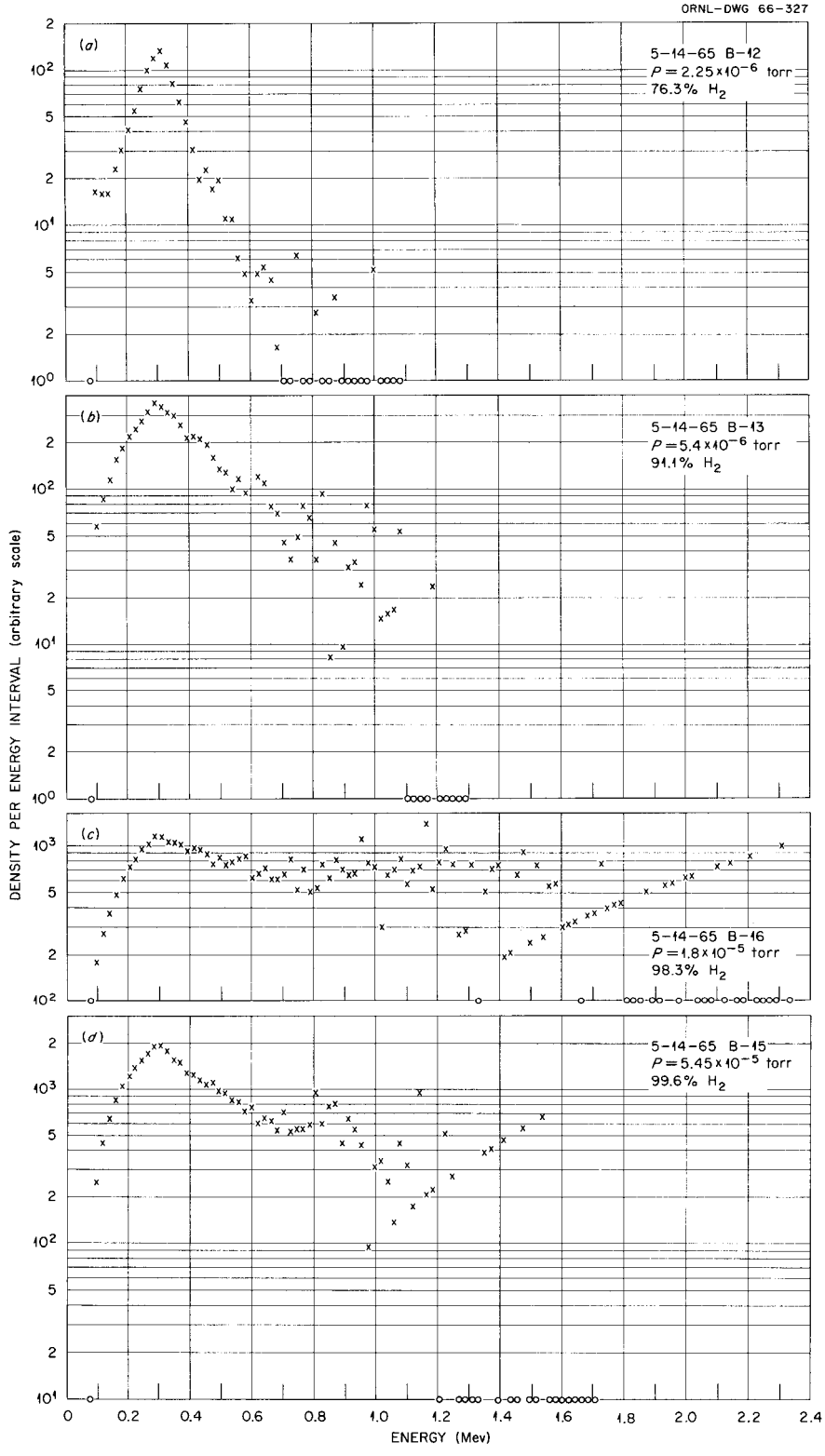

Fig. 2.4. Energy Spectra of Contained Energetic Particles for Four Different Pressures: (*a*) 2.25×10^{-6} Torr; (*b*) 5.4×10^{-6} Torr; (c) 1.8×10^{-5} Torr; (*d*) 5.45×10^{-5} Torr. The open circles on the bottom line correspond to zero counts. The values of charge-exchange cross section were corrected for the percentage of hydrogen shown in the figures.

Table 2.2. Results of Analysis of Data for Hydrogen-Arc Dissociation at Two Injected Beam Currents

Injected Beam Current, $I_{H_2^+}$ (ma)	Dissociated Current (ma)	Inverse Average Loss Rate per Neutral Particle, $\left\langle \frac{1}{\sigma_{cx} v} \right\rangle$ $(cm^3/sec)^{-1}$	Inverse Loss Rate per Neutral Particles for Ions of 300 kev, $\left(\frac{1}{\sigma_{cx} v} \right)_{300\ kev}$ $(cm^3/sec)^{-1}$	Mean Energy of Trapped Plasma, $\bar{E}$ (kev)	Integral of Charge-Exchange Current, $\int I_{cx}\, dE$	Average Density, $\bar{n}_+$ (cm^{-3})
2.4	2.1	3.0×10^9	$\sim 6.5 \times 10^9$	439	77.1	6.7×10^7
26.6	23.1	7.0×10^9	$\sim 6.5 \times 10^9$	772	601	1.2×10^9

pitch angles (see below). A quantitative detailed study of this phenomenon must still be carried out.

Experimental data were also taken with nitrogen bled into the liner to raise the pressure, with the beam current the same as in the hydrogen gas feed experiments. The densities obtained from these data are also shown in Fig. 2.1. The density at high pressure falls off somewhat less rapidly than the hydrogen bleed data, but a density peak implying an increase in $\langle 1/\sigma_{cx} v \rangle$ over that at the base pressure was observed.

The hydrogen arc has been operated under conditions similar to those when the gas dissociation data were taken, and a meaningful comparison of average lifetime, charge-exchange current, and density may be made between the two cases.

The densities determined from the energy analyzer, 3.7 and 4.9×10^9 ions/cm^3, are somewhat higher than the values resulting from the neutral flux after beam turnoff, 0.9 and 1.2×10^9 ions/cm^3. One error which may arise, although purely speculative, is connected with the high count rate in this case. A possibility of pulse pileup distortion of the energy spectrum at high energies would result in an error which might make a significant difference in the value $\int (I_{cx}/\sigma_{cx} v) dE$ as a result of the extreme energy dependence of σ_{cx}. The total current, however, should be unaffected, and the value obtained fits well with the gas breakup data (Fig. 2.2). The density is at least a factor of 4 higher than the gas breakup data at the same pressure, and the charge-exchange current is 3.4 times as great.

At a later date the arc was run and the density determined for injected molecular beam currents of 2.5 and 26.6 ma. The dissociation percentage was 87%. The densities determined by the two methods were in good agreement for the highest value (1.2×10^9 ions/cm^3); but at the lower current the foil detector clearly exhibited difficulties from cold plasma current, and the energy-analyzer data yielded the only reliable figure (6.7×10^7 ions/cm^3). These data show that the density is increasing more rapidly than linearly with current as a result of the increased lifetime (higher mean energy) in the case of higher current. The results of the analysis are shown in Table 2.2.

2.2 PITCH ANGLE DISTRIBUTIONS

As described previously,[3] scanning in angle along the magnetic field axis, with the 5-μ collimating slit of the energy-sensitive silicon barrier detector oriented perpendicular to the direction of the scan, yields the pitch angle distribution of the charge-exchange neutral flux. If only particles within a certain energy range are counted during the scan, then the pitch angle distribution of the trapped protons in that energy interval is obtained. Two types of pitch angle distributions have been observed. The more common (shown in Fig. 2.5), observed at high densities with both arc and gas dissociation, has a central peak of high-energy protons with small axial energies and two symmetrically positioned side lobes of lower-energy protons with axial energies close to the value at injection. These two separate groups of

[3] *Thermonuclear Div. Semiann. Progr. Rept. Oct. 31, 1964*, ORNL-3760, p. 17.

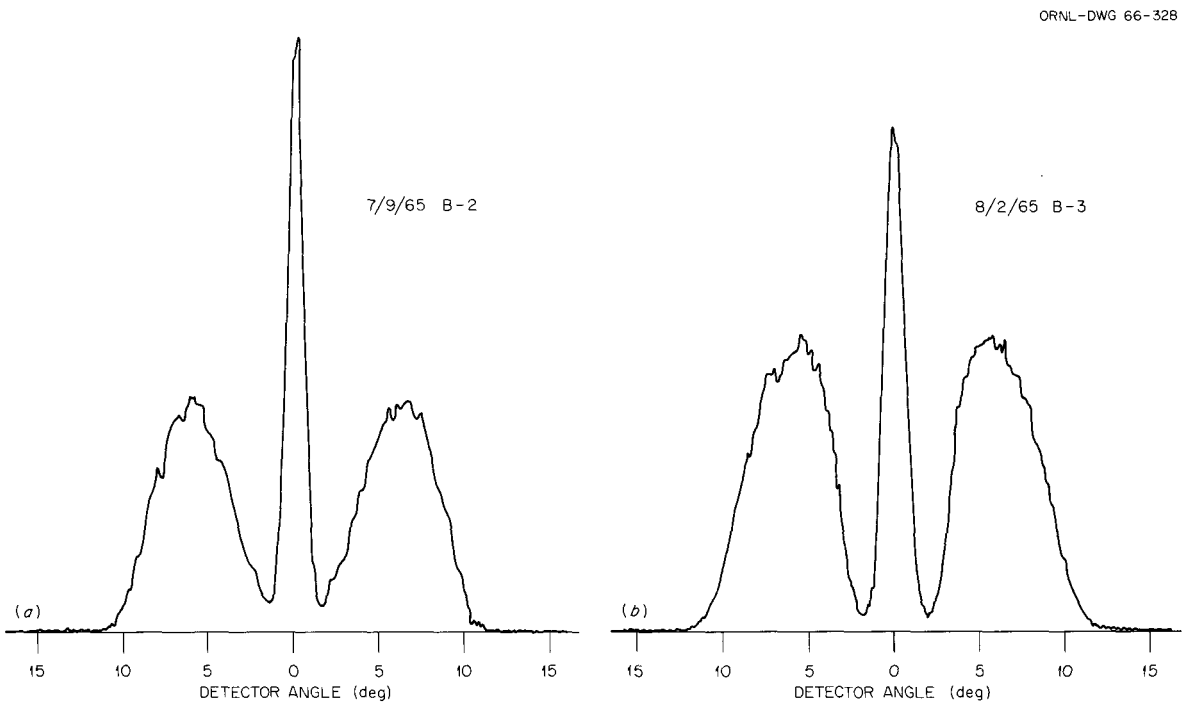

Fig. 2.5. Perpendicular-Slit Scans of the Charge-Exchange Current Above 75 kev as Seen from Port Position 4-4 for Hydrogen Gas Dissociation. (*a*) Gas pressure, 2.65×10^{-6} torr; (*b*) 2.45×10^{-5} torr. (Fig. 2.1 in ORNL-3472 is a key to port locations; position 4-4 means ring 4, position 4, etc.)

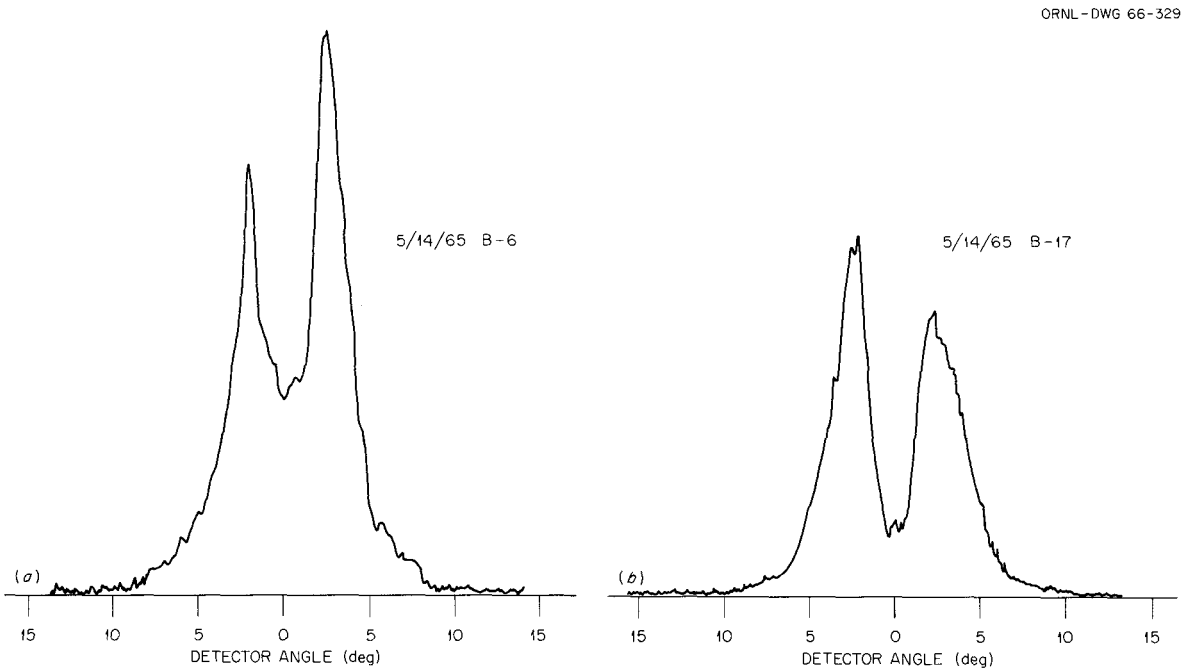

Fig. 2.6. Perpendicular-Slit Scans of the Charge-Exchange Current Above 75 kev as Seen from Port Position 4-4 for Hydrogen Gas Dissociation. (*a*) Gas pressure, 1.8×10^{-6} torr; (*b*) 1.7×10^{-5} torr. This is the second kind of pitch-angle distribution discussed in the text.

energetic protons have previously been discussed in detail.[4,5] In this type of distribution the central peak contains the majority of the energetic protons.

The second kind of pitch angle distribution (shown in Fig. 2.6), observed only with gas dissociation, lacks this central peak, although it is associated with the highest density of trapped protons observed with gas dissociation. Figure 2.6*b* is the pitch angle current distribution obtained at the peak of the n_+ vs n_0 curve in Fig. 2.1. In both figures the plasma was obtained by dissociation on hydrogen gas. The same types of distribution are obtained for gas pressures a factor of 10 apart. Note, however, that the pressures (and presumably the cold plasma densities) are approximately the same for Fig. 2.5*a* and Fig. 2.6*a* and also for Fig. 2.5*b* and Fig. 2.6*b* although the pitch angle distributions are quite different. It may be that small differences in the magnetic field shape cause this difference, although the data in Fig. 2.5*a* and in Fig. 2.7, taken the same day (and presumably at the same field shape) and a factor of 20 apart in pressure, also exhibit this difference. It is unclear what causes the two

[4] *Ibid.*, pp. 17–20.

[5] *Thermonuclear Div. Semiann. Progr. Rept. Apr. 30, 1965*, ORNL-3836, pp. 27–29.

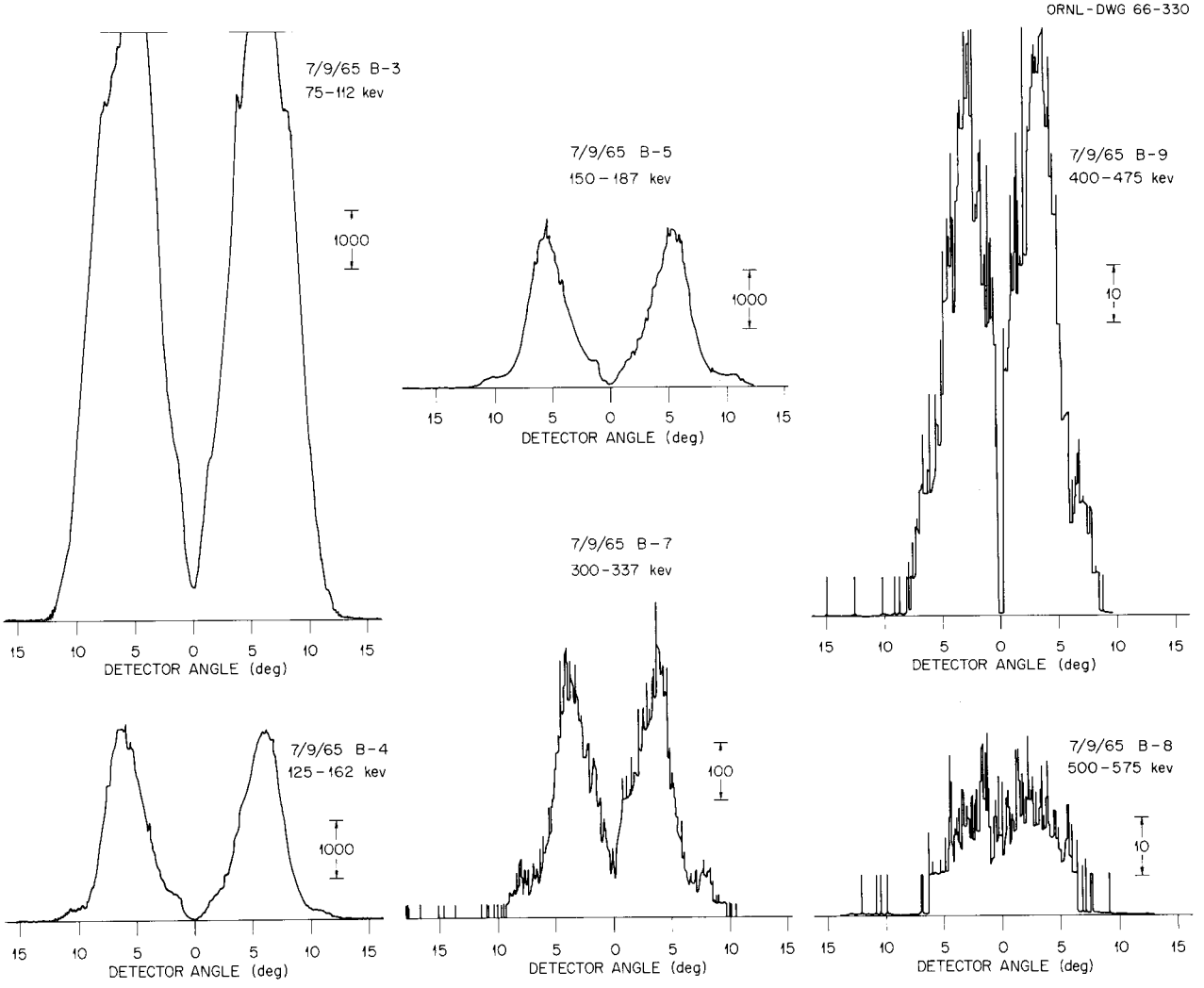

Fig. 2.7. Energy-Resolved Pitch Angle Distributions of the Trapped Protons Obtained by Hydrogen Gas Dissociation as Seen from Port Position 4-4. The gas pressure was 5.5×10^{-5} torr. The relative vertical scales are shown on the individual pictures in counts per second.

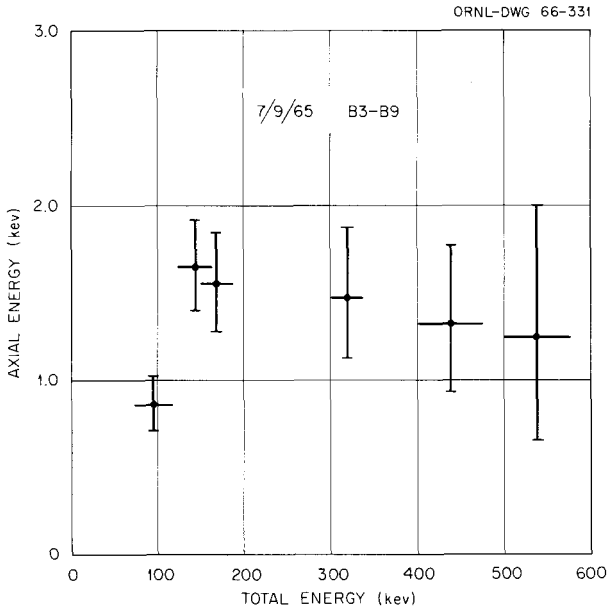

Fig. 2.8. Axial Energy Component of the Side Lobe Peaks for Different Total Proton Energies.

types of pitch angle distributions, and further study is needed to clarify this point.

Figures 2.5 and 2.6 give the pitch angle distribution of the total charge-exchange current and hence are heavily weighted by the lower-energy particles. Energy-resolved pitch angle scans for the type of pitch angle distribution exhibiting a central peak have been discussed previously.[6] Energy-resolved pitch angle scans for the type without a central peak are shown in Fig. 2.7. Note that the lack of a central peak persists up to the highest energy range examined, and in this region the energetic protons do not seem to be trapped by the slight depression of the magnetic field in the central region as occurs in the other type of pitch angle distribution. The significance and density limitations, if any, which may result in these two apparently different cases are still to be determined.

The axial component of the energy corresponding to the peak of the side lobes in Fig. 2.7 can be obtained from the total energy and the peak pitch angle. The result of this calculation is shown in Fig. 2.8. It is seen that except for the lowest energy interval the axial energy is approximately constant at 1.5 kev. The pitch angle of injected H_2^+ beam was not measured; but if the 270-kev dissociation protons are assumed to have an axial energy of 1.5 kev, a pitch angle of 4.3°, a not unreasonable value, is obtained. This same result was also obtained for the other type of pitch angle distribution.[6]

[6] *Thermonuclear Div. Semiann. Progr. Rept. Oct. 31, 1964*, ORNL-3760, p. 20.

2.3 RADIO-FREQUENCY MEASUREMENTS

The improved radio-frequency probes described in the previous semiannual report[7] have been examined and found to be free from spurious resonances, at least to 1000 Mc; there is evidence that there are no resonances to several thousand megacycles. The sensitivity of these probes has been measured by exposing them to electric fields. The detection sensitivity of short electric probes should increase linearly with frequency until the capacitive reactance becomes equal to the load impedance. In this case this should occur at about 3000 Mc. A calibration curve for one of these probes is shown in Fig. 2.9.

Some of the spectra from DCX-2 have been corrected to show the apparent electric field strength seen at the chamber wall for a number of the harmonics (see Figs. 2.10 to 2.12). Since there is a small amount of cold plasma at the wall, the actual electric field outside the plasma would likely be somewhat different. The electric fields

[7] *Thermonuclear Div. Semiann. Progr. Rept. Apr. 30, 1965*, ORNL-3836, p. 22.

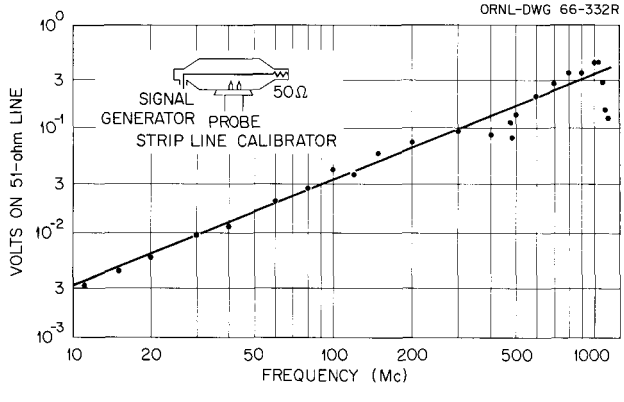

Fig. 2.9. Radio-Frequency Probe Response to an Electric Field of 1 v/cm, Measured as a Function of Frequency.

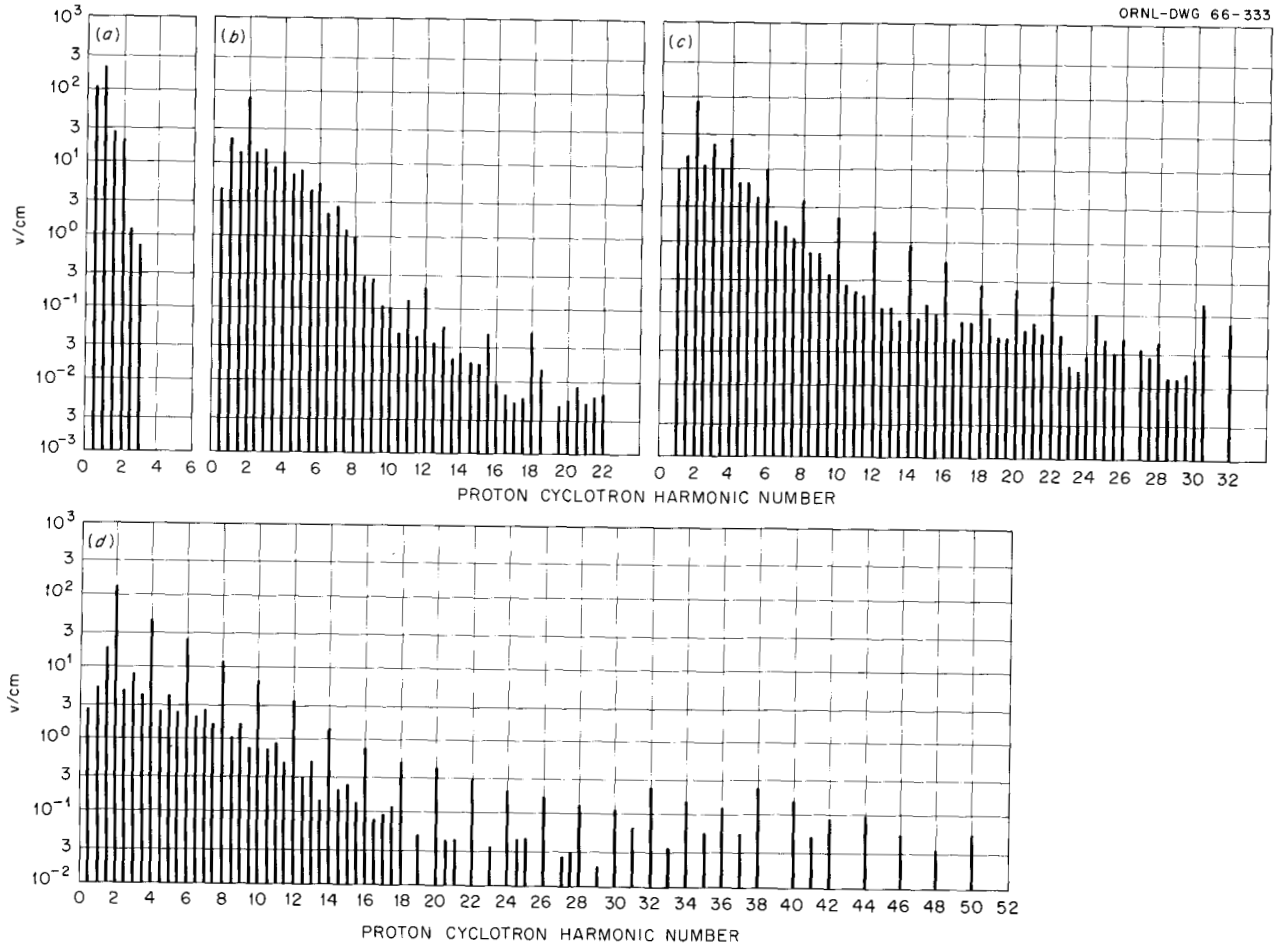

Fig. 2.10. Radio-Frequency Electric Field Intensity at the Liner Wall in DCX-2 with No Arc and with Hydrogen Gas Added to Adjust the Pressure. These field values represent roughly the maximum intensity at each frequency during an exposure of several seconds.

(*a*) Gage pressure, 1.4×10^{-6} torr. No lines were visible above the third proton cyclotron harmonic.

(*b*) Gage pressure, 5.4×10^{-6} torr. The lines were lost in noise above the 22d proton cyclotron harmonic.

(*c*) Gage pressure, 1.35×10^{-5} torr. Lines were visible but poorly resolved beyond the 32d proton cyclotron harmonic.

(*d*) Gage pressure, 4.5×10^{-5} torr. The lines were hard to resolve beyond the 50th proton cyclotron harmonic.

are seen to be rather large. The strongest line (fundamental) of the lowest-pressure gas breakup spectrum was 200 v/cm, and similar fields were found for the second or third harmonics for hydrogen arc spectra. At the highest gas pressure for H_2 gas breakup the most intense line (second harmonic) was 125 v/cm, while for gas breakup with nitrogen, the line intensities are considerably lower (second harmonic, 3.5 v/cm). The values quoted correspond to peak electric fields; each line fluctuates strongly, and average values are lower by 10 db or more.

Perhaps the most notable feature of the radio-frequency spectrum when the plasma results from gas breakup is that the spectrum extends to higher frequencies for higher gas pressure. At high pressures the spectrum closely resembles that resulting with an arc in the machine except for the near absence of all the odd proton harmonics. A closer examination shows that as the pressure is increased, the spectrum grows toward higher frequencies; then with further increase of pressure the odd proton harmonics and molecular-ion harmonics decrease in amplitude. The even proton

harmonics reach a maximum intensity and remain approximately constant at the higher pressures.

With high resolution the sides of the lines are observed to be straight on a semilog plot to a good approximation, that is, the intensity falls off exponentially on either side of the peak. When the inverse of the square root of the slope of this falloff is plotted vs harmonic number, straight-line relationships are obtained. Figure 2.13*a* shows this at two different hydrogen gas pressures. Figure 2.13*b* gives the same plot with nitrogen gas added, and Fig. 2.13*c*, with a hydrogen arc. Usually the lines are not simple. There are two or more components with different amplitudes and widths and sometimes different frequencies as well. Where the intensities of two components were comparable, they were both measured, and the graph shows two points. In Fig. 2.13*b* (nitrogen gas) a step appears; the lines at lower frequency (below the step) are one component, and the lines at higher frequency are the other component. Similarly, with the hydrogen arc (Fig. 2.13*c*) two components appear in several cases.

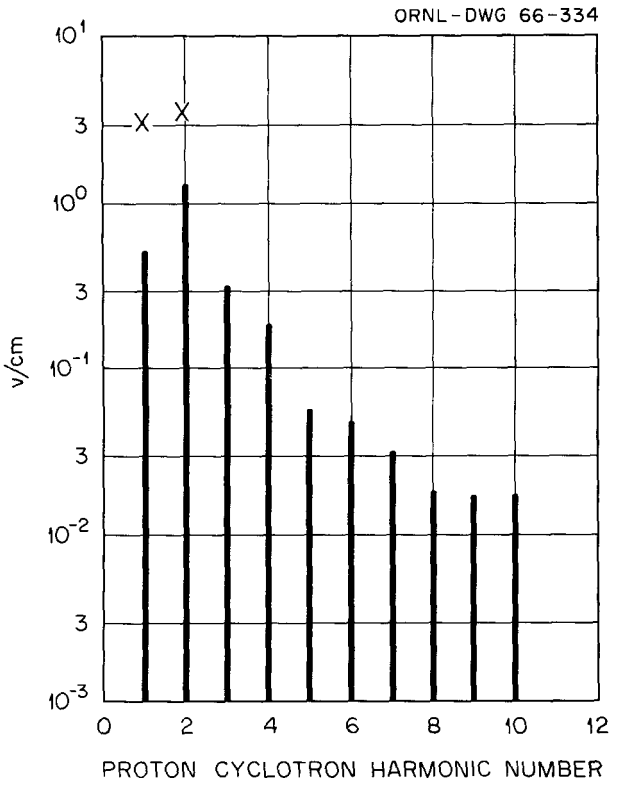

Fig. 2.11. Average Radio-Frequency Electric Field Intensity at the Liner Wall in DCX-2 with No Arc and with Nitrogen Gas Added to Adjust the Pressure. The gage pressure is 1.6×10^{-5} torr. The two crosses are peak electric fields (see Fig. 2.10) at a pressure of 7.1×10^{-6} torr.

2.4 CHARGE-EXCHANGE CROSS SECTIONS ABOVE 1 Mev

A knowledge of the charge-exchange cross sections in H_2 and N_2 for protons with energies up to 2.5 Mev is needed in obtaining the trapped proton energy distribution from the charge-exchange-current energy spectrum. An analytic fit to the experimental data of Barnett[8] in H_2 and N_2 for proton energies below 1 Mev had previously been obtained,[9,10] and this had been used to

[8] C. F. Barnett, J. A. Ray, and J. C. Thompson, *Atomic and Molecular Collision Cross Sections of Interest in Controlled Thermonuclear Research*, ORNL-3113(rev.) (August 1964).

[9] *Thermonuclear Div. Semiann. Progr. Rept. Oct. 31, 1964*, ORNL-3760, p. 21.

[10] *Thermonuclear Div. Semiann. Progr. Rept. Apr. 30, 1964*, ORNL-3652, p. 30.

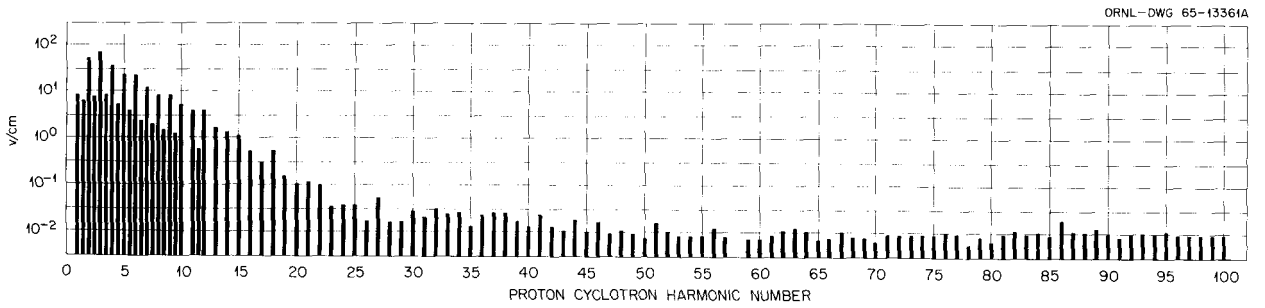

Fig. 2.12. Peak Radio-Frequency Electric Field Intensity at the Liner Wall in DCX-2 with a Hydrogen Arc Used to Enhance Dissociation of the Molecular Ion Beam. Gage pressure is 5×10^{-6} torr, and the hot-ion density is 2×10^{9} cm^{-3}.

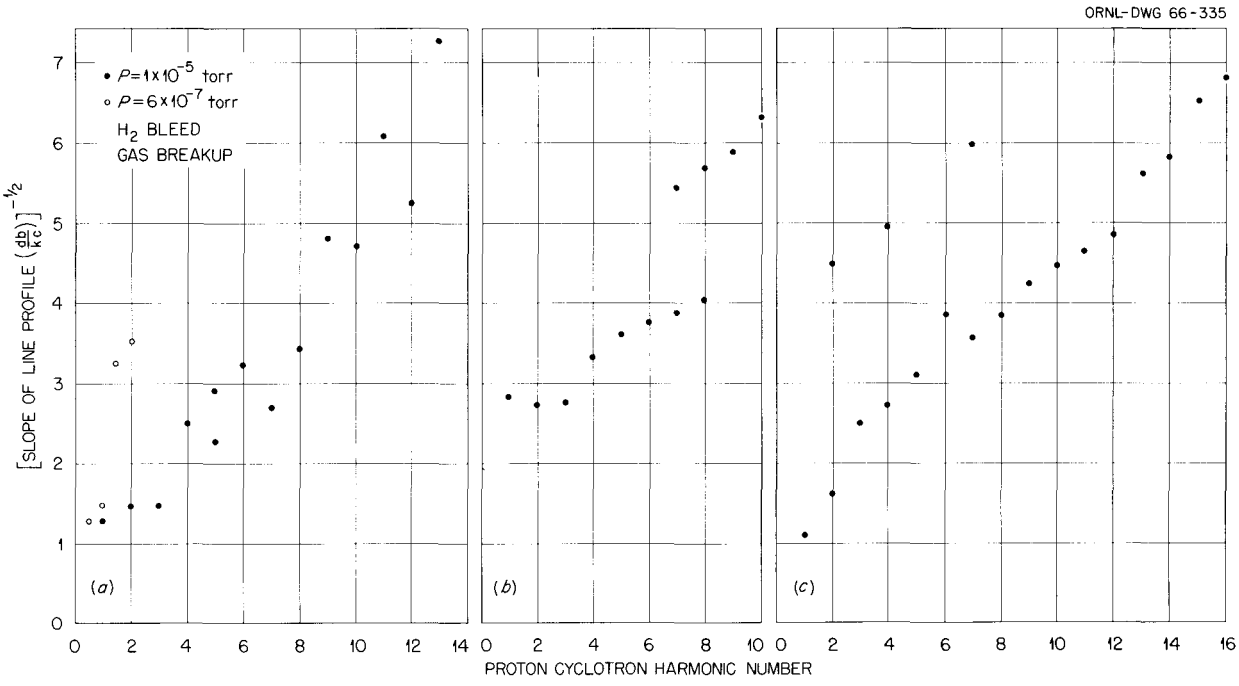

Fig. 2.13. Variation of Proton Cyclotron Harmonic Line Profile with Harmonic Number. *The line intensity falls* exponentially with frequency about the line center.

(*a*) Hydrogen gas was added to raise the pressure to 6×10^{-7} torr and 1×10^{-5} torr. No arc.

(*b*) Nitrogen gas was added to raise the pressure to 1.6×10^{-5} torr. No arc.

(c) Hydrogen arc used to enhance dissociation of the molecular ion beam.

extrapolate his charge-exchange data above 1 Mev. The accuracy of this extrapolation can now be demonstrated by comparing it with some recent data by Pyle.[11] This comparison is shown in Figs. 2.14 and 2.15. For protons in N_2 (Fig. 2.14) the analytic extrapolation is an exceptionally good fit to Pyle's data, even at the lower energies. The extrapolation deviates significantly from his experimental data only at energies above 2.5 Mev, energies higher than those of particles we have measured. The largest discrepancy occurs at 2.5 Mev and is of the order of 25%. For protons in H_2 (Fig. 2.15) the analytic extrapolation is again quite good, with a difference of 20% at 2.5 Mev, the largest discrepancy with Pyle's data (less than 50%) occurring at 850 kev.

2.5 TRANSVERSE FIELD MEASUREMENTS IN THE INJECTION DUCT

We have found that with full magnetic field in DCX-2, at certain settings of the dip coil it was impossible to steer the molecular-ion beam so as to avoid striking the inside of the injection duct tube near its lower end. The duct was designed to be compensated under the nominal flat-field conditions (12 kilogauss central field, 1.5% dip), and under these conditions the Hiperco was operated at its nominal saturation flux density. Since small variations in the current in the nearby dip coil make large changes in the longitudinal component of the flux in the Hiperco, saturation was suspected.

A systematic study of the field component in the injection duct perpendicular to its axis has shown a significant field penetration that varies with the current in the dip coil and with the central flat-field value, as shown in Fig. 2.16. The 10.2- and 11.4-kilogauss values are 85 and 95%, respectively, of the 12.0-kilogauss flat-field value. The first 4 in. of the duct length is required to produce the main decrease in the field, due to the difficulty in shielding the tip of the duct; after that the field decreases much more

[11] K. H. Berkner *et al.*, *Phys. Rev.* **140A**, 729 (1965).

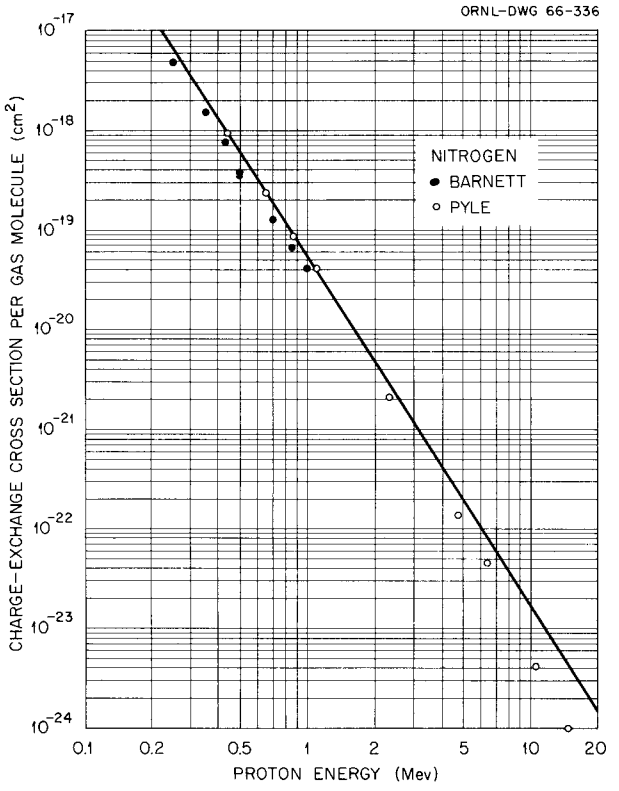

Fig. 2.14. Charge-Exchange Cross Section vs Energy for Protons in N_2. The curve is an analytic fit to Barnett's data given by $\sigma_{cx} = 1.73 \times 10^{-10} [\sqrt{E}\ (E^3 + 6.46 \times 10^5)]^{-1}$.

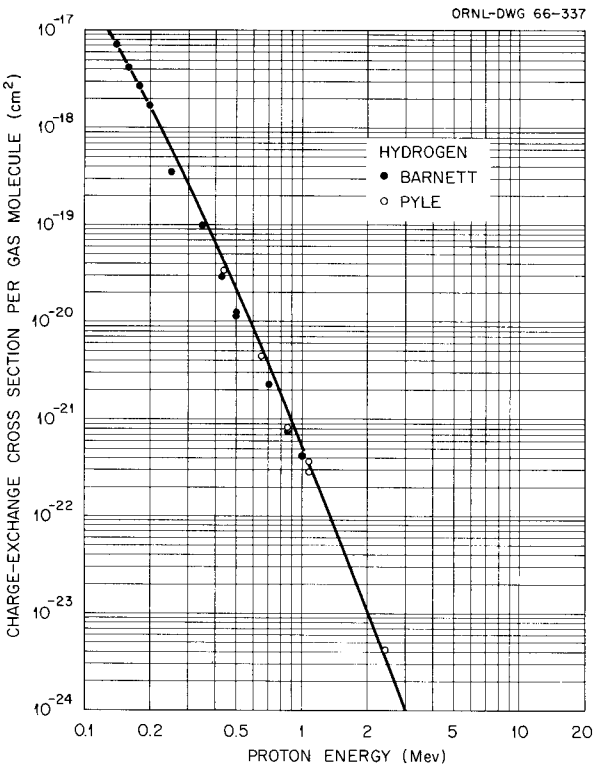

Fig. 2.15. Charge-Exchange Cross Section vs Energy for Protons in H_2. The curve is an analytic fit to Barnett's data given by $\sigma_{cx} = 8.32 \times 10^{-4}\ E\ [(E + 100)^5\ (E^2 + 625)]^{-1}$.

slowly with distance upward into the duct. For the same dip current (1300 amp) the field at 4 in. inside the duct is 0.36, 1.6, and 3.3% of the external field for 10.2-, 11.4-, and 12.0-kilogauss flat-field values respectively. Note that decreasing the flat-field value by 5 or 15% changes the field penetration by about a factor of 2 or 10, respectively, indicating saturation. At the 11.4-kilogauss setting the field penetration is tolerable, and at 10.2 kilogauss it is negligible.

Changing the dip current at a fixed central field value also changes the field penetration, but to a lesser extent. Increasing the dip current decreases the field penetration at each of the central field settings. This is important at the 12.0-kilogauss central field setting, where the transverse field in the injection duct is comparatively large over a long length of the duct and significantly affects the injection of the H_2^+ beam. Thus in the past, varying the dip coil current to optimize the trapped plasma density affected both the injected current and the trapped protons. One effect could not be separated from the other without also measuring the injected current vs dip current.

As a result of these measurements we now operate with a central field of 11.4 kilogauss and an acceleration voltage of 540 kv, so that the molecular-ion orbits are unchanged.

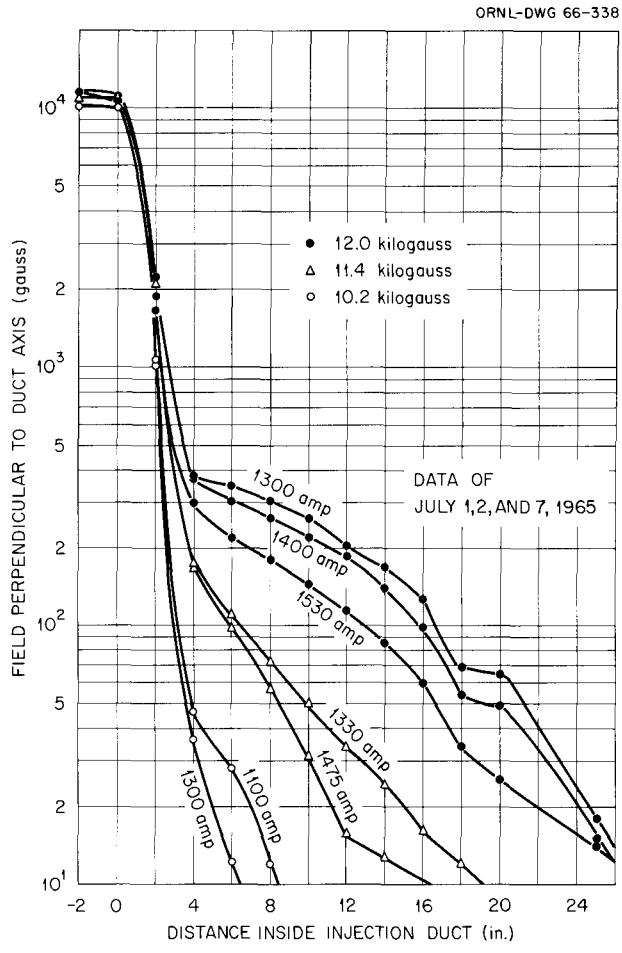

Fig. 2.16. Transverse Field in the Injection Duct vs Distance Inside the Duct for 10.2, 11.4, and 12.0 kilogauss. Central field settings and different dip coil currents are indicated.

3. Electron-Cyclotron Heating

3.1 INJECTION OF NEUTRALS AND TRAPPING ON AN ELECTRON RESONANCE ENVIRONMENTAL MEDIUM (INTEREM)

W. B. Ard
M. C. Becker[1]
R. A. Dandl[1]
H. O. Eason
A. C. England
G. M. Haas
H. C. Hoy
R. L. Knight
N. H. Lazar
R. L. Livesey
O. D. Matlock
M. W. McGuffin

3.1.1 Introduction

The EPA magnetic geometry has been modified to a three-region system. The facility will henceforth be called INTEREM. The injected 20-kev neutral beam has been increased to approximately 60 ma equivalent. As a result of these changes the density and lifetime of the 20-kev protons trapped by the electron-cyclotron plasma (ECP) have significantly increased. Hot-ion instabilities have as yet not been observed in the presence of the ECP environmental medium. However, more sensitive methods for the detection of ion cyclotron activity are being devised. Data from this experiment have been interpreted to give the cold-ion density of the ECP. Further measures are being taken to decrease the neutral pressure in the region of the trapped 20-kev protons.

3.1.2 Neutral-Beam Injection Studies

Modifications. – The 20-kev energetic neutral beam, described in the last three semiannual reports,[2] has been used for continuing proton-trapping studies in the ECP in the INTEREM Facility. At the present time up to 60 ma equivalent of 20-kev neutrals have been injected into the ECP with the prospect of considerably more current in the near future.

Two major changes took place during the period of this report. The first was to replace the old 3:1 mirror coils with a pair of coils identical to the DCX-1 outboard coils. Along with this change the cavity was modified to increase the mirror throat diameter. The new coils were installed with a separation appropriate to give a 2:1 mirror ratio.

This first change resulted in immediate improvement. The decay time of the protons trapped in the ECP increased to ~ 100 μsec from the previously reported 50 μsec.

Figure 3.1 shows the midplane of INTEREM in a schematic view. Shown are the ion source, accelerator, and 20-ft.-long drift tube for beam neutralization. Also shown are the cavity, detector mounts, vacuum tank, and pump manifolds. A trapped equilibrium orbit in a 2-kilogauss field is also shown (although the centered orbit is nontypical). Normally, the field is higher than this and the orbit is correspondingly reduced.

The second major change was the extension of the microwave cavity and magnetic field in the axial direction. This change involved placing the EPA outboard coils at the ends of the INTEREM Facility, adding vacuum extensions, and adding two cavity end sections to the existing cavity. Figure 3.2 shows a schematic longitudinal view of the facility as it now exists. Typical zones of constant $|B|$ over which electron-cyclotron resonant heating occurs are shown as dotted lines.

The purpose of this change is to provide gas feed into the ends of the machine as shown in the figure. The gas feed produces cold plasma in the outboard cavity sections which then can flow into the center section to provide a trapping medium for the 20-kev neutral beam. This also removes

[1] Instrumentation and Controls Division.

[2] *Thermonuclear Div. Semiann. Progr. Rept. Apr. 30, 1964*, ORNL-3652, sect. 7.5; *Thermonuclear Div. Semiann. Progr. Rept. Oct. 31, 1964*, ORNL-3760, sect. 3.1.3; *Thermonuclear Div. Semiann. Progr. Rept. Apr. 30, 1965*, ORNL-3836, sect. 3.1.2.

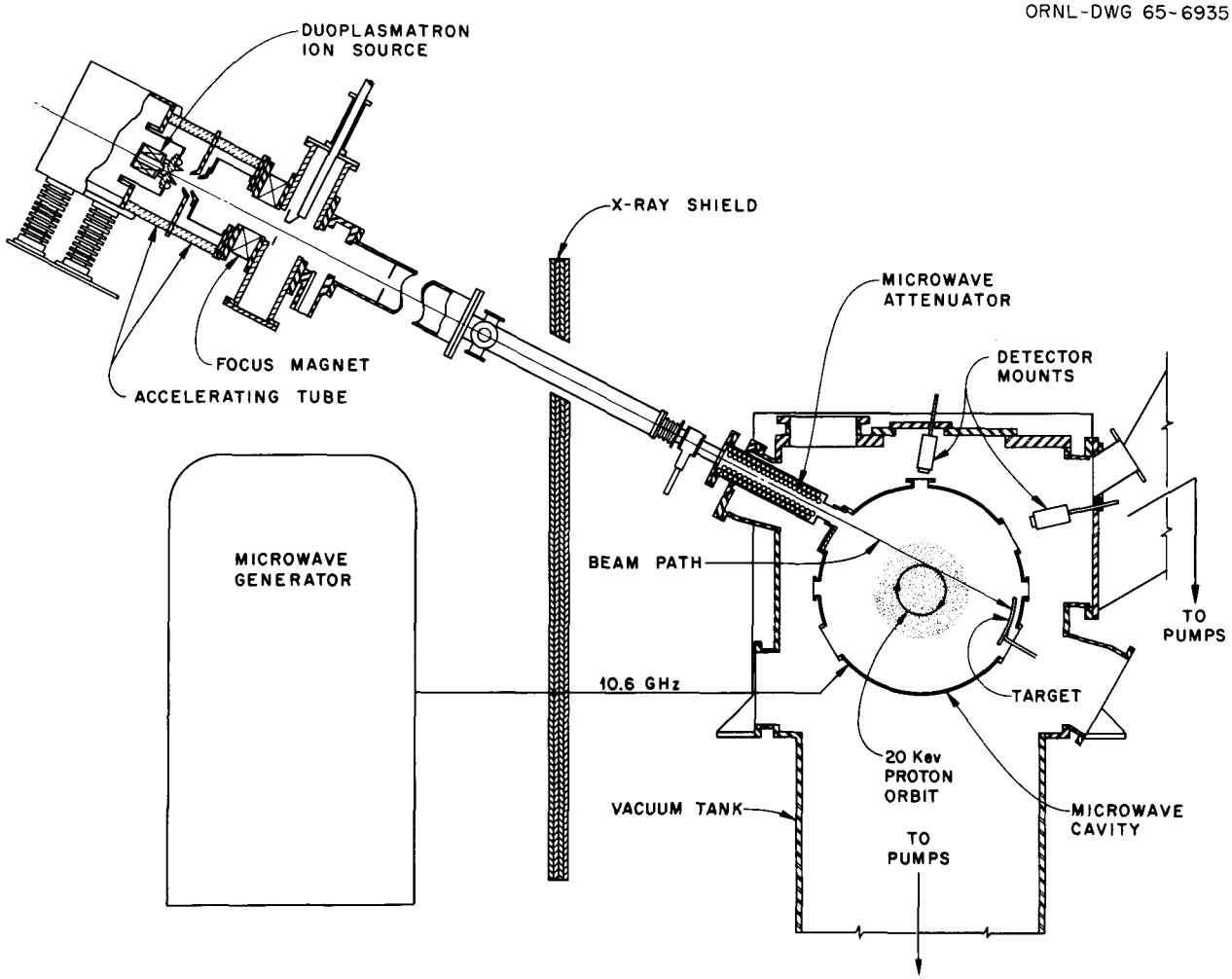

Fig. 3.1. Schematic Cross Section of the Midplane of the INTEREM Facility. Twenty-kev neutrals are trapped between magnetic mirror coils by ionization in an electron cyclotron plasma. The size of a trapped proton orbit is shown, but of course there is no preference for trapping on a centered orbit.

the gas sources from the center cavity so that more efficient ionization of the gas can take place and less neutral gas will appear in the center section, which helps to increase the charge-exchange lifetime of the trapped protons.

An obvious disadvantage of this arrangement is that it reduces the microwave power density throughout the cavity volume and hence reduces the ECP density. This effect has occurred, but it is expected that more power will be installed in the near future. Even so, it may be necessary to decrease the radial cavity dimension in order to raise the specific microwave power and decrease the vacuum conductance between the three regions.

Figure 3.2 shows that microwave power is fed to all three sections of the cavity, but most of the data presented here were obtained when power was applied to the center section only. Only the latest experiments involved microwave power feed to the end sections; the preliminary results are discussed in Sect. 3.1.4.

Analytical Treatment of 20-kev Proton Density Buildup and Decay. – In this section we discuss the mechanism by which we gain and lose 20-kev ions. Neutral atoms entering the ECP may become ions by a number of processes. First, since the ECP has a higher density of cold ions than cold neutrals, charge-exchange trapping of

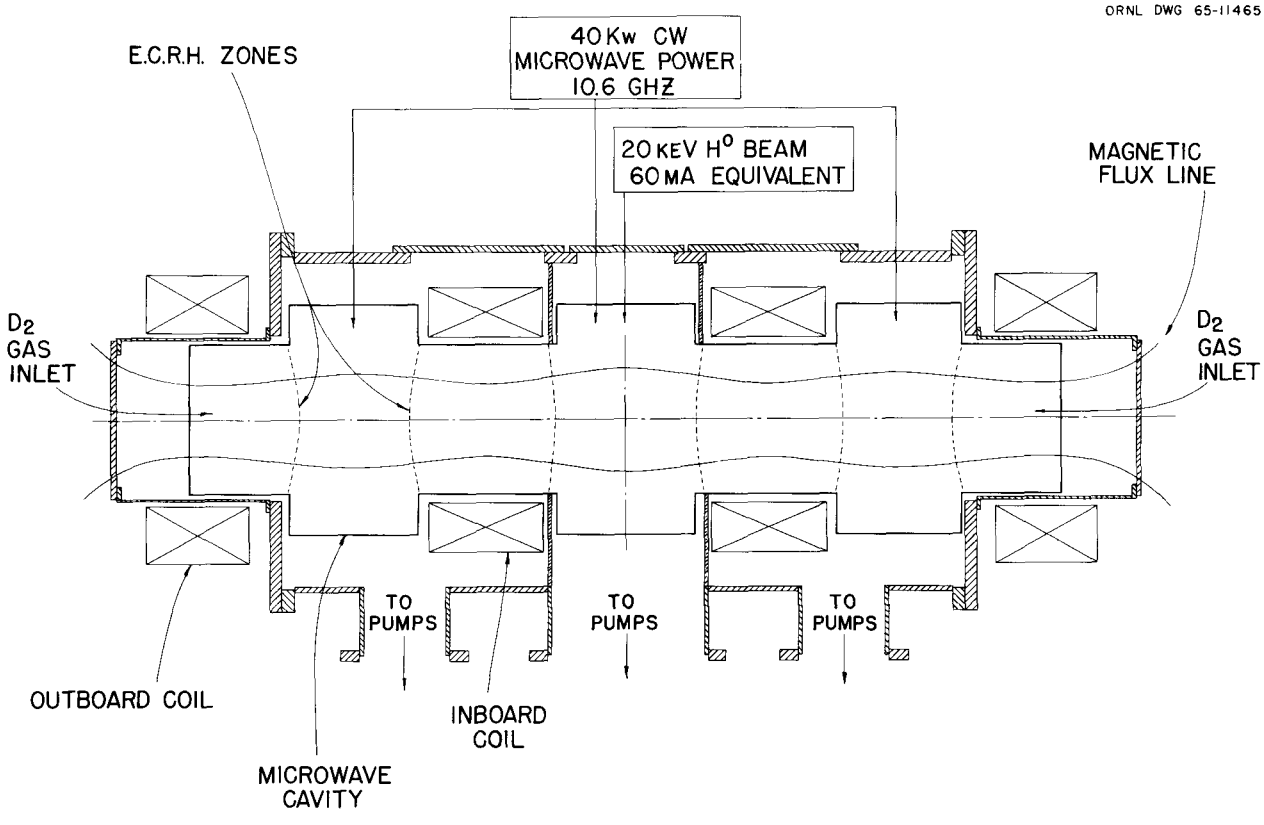

Fig. 3.2. Schematic Longitudinal View of the INTEREM Facility. The microwave cavity is 350 cm from end to end, 55 cm in diameter in the coil throats, and 92 cm in diameter between coils.

the 20-kev neutrals on the cold ions is a significant process.[3] Second, the cold ions may also ionize the incoming neutrals. At 20 kev the cross section for both of these processes is $\sigma_{ii} = 7 \times 10^{-16}$ cm^2/atom.[4] Third, cold neutrals which remain in the ECP may ionize the incoming 20-kev neutrals. The cross section for this process is $\sigma_{01} = 7 \times 10^{-17}$ cm^2/atom.[5] Next, the cold electrons ($\sim$100 ev) in the plasma may ionize the incoming neutrals. The cross section for this process is $\sigma_{ie} \tilde{=} 7 \times 10^{-17}$ cm^2/atom.[6]

The only loss is charge exchange, and the cross section is $\sigma_{10} = 6 \times 10^{-16}$ cm^2/atom.[7] Combining these processes we have for the rate of change of 20-kev proton density, n_+, in the ECP:

$$\frac{dn_+}{dt} = \frac{I_0 L}{V}\left(n_c\sigma_{ii} + n_0'\sigma_{01} + n_e\sigma_{ie}\frac{v_e}{v_0}\right) - n_0' n_+ \sigma_{10} v_0 .$$

Here n_0' is the neutral density inside the plasma, n_c is the cold-ion density, n_e is the cold-electron density ($\tilde{=} n_c$), L is the path length in the trapping region, I_0 is the beam current, V is the hot-ion volume, and v_0 is the velocity of a 20-kev atom or ion.

At steady state we have:

$$n_+ = \frac{I_0}{V}\frac{L}{v_0}\left(\frac{n_c\sigma_{ii} + n_0'\sigma_{01} + n_e\sigma_{ie}v_e/v_0}{n_0'\sigma_{10}}\right).$$

In practice $n_0'\sigma_{01}$ and $n_e\sigma_{ie}v_e/v_0$ are both small, so that we may neglect them here. Hence, we have approximately

$$n_+ \tilde{=} (\text{const})\frac{n_c}{n_0'} I_0 .$$

[3] This process was first suggested to us by J. R. McNally, Jr.

[4] *Atomic and Molecular Collision Cross Sections of Interest in Controlled Thermonuclear Research*, ORNL-3113 (rev.), p. 61 (Aug. 1964).

[5] *Ibid.*, p. 60.

[6] *Ibid.*, p. 133.

[7] *Ibid.*, p. 60.

The important point to be emphasized is that the hot-ion density is proportional to injected beam current, is also proportional to the cold-ion density which provides the trapping, and is inversely proportional to the neutral density inside the ECP which causes the charge-exchange loss. The paths to higher hot-proton density are: increased beam current I_0, increased cold-ion density n_c (by increasing the microwave power per unit volume), and/or decrease of the neutral density n_0' (by more efficient axial pressure differential).

In the future it may be possible to utilize inverse cascading as described by Hiskes[8] to increase the effective beam current. The process would involve exciting a reasonable fraction of incoming neutrals to perhaps the $n = 6$ atomic level. Upon entering the cold-ion plasma, inverse cascading might occur in such a way that states up to $n = 18$ may be appreciably populated. Even in the weak field normally used, Lorentz ionization can occur for these highly excited states and additional trapping may ensue.

Density and Lifetime of 20-kev Trapped Protons. – A beam pulser allows the beam to be turned on and off repetitively while the microwave power is on or off continuously. The measured beam turnoff time is 6 μsec. The detectors measure a neutral current, I, and a current decay time, τ, due to charge exchange. The product $I\tau$ for a directional detector is proportional to the density of trapped protons, n_+, since $KI\tau/V = n_+$. Here we assume that the average volume, V, seen by the detector, is fixed and that charge exchange is the only loss process. The constant K includes the geometric effects.

The ratio of $I\tau$ measured with the ECP to $I\tau$ measured with gas trapping only should be a measure of the ratio of the trapped proton density with ECP to that with gas. This again assumes that the volume occupied by trapped protons does not change. This assumption has not yet been checked in detail, but there is evidence to the effect that it is correct.

The decay curves taken with microwave power on are actually not simple exponentials. A typical curve exhibits two linear slopes when plotted semilogarithmically. When the initial e-folding time is $\sim$100 μsec, the second, longer e-folding time is $\sim$1 msec or more. The $I\tau$ product of the second slope is generally as large or larger than the initial fast $I\tau$ product.

Although there is the remote possibility of an instrumental effect, for example, perhaps simultaneous irradiation of the detectors by ultraviolet light, x rays, and protons yields spurious results, nevertheless, the dominant possibility is that the two-component effect is real. The longer-lived component then might arise from: (1) protons coming from a highly ionized region of the machine where the charge-exchange lifetime is lengthened, or (2) protons which have undergone energy spread, so that at their new mean energy the effective charge-exchange cross section is smaller. These two possibilities are being investigated.

Figure 3.3 shows the $I\tau$ product for 20-kev protons as a function of the central gage pressure

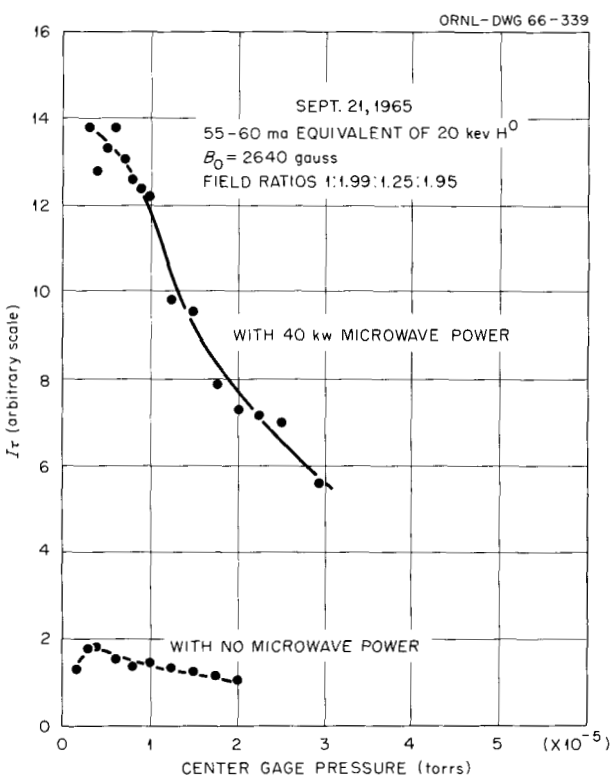

Fig. 3.3. Plot of $I\tau$ for a Detector vs Gage Pressure for Gas Trapping and ECP Trapping. This curve is for 20-kev neutral injection. The quantity B_0 refers to the axial midplane field. The field ratios are for respectively: (1) B_0, (2) maximum inboard mirror field, (3) minimum outer region field, and (4) maximum outboard mirror field. I is the current to the detector, and τ is the decay period for the fast component of the decay curve.

[8] J. R. Hiskes, *Phys. Rev. Letters* **10**, 102 (1963).

with and without microwave power. Only the $I\tau$ product of the initial fast decay is plotted. Because of the gas feed from the ends, the minimum center gas pressure at which the ECP can be made stable has been reduced from the previous operating pressure near 10^{-5} torr (with a single-section cavity) to 3×10^{-6} torr. The $I\tau$ product with 40 kw of microwave power generally increases as the pressure is lowered. At a pressure of 3×10^{-6} torr the decay time (fast component) is in excess of 100 μsec.

The $I\tau$ product with gas trapping is approximately independent of gas pressure, as it should be. Some variation with pressure is observed, but this may be instrumental. This is especially true of the dropoff of the $I\tau$ product at high pressures, which is probably caused by the orbit precession period being longer than the charge-exchange time. Hence, many of the captured protons charge exchange before they precess into the region viewed by the collimated detectors. However, the dropoff of the $I\tau$ product at low pressures may well be evidence of an instability in this pressure region.

In the gas trapping case the density of trapped protons can be calculated, providing a convenient detector calibration. The calculated hot-proton density is $n_+ = I_0 L \sigma_{01} / V v_0 \sigma_{10}$, and measured effect is $n_+ = K' I\tau$, where I is the neutral detector current and τ is detector current decay time. Then K' relates the detector geometry to the density. Thus $K' = n_+$ (calculated)$/I\tau$ (measured). This K' then should be correct for both gas trapping and ECP trapping.

Since both σ_{01} and σ_{10} are well known, reasonable assumptions about the volume of trapped protons and the length of the trapping path give the resulting $n_+ = 3.6 \times 10^6$ protons/cm^3 for gas trapping. When trapping on the ECP, the $I\tau$ product is roughly an order of magnitude greater and $n_+ \tilde{=} 3 \times 10^7$ protons/cm^3.

Figure 3.4 is a plot of $1/\tau$ vs pressure both with and without the microwave plasma. These data indicate charge exchange to be due to the hydrogen gas let into the system rather than to residual impurities, which would be manifest by nonlinear $1/\tau$ plots.

Figure 3.5 shows the $I\tau$ product for two detectors as a function of microwave power. The $I\tau$ products are seen to increase more rapidly than linearly with power, indicating that increased microwave power increases the ratio of n_c/n_0' and thereby increases the hot-proton density. The detector which is looking at the equilibrium orbit shows a bigger increase with power, hinting that the interior is becoming better shielded as the power is increased.

Figure 3.6 is a plot of $I\tau$ product vs equivalent beam current. The plot of $I\tau$ is linear with current within the accuracy of the measurement. This would seem to indicate the absence of density-limiting mechanisms in that the $I\tau$ product does not saturate with increased beam current.

Density and Lifetime of 40-kev Trapped Protons. — Figure 3.7 shows the $I\tau$ product for 40-kev protons as a function of the central gage pressure with and without microwave power. As with the 20-kev protons, the $I\tau$ product is about

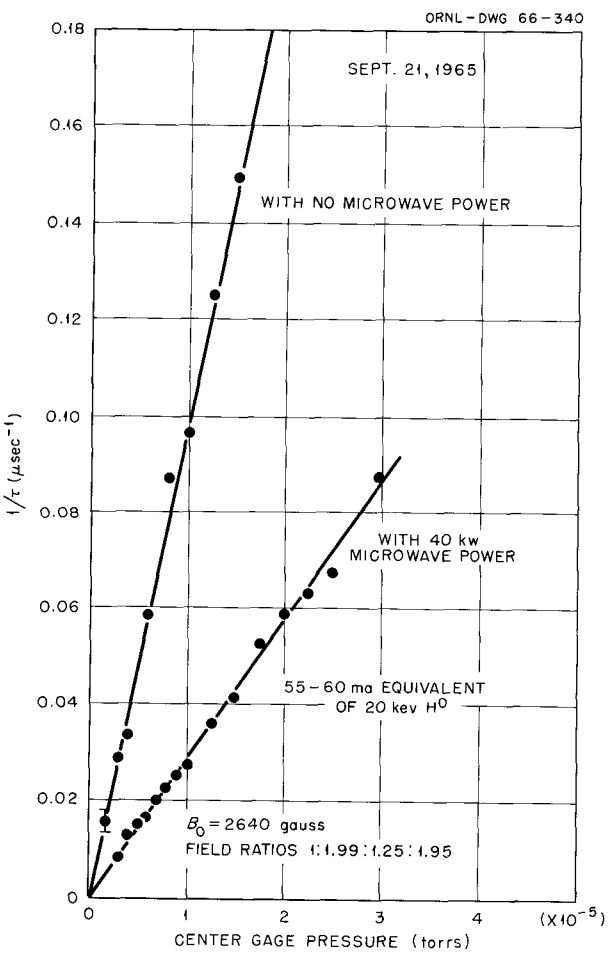

Fig. 3.4. Plot of $1/\tau$ vs Pressure for Gas Trapping and ECP Trapping. This curve is for 20-kev neutral injection. The quantities B_0 and field ratios are as defined in the previous figure.

an order of magnitude larger with 40 kw of microwave power at the lowest pressures.

Again the gas trapping $I\tau$ product should be independent of the gage pressure. The variation seen may be due to the causes mentioned for 20-kev protons, that is, precession effects at high pressures and a possible instability at low pressures. Because of the changes in energy and beam current, a given $I\tau$ product does not correspond to the same trapped density at 20 kev and 40 kev. With gas trapping the maximum $I\tau$ product corresponds to a density of 8×10^5 protons/cm^3. With 40 kw microwave power the maximum density of trapped protons is 7×10^6 protons/cm^3.

Figure 3.8 is a plot of $1/\tau$ vs pressure for the 40-kev protons with and without microwave power. Again it shows the two curves to be linear and to extrapolate through zero.

The experiment is obviously not ideal with 40-kev injection. The proton orbits are quite large,

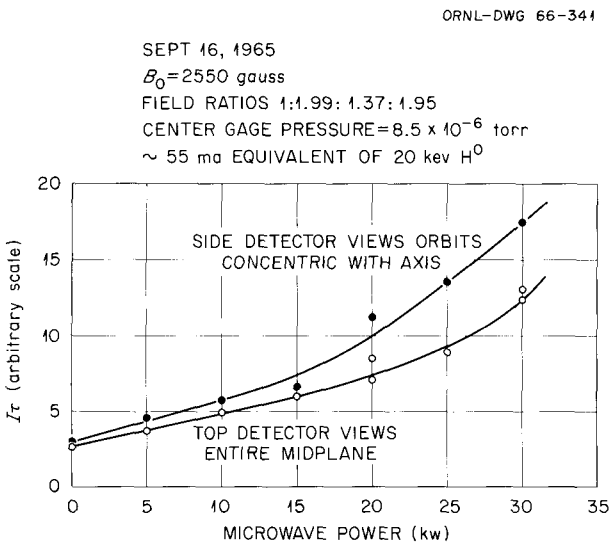

Fig. 3.5. Plot of $I\tau$ vs Microwave Power for Two Detectors. The quantities B_0 and the field ratios are as defined previously.

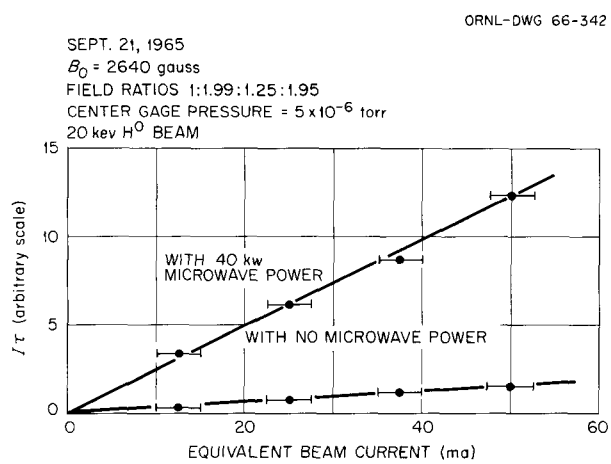

Fig. 3.6. Plot of the $I\tau$ Product for a Detector vs the Input 20-kev Neutral Beam Current (Power Equivalent). The quantity B_0 refers to the axial midplane magnetic field. The field ratios are as defined previously.

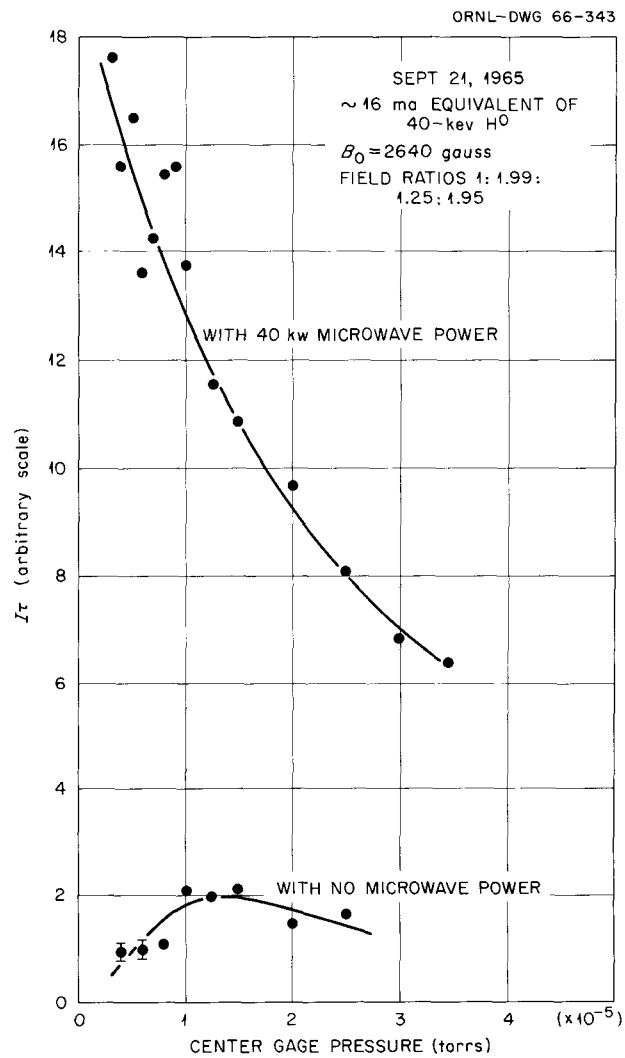

Fig. 3.7. Plot of the $I\tau$ Product for a Detector vs the Gage Pressure. This curve is for 40-kev neutral injection. All terms are as defined previously.

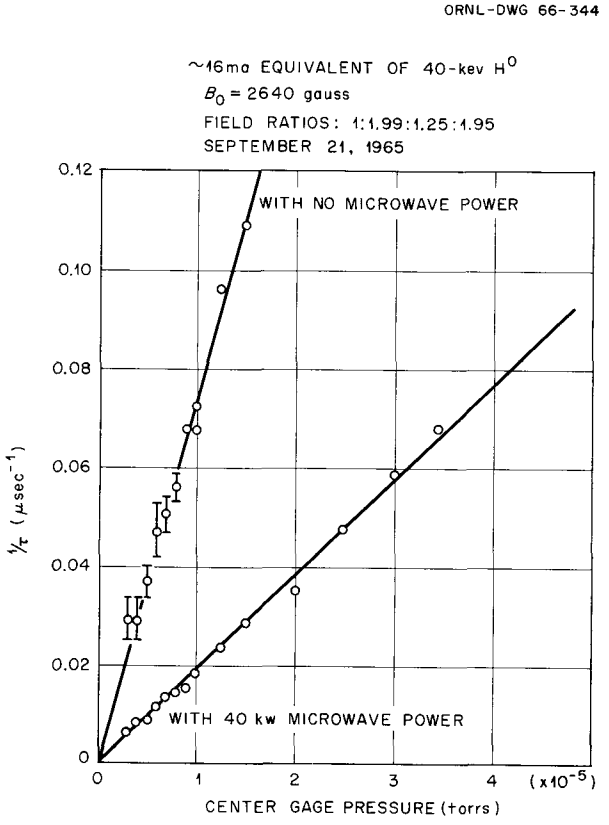

Fig. 3.8. Plot of $1/\tau$ vs Pressure for a Detector with 40-kev Injection. All terms are as previously defined.

and hence the ECP thickness is no longer sufficient to provide a good blanket effect for shielding against neutral gas. The experiment was performed to measure the charge-exchange decay time and $I\tau$ product at another energy as a consistency check.

3.1.3 Cold-Ion Density

We have also been able to indirectly measure the cold-ion density. The measurement gives the cold-ion density across the midplane weighted in an unknown way by the trapped 20-kev proton density, which peaks near the axis.

The calculation is as follows. The neutral charge-exchange current to the detector with the ECP is given by

$$I_{ECP} = K_1 \left(n_c \sigma_{ii} + n_0' \sigma_{01} \right) , \qquad (1)$$

where K_1 includes geometric factors and the input beam current. All other quantities are as previously defined.

For gas trapping at the same external pressure, the neutral current to the detector is given by

$$I_{gas} = K_1 n_0 \sigma_{01} , \qquad (2)$$

where the quantities are as before but now n_0 is the neutral-gas density as determined from a vacuum gage reading.

Combining Eqs. (1) and (2), we have, after some algebra,

$$n_c = n_0 \left(\frac{\tau_{gas}}{\tau_{ECP}} \right) \left(\frac{I_{ECP} \tau_{ECP}}{I_{gas} \tau_{gas}} - 1 \right) \left(\frac{\sigma_{01}}{\sigma_{ii}} \right) . \qquad (3)$$

Here we have used the fact that $n_0'/n_0 = \tau_{gas}/\tau_{ECP}$, where τ_{gas} and τ_{ECP} are the charge-exchange current decay times with gas trapping and ECP trapping respectively.

Thus, it is possible to calibrate the detector at a given pressure and then, using the $I\tau$'s obtained with the ECP present, calculate the cold-ion density in the ECP. Unfortunately, this procedure does not work well at high pressures, since Eq. (2) is not correct above 1×10^{-5} torr, probably because of the precessional effects mentioned in Sect. 3.1.2. At higher pressures a comparison is made between the detector currents and decay times with microwave power on at two different pressures. Since n_c is known at one pressure, a relation giving n_c at another pressure can be found.

Figure 3.9 shows the variation of n_c with gage pressure. It is seen that the density does not rise linearly with pressure, which means that the gas is less efficiently ionized at high pressures. This accounts for the decrease in $I\tau$ with microwave power at high pressures. Because of the reasons mentioned above, no great precision is claimed for the values plotted.

The cold-plasma density has also been calculated as a function of power. The calculation shows that n_c increases approximately linearly with power up to 25 kw and apparently faster than linear above 25 kw.

While there is no good way to compare this determination of the cold-plasma density with older data, there is reason to believe that the density is lower now than it was prior to the installation of the cavity end sections and the external field coils. The ratio of decay time with and without

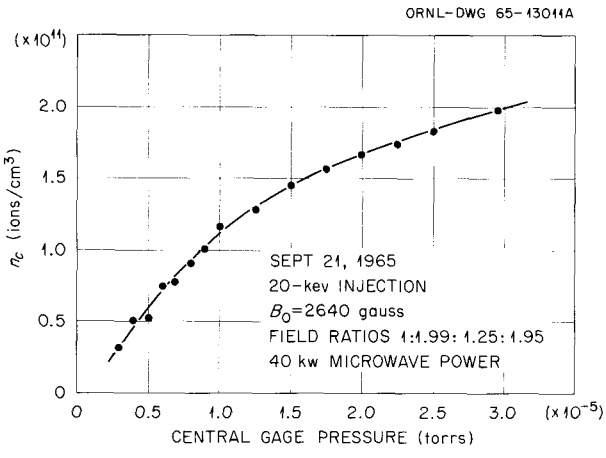

Fig. 3.9. Plot of the Cold Plasma Density vs Pressure as Determined by Measurements with the Neutral Beam. No great accuracy is claimed, as this represents a sampling across the midplane weighted by the trapped 20-kev proton distribution, which is maximum near the axis. All terms are as defined previously.

power was higher then than it is now, making evident the need for higher specific microwave power. Compensating this effect (in single-region system) was the fact that the external neutral pressure could not be lowered below about 1×10^{-5} torr, and hence the overall effect in terms of neutral pressure reduction was not as good. It is reasonable to expect that more microwave power in the larger cavity will result in higher cold-plasma density and lower neutral-gas density.

3.1.4 Operation with Power in End Cavities

During the latter part of the period of this report, microwave "plumbing" was added so that some power could be fed directly into the end cavities. This is shown schematically in Fig. 3.2. One of the klystrons was used to feed both end cavities with a maximum power of 7 kw continuous wave in each end.

The purpose of this modification was to utilize the microwave power more effectively in order to get more complete ionization of the gas fed into the ends. Only a short period of operating experience was gained before difficulties were experienced with the vacuum. Apparently, as a result of several abrupt vacuum failures, a considerable amount of pump oil had coated the interior of the microwave cavity. Because of the efficient use of the microwave power, the input deuterium gas feed could be reduced significantly and the ECP was supplying itself with gas from the pump oil "varnish" on the cavity interior.

Beam injection studies were continued down to central gage pressures of 1.6×10^{-6} torr. When the outgassing from the wall was not large, the usual two-component decays were seen at beam turnoff. The short-decay e-folding time was as long as 200 μsec, and the e-folding time of the tail was several milliseconds. However, when conditions were such that the input gas feed was cut off completely, the ECP would establish itself on the materials which were sputtered or which were otherwise removed from the cavity wall, necessitating the interruption of the experiment. The short-component e-folding times did reach 300 μsec. For these short-component decays, the $I\tau$ product was $\tilde{=}15$ times larger than that obtained with deuterium gas trapping. When the "varnish plasma" was present, the vacuum gage reading apparently bore no relation to the actual pressure in the cavity because of the high partial pressure of condensables. The light from the ECP in the cavity changed from the characteristic blue-pink of a deuterium-fed plasma to a blue-white for the varnish plasma.

The apparatus has now been dismantled for cleaning.

3.2 ELECTRON-CYCLOTRON HEATING EXPERIMENTS IN THE ELMO FACILITY

W. B. Ard
M. C. Becker[9]
R. A. Dandl[9]
H. O. Eason
A. C. England
G. M. Haas
R. L. Livesey
M. W. McGuffin

3.2.1 Introduction

Since the last semiannual report the microwave power source and associated apparatus have been sufficiently refined to allow routine operation of the 8-mm electron-cyclotron plasma in ELMO. The technical details of the microwave complex constitute the first part of this report.

Experiments with the 8-mm electron-cyclotron plasma have centered around the two extremes of plasma operation occurring at the limits (in this

[9]Instrumentation and Controls Division.

apparatus) of magnetic mirror ratio and axial resonant heating zone position. When the heating zone is near the mirror maximum and when the mirror ratio is relatively low (approximately 1.6:1), the hot-electron temperature is less than 30 kev. When the mirror ratio is higher (approximately 3:1) and when the heating zones are nearer the midplane, a very energetic electron gas can be formed, and some details of the most energetic component of this plasma are described later on.

Depending on cold-plasma density (as controlled by varying neutral gas density) and axial heating zone position, gross instabilities can occur in the afterglow in either the very high or relatively low electron temperature cases. In the low-temperature case as many as four distinct instabilities, each involving a fair fraction of the total energy, have been observed diamagnetically in the afterglow. The time separation of these energy dumps is in the neighborhood of 200 μsec. In the high-temperature case one to three energy dumps have been observed in the afterglow. The time separation of these events is of the order of $\frac{1}{2}$ sec. Experiments permitting more detailed analysis of these plasma conditions will be undertaken in the near future.

However, it is encouraging to note that the lower-temperature hot-electron gas might be formed at sufficiently high density to permit extension of the environmental plasma injection program (described in Sect. 3.1) to stronger magnetic fields and higher energetic-proton densities. Detailed studies of this regime are in progress. The very energetic hot-electron gas case is interesting for the mechanisms that provide the heating.

3.2.2 Description of the ELMO Experimental Facility

The ELMO Facility (as shown in Fig. 3.10) has been operated as a variable-ratio magnetic mirror device for short-wavelength electron-cyclotron heating studies during this report period. The physical configuration of this facility has been reported previously.[10,11] Variable mirror ratio is achieved by adding, in selected proportions, the uniform field produced by a pair of Helmholtz coils (maximum midplane field ~7 kilogauss) to the field produced by a pair of 3.2:1 ratio mirror coils (maximum midplane field ~6 kilogauss) placed on the same coordinates. This arrangement permits operation at any mirror ratio between 1.6:1 and 3:1 with a 12.6-kilogauss electron-cyclotron resonance field present in the mirror regions.

The microwave power source supplying the ELMO Facility consists of two type WJ-282 traveling-wave-tube (TWT) oscillators, each having a continuous-wave power output capability of 1000 w at a frequency of 35.7 ± 0.2 gigahertz. To minimize waveguide losses, these tubes are located as close as possible to the ELMO Facility. The large fringing field from the Helmholtz coils required that the tubes be magnetically shielded to prevent defocusing of the electron beams and consequent damage to the tubes. The outputs of the tubes are fed to the cavity through individual WR-28 (dominant-mode) waveguides matched to the cavity with sidewall hybrid junctions.[12] No interconnection exists between the outputs of the tubes except for a small amount of mutual coupling through the cavity. Half-wavelength beryllia ceramic waveguide windows obtained from the tube manufacturer are used to gain entry to the vacuum system. The output waveguides are water cooled and pressurized to 15 psig with dry nitrogen. Usual principles of good high-power practice are observed with regard to cleanliness, alignment and contact of mating flanges, component selection, etc., in order to minimize the possibility of waveguide arcs which could destroy the oscillator tubes. Multihole sidewall directional couplers are used to sample power output and reflected power due to load mismatch or waveguide arcs.

Existing high-voltage power supplies were used to meet the 25 kv at 0.4 amp beam requirements of the WJ-282 oscillator tubes. However, since beam voltage control offers the only external control over power output, extensive additions and modifications were required in order to meet the following operational and fault-protection considerations.

1. Thermal considerations in the delicate coupled-cavity structures of the tubes required that the beam voltage be removed within a few microseconds in the event of an internal arc to the

[10] *Thermonuclear Div. Semiann. Progr. Rept. Oct. 31, 1964*, ORNL-3760, sect. 3.2.1.

[11] *Thermonuclear Div. Semiann. Progr. Rept. Apr. 30, 1965*, ORNL-3836, sect. 3.2.

[12] *Thermonuclear Div. Semiann. Progr. Rept. Oct. 31, 1963*, ORNL-3564, sect. 3.1.2, pp. 30–31.

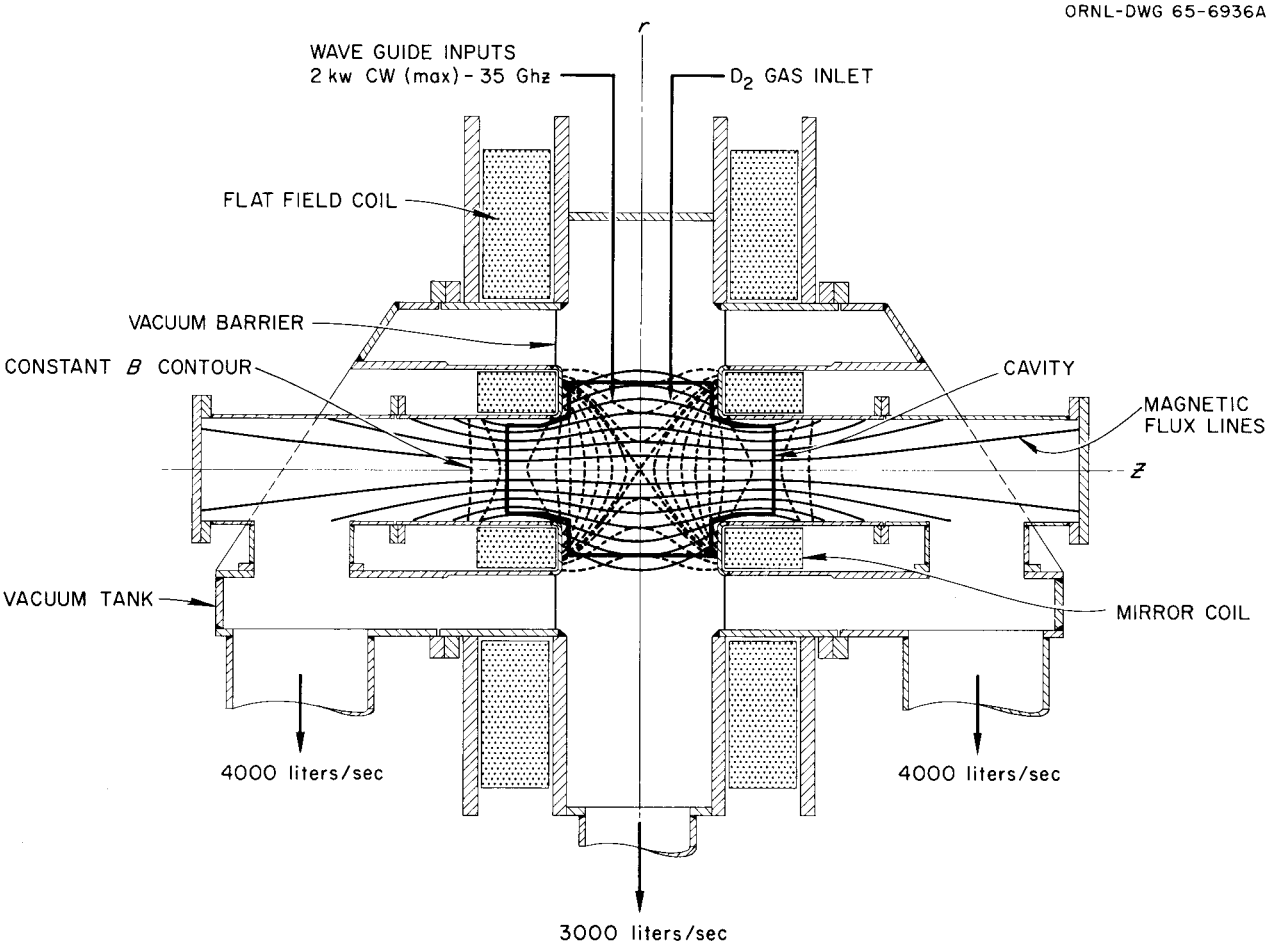

Fig. 3.10. Schematic of the ELMO Facility.

structure or excessive defocusing of the electron beam.

2. Protection of the output waveguide window in the event of a waveguide arc or excessive load mismatch requires removal of the output power within a few microseconds after such a fault occurs.
3. Plasma decay measurements require fast turn-off of the microwave power when desired, with minimum time required to restore normal operation for expedient performance of a series of such measurements.

All of the preceding considerations point to the need for a fast switch or crowbar on the output of the beam supply capable of removing beam voltage from the tube within a few microseconds upon sensing a fault or receipt of an external command. These requirements were met by the system shown in the block diagram of Fig. 3.11.

A type 893 triode vacuum tube driven by a dc amplifier is used as a high-voltage switch in the negative output lead of the supply to disconnect the supply from the oscillator tube. Input to this amplifier is telemetered from ground by a radio-frequency link, with the transmitter operated at ground potential and the receiver at negative high voltage.

The 893 triode is normally conducting when the rf transmitter is operating and is cut off rapidly upon loss of the rf signal. The transmitter is turned off by operation of any one of the three flip-flops. An auxiliary circuit in the receiver provides latching action to render it inoperative subsequent to high-voltage turnoff and thus to prevent operation from spurious signals. Signals actuating the flip-flops are derived from a manually operated switch, from a resistor through which body current of the TWT flows, and from a wave-

ORNL-DWG 66-345

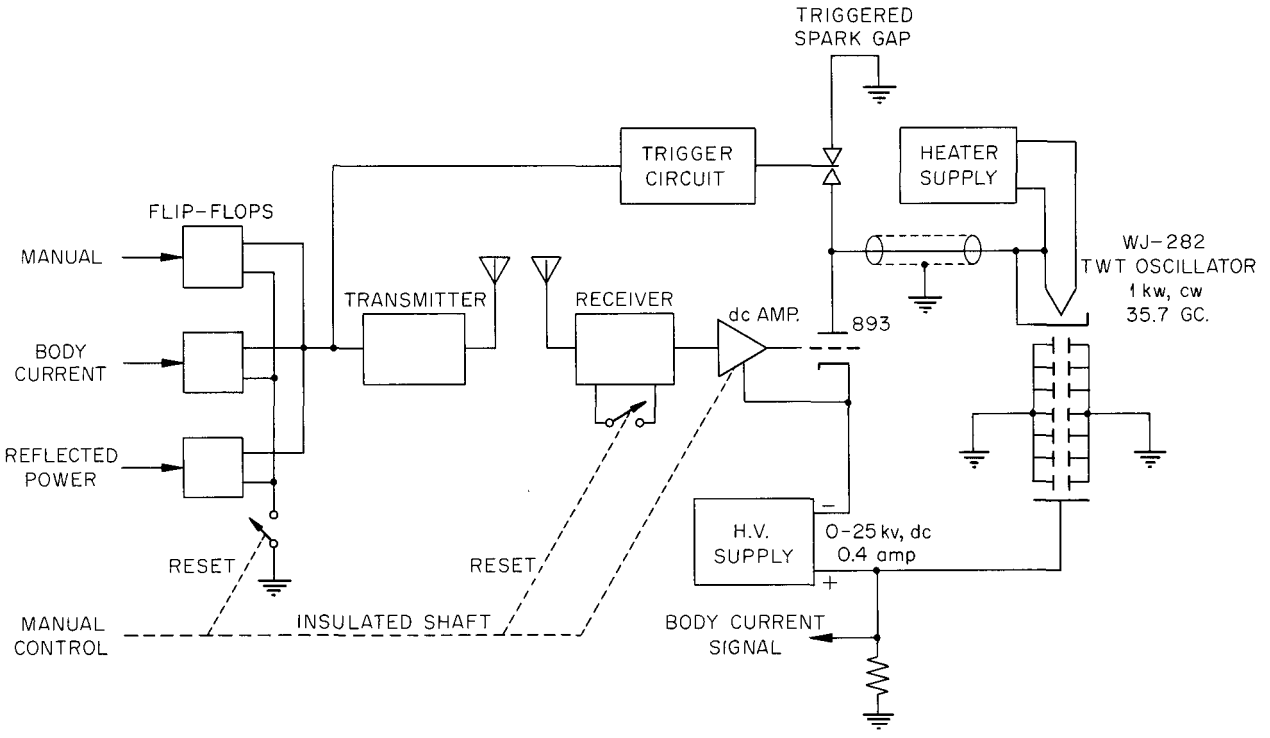

Fig. 3.11. Block Diagram of Protective and Control System Used with TWT Power Supply.

guide crystal mount connected to the side arm of a reverse-power directional coupler in the output waveguide. Manual control of the 893 grid bias through a control with an insulated shaft provides fine adjustment of the beam voltage and permits smooth, rapid restoration of beam voltage after a turnoff operation. The flip-flop reset circuits and the latching circuit in the receiver are interlocked with this manual control to prevent sudden, inadvertent application of high voltage to the TWT.

An auxiliary triggered spark gap is connected across the TWT to discharge the residual capacitance (approximately 0.01 μf) to ground of the high-voltage cables and heater supply. This triggered spark gap operates simultaneously with the opening of the vacuum tube switch. Total decay time for the high voltage using this turnoff system is about 5 μsec after receipt of a signal. Operation has been very satisfactory, and, due to the small amount of energy dissipated in crowbar operation, no difficulty with spurious signals has been encountered.

The microwave cavity or plasma chamber used for most of the short-wavelength heating studies during this period has been of conventional water-cooled perforated copper construction with tight metallic joints. The diameter in the central region was 12 in. Short sections on either end, of $6\frac{1}{2}$-in. diameter, extended into the mirror throats, giving a cavity volume of 25 liters. A 4-in.-diam cavity of stainless steel and perforated copper construction has recently been installed for the purpose of attaining increased microwave power density with the available 2-kw input power. It also provides an increased speed of response for $d\phi/dt$ measurements due to the reduction in shunting effect of the thin stainless steel walls.

Operation of the 35.7-gigahertz power source has been much more difficult than operation of the lower-frequency sources previously used for electron-cyclotron heating. These operational problems are due to the extreme sensitivity of oscillators of this type to small changes in load impedance, their highly nonlinear beam voltage vs power out-

put characteristic, and the lack of availability of suitable ferrite devices for load isolation at this power and frequency range. These problems are compounded by the fact that two tubes are being used, since the output of a given tube is affected by the small coupling to the other tube through the mutual impedance of the cavity. This mutual impedance includes, of course, the effect of the plasma, which is in turn dependent upon microwave power as well as magnetic and gas-feed parameters.

The net result is that power output does not vary smoothly with beam voltage except within very narrow limits determined by the combination of many parameters. Outside these limits the power output may fluctuate wildly due to "moding" of the oscillators with a period determined by the plasma time constants. A useful operational monitor, in addition to the usual microwave noise and pressure indicators, has been a dual-beam oscilloscope display of signals proportional to the output power amplitudes of the two oscillators. These signals are derived from crystals and forward-power directional couplers in the output waveguides. In operation the beam voltages, gas feed to the plasma, and the magnetic field are varied slightly about the desired values until a combination is found which produces a stable microwave power input together with stable plasma conditions. Once a stable set of operating conditions is found, these conditions can generally be reproduced for successive decay measurements without difficulty.

3.2.3 Plasma Characteristics

In the plasma formed in the ELMO Facility with the 8-mm microwave, four rather distinct energy groups of electrons have been identified. For the purpose of discussion, these groups shall be labeled 1 to 4 in order of increasing temperature or mean energy.

The first group (1) is a very low-energy plasma, termed the "cold" plasma. This plasma was studied by means of biased probes located outside the ends of the cavity. The axial current probes used had a 3.18-mm hole and were biased to +45 v. These probes were located about 2.5 cm past the end of the cavity, placing them about 25 cm from the center of the cavity. Maximum currents of 10 to 15 ma were observed to decay with a τ of approximately 80 to 100 μsec. These current measurements indicate a maximum cold plasma density in the neighborhood of 10^{12}/cc. No direct measurement of the electron energies in the "cold" plasma have been made, but it can be argued that these energies are rather low. By using an array of probes, it is found that the cold plasma is fairly uniform over the volume. If one *assumes* that the cold plasma fills most of the volume and that a substantial part of the power (2 kw) goes into the cold plasma, then conservation of energy per unit time requires that the electron temperature be of the order of a few tens of ev.

Information on the second and third groups was obtained by measuring the bremsstrahlung spectrum from the plasma. Figure 3.12 shows the x-ray collimator as it was used for the group 3 measurements. For the low-energy (group 2) measurements a vacuum pipe was connected from the machine through the collimator, and a 1 in. $\times$ 3 mm NaI crystal with a 5-mil beryllium window was mounted in the vacuum chamber along with the photomultiplier. Peak widths for this system were approximately 8 kev. Figure 3.13 shows a typical spectrum in which there is a distinct low-energy group superimposed on the spectrum of a high-energy group. A good deal of difficulty is encountered in these measurements because of the backscatter from the aluminum windows due to illumination by the cavity ends. These low-energy measurements indicate temperatures of 15 to 30 kev with densities up to approximately 5×10^{11}/cc. X-ray pinhole photographs have been made, and no high-density plasma of small volume has been observed, implying that this plasma fills a significant portion of the cavity.

Group 3 was analyzed with the collimator shown, but with the 3 $\times$ 3 in. NaI crystal. Two spectra for two different mirror ratios are shown in Fig. 3.14. In the upper case (No. 1) the "temperature" is approximately 400 kev with a density of 6.2×10^{10}/cc, and in case No. 7 the "temperature" is also 400 kev but with a density of 6.8×10^{11}/cc. The bremsstrahlung calculations were made using nonrelativistic equations and assuming isotropy. It is believed that the energetic plasma is rather anisotropic and hence the above assumptions produce some error. Calculations have shown that the relativistic effect is small, but no calculations have been made on the effect of anisotropy. In addition, it was assumed that no ions of $Z > 1$ were present in the plasma.

ORNL-DWG 65-10778A

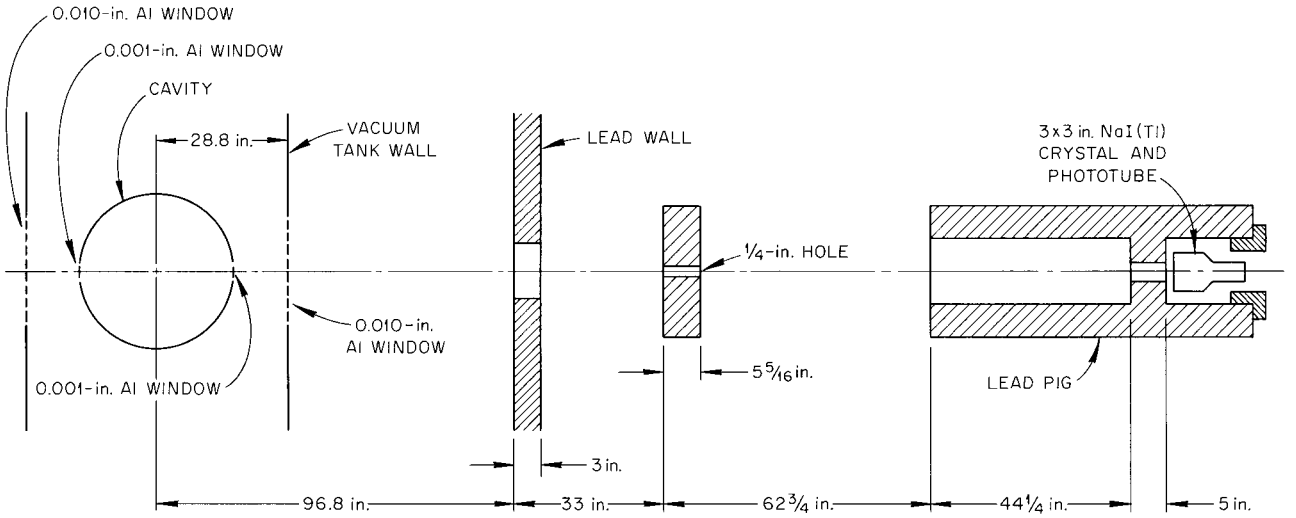

Fig. 3.12. Schematic Diagram of the New Bremsstrahlung Collimator and ELMO Cavity.

Figure 3.15 shows how the electron density (400-kev group), neutron intensity, and stored energy varied with mirror ratio for a fixed axial position of the resonant constant-B surface. As can be seen, there is a definite relation between density, neutron intensity, and stored energy, and these are strongly dependent on mirror ratio. The same sort of phenomenon is observed with changes in the axial position of the resonant constant-B surface for a fixed mirror ratio.

Information on group 4 is obtained by studying the neutron intensity and the change of intensity with time after the microwave power is turned off. The neutrons were detected using a high-pressure ^{3}He proportional counter surrounded by a paraffin pig. The signal from the counter was fed into a 400-channel analyzer operating in the multiscaler mode with 10 msec/channel. Figure 3.16 shows the neutron intensity as a function of time after the microwave power is switched off. It is found for this case that the neutron intensity dropped to $\frac{1}{2}$ in approximately 0.2 sec.

Previous experiments with plasmas created by electron-cyclotron heating at 3 cm have shown[13] that the bulk of the neutron production in these plasmas is due primarily to Coulomb or electrodissociation of deuterium by high-energy electrons

ORNL-DWG 65-10306A

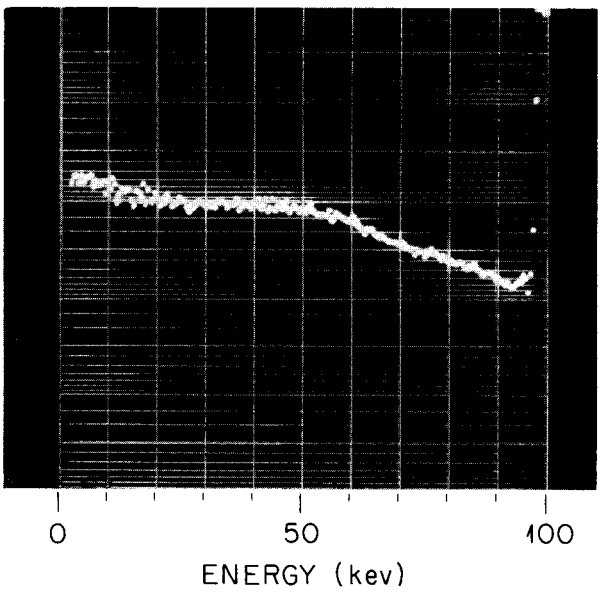

Fig. 3.13. Low-Energy X-Ray Spectrum. B_{00} is the magnetic field on axis midway between mirror coils.

[13] W. B. Ard *et al.*, *Phys. Rev. Letters* **10**, 87 (1963).

ORNL-DWG 65-10771A

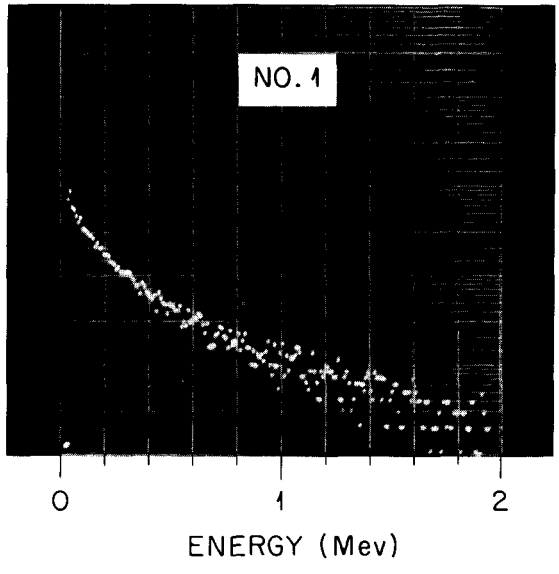

800 watts, 8 mm
1.57×10^{-5} torr, $B_{00} = 9.7$ kG
MR = 1.77, $z = 5$ in., 1-min count
ELMO, JUNE 10, 1965

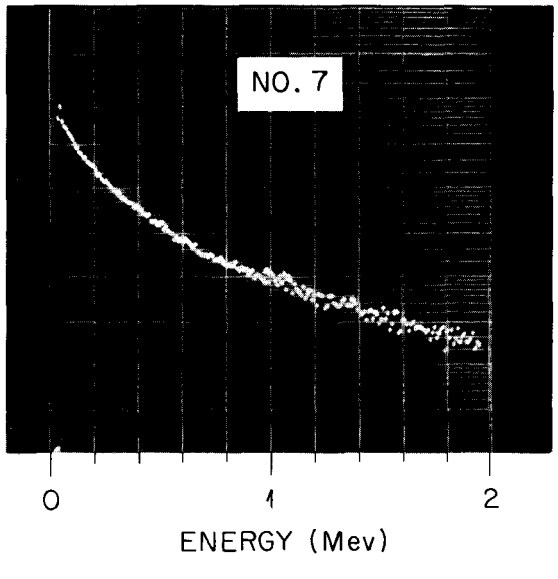

1000 watts, 8 mm
2.1×10^{-5} torr, $B_{00} = 7.1$ kG
MR = 2.70, $z = 5$ in., 1-min count
ELMO, JUNE 10, 1965

Fig. 3.14. High-Energy X-Ray Spectrum. Two different mirror ratios were used.

(i.e., $e + d + 2.2$ Mev $\rightarrow e + n + p$). The cross section for this reaction has been calculated by Soper[14] based on the formulas of Guth and Mullin.[15]

For the neutron production, the total reaction rate per unit volume may be written as

$$R = \int_{v_1, v_2} [n_1 f_1(\vec{v}_1)] [n_2 f_2(\vec{v}_2)] |\vec{V}| \sigma(v) \, d\vec{v}_1 \, d\vec{v}_2 .$$

For the case of Coulomb dissociation of neutrals by relativistic electrons ($v \sim c$), the reaction rate may be written in terms of energy approximately as

$$R \tilde{=} n_0 c \int_{2.2}^{\infty} n_e f_e(E) \sigma_{ed}(E) \, dE .$$

The reaction rate as a function of time may then be written as

$$R(t) \tilde{=} n_0 n_e c \int_{2.2}^{\infty} f_e[E(t)] \sigma_{ed}[E(t)] \, dE .$$

For radiation cooling the energy of an electron as a function of time (sec) in a magnetic field B (gauss) is given by

$$\frac{E_\perp(t)}{E_\perp(0)} = \left[\exp\left(\frac{B^2 t}{2.58 \times 10^8}\right) + \frac{E_\perp(0)}{m_0 c^2} \left(\exp \frac{B^2 t}{2.58 \times 10^8} - 1 \right) \right]^{-1} .$$

If one assumes an initial distribution in energy at time $t = 0$, then the relative intensity as a function of time may be calculated as

$$\frac{I(t)}{I(0)} = \frac{\int_{2.2}^{\infty} f_e[E_\perp(t)] \sigma_{ed}[E_\perp(t)] \, dE_\perp}{\int_{2.2}^{\infty} f_e[E_\perp(0)] \sigma_{ed}[E_\perp(0)] \, dE_\perp} .$$

The relative intensity at 0.2 sec for several distributions in two different magnetic fields has been calculated, and the results are shown in Table 3.1. For the data of Fig. 3.16 with a B_{00} of 6.8 kilogauss, the relative intensity at 0.2 sec is 0.5.

[14] *Thermonuclear Div. Semiann. Progr. Rept. Oct. 31, 1962*, ORNL-3392, sect. 6.6.

[15] E. Guth and C. J. Mullin, *Phys. Rev.* **76**, 239 (1949).

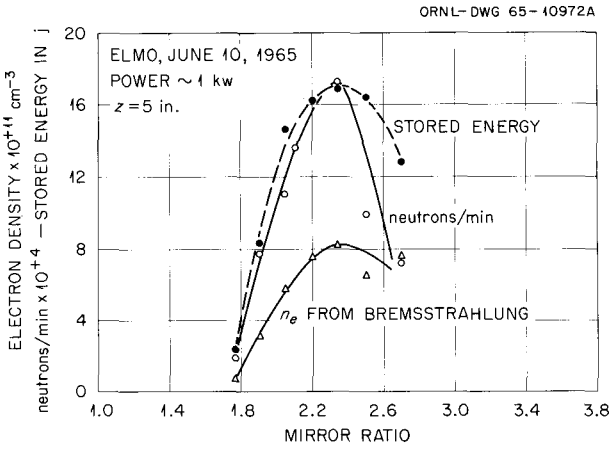

Fig. 3.15. Stored Energy, Neutrons per Minute, and Electron Density as a Function of Mirror Ratio.

A comparison of the experimental value with those of Table 3.1 indicates that the velocity distribution is peaked in the neighborhood of 6 Mev. Figure 3.17 shows the experimental points of Fig. 3.16 plotted along with the calculated curve for a 6-Mev monoenergetic group in a 6-kilogauss magnetic field. This agreement is reasonably good out to times of 0.4 and 0.5 sec. Beyond 0.5 sec the experimental decay is faster than that calculated. This difference could be due to the diamagnetic effect. For this case the measured stored energy

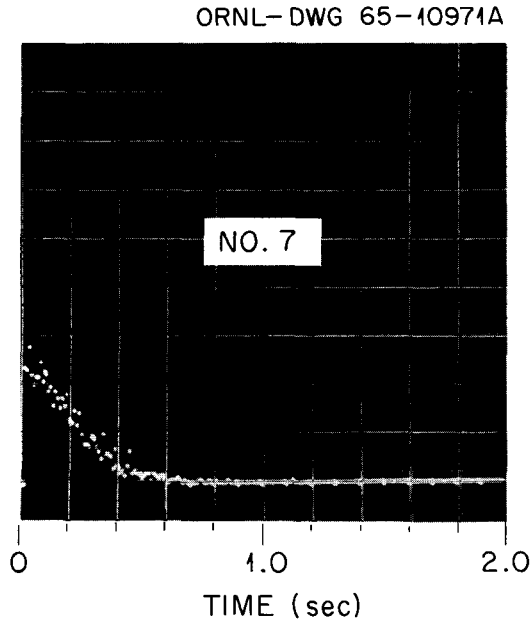

$P = 1$ kw, 8 mm
PRESSURE = 2.88×10^{-5} torr
MR = 2.3, $z = 6.35$ in., $B_{00} = 6.8$ kG
187,000 counts/min BEFORE TURNOFF
ELMO, JUNE 29, 1965

Fig. 3.16. Neutron Intensity as a Function of Time After Microwave Turnoff.

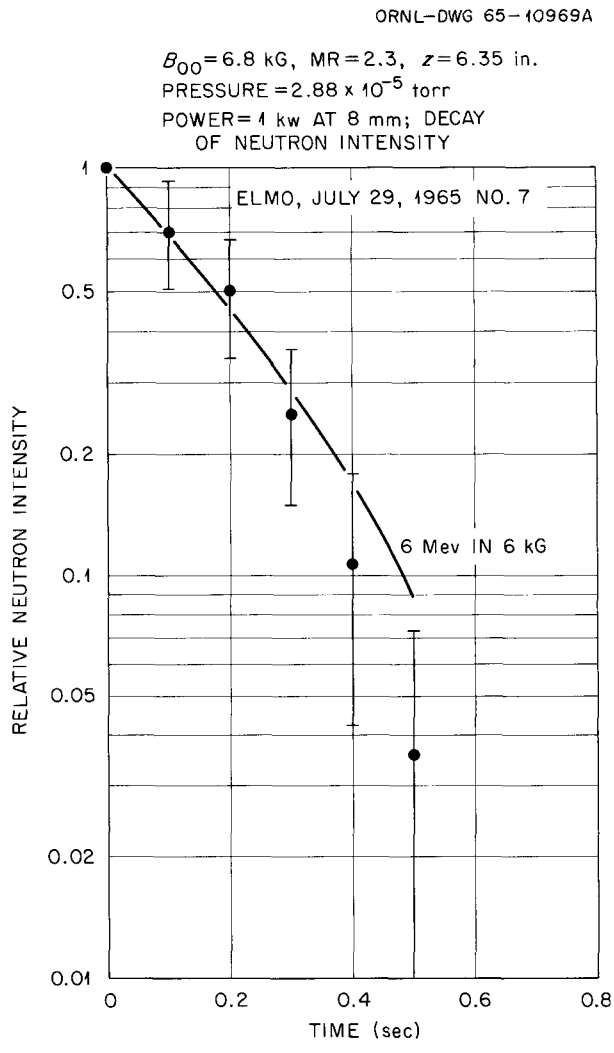

Fig. 3.17. Relative Neutron Intensity as a Function of Time After Microwave Turnoff. Points: experimental from Fig. 3.16; curve: calculated on the basis of radiation cooling of 6-Mev electrons.

was approximately 18 j. However, since no measurement of the volume occupied by the energetic electron plasma is available, the magnitude of ΔB cannot be calculated. The value of ΔB as a function of volume for this case is $\Delta B \simeq (340/V)$ gauss, where V is the volume in liters. As time increases after turnoff, ΔB decreases and the energy loss rate increases. The fact that the observed decay can be accounted for by having the particles in a field of the order of 6 kilogauss implies that they are located near the midplane and that $E_{\perp}/E_{||} \gg 1$. Using a 6-Mev monoenergetic distribution and assuming a volume, one can calculate the electron density. The density is given approximately as $(2 \times 10^{13}/V)$ cm^{-3}. The radial distribution of these Mev electrons was investigated by inserting a radial skimmer into the plasma. The neutron intensity as a function of skimmer position is shown in Fig. 3.18 and indicates that the Mev electrons are distributed fairly uniformly over the midplane.

Table 3.1. Relative Neutron Intensity for Several Distributions

Distribution	$I(0.2)/I(0)$	
	5 kilogauss	6 kilogauss
Maxwellian (T = 500 kev)	0.31	0.18
Rectangular (E_{max} = 6 Mev)	0.36	0.25
Triangular (E_{max} = 6 Mev)	0.38	0.18
Monoenergetic (E = 6 Mev)	0.60	0.46

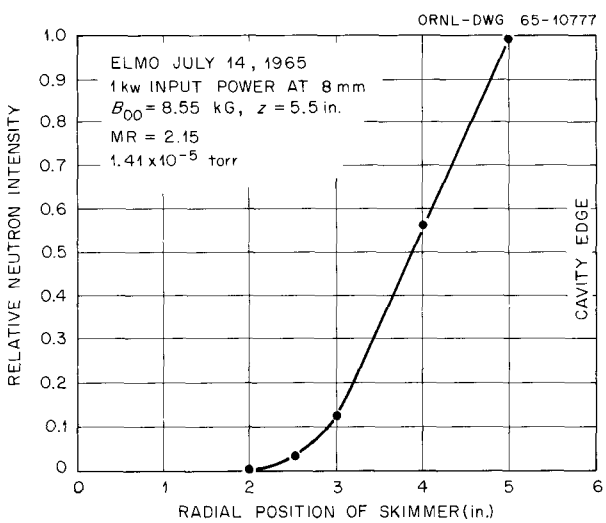

Fig. 3.18. Relative Neutron Intensity as a Function of Radial Skimmer Position.

Measurements of the stored energy and decay times for the 8-mm plasma indicate that a larger fraction of the applied power is going into the hot plasma as compared to the fraction for the 3-cm plasmas. No apparent density limits with power have been observed, and it is believed that the present power per unit volume is too small to achieve cutoff densities. Since it is impossible to increase the available power, experiments are being pursued in a smaller cavity in order to study the effect of increased power density on the plasma density.

3.3 ELECTRON-CYCLOTRON HEATING EXPERIMENTS IN THE PHYSICS TEST FACILITY (PTF)

W. B. Ard
M. C. Becker[16]
R. A. Dandl[16]
H. O. Eason
A. C. England
G. M. Haas
R. L. Livesey
M. W. McGuffin
R. F. Stetson[17]

3.3.1 Instability Studies

Hot-electron plasmas produced in magnetic mirrors by radiation at the electron cyclotron frequency have been found to be unstable under certain conditions.[18] The evidence indicating the presence of instability in this plasma was the observation of large bursts of x rays accompanied by sudden decreases in stored plasma energy. Recent investigations of the plasma in the Physics Test Facility (PTF) device have shown that these x-ray bursts are due to two different types of electron losses. In one type of loss the electrons cross the magnetic field lines and strike the wall on the midplane of the mirror field. In the other type of loss the electrons leave the plasma along the magnetic field lines.

Under typical operating conditions, the hot-electron component of the plasma in the PTF device has the following properties. The total

[16]Instrumentation and Controls Division.

[17]Research Participant from Florida Atlantic University, Boca Raton, Florida.

[18]R. A. Dandl *et al.*, *Nucl. Fusion* **4**, 344 (1964).

energy stored in the plasma is 9 j. The average electron energy is from 50 to 100 kev. The plasma volume is about 4×10^3 cc. This gives a density of from 1.5 to 3×10^{11}/cc and a β of 0.06. The plasma is maintained by a continuous feed of neutral gas into the region occupied by the plasma and continuous feed of microwave energy into the same region. The pressure outside the plasma is typically about 10^{-5} torr. There is therefore a background density of much cooler electrons always present in the plasma. The density of cooler electrons is estimated to be about the same as that of the hot electrons. This estimate is based on the current collected by probes outside the magnetic mirrors.

Shown in Fig. 3.19 is the arrangement of various probes for investigating instabilities. Fast electrons lost along field lines are detected by silicon solar cells placed outside the mirrors. The four solar cells are positioned on field lines that come through holes in the end of the liner at 0, 1, 2, and 3 in. from the magnetic axis. The cells are shielded from the plasma by thin aluminum foils. Since signals were observed from the solar cells only when they were placed along the field lines that came through a hole in the liner, it was determined that the signals were due to fast electrons and not due to x rays. The cells were operated short-circuited to give a current output proportional to the incident flux. The response time of the cells operated in this way is less than 1 μsec.

A collimated x-ray detector was used to detect x rays from electrons striking the liner in the mirror region. The response time of the x-ray detector was 0.02 μsec. An rf pickup loop was placed just inside the liner on the midplane in order to look for oscillations at very high frequency. Lower-frequency oscillations could be

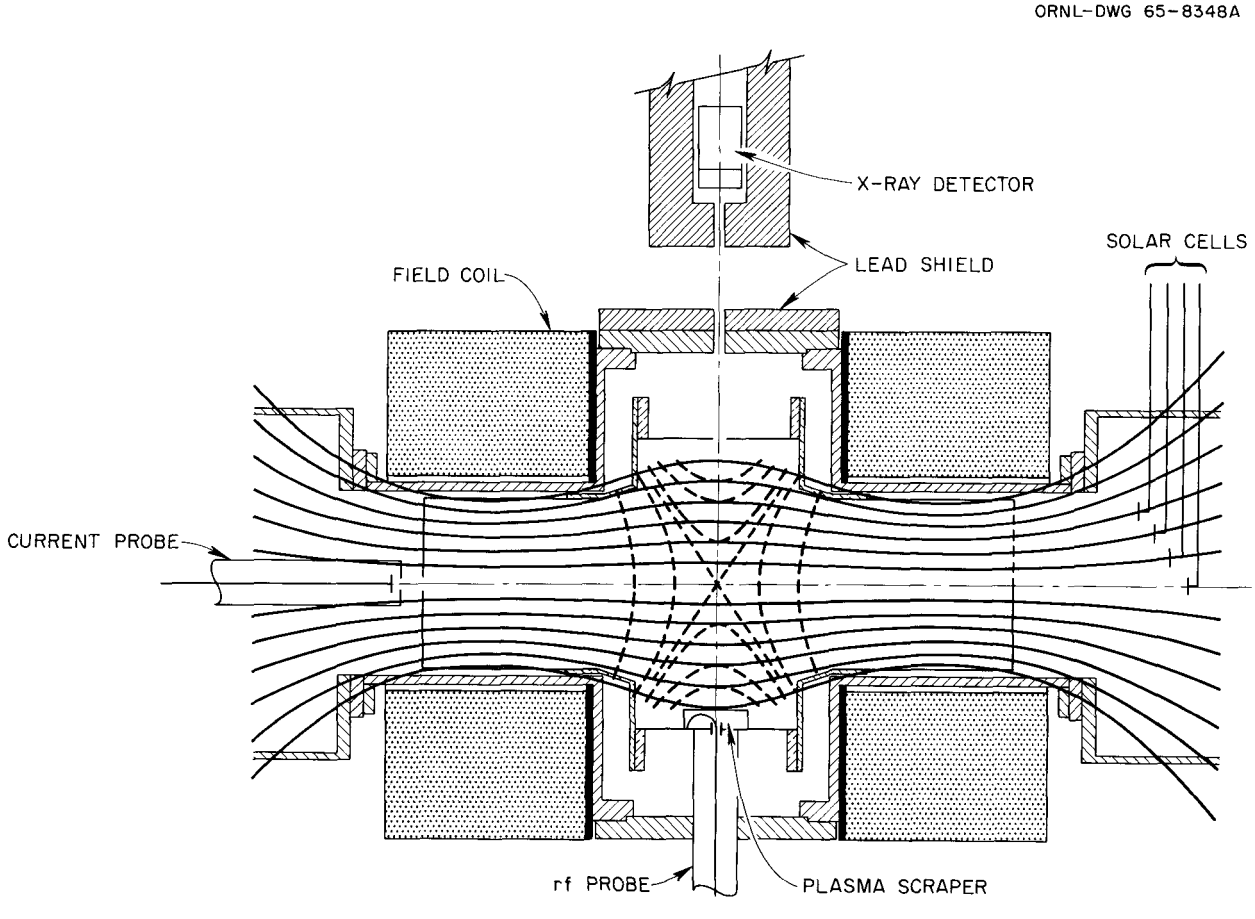

Fig. 3.19. Diagram of Physics Test Facility, Showing Location of Detectors Used for Instability Studies. Solid lines are flux lines; dashed lines are lines of constant B.

detected by the current probe located just outside the mirror. The stored plasma energy was measured with a diamagnetic loop.[19] Since the loop was wound around the copper liner, its response time was much too long to follow the change in energy during an instability. However, the response time was considerably shorter than the plasma buildup time so that the total energy lost during the instability could be measured quite accurately. The times involved were as follows: duration of instability – several microseconds; response time of diamagnetic loop – 10 msec; plasma buildup time – around 100 msec.

During one type of instability, the solar cells detected bursts of energetic electrons that lasted for about 2 to 10 μsec. All four of the cells gave signals at the same time; however, variations in signal level during the bursts were not well correlated among the detectors located on different field lines, although the beginnings and ends of the signals from the cells were well correlated. During the time that the solar cells indicated a large flux of energetic electrons out the mirror, the current probe showed a decrease of plasma current out the mirrors. Radiation was detected on the rf loop during the bursts. The radiation was in a frequency band about 50 Mc wide, centered at 5.3 kMc. This frequency is half the frequency of the microwave power source used to heat the plasma. Figures 3.20 and 3.21 show typical responses of the solar cell (upper traces) and the microwave receiver (lower traces) during an instability. The large variation in output from the receiver is mostly due to the frequency of the oscillation drifting out of the bandwidth of the receiver. In order to determine whether or not the 5.3-kMc oscillation was a plasma resonance driven by the microwave source, the source was turned off as soon as the electron burst could be detected. The source could be turned off less than 0.5 μsec after the burst started. The result was that the bursts continued for several microseconds and the 5.3-kMc radiation also continued. There was apparently no change in either the intensity or the spectral character of the rf with or without the microwave source on. While this shows that the oscillation is not just a parametric amplification of the applied microwave radiation, it does not rule out the possibility that the oscillation is triggered by the presence of the applied microwave power.

The average time interval between the bursts could be made arbitrarily long. This time was essentially determined by the magnitude of the static magnetic field intensity. In fact, if the field were set below a critical value, no bursts were observed.

The fact that the instability is influenced by the magnitude of the magnetic field suggests that the important parameter is the location in the

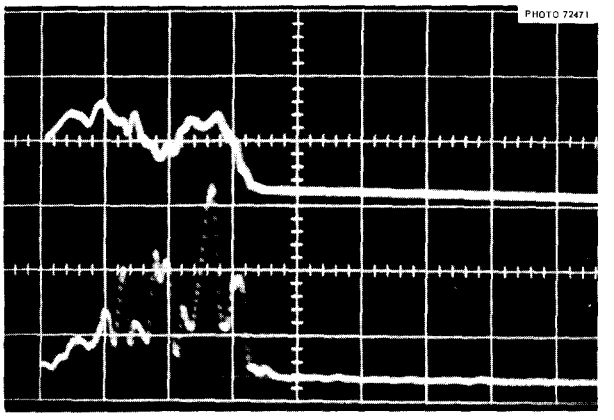

Fig. 3.20. Response of the Solar Cell and the Microwave Receiver During Instability. Upper trace: solar cell signal. Lower trace: microwave receiver output with tuning at 5300 Mc. Sweep rate: 2 μsec/cm.

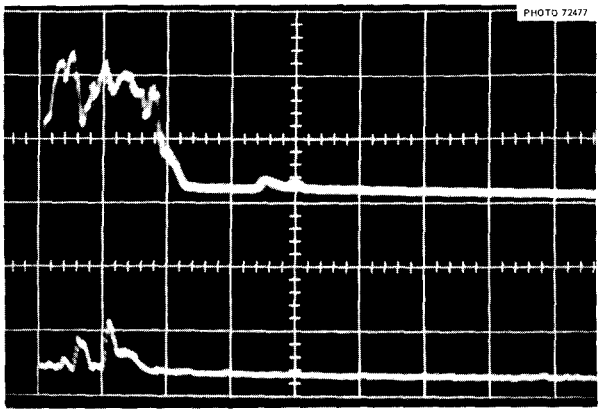

Fig. 3.21. Response of the Solar Cell and the Microwave Receiver During Instability. Upper trace: solar cell signal. Lower trace: microwave receiver output with tuning at 5300 Mc. Sweep rate: 2 μsec/cm.

[19] W. B. Ard *et al., Compt. Rend. Conf. Intern. Phenomenes Ionisation Gaz, 6^e, Paris, 1963* IV, 75 (1964).

mirror field of the region where the electron cyclotron frequency is resonant with the microwave power source. The onset of the instability occurred when the minimum field in the mirror, B_0, was 0.8 times the resonant field, B_r. If we assume that electrons gain energy from the microwave source only when they are in resonance and that they gain energy only transverse to the magnetic field, then the ratio $E_\perp/E_{||}$ is determined by the ratio B_r/B_0. Electrons whose turning points in the mirror are at a field less than B_r do not gain energy until they scatter enough to have their turning points in the resonant region. Electrons whose turning points lie at fields larger than B_r gain transverse energy until their turning point is at B_r. This assumption seems reasonable if, for those electrons that traverse the resonant region, $(\overline{dv_\perp}/dt)$ from interaction with the microwave field is larger than $(\overline{dv_\perp}/dt)$ from scattering. If the contained energetic electrons turn at $B < B_r$, then we have the relation

$$(E_\perp/E_{||})_{\min} = \frac{1}{(B_r/B_0 - 1)} .$$

As B_0 is increased, $(E_\perp/E_{||})_{\min}$ increases rapidly. The fact that the instability sets in as B_0 is increased therefore suggests that the instability is due to temperature anisotropy. The finite β of the plasma further suggests the "mirror instability."[20] The condition for this instability in an infinite plasma is given by

$$2\beta(E_\perp/E_{||} - 1) > 1 .$$

For $B_r/B_0 = 1.25$, $(E_\perp/E_{||})_{\min}$ is 4. This gives a critical β of 0.17. This is about 3 times the observed β. However, the average $E_\perp/E_{||}$ might be considerably larger than 4. The result of this instability would be a magnetic compression of the plasma toward the midplane of the mirror. While the plasma is compressed, the cold plasma current out the mirror should be very small. As the plasma surface moves toward the midplane, the oscillation frequency of the electrons between their turning points in the mirror field resulting from the instability would rise rapidly. We propose that when this frequency reaches $\omega_c/2$, the motion of the electrons between the mirror is coupled to the transverse motion of the electron at the cyclotron frequency. A modulation of the compression field at the cyclotron frequency would couple in this way. (It is analogous to the case of a weight supported by a string hanging from a vertically oscillating rod. The string will oscillate if the natural frequency of the string is half the frequency of the rod.) The result of this type of oscillation is to convert transverse electron energy to parallel energy. This could account for the observed enhanced loss of electrons through the mirrors. The compression field collapses due to the decrease in transverse energy and the increase in the parallel pressure. However, the total transverse energy lost during the instability is never more than about 10% of the total transverse energy. This measurement is made by measuring the total change in the magnetic moment of the plasma. We have not determined what fraction of this loss is due to actual particle loss and what fraction is due to increased parallel energy of the remaining plasma. The nearness of the frequency of the observed oscillation to one-half the klystron frequency is probably accounted for by some phasing of electrons in their Larmor orbits by the microwave field. These "phased" electrons would then very likely determine the frequency at which oscillation would start to grow.

A second type of instability observed appears to be the same as one observed by Post and Perkins in a hot-electron plasma.[21,22] This instability is characterized by a loss of energetic electrons to the wall at the midplane of the field. The electrons that strike the wall are detected by looking at the wall with a collimated x-ray detector. The drift velocity of the electrons across the field lines is much smaller than their precessional velocity due to the gradient in the magnetic field. In fact, a scraper extending about an inch inward from the liner intercepts all the electrons that are lost radially from the plasma. Oscillating electric fields are observed when the plasma is subject to this instability. Oscillations have been observed with frequencies from 3 Mc up to about 30 Mc. The oscillations last for a few microseconds and may recur several times within a period of about 50 μsec. Frequencies around 10

[20] H. P. Furth, *Phys. Fluids* **6**, 48 (1963).

[21] R. F. Post and W. A. Perkins, *Phys. Rev. Letters* **6**, 85 (1961).

[22] W. A. Perkins and R. F. Post, *Phys. Fluids* **6**, 1537 (1963).

Mc seem to be most prevalent. Bursts of x rays from the scraper usually accompany these oscillations. In fact, the x-ray intensity from the scraper can be modulated at the same frequency as the electric field fluctuations. Figure 3.22 is a photograph of the output from the x-ray detector and the signal from an electrostatic probe just outside one of the magnetic mirrors. The surface of the plasma is apparently rippled, and the variations in x-ray intensity are due to the precession of the ripples around the magnetic axis. The frequency of precession around the magnetic axis is 1 Mc for a 100-kev electron. Since frequencies of several megacycles are prevalent, modes with $m > 1$ predominate.

This instability can be suppressed by increasing the neutral gas pressure in the region of the plasma. This suggests that the instability is suppressed by increasing the conductivity of the plasma to the copper end walls of the vacuum liner. This behavior also agrees with Post's observations, and we, too, believe this to be a flute instability.

If the neutral gas pressure is low enough and the ratio B_r/B_0 is small enough, the plasma is subject to both types of instability and both types are observed to occur more or less at random.

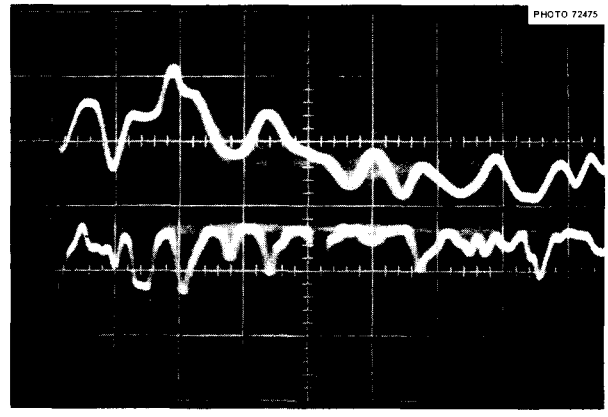

Fig. 3.22. Output from X-Ray Detector and Signal from Electrostatic Probe Just Outside One of the Magnetic Mirrors. Upper trace: current probe rf signal. Lower trace: x-ray detector signal. Sweep rate: 0.2 μsec/cm.

4. Plasma Physics

Igor Alexeff R. V. Neidigh
W. D. Jones W. F. Peed
W. L. Stirling

4.1 BEAM-PLASMA INTERACTION EXPERIMENTS

4.1.1 Burnout V

The experimental work on Burnout V (Fig. 4.1) has been in three categories: (1) modification of the equipment for the purpose of increasing the power density in the electron beam, (2) observations and experiments to determine the efficiency with which ions are heated, and (3) probe measurements to determine temperature and density. The three categories will be discussed in order.

Equipment Modification. – We define power density as the output of the electron beam power supply divided by the electron beam volume between points of maximum magnetic field strength. We have been unable to retain in the larger devices the power density of 1 kw/cm^3 observed in Burnout I.[1] We find the power density is less, though the power input is greater. The power density in Burnout IV was 400 w/cm^3. The power density in Burnout V is now about 300 w/cm^3 with $\frac{3}{4}$-in.-diam mirror throats. Table 4.1 gives each step from Burnout I through Burnout V.

We have nearly tripled the power density in Burnout V by reducing the size of the orifice in the mirrors. At each step we have been limited by increased gas pressure in the region of the end electrodes, accompanied by difficulty in holding bias voltage on the filament and a rise in impurity spectra in the plasma. Space at the ends has always been limited because we have used existing

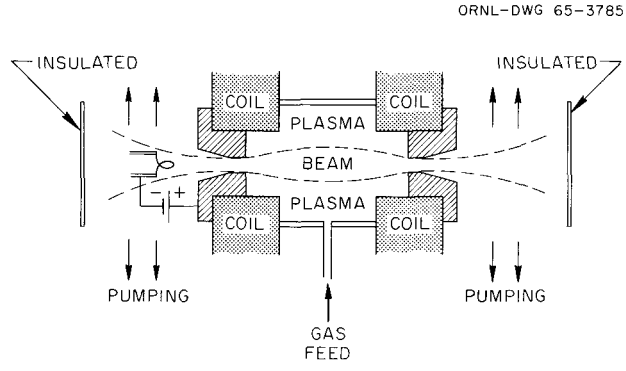

Fig. 4.1. Burnout V. The beam volume has been reduced to 200 cm^3 by reducing the diameter of the carbon orifices in the mirror throats to $\frac{3}{4}$ in.

calutron-type vacuum systems sandwiched between magnet pole pieces. We believe that some additional volume and increased pumping speed in this region will permit improvement in the beam power density.

Observations and Experiments. – The success of a beam-plasma interaction (turbulent heating) experiment, such as Burnout V, may be measured by the efficiency with which energy is transferred from the electron beam to the ions. The following observations indicate that up to 10% of the energy in the beam goes into heating ions in Burnout V and that perhaps as much as 0.2% is in ions over 100 kev.

The first information comes from power measurements. We have previously reported that 8.7% of the beam power was dissipated in the midplane

[1] *Thermonuclear Div. Semiann. Progr. Rept. Oct. 31, 1964*, ORNL-3760, sect. 4.1, p. 30.

Table 4.1. Power Density in Burnout I Through Burnout V

Burnout	Orifice Diameter (in.)	Power Input (kw)	Volume (cm^3)	Power Density (w/cm^3)
I	1/4	1.000	1.0	1000
II	1/4	3.5	5	700
III	3/8	7.0	18	400
IV	3/8	7.0	18	400
V_1	1 3/8	50	450	110
V_2	1	75	320	235
V_3	3/4	60	200	300

section of the liner.[2] This was determined from cooling water flow to that portion of the liner and its change in temperature, and is a crude measurement, probably less than the true value. We have repeatedly observed the power dissipated in the midplane section of the liner to increase with increased magnetic field. Dissipation of up to 10% of the input beam power has been observed.

A water-cooled probe (about 1 $in.^2$ of surface) was inserted into the plasma in the midplane region, as shown in the sketch on Fig. 4.2. Power measured from the cooling water flow rate and temperature change is given on the graph for different positions of the probe as a function of magnetic field strength. Note that the power to the probe increases with increased magnetic field to as much as 1 kw per square inch of probe surface. The beam power did not change significantly over this range in magnetic field strength. It appears that turbulent heating is more effective at higher magnetic fields in this device.

We find the liner surface near the midplane severely sputtered. A plug and collar from midplane ports in the liner are shown in Fig. 4.3. The top surface of the plug (left) was originally machined

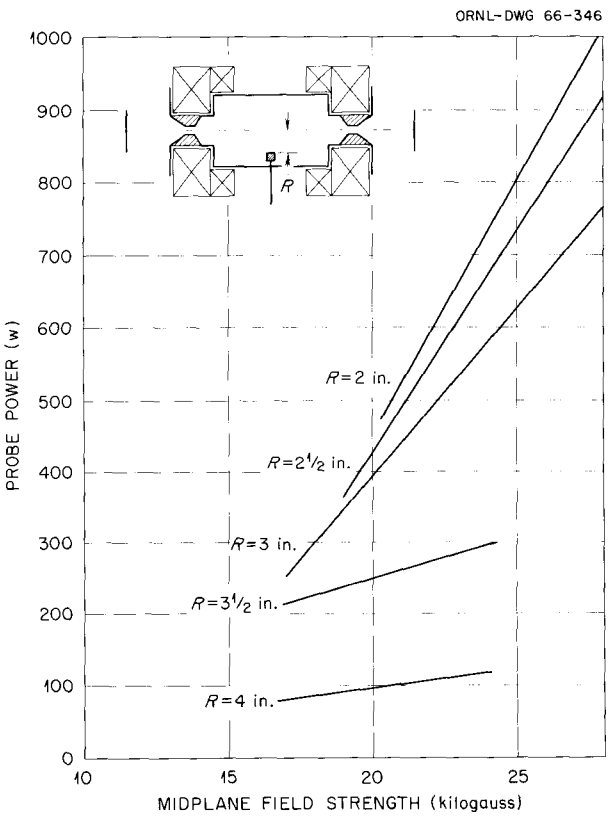

Fig. 4.2. Probe Power vs Magnetic Field Strength. The curves are for different probe positions as indicated in the sketch.

[2] *Thermonuclear Div. Semiann. Progr. Rept. Apr. 30, 1965*, ORNL-3836, sect. 4.1, p. 36.

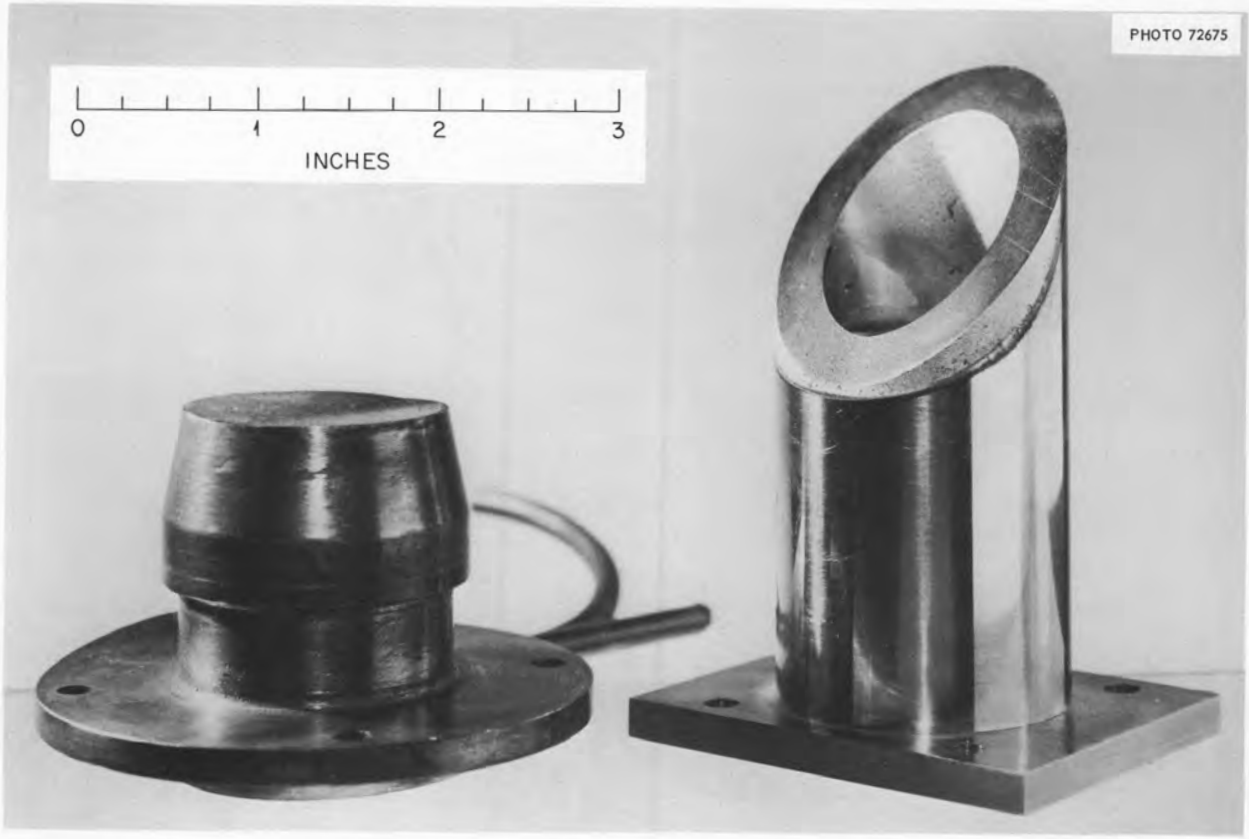

Fig. 4.3. Ion Sputtering. The upper surfaces of the liner port plug (left) and port collar (right) were originally machined smooth and polished. The deeply sputtered trough across the plug coincides with the midplane intersection. The collar shows sputtering over all the area exposed to the plasma inside the liner.

smooth and polished. After some hours of use the midplane intersection can be clearly seen on the sputtered surface. The collar (right) is similarly sputtered on the unprotected portion which extended inside the liner.

We attempted to identify the ions by their sputtering rate. Published calutron-type data[3] for deuterons in the 9-to-44-kv range (Fig. 4.4) gave sputtering rates as great as 0.06 copper atom sputtered per incident deuteron. We observe sputtering rates as great as 0.1. Lack of information below 9 kv and impurity sputtering could account for the difference.

Neutron production is a measure of deuteron energy. When a deuterium plasma is formed in Burnout V, neutrons can arise from D-D reactions

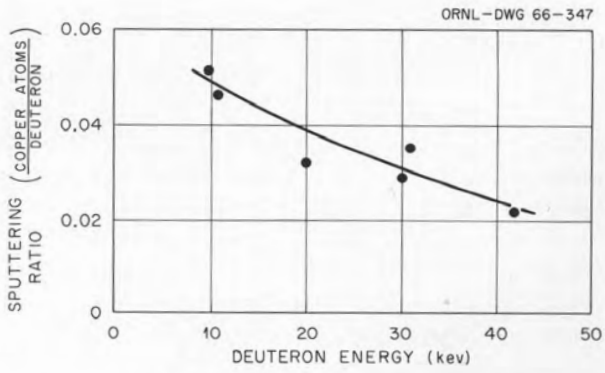

Fig. 4.4. Sputtering Ratio vs Deuteron Energy.

in the occluded gas on the metal surfaces. We suspect three principal sources. The two end electrodes are several kilovolts negative with respect to ground, and can accelerate ions into

[3]O. C. Yonts *et al.*, *J. Appl. Phys.* 31, 447 (1960).

themselves. The midplane portion of the liner is at ground potential, and ions must cross the magnetic field to strike its surface. Therefore, neutrons from the midplane region are assumed to indicate turbulent heating of ions to energies greater than the threshold of our detection system, which has detected neutrons from a deuteron current of 1 ma at 6 kv on a water-cooled copper target.

Our detection system (described in the previous semiannual report[2]) on the Burnout V experiment uses directional BF_3 counters. A source strength of 6×10^5 neutrons/sec was assigned. Further refinement of the counter technique has reduced this number to 2.4×10^5. Additional confirmation of the neutron source strength of the midplane region has been obtained from nuclear track plates. Analysis of the recoil proton tracks (Fig. 4.5) found in a plate placed on the midplane but outside the liner and the almost complete absence of tracks on a similarly located plate exposed to only neutron sources placed at the positions of the end electrodes yielded a source strength for the midplane region of 6.6×10^4 neutrons/sec.

Magnetic and electrostatic analysis of escaping ions gives additional verification. A small hole in the liner at the midplane (Fig. 4.6) permitted a "pencil" of ions to pass through for analysis. The ions, still in the focusing field of the magnetic midplane, were displaced parallel to the magnetic axis by an added electrostatic field. An MoO_3 plate was used to locate the ion paths.[1] Both energy and charge-to-mass ratio may be determined. In one experiment a current of 10^{-8} amp at the 80 to 120 kv position was measured directly.

The marks left on the MoO_3 plates by the deuterons are somewhat diffuse. Therefore, the mass number could not be resolved more accurately than from 0.8 to 39. If mass 2 is assumed (only mass 2 makes the blue mark on the MoO_3 plate), the energy varies from 14 to 170 kev.

The analyzed beam (10^{-8} amp, Faraday cup measurement) was collimated by two apertures of 0.02 cm^2 ($\frac{1}{16}$-in.-diam holes). Assuming that the ions are random but restricted to the two degrees of freedom of the midplane and that the analyzer accepts only 2°, then the flux density is about 3×10^{14} hot ions cm^{-2} sec^{-1}, or a density of 10^6 cm^{-3} for 100-kev deuterons (the approximate energy required for collection in the Faraday cup). The ions are well focused in the midplane and have sputtered a groove inside the liner marking the liner-midplane intersection. The approximate deeply sputtered area is 20 cm^2. The total current is then 1 ma, assuming uniform current density over this area.

Table 4.2. Summary of the Neutron Source Experiments

Experiment	Midplane Neutron Source Strength (neutrons/sec)
BF_3 counters	2.4×10^5
Nuclear track plates	6.6×10^4
Ion flux measurement	$\sim 10^5$

The neutron yield for 100-kev deuterons striking a water-cooled copper target which has occluded deuterium is not accurately known and, indeed, varies with the experiment. J. F. Lyon has calculated (DCX-2 Technical Memo No. 119) an expected yield for 600-kev deuterons on copper from published data[4] on zirconium target material. The expected yield is 26 neutrons $steradian^{-1}$ $microcoulomb^{-1}$. If the yield is reduced by a factor of 3 (the D-D reaction cross section is smaller by a factor of 3) for 100-kev deuterons and the approximate area is 20 cm^2, then the neutron source strength in Burnout V should be about 10^5 neutrons/sec, in fair agreement with the other observations (Table 4.2). It now seems reasonable that the neutrons which appear to come from the midplane region of Burnout V really do so, and that they can be due to reactions of something like 100-kev deuterons with the occluded gas in the walls. The power in the estimated total wall current of 1 ma in this energy range is 100 w, or about 0.2% of the beam power.

Probe Measurements. – Recently solid probes of various kinds have been used in plasma diagnostic efforts in Burnout V. Since only a few preliminary experiments have been done, the following results and estimates are tentative:

1. Electron temperature measurements have been made only for the first 2 in. of penetration into the plasma. The estimates for T_e range from 50 to

[4] J. B. Marion and J. L. Fowler, eds., *Fast Neutron Physics, Part I*, chap. III, A, Interscience, New York, 1960.

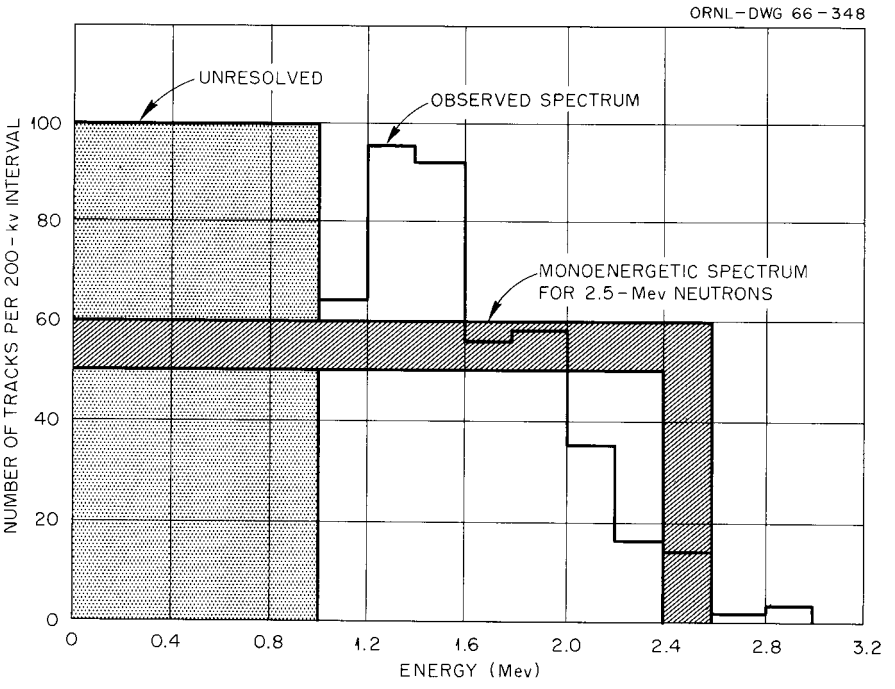

Fig. 4.5. Spectrum of Recoil Proton Tracks.

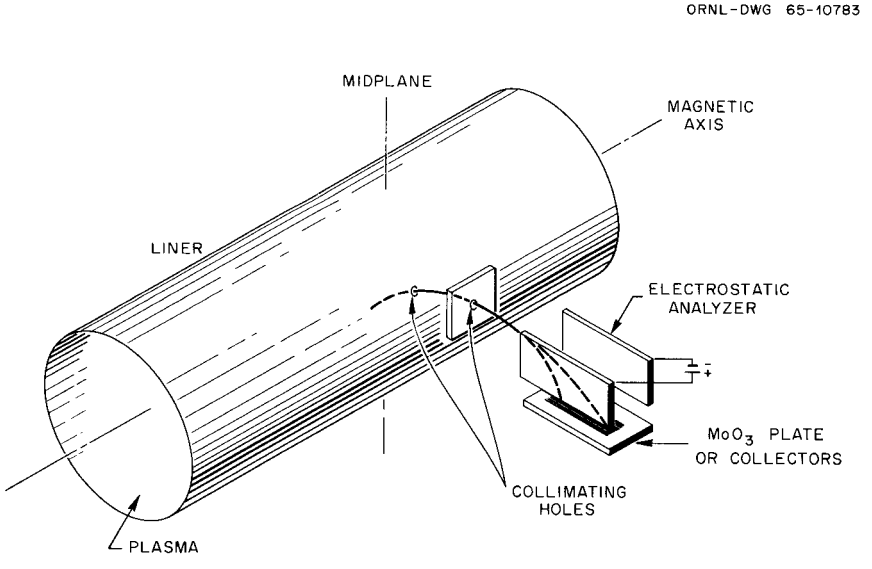

Fig. 4.6. Magnetic and Electrostatic Analysis of Some Plasma Ions. A Faraday cup replaced the MoO_3 plate in some experiments.

200 ev. No clear-cut variation with radius of the plasma has been observed, nor, on the basis of one mode I experiment, is there appreciable difference in electron temperature between mode I and mode II.

2. No estimate has been made for mode I, but the ion temperature in mode II is estimated to be approximately 550 ev.

3. A lower limit on ion density for mode II, based on ion saturation current and estimated probe collection area, is estimated to be approximately 10^{11} cm^{-3}, this being an order of magnitude larger than that estimated for mode I. The density seems to decrease rather slowly with radius. A density of approximately 3×10^{12} cm^{-3} is indicated, however, if one interprets a rather strong, coherent rf signal observed near 250 Mc as the ion plasma frequency.

4. In addition to the above-noted rf signal at 250 Mc, two other rather well-defined frequencies, at approximately 4 and 8 Mc, were observed. (The calculated ion cyclotron frequency at the midplane was 20 Mc.)

5. The floating probe potential for both mode I and mode II is positive and increases monotonically (from ~50 v to ~150 v for mode II; from ~0 v to ~20 v for mode I) from the outer edge of the plasma toward the center for the first 2 in. For mode II, however, at ~$2\frac{1}{4}$ in. from the liner (~$1\frac{1}{2}$ in. from the machine axis) the potential suddenly reverses. At this depth of penetration the exact position of the probe becomes very critical. By careful adjustment of the probe position a negative dc potential of several hundred volts can be observed. Further penetration of the probe into the plasma by only a small fraction of an inch, however, perturbs the plasma so violently that the arc is extinguished. Just prior to the extinction of the arc the floating potential of the probe appears to go extremely negative, but this is not certain because of the rapid irreversible transient behavior of the system. In any case, it would appear that large radial electric fields are present in mode II. Unfortunately, floating probe potential measurements of mode I have not yet been made farther in than 2 in. from the outer edge of the plasma.

6. Observation of the ion saturation current to a probe centrally located at the midplane, but having limited axial motion, indicated that the plasma density is constant along the axis for at least $\frac{1}{2}$ in. on either side of the midplane.

Previous experience had suggested that it would probably be necessary to utilize water cooling in order to prevent rapid deterioration of the probes by the energetic plasma. Therefore, the first probe work was done using water-cooled copper probes, and, indeed, rather rapid abrasive action at the tips of the probes was found. It was soon found, however, that small cylindrical probes made of carbon could be used without appreciable ill effects from the plasma, even without water cooling. Thus, with the exception of power probe measurements and some beginning Langmuir probe measurements, most of the probe work has been done using non-water-cooled carbon probes. All measurements were made in deuterium plasmas.

Water-Cooled Probes. – Figure 4.7 shows two of the water-cooled probes, as well as the manner in which they were used. All water-cooled-probe measurements were made on the midplane. The larger probe was used first; however, calculations of the ion flux to the probe vs the neutral particle

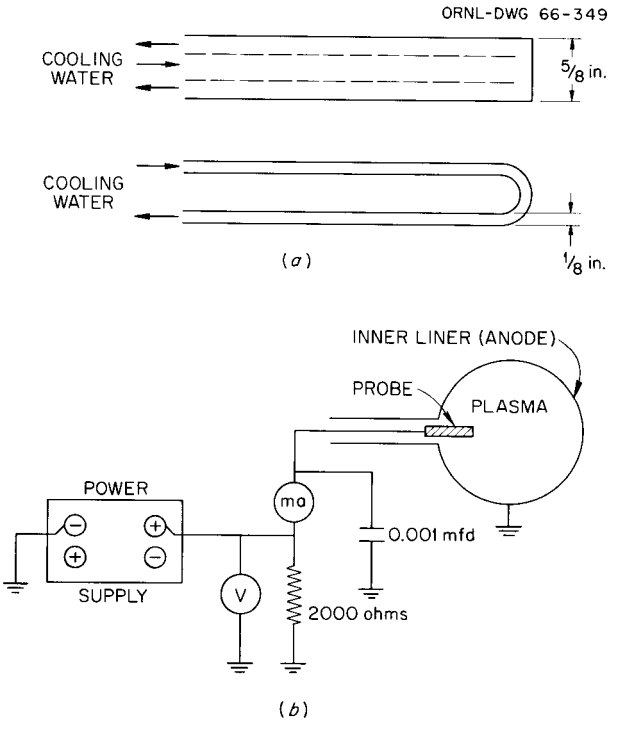

Fig. 4.7. Use of a Water-Cooled Probe as a Plasma Diagnostic Instrument. (*a*) Two of the probes used; (*b*) schematic showing how the probe was used as a Langmuir probe.

flux into the machine showed that approximately 10% of the input neutrals were appearing as ions on the probe. Thus the larger probe was probably appreciably perturbing the plasma. Unfortunately, when the smaller probe was used, the degree of perturbation of the plasma was not appreciably decreased. In view of the observed rapid abrasive effect of the plasma on the probe, primarily at the tip end, the smaller probe is probably about as small as is practical for a water-cooled probe.

Previous work has indicated that the ion motion in the midplane of the burnout machines is primarily Larmor motion with relatively little axial motion. Therefore the effective collecting area of the probes has been taken as the projected area of the probes in the direction of the circulating bombarding particles. The plane of the smaller probes was oriented perpendicular to the machine axis so that the projected area of the entire probe was the same as that of only the upper half of the probe. Thus (see upper diagram, Fig. 4.7) the projected area of the smaller probe was only one-fifth that of the larger probe. Since the abrasive action of the plasma has been noted only on the upper tip end of the probes, however, the projected areas may be much larger than the actual collecting areas. Thus the calculated densities may be an order of magnitude too low, and the density gradient may be greater than it would appear to be. The density calculations were made using the expression by Guthrie and Wakerling for ion saturation current to a cylindrical probe in a strong magnetic field:[5]

$$n_+ = \frac{2.5 J_+}{Ae} \sqrt{\frac{m_+}{2kT_e}} , \qquad (1)$$

where n_+ is the ion density, J_+ is the ion saturation current to the probe, A is the collecting area of the probe, e is the electron charge, m_+ is the ion mass, k is Boltzmann's constant, and T_e is the electron temperature.

Figure 4.8 shows two sets of data taken simultaneously using the smaller probe. The power measurements were made calorimetrically. Only one such run has been made. At the time of this run, an effort was made to make a similar run for mode I operation, but the cooling-water flow rate

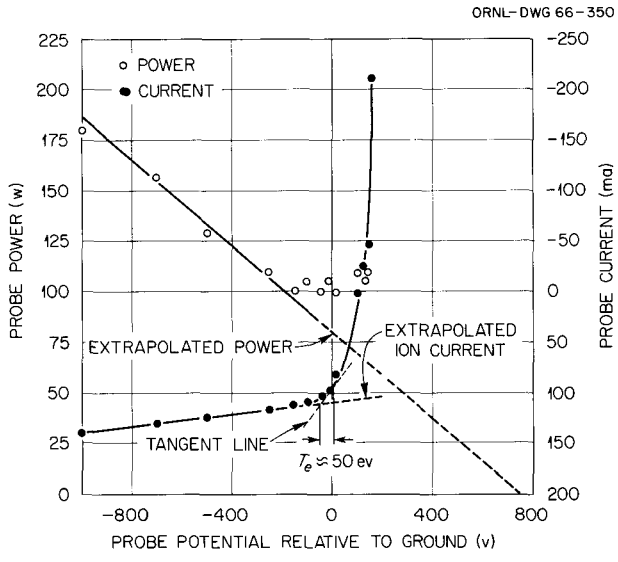

Fig. 4.8. Power Probe and Langmuir Probe Measurements in Burnout V, Using a Water-Cooled Probe.

was too large to allow the small temperature changes in the cooling water to be seen. Based on the observed temperature changes for mode II and the smallest temperature change which could be reasonably observed on the thermometers used, however, one can estimate an upper limit of about 10 w to the probe during mode I operation.

The estimates of ion temperature are based on information contained in both sets of data of Fig. 4.8. The first estimate is based on an extrapolation of the power data: It is noted that for the power data there is a relatively large section of the potential range over which the power varies fairly linearly. The assumption is made that, as a first approximation, this section of the curve can be extrapolated linearly to zero power. Doing this, zero power is seen to occur at a probe voltage of approximately +750 v. A second assumption is made that the extrapolated zero power to the probe occurs when the probe is biased positively with respect to the plasma by an amount approximately equal to the voltage equivalent of the ion temperature. Therefore, if we know the plasma potential, we can obtain the ion temperature. So far we have not been able to see electron current saturation occur, so that we cannot obtain the plasma potential directly from our probe characteristic. We can, however, probably make a fairly good estimate from the observed data. Referring to Fig. 4.8, it is

[5] A. Guthrie and R. K. Wakerling, *The Characteristics of Electrical Discharges in Magnetic Fields*, chap. 2, McGraw-Hill, New York, 1949.

seen that the electron current to the probe is increasing quite rapidly with positive voltage. From physical considerations this increase cannot continue for long. Therefore, the estimate is made that the plasma potential must be near +200 v. This gives, then, an ion temperature of about 550 ev.

The second estimate of ion temperature is based on a calculation involving the power to the probe and the net number of charged particles to the probe, both under ion saturation current conditions. The relationship used was

$$P = \bar{n}\bar{v}A\bar{E} \quad , \tag{2}$$

where P is the power measured to the probe, $\bar{n}$ is the average density of charged particles striking the probe surface, $\bar{v}$ is the average velocity of the incoming particles, A is the collecting surface of the probe, and $\bar{E}$ is the average energy possessed by each incoming charged particle and given to the probe upon being collected. Under the conditions of ion saturation current to the probe, the product of the first three terms on the right-hand side of Eq. (2) is simply equal to the ion saturation current J_+ in milliamperes, say, times the number of charged particles required to give a current of 1 ma for 1 sec. If J_+ is in milliamperes, then for ion saturation conditions, Eq. (2) can be written as

$$P_+ = J_+\bar{E} \times 6.25 \times 10^{15} \quad , \tag{3}$$

where P_+ is the power to the probe at the ion saturation current. From Fig. 4.8 it is seen that $J_+ \approx 120$ ma and $P_+ \approx 100$ w. Using these values in Eq. (3) and making suitable conversions, we obtain $\bar{E} \approx 850$ ev. From Fig. 4.8, ion saturation is observed to occur when the probe is about 100 v negative relative to ground, or, in other words, when approximately 300 v negative with respect to the plasma. Thus each ion collected by the probe is accelerated through a potential of about 300 v. When the 300 ev given to the ions electrostatically is subtracted from the thermally observed ion mean energy of 850 ev, the calculated value is in remarkably good agreement with the value of 550 ev obtained above by the extrapolation procedure. Any power sources to the probe not included in the calculation, such as neutral current, recombination, and sputtered copper, would, if considered, lower the calculated value of $\bar{E}$.

The usual criterion – that the voltage equivalent of the electron temperature is equal to that voltage change on the Langmuir probe required to change the electron current to the probe by one e-fold – was used to obtain the electron temperature from the Langmuir probe characteristics. Since the simple free-fall theory of Langmuir does not apply to probe measurements in strong magnetic fields, the values obtained may not be very meaningful. In those cases where only very little of the electron-current part of the Langmuir probe characteristic could be obtained, T_e was obtained by sampling only the high-energy tail of the electron distribution, as shown in Fig. 4.8. For the smaller probe the results obtained in this manner agreed with those obtained in the more conventional manner (using a semilog plot), when a comparison could be made. For the larger probe, however, the more conventional technique gave somewhat higher values of T_e.

From fear of vaporizing a water-filled line in the vacuum system the water-cooled probes were never inserted into the plasma more than 2 in. It was found that the floating potential of these probes in both mode I and mode II was positive and increased monotonically from the edge of the plasma towards the center. Using the carbon probes discussed below, however, it was found that in mode II (no carbon probe measurements were made in mode I) the polarity of the floating potential was reversed beyond the $2\frac{1}{4}$-in. position. This latter observation is in qualitative agreement with the results of some previous work[6] which indicated that the center of the plasma, at least, is near the cathode potential, that is, near –20 kv. In any event, a very strong radial electric field seems to be present in Burnout V.

Carbon Probes. – Non-water-cooled cylindrical carbon rods, 4 in. long and $\frac{1}{8}$ in. in diameter, have been used to look for coherent rf emission from the plasma, to investigate the axial dependence of plasma density in the vicinity of the midplane, to look at the probe floating potential, and to look for correlations of any macroscopic activity occurring

[6]Igor Alexeff, R. V. Neidigh, and W. F. Peed, *Thermonuclear Div. Semiann. Progr. Rept. Oct. 31, 1964*, ORNL-3760, p. 30; I. Alexeff *et al.*, paper to be published in the Proceedings of the Culham Conference, Sept. 6–10, 1965, held at Abingdon, Berks., England, Paper CN-21/102 (this will be an International Atomic Energy Agency publication and probably will appear as a supplement to *Nuclear Fusion*).

in the plasma. Unfortunately, the entire 4-cm length of all these probes was active, so that some of the measurements were not as definitive as might be desired. In future experiments all of the probe except a small known section will be well shielded.

The lead-in wire of the probe used to look for coherent rf emission of the plasma was electrostatically shielded from the probe base to the oscilloscope. A Tektronix 519 oscilloscope was operated in the single-sweep mode to monitor signals detected by the probe. In the range of the oscilloscope (dc to 1000 Mc), only three coherent modes were found: at approximately 250, 8, and 4 Mc. Since the high-frequency mode is much higher than the calculated ion cyclotron frequency ($\sim$20 Mc) and is much lower than the calculated electron cyclotron frequency or the electron plasma frequency for a reasonable density, this mode is tentatively interpreted as the ion plasma frequency. This implies, then, a plasma density of approximately 3×10^{12} cm^{-3}.

The probe used to investigate the axial dependence of the plasma density in the neighborhood of the midplane was on a rotatable conducting lead-in rod located at the midplane, and was mounted approximately $\frac{1}{2}$ in. off the axis of the rod. In this manner the probe could, by rotating the lead-in rod, be used to sample the plasma along the machine axis for a distance of approximately 1 in. centered about the midplane. With the probe biased to collect only ions, it was found that for a given depth of penetration into the plasma there was little or no variation in the ion saturation current to the probe, thus indicating that the plasma density was approximately independent of axial position for at least $\frac{1}{2}$ in. on both sides of the midplane. This result was mildly surprising, since the sputtering pattern on the inner liner wall has always shown that most of the sputtering occurs in a 1- to 2-cm-wide ring at the midplane.

The average dc potential assumed by a floating (actually grounded by the standard internal 1-megohm oscilloscope resistor) probe located at the midplane was monitored on an oscilloscope, as a function of the depth of penetration of the probe into the plasma. As was noted above, at least in mode II, the probe indicates that a large radial electric field exists in the plasma, primarily in the first $1\frac{1}{2}$ in. from the machine axis. Variation of the magnetic field seemed to produce little or no effect on the critical depth in the plasma at which the probe floating potential reversed polarity.

Two floating (grounded through 1-megohm resistors), electrostatically shielded probes, located on the midplane but separated some 10 to 15 cm in azimuth, have been used to make correlation studies in the plasma. As yet, however, no conclusive results have been obtained.

4.1.2 An Optical System for Studying the Light in Burnout V

Igor Alexeff

The study of the light emitted from the inside of Burnout V is difficult, because the observer must look into a cylindrical chamber 7 in. in diameter through a long pipe only 2 in. in diameter, and therefore can see only a small part of the plasma volume.

To obtain a better view of the plasma, the wide-angle viewing system shown in Fig. 4.9 was constructed. In this system, a pinhole image of the plasma is projected onto a field lens system formed of three convex lenses. The field lens system then projects the image of the plasma through the viewing pipe to the observer. The diaphragm with the pinhole also serves to protect the lens system from sputtered material. The lenses need not be achromatic, and in this case were obtained from simple hand magnifiers.

Experimental tests of the system reveal that it works quite well and projects back almost a wall-to-wall image of the plasma. Small objects located inside the plasma container are seen easily.

Photographs of the Burnout V plasma in both mode I and mode II operation are shown in Fig. 4.10. The circular object in the center of each

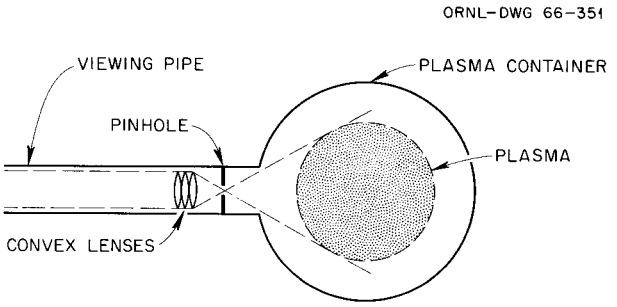

Fig. 4.9. Wide-Angle Viewing System.

ORNL-DWG 65-8603

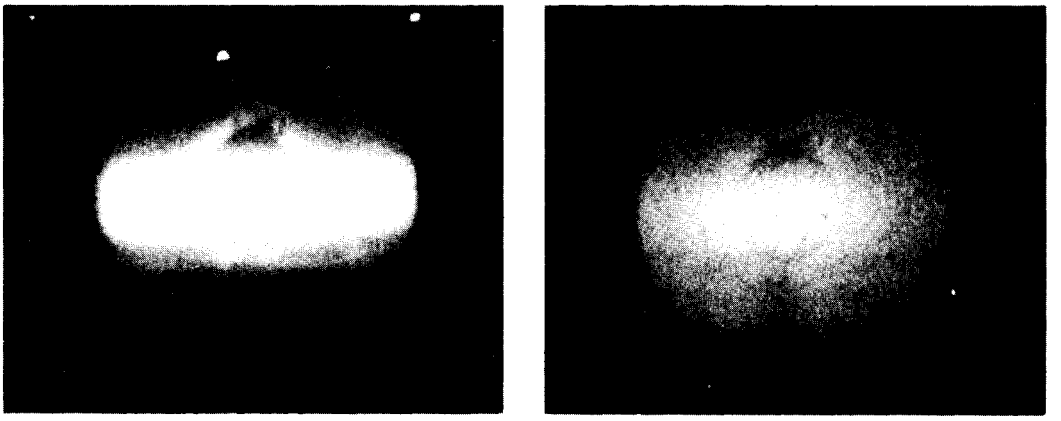

MODE I MODE II

Fig. 4.10. The Plasma in Burnout V. Mode I: sharply defined column; bright center – dim elsewhere; 10-kw power input. Mode II: poorly defined column; general illumination rather uniform; 50-kw power input.

image is a plug filling a hole 2 in. in diameter on the side of the plasma container opposite the wide-angle viewing system.

4.1.3 Spectroscopy of Burnout IV

W. B. Pardo[7] R. V. Neidigh
W. F. Peed

The distribution of spectral light from a helium plasma described in the preceding semiannual report[8] is being investigated in more detail. A set of narrow-band interference filters, typically 5 A full width at half maximum with peak transmission of 30 to 50%, has been secured. Six lines of the neutral spectrum, three each of the triplet and of the singlet series, as well as two lines of the singly ionized spectrum, can now be observed. Cross sections for excitation of each of these lines, by all processes, for monoenergetic electrons interacting with helium gas are available from published literature.[9]

Experimentally, the plasma is probed line by line with an optical scanning assembly consisting of a lens, a filter, a slit, and a multiplier phototube mechanically constrained so that a diametrical section on the midplane is examined.

In general, for any excitation process,

$$I_{\lambda_{ij}} = C_1 C_2 n_e n_0 \sigma_{ij}(v_e) v_e .$$

In this equation, $I_{\lambda_{ij}}$ is the total monochromatic intensity emitted by the plasma in the zone of observation; C_1 is a constant involving only geometric factors, such as the solid angle of the viewing system; C_2 is a constant involving only wavelength-dependent factors, such as filter response and multiplier phototube sensitivity; n_e is the number of electrons per unit volume; n_0 is the number of neutral target atoms; σ_{ij} is the total cross section which results in emission of energy λ for all processes, including direct excitation to the ith state as well as excitation to higher states which cascade so as to contribute to the population of the ith state (this cross section is, of course, a function of electron velocity distribution); v_e is the electron velocity distribution, which for the purpose of this experiment must be assumed.

A complete set of experimental data for each line, as well as necessary calibration data, have been taken, and the first evaluation is being made at present. No firm results are available, but a striking difference exists between the spatial intensity distribution in the discharge of the

[7]Consultant, University of Miami, Coral Gables, Florida.

[8]I. Alexeff *et al.*, *Thermonuclear Div. Semiann. Progr. Rept. Apr. 30, 1965*, ORNL-3836, p. 36.

[9]R. M. St. John, F. L. Miller, and C. C. Lin, *Phys. Rev.* 134, A888–97 (1964).

$\lambda = 5015\ 3^3P \rightarrow 2^3S$ (a metastable state) and those of the other neutral lines; the intensity distribution of the $\lambda = 4686$ ion line $4^1P \rightarrow 4^1S$ is also grossly different.

It is expected that this experiment will give information regarding electron density, ion density, and electron temperature.

4.1.4 Hot-Electron Plasma Blanket

V. J. Meece W. L. Stirling

Introduction. – The electron plasma blanket experiment produces at least two separate electron distributions from a reflex or mode II discharge. One is a relatively cool distribution having a temperature of about 100 ev. The second is a hot or x-ray-producing distribution of about 100 kev. These two distributions comprise a plasma blanket or annulus about the magnetic axis with the 100-ev electrons concentrated in the approximately 2-in.-thick, visible annulus center. The 100-kev electrons are distributed both radially inward and outward from the central region. Experiments in which paddles are projected into the annulus show that one or more passes through the primary discharge are necessary before the electrons are elevated into the hot distribution. The 100-ev electrons are always present in the annulus.

Arc Electrode Modifications. – Two major modifications have been made on the original electrode configurations.[10] Gas is now fed into the discharge from both the anode, as before, and the anticathode. Between 60 and 90% of the gas is fed into the anticathode, depending upon operating conditions. Feeding gas into the anticathode has the desirable effect of increasing the electron density and improving the operational stability of the discharge and the annulus.

Another important development has been the positioning of a shield between the anode and the cathode in order to eliminate the dc power losses which cause rapid and severe erosion of the anode. The shield operates at cathode potential. Proper operation of the discharge is sensitive to the exact location of the shield, which is a $\frac{1}{16}$-in.-thick, water-cooled copper plate with a $\frac{5}{16}$-in. hole into which the cathode filament projects. Optimum conditions are achieved when the $\frac{1}{4}$-in.-OD cathode is positioned with its emitting surface flush with that side of the shield facing the anode. If the emitting surface of the cathode projects through the aperture in the shield more than $\frac{1}{32}$ in., the electron density in the annulus decreases. If the cathode is placed behind the shield, a strong focusing of the back-bombarding ions results, which destroys the cathode within about $\frac{1}{2}$ hr. Under proper operating conditions, the cathode lasts through 20 to 30 hr of operating time.

A second arc has been operated in conjunction with the first. The electrodes of the second arc are displaced radially 6 in. from the magnetic axis, like the first. However, the two arcs are azimuthally 180° apart. The two arcs may be operated simultaneously or separately. In either case the background pressure is about 3×10^{-5} torr. Figure 4.11 shows a schematic of the apparatus with both arcs in place. In addition, the figure shows an inner liner which will be used for arc pumping and diffusion experiments.

There is an outer liner in the vacuum chamber (not labeled in Fig. 4.11) which can be cooled with liquid nitrogen. The outer liner is perforated, and since it completely encloses the electron plasma annulus, the cooling serves as an effective cold trap for pump-oil vapors, etc. Electron density has been increased by a factor of 2 to 3 with nitrogen cooling. However, it is necessary to increase gas flow a little; otherwise, the power delivered to the anticathode exceeds the present cooling rate, thereby causing the anticathode to melt. Gage background pressure (gage located between pump and nitrogen-cooled liner) remains at about 3×10^{-5} torr.

The present limitation on electron density is due to failure of the anticathode. The electron density increases rapidly with increasing arc voltage or decreasing gas feed. In either case the failure of the anticathode determines the applied voltage and gas feed rate. An anticathode with five times the power dissipation presently available is being constructed.

Temperature and Density Measurements. – Temperature and density of the electron plasma have been measured by a combination of four different methods: (1) x-ray energy distribution and total energy emitted, (2) Langmuir probe, (3) power probe, and (4) microwave cutoff experiment. The

[10] *Thermonuclear Div. Semiann. Progr. Rept. Apr. 30, 1965*, ORNL-3836, p. 40.

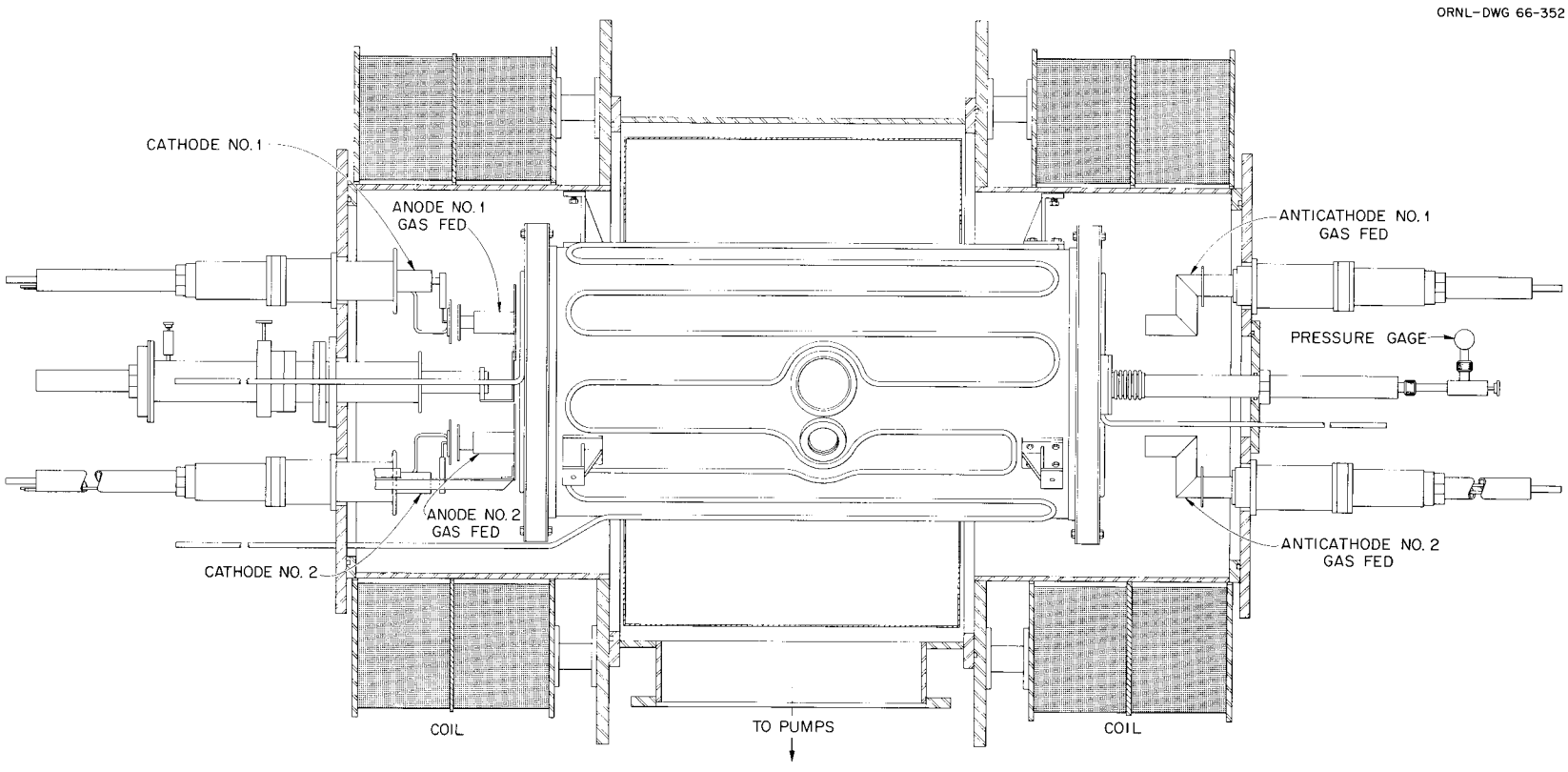

Fig. 4.11. Schematic of Apparatus.

x-ray measurements were previously described.[10] The hot-electron distribution is measured to have a temperature of about 100 kev at a density between 10^8 and 10^9 cm^{-3}. The low-energy-electron distribution has been investigated only with the probes and microwaves, since no x rays are detected on the scintillation spectrometer when a paddle experiment removes the hot electron distribution.

Table 4.3 shows the results of a typical run taken from a Langmuir probe positioned in the throat of the mirror coil on the anticathode end. This probe sees the plasma flowing out through the mirror. A cold (background) plasma of 1.9×10^{10} cm^{-3} and 2.5 ev is present. Also present are the hot and warm distributions mentioned above. The densities of the latter two are inferred from the ion saturation current to the probe. At steady state there is equilibrium between production of ions, proportional to $\langle \sigma v \rangle$ for ionization, and the loss of ions, proportional to $j \times A$, where j is ion current per unit area to the probe and A is area of plasma. In a previous report,[11] it was assumed that all ions move longitudinally through an area equal to the cross-sectional area of the annulus. This assumption does not account for ions that escape radially, and thus yields too low a value for the density. Using an area equal to the total surface area of the plasma, the density is found to be about 10^{12} cm^{-3}.

Table 4.3. Hot-Electron Plasma Blanket Measurements in the Mirror with a Langmuir Probe

1. Background plasma:
   $n_e = 1.9 \times 10^{10}$ cm^{-3},
   $T_e = 2.5$ ev.

   Basic Equation Used for Results Below:

   $$\frac{dN}{dt} = N_e N_g \sigma v_e , \qquad \sigma v_e \approx \text{constant} .$$

2. Total ionizing electrons in blanket
   at $t = 0$:
   $n_e = 10^{12}$ cm^{-3}.

3. X-ray-emitting electrons (measurements extrapolated to $t = 0$):
   $n_e = 5 \times 10^8$ cm^{-3}.

In part 3 of Table 4.3, a calculation has been made for a long-lived component of the ion saturation current. This was done by extrapolating the long-lived component back to zero time. The ion saturation current at $t = 0$ then yields the electron density of 5×10^8 cm^{-3}. Since the decay of this distribution matched the x-ray decay after arc turnoff, and since the electron density agrees within a factor of 3 with that from the x-ray energy calculation, it is assumed that the long-lived electron group inferred from part 3 is the x-ray-emitting group.

Figure 4.12 shows three curves related to the position of the power probe relative to the annulus. Curve 1 shows the power, measured calorimetrically, delivered to the probe in a radial cross section at midplane. Both arcs were on, and the probe intercepted the annulus at 90° from either arc. Curve 2 shows the ion saturation current streaming out the mirror in a flux tube of the annulus 180° from the power probe. The current

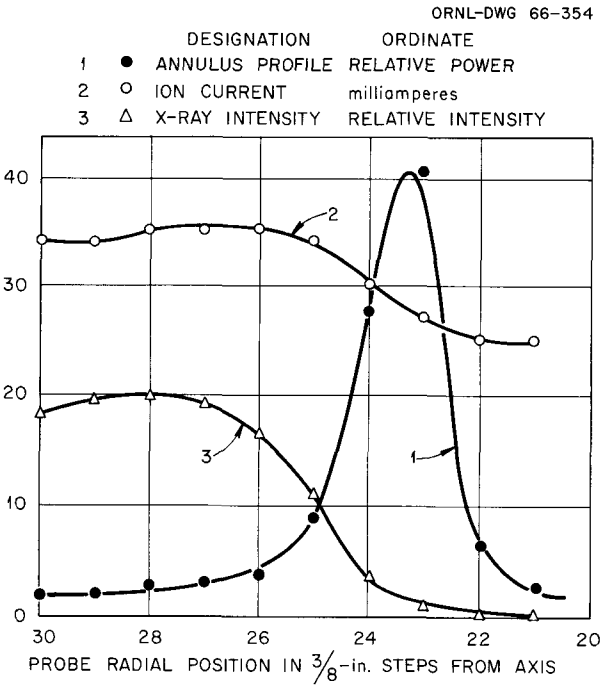

Fig. 4.12. Measurements on Plasma Annulus with Power Probe.

[11] W. L. Stirling *et al.*, "Development of a Hot-Electron Plasma Blanket," to be published in the *Journal of Nuclear Energy, Part C*.

probe traversed the entire radial extent of the annulus. The ion saturation current behavior shows that the presence of the power probe lowers the electron density of the annulus by about 30%. Curve 3 shows the decrease of x-ray intensity (x rays originating in the plasma annulus) as the power probe is inserted into the annulus.

In a typical run, the peak power delivered to the probe is between 600 and 900 w per square centimeter of probe area. A density measurement of this non-x-ray-producing electron distribution may be found from the expression

$$\text{Power} = \frac{n_e m^2 \nabla B}{4eB^2} v_\perp^4 , \qquad (1)$$

in which n_e is the electron density, m is the electron mass, e is the electronic charge, ∇B is the magnetic field gradient, B is the magnetic field strength, and $v_\perp$ is the electron perpendicular velocity. This expression assumes that the electrons drift in the magnetic field gradient with a drift velocity proportional to $v_\perp^2$ and that the energy delivered to the probe per electron is proportional to $v_\perp^2$. To calculate n_e, an independent measurement of $v_\perp$ must be made. One such measurement is the calculated value of 0.3 msec for the decay time of the ion saturation current to the Langmuir probe (Table 4.3, part 2), assuming that the decay time is the relaxation time for scattering the trapped electrons into the mirror loss cone. In this manner the electron density is estimated at about 10^{12} cm^{-3} at the maximum power position of the probe, falling to about 10^{11} cm^{-3} in a distance of $\frac{5}{8}$ in. on either side.

A probe characteristic was run on the power probe when positioned at point 23 in Fig. 4.12. The characteristic yielded an electron temperature of 100 ev and a density of 2×10^{12} cm^{-3}. The density figure is in agreement with that determined from power considerations, although the temperature of 100 ev yields an electron density of 10^{14} when inserted in Eq. (1).

Observation of the plasma annulus shows that the power probe sweeps out one entire quadrant of the annulus. Thus the effective area of the probe is not the geometrical cross section (probe length times probe width), but is probe length times annulus (or machine) length. The power per unit area is now reduced by a factor of 200, and thus a $v_\perp$ given by an electron temperature of 100 ev yields an electron density of 10^{12} cm^{-3}.

If one considers the decay of the ion saturation current to be limited by the time required for ion drift out of the mirrors, the decay time is dependent on ion temperature rather than electron temperature. For an ion temperature of 1 ev, the transit time is about 0.15 msec, which is in good agreement with the measured value of 0.3 msec.

A microwave cutoff experiment has been installed in the apparatus. Preliminary results show that the density is of the order of 10^{12} cm^{-3} through a plasma thickness of 1 cm. Thus three independent measurements – power, probe characteristic, and microwave cutoff – give a density value of the order of 10^{12} cm^{-3}.

A summary of most of the operational modes is shown in Table 4.4. The last semiannual report[12] was concerned with single-arc operation with the $\frac{5}{8}$-in.-ID anode at 2200 gauss. A subsequent report[11] discusses the single-arc operation with the $\frac{5}{16}$-in.-diam anode. As illustrated in Table 4.4, very large increases in hot-electron density were achieved with small changes in the anode structure. Operation at 2200 gauss and relatively low arc voltage was characterized by the condition

$$\frac{VP^{1/2}}{B} \approx \text{constant} , \qquad (2)$$

where V is the accelerating voltage, P is the operating pressure, and B is the magnetic field strength. This expression states a condition on the emitted x-ray intensity. For a given gas flow, or operating pressure, the voltage and magnetic field both could be optimized for maximum x-ray intensity. A plot of $VP^{1/2}/B$ vs x-ray intensity (where the optimum values for V, B, and P are chosen for each operating point) yielded the result that $VP^{1/2}/B$ was a constant independent of x-ray intensity, or hot-electron density.

It is interesting to compare this expression with the one for the maximum linear growth rate for an interaction between a beam electron wave and a plasma cyclotron wave:

$$\tfrac{1}{2} \frac{\omega_b \omega_p}{\omega_c} \sin^2 \theta \qquad (\omega_p \ll \omega_c) ,$$

[12] *Thermonuclear Div. Semiann. Progr. Rept. Apr. 30, 1965*, ORNL-3836, p. 40.

Table 4.4 Operational Characteristics

Inside Diameter of Anode (in.)	Field (gauss)	Power Input[a]		Electron Density (cm^{-3})		Temperature (kev)		Remarks
		Kilovolts	Amperes	Hot	Warm	Hot	Warm	
				Single Arc				
5/8	2200	7	0.5	$\sim 10^5$		~50		$VP^{1/2}/B \approx$ constant
5/8	<900	7	0.5	$\sim 10^7$				Minimum B and maximum V
3/8, 5/16	1600	23	0.8	$\sim 10^8$	$\sim 10^{12}$	~100		Minimum P and maximum V
5/16	4500	~20	1	$\sim 10^5$				
				Double Arc				
5/8	2200	7	1.5	$<10^5$		50		No gain[b] over single arc
5/16	1600	23	0.8	$\sim 5 \times 10^8$	$\sim 2 \times 10^{12}$	100	0.1	× 5 (10) gain[b] over single arc
5/16	800	23	0.7	$\sim 5 \times 10^8$	$\sim 4 \times 10^{12}$	100		× (40) gain[b] over single arc

[a]The power inputs listed for double-arc operation are for each arc.

[b]Gain refers to the gain in hot-electron density.

where ω_b is the plasma frequency in the beam, ω_p is the plasma frequency in the plasma, ω_c is the electron gyrofrequency, and θ is the angle between the direction of propagation and the magnetic field. Let us compare this expression with (2), remembering that B is proportional to ω_c. If the plasma density is proportional to the neutral density, a reasonable assumption, $P^{1/2}$ will be proportional to ω_p. The variation of beam density with applied voltage in a reflex discharge is not known. For V to be proportional to ω_b, the beam density, n_b, must be proportional to V^2. (For space-charge-limited current emission, n_b is proportional to V.) Thus, the experimental results at 2200-gauss operation suggest that the instability responsible for electron heating may be an interaction between beam cyclotron and plasma cyclotron.

Double-arc operation has been attractive for the small-inner-diameter-anode, high-arc-power operating conditions. The warm-electron densities given in Table 4.4 are those inferred from probe measurements of ion saturation current. For double-arc operation at 1600 gauss, two values for gain are given; they differ because a single arc can be operated in either of two ways. When both arcs are operating, it is necessary to feed gas into both arcs. Thus double-arc operation can be compared with single-arc operation with gas fed into both arcs (the value in parentheses), or compared with single-arc operation with gas fed only to the single operating arc. The latter single-arc operation yields higher densities, because of the lower gas loading of the system. It is not clear why such large gain factors are observed. Assuming that the hot electrons are heated stochastically upon passing through the main discharge column each revolution around the annulus, two arcs would at most double the number of drifting electrons and double the number of passes through the accelerating fields each revolution. Thus, two arcs would increase the density by no more than $2(2)^{1/2}$.

On one occasion, the double-arc high-density mode was operated at 2100 gauss. At present this type of operation is difficult, but it is believed that the new high-power-dissipation anticathodes will facilitate achieving stable operating conditions at higher magnetic fields.

4.2 FURTHER STUDY OF IONIC SOUND WAVES

Igor Alexeff W. D. Jones

Not a great deal of work has been done on ionic sound waves during the period covered by this report. We have made preliminary measurements of gas damping of the waves and have found a new, more sensitive detector of the waves. We have also reconfirmed some of our previous results.[13] For example, we have reinvestigated the value of the adiabatic compression coefficient, γ, of the plasma electron gas and have reconfirmed that the valve of γ is unity.[14] Recently we have presented a general summary of the results of our study of the properties of ionic sound waves at an international conference,[15] the proceedings of which are to be published.

4.2.1 Gas Damping

The gas damping was studied under conditions similar to those previously described.[13] In these experiments, however, the usual flat disk emitter probe was replaced by a spherical one 2.5 cm in diameter. The probe arrangement is shown schematically in Fig. 4.13. For each background gas pressure (measurements have been made only in xenon) a series of photographs was taken of the detector probe response for various separations of the emitter and detector probes. From these photographs we could not only measure the relative amplitudes of the received ion wave signals, but we could also determine the wave velocity and the combined thickness of the probe sheaths in a manner described previously.[13]

Since the emitter probe is spherical, it behaves like a point source for ion waves, so that the decrease in ion wave signal due to geometry obeys a $1/r^2$ dependence, where (see Fig. 4.13) r is the

---

[13] Igor Alexeff and W. D. Jones, *Thermonuclear Div. Semiann. Progr. Rept. Apr. 30, 1965,* ORNL-3836, p. 45; *Bull. Am. Phys. Soc.* **10**, 509 (1965), papers GH9 and GH10.

[14] Igor Alexeff and W. D. Jones, *Phys. Rev. Letters* **15**, 286 (1965).

[15] W. D. Jones and Igor Alexeff, Seventh International Conference on Phenomena in Ionized Gases, Belgrade, Yugoslavia, Aug. 22–27, 1965, paper 4.4.2.(7) (to be published in the Proceedings).

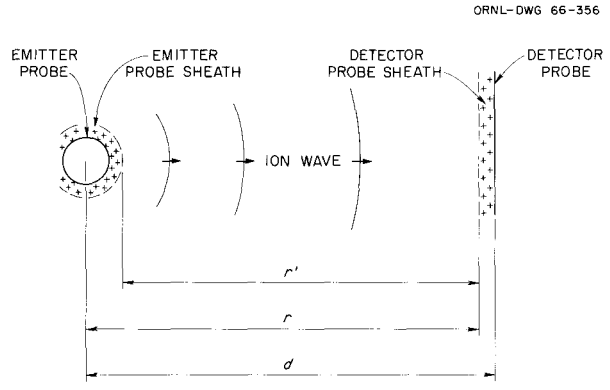

Fig. 4.13. Probe Arrangement for Making Gas Damping Measurements.

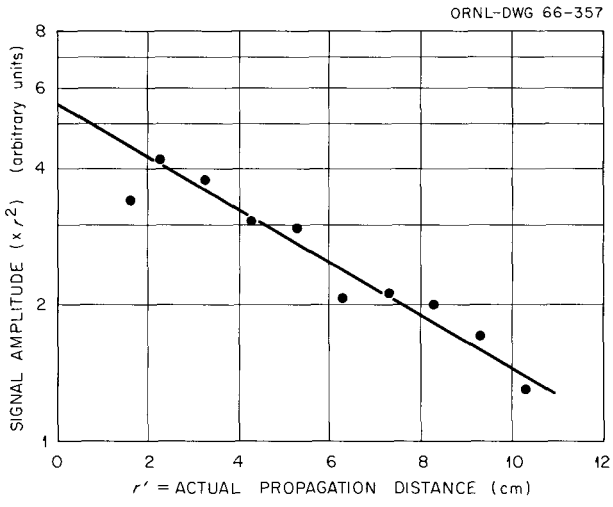

Fig. 4.14. Gas Damping of Ionic Sound Waves Propagating in a Weakly Ionized Xenon Plasma.

distance from the point source to the point at which the wave amplitude is measured. Therefore the "geometrical damping" of the ion waves can be taken into consideration easily. The technique used here was multiplication of the measured value of each amplitude by its corresponding r^2. It was then assumed that any amplitude decrease remaining after this correction for $1/r^2$ losses was due to gas damping.

Figure 4.14 shows some typical results. Here the measured ion-wave-signal amplitudes, corrected for $1/r^2$ losses, have been plotted against r', the actual propagation distance in the gas for ion waves emitted and detected at the sheath edges (see Fig. 4.13). It is seen from the figure that after $1/r^2$ losses have been taken into consideration there remains a damping having an e-folding distance of approximately 8 cm. In determining r from the known separation d of the two probes, it was assumed that the two probe sheaths were of equal thickness. This assumption, even if incorrect, does not introduce serious error as long as d is somewhat larger than the total sheath thickness ($\sim$1 cm for the data of Fig. 4.14). No such assumption was required to determine r', since it was the combined sheath thickness which had to be considered.

If the above damping is assumed to be due to ion-neutral collisions, the observed damping can be compared with that expected theoretically.[16]

For the case of ω real and k complex ("space damping"), it was found that the damping factor was given by[16]

$$\text{d.f.} = \exp\left\{-\frac{\nu_c}{2v_0}\left[\tfrac{1}{2} + \tfrac{1}{2}\sqrt{1+\left(\frac{\nu_c}{\omega}\right)^2}\,\right]^{-1/2} x\right\} . \qquad (1)$$

For k real and ω complex ("time damping"), the damping factor was given by[16]

$$\text{d.f.} = \exp\left(-\frac{\nu_c}{2}\,t\right). \qquad (2)$$

In these equations ν_c is the ion-neutral collision frequency, ω is the ion-wave angular frequency, v_0 is the wave phase velocity for $\nu_c \ll \omega$, and x and t are the wave propagation distance and propagation time respectively. From the two equations it is seen that the space damping is dependent upon wave frequency, whereas the time damping is not. A point to note, however, is that for $\nu_c \ll \omega$ the two damping equations become equal. On the other hand, for $\nu_c \gg \omega$ the space damping becomes insignificant compared with the time damping. In our experiments, the lowest ω

[16] Igor Alexeff and W. D. Jones, *Thermonuclear Div. Semiann. Progr. Rept. Apr. 30, 1964*, ORNL-3652, p. 56.

present in the pulse was large compared with ν_c, so the two damping equations are similar. If we assume that only time damping is present, we can write

$$A = A_0 \exp\left(-\frac{\nu_c}{2} t\right) = A_0 \exp\left(-\frac{\nu_c}{2v_0} x\right), \quad (3)$$

or

$$\ln A = -\frac{\nu_c}{2v_0} x + \text{const}, \quad (4)$$

where A is the ion-wave signal at time t and A_0 is the amplitude at $t = 0$. Replacing ν_c by $1.23 \times 10^4 p$,[16] where p is in μ Hg, and v_0 by the experimentally determined value of 9×10^4 cm/sec, we obtain

$$\ln A = -\frac{p}{14.6} x + \text{const}. \quad (5)$$

Thus, from the slope of a plot of ln A vs x, we can obtain the background gas pressure p from the relation

$$p = -14.6\left(\frac{\ln A_2 - \ln A_1}{x_2 - x_1}\right), \quad (6)$$

where $(\ln A_2, x_2)$ and $(\ln A_1, x_1)$ are arbitrary points on the experimental curve. For the results shown in Fig. 4.14, Eq. (6) gives a pressure of approximately 2 μ Hg. The reading of the system vacuum pressure gage was approximately 1 μ Hg; however, this is an uncertain region for our gage, so the recorded pressure reading may be somewhat in error. Thus, experiment and theory seem to be in agreement for these preliminary measurements.

4.2.2 A New Ion-Wave Detector

If the large flat detector probe shown in Fig. 4.13 is replaced by a short thin wire which can be heated to incandescence, an interesting phenomenon is observed. With no heating current passing through the wire, the wire behaves as an ordinary ion-wave detector. If, however, the wire is heated to the electron-emitting point, its sensitivity as an ion-wave detector is greatly enhanced. The increase in signal amplitude with the probe in the emitting condition over that in the nonemitting condition is observed to be about a factor of 40. The two upper traces in Fig. 4.15 show typically the relative sensitivity of the detector in the emitting and nonemitting conditions for ion waves generated by step-function driving voltages (bottom trace). Much of the noise seen on the upper trace originated in the filament current transformer, although some of the observed increase in noise seems to be inherent in the emitting probe.

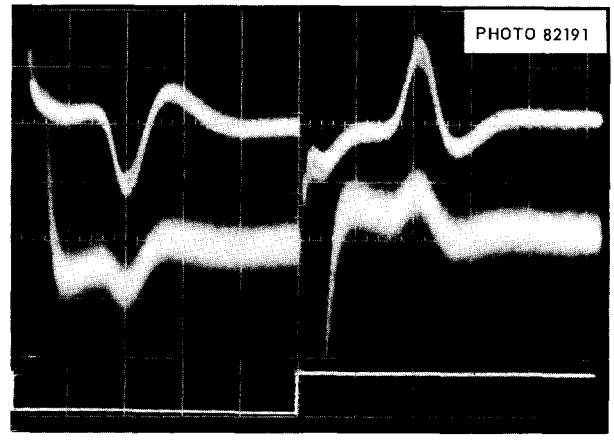

Fig. 4.15. Enhanced Sensitivity of an Emitting Probe (Upper Trace; 1 v/cm) over a Nonemitting Probe (Middle Trace; 0.05 v/cm) for Detection of Ionic Sound Waves Generated by Step-Function Driving Voltages (Bottom Trace; Negative Step at 0 μsec and Positive Step at 250 μsec). Sweep speed = 50 μsec/cm. Note that whereas the emitting probe is much more sensitive to the ion-wave signals (at $\sim$100 and 350 μsec) its sensitivity for the directly coupled signals (at $\sim$0 and 250 μsec) is apparently not enhanced.

In our earlier time-of-flight work,[17] ionic sound waves were propagated directly between the anode and the hot cathode. At that time it was postulated that the cathode was acting as a detector by having its space-charge sheath perturbed by the arriving ion wave, thus giving rise to a large

[17] Igor Alexeff and W. D. Jones, *Thermonuclear Div. Semiann. Progr. Rept. Apr. 30, 1963*, ORNL-3472, p. 45; *Compt. Rend. Conf. Intern. Phenomenes Ionisation Gaz, 6e, Paris, 1963*, vol. III, p. VI 36.

momentary increase in electron emission. Although further work will be necessary to demonstrate this conclusively, the preliminary behavior of this new hot-cathode detector suggests that the original hypothesis may be correct.

4.3 MOVING STRIATIONS PRODUCED BY A SIMPLE THERMAL INSTABILITY

Igor Alexeff

One of the more interesting unsolved problems in physics is the nature of moving striations in cylindrical discharge tubes. In previous work,[18] we described an equation that predicts the velocity of this wavelike phenomenon. In this report, we discuss a possible driving mechanism for the striations.

One clue to the source of moving striations is that they tend to occur only in certain gases – for example, argon, krypton, and xenon. Other gases – for example, mercury vapor and cesium vapor – are remarkably striation free. If one studies the two sets of gases, one finds that for the first set, the scattering cross section for electrons on gas atoms is a rapidly *increasing* function of energy in the region of interest, while for the second set, it is a *decreasing* function of energy. That this scattering cross section variation with electron energy can cause instability or stability is easily understood if one considers the production and loss of heat in a local section of the discharge tube.

The production of heat per unit volume is given by j^2/σ_e, where j is the current density (a constant in a discharge tube which is generally fed through a series resistor) and σ_e is the electrical conductivity. The value of σ_e can be written as $e^2n/2m_e\nu N\sigma_s$, where e is the electron charge, n is the electron density, m_e is the electron mass, ν is the mean electron velocity, N is the neutral gas density, and σ_s is the electron-atom scattering cross section.[19] Thus, if σ_s increases rapidly with electron energy, the hotter a hot spot in the discharge tube, the more power will be dissipated in that spot. Conversely, the cooler the spot, the less power will be dissipated there. Thus, the fact that σ_s increases rapidly with energy suggests that an instability can result.

Table 4.5. The Existence of the Thermal Instability in Various Gases

Gas	Average Electron Temperature (ev)	Stability Prediction	Striation Production
He	3	Stable	Difficult
Ne	1	Indefinite	Easy
Ar	1	Unstable	Easy
Kr	1	Unstable	Easy
Xe	1	Unstable	Easy
Hg	1	Stable	Difficult
Cs	0.2	Stable	Not observed

The instability is enhanced if one considers the effect of thermal conduction of the electrons from the hot spot to cooler parts of the tube. The thermal conductivity σ_T is given by $knv/2N\sigma_s$, where k is Boltzmann's constant and the other quantities are defined above.[19] We see that if σ_s increases rapidly with electron energy (a condition which has been shown to cause more heat to be deposited in a hot spot), then the thermal conductivity *decreases*, and a hot spot tends to become isolated from the cooler regions of the discharge tube. Thus, the variation of thermal conductivity with temperature enhances the thermal instability.

Of course, if σ_s decreases with increasing electron energy, the above arguments can be inverted, and a stable discharge is then predicted. The predictions of the above instability model are compared with the results of many experiments, described in the literature, in Table 4.5, and reasonable agreement is found.

4.4 SIZE RESTRICTION ON LANGMUIR PROBES

Igor Alexeff W. D. Jones

As a consequence of the studies of the ionic sound wave velocity, described previously,[20–21]

[18]Igor Alexeff and W. D. Jones, *Thermonuclear Div. Semiann. Progr. Rept. Apr. 30, 1964*, ORNL-3652, p. 56.

[19]G. Joos, *Theoretical Physics*, 2d ed., pp. 445–47, Hafner, New York, 1950.

[20]Igor Alexeff and W. D. Jones, *Thermonuclear Div. Semiann. Progr. Rept. Apr. 30, 1965*, ORNL-3836, sect. 4.2, p. 45.

[21]Igor Alexeff and W. D. Jones, *Phys. Rev. Letters* 15, 286 (1965).

we carefully studied the Langmuir probe as a tool for measuring electron temperature. We found that Langmuir probes having a large area gave results that disagreed both with the ion-wave velocity measurements and with what was expected. For example, the large probes indicated that the plasma potential corresponded to anode potential, although logically one expects the plasma potential to be several volts more positive than anode potential.

The discrepancy is resolved if one remembers that the plasma in the discharge tubes is remarkably noise free. Therefore, the plasma electrons thermalize at the very slow rate given by collision processes.[22] Consequently, Langmuir probes used to measure the electron temperature must be quite small in area, or else they drain away the plasma electrons so rapidly that the equilibrium energy distribution is distorted. The critical size of the probe can be computed from the following inequality. The probe current i (electrons/sec) must be much lower (say by a factor of 10) than nV/τ, where n is the electron density in the discharge tube, V is the volume of the tube, and τ is the relaxation time[22] for the plasma electrons.

4.5 PLASMA DECAY TECHNIQUE FOR MEASURING PLASMA DENSITY IN DISCHARGE TUBES

Igor Alexeff J. Lohr

As discussed in the preceding section, a Langmuir probe cannot be too large, or it will drain away the plasma electrons so rapidly that the equilibrium distribution of plasma electrons will be distorted. However, in discharge tubes of small volume (a few liters) and low density (10^8 or lower), the Langmuir probe cannot be too small, or its physical dimensions will become smaller than the Debye radius. Under this operating restriction, the characteristic Langmuir probe curve is not obtained, and values of electron temperature and density are difficult to obtain.

To measure density in the low-density regime where Langmuir probes are unsatisfactory, a plasma decay technique was developed. In this technique, a negatively biased plate at the wall of a spherical discharge tube collects the ions that flow radially. To make a measurement, the power supply to the discharge tube is turned off, and the total number of ions, N, reaching the plate from the decaying plasma is measured. Knowing the area of the ion collector, a, the average ion density, $\bar{n}$, in the tube is easily seen to be $\bar{n} = AN/aV$, where A is the area of the wall and V is the volume of the discharge tube. From $\bar{n}$, the density of ions at any point in the tube is easily found if the relative density profile is known. The relative density profile can be computed theoretically, found experimentally by measurements of ion saturation current to a Langmuir probe, or extrapolated to low plasma densities from measurements made at high plasma densities by ordinary Langmuir probe techniques.

In this plasma decay technique, ion recombination losses are not expected to be serious for gas pressures below several millimeters of mercury.[23] The technique is quite similar to the "plasma sweeper" method used earlier in a magnetic field.[24]

4.6 SIMPLE MOMENTUM PROBE FOR PLASMA STUDIES, PART II[25]

Igor Alexeff D. Montgomery[26]
W. D. Jones Mozelle Rankin

4.6.1 Introduction

Theoretical work on the momentum probe[25] has continued. In these calculations, we investigate what happens if both the electric field and the magnetic field surrounding a current-collecting wire are varied. The results are quite interesting, although not derived in a completely consistent manner.

---

[22]Lyman Spitzer, Jr., *Physics of Fully Ionized Gases*, 2d ed., p. 131, Interscience, New York, 1962.

[23]M. J. Mulcahy and J. J. Lennon, *Proc. Phys. Soc. (London)* **80**, 626 (1962).

[24]Igor Alexeff and R. V. Neidigh, *Eng. Aspects Magnetohydrodyn., Proc. Symp., 3rd, Rochester, N.Y., 1962*, p. 141 (1964).

[25]Igor Alexeff, W. D. Jones, D. Montgomery, and Mozelle Rankin, *Thermonuclear Div. Semiann. Progr. Rept. Oct. 31, 1964*, ORNL-3760, p. 36.

[26]Consultant, State University of Iowa, Iowa City.

The momentum probe[25] is simply a bare wire placed in the plasma. When a high current is passed through the wire, it is surrounded by a magnetic field that tends to deflect charged particles away from the wire, as shown in Fig. 4.16. The current of charged particles reaching the wire as a function of magnetic field gives information about the *momentum* distribution of the charged particles. Thus the information obtained differs from that of the Langmuir probe, which studies the *energy* distribution of the charged particles.

When combined with electrostatic biasing, the momentum probe becomes a very versatile tool. For example, a positive bias on the probe suppresses secondary electron emission, yet the magnetic analysis still can be performed. Thus, the probe possibly can be used while incandescent in, for example, a cesium machine,[27] or can be used in the presence of an energetic high photon flux.

4.6.2 Theoretical Discussion

The basic equation governing the magnetic behavior of the momentum probe can be written as follows:

$$B = \frac{mvc}{er_w \ln (r_c/r_w)} . \qquad (1)$$

Here B is the magnetic field (gauss) at the surface of the probe required just to prevent the charged particle from reaching the probe, m is the mass of the particle (g), and v is the velocity of the particle (cm/sec). We have assumed that the particle initially is directed normally toward the wire, and that there is zero electrostatic potential on the wire. The constant c is the speed of light (cm/sec), e is the charge of the particle (esu), r_w is the radius of the wire (cm), and r_c is the effective range of the magnetic field (cm) discussed below. Note how the magnetic field given by Eq. (1) depends on the product of mv, that is, on the *momentum* of the particle.

The range r_c of the magnetic field under vacuum conditions corresponds to that distance from the probe at which the magnetic field drops off faster than the r^{-1} dependence of a straight wire. If the probe is a wire loop, r_c is about twice the loop radius. Beyond this distance the magnetic field begins to drop with the r^{-3} dependence of a dipole.

In a plasma, the value of r_c can be modified drastically. A magnetic field strong enough to deflect isolated electrons may not be strong enough to deflect ions, since the ions may have much more momentum. Therefore, the ions drag electrons with them across the magnetic field, as was pointed out to us by J. L. Tuck of Los Alamos.[28] Experimentally, as is shown below, we find that r_c corresponds to the Debye distance. This occurs because at approximately one Debye distance from the wire the restriction that the plasma be electrically neutral breaks down, and the electrons must force their way across this narrow gap without help from the ions.

The simple equation, Eq. (1), gives remarkably good order-of-magnitude results when applied to plasma measurements. If v is assumed to be equal to $(2kT_e m^{-1})^{1/2}$, where k is Boltzmann's constant, T_e is the electron temperature, and m is the electron mass, Eq. (1) is found to give approximately the value of magnetic field required to reduce the electron current to e^{-1} of its value at zero field.

However, to find a more accurate equation than Eq. (1), we must assume that the undisturbed charged particles beyond the magnetic field cutoff r_c have a Maxwellian distribution and are moving in random directions. We must then solve for the flux of particles reaching the wire. We have been able to solve this problem for arbitrary magnetic fields and arbitrary electrostatic potentials on the wire. Unfortunately, the solutions cannot be obtained in analytic form, but must be found by digital computer. We do not have sufficient space here to discuss the mathematical details of the solution. However, the resulting basic equation is shown below:

$$i = \alpha \left[\int_{A/2-C/2}^{\infty} e^{-z^2} dz \int_{-\infty}^{0} y e^{-y^2} dy \int_{0}^{p} e^{-x} dx \right.$$

$$\left. + \int_{-\infty}^{A/2-C/2} e^{-z^2} dz \int_{-\infty}^{q} y e^{-y^2} dy \int_{0}^{p} e^{-x^2} dx \right], \qquad (2)$$

[27] L. Enriques and F. Magistrelli, *Rev. Sci. Instr.* 35, 1708 (1964).

[28] Private communication, 1964.

where

$$\alpha = -2\,\frac{2\pi r_c\, l n_0\, e}{\pi^{3/2}}\left(\frac{2kT_e}{m}\right)^{1/2},$$

$$p = \frac{\sqrt{y^2 + 2Az - A^2 + AC}}{B},$$

$$q = -\sqrt{-2Az + A^2 - AC},$$

$$A = \frac{(e/c)\, B_w r_w \ln (r_c/r_w)}{\sqrt{2mkT_e}},$$

$$B = (r_c/r_w)^2 - 1,$$

$$C = \frac{2me\,[V_{(r_c)} - V_{(r_w)}]}{[(e/c)\, B_w r_w \ln (r_c/r_w)]\sqrt{2mkT_e}}.$$

In this equation, the integrals are evaluated over all regions where the radicals in the limits are real. The variable i is the received current (esu), r_c is the cutoff radius of the magnetic field (cm), l is the length of the probe (cm), n_0 is the unperturbed electron density (cm^{-3}), e is the electron charge (esu), k is Boltzmann's constant (ergs/°K), T_e is the electron temperature (°K), m is the electron mass (g), c is the speed of light (cm/sec), B_w is the magnetic field at the surface of the wire (gauss), r_w is the radius of the wire (cm), and $V_{(r_c)}$ and $V_{(r_w)}$ are the plasma potential beyond r_c and the potential on the wire, respectively (statvolts). If the magnetic field is allowed to go to zero, and if the constant B is small (which corresponds to the sheath being small compared with the wire radius), a limiting procedure shows that the triple integral yields the classical Langmuir probe curve.

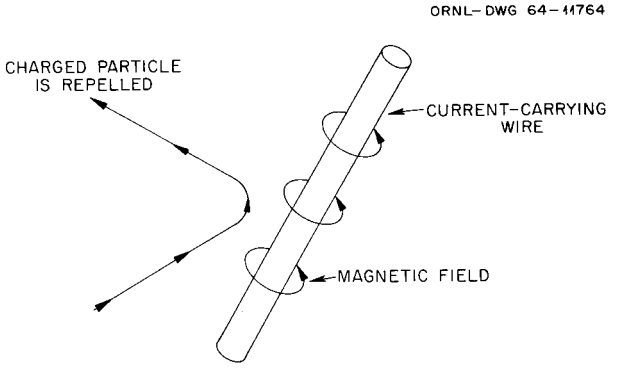

Fig. 4.16. Principle of Momentum Probe. A wire carrying a large current deflects charged particles away from the wire.

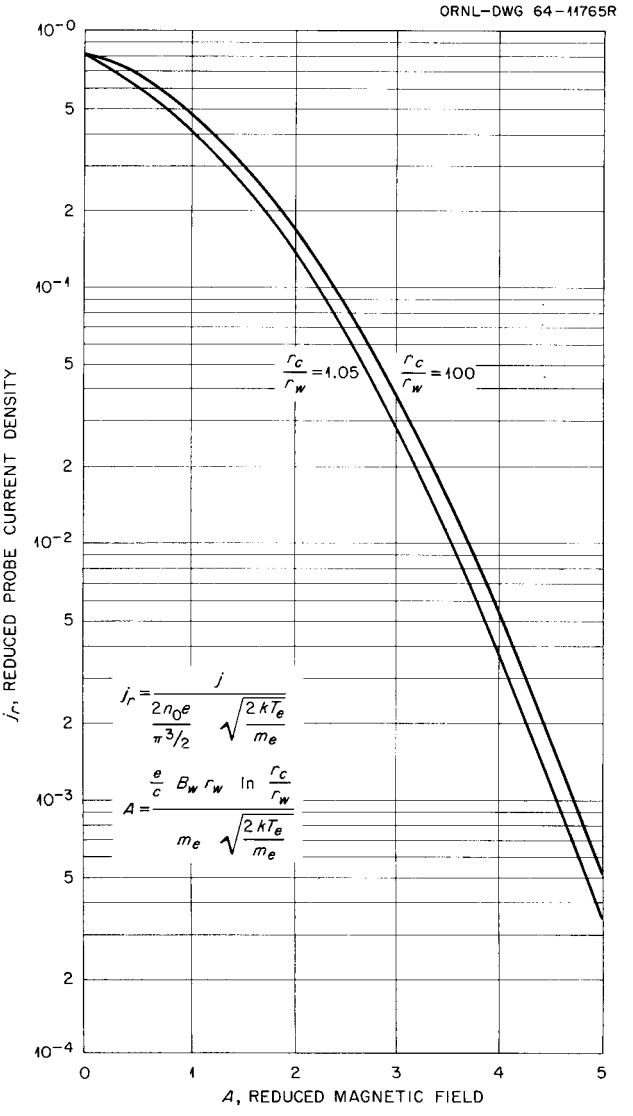

Fig. 4.17. Computed Momentum Probe Response. The variables are as follows: j is electron current density (amp/cm^2), n_0 is electron density (cm^{-3}), e is the electron charge (coulombs), k is Boltzmann's constant (ergs/ev), T_e is electron temperature (ev), m_e is the electron mass (g), c is the speed of light (cm/sec), B_w is the magnetic field at the surface of the wire (gauss), r_w is the radius of the wire (cm), and r_c is the effective range (cm) of the magnetic field measured from the center of the wire.

Computer solutions for two different magnetic-field cutoff distances are shown in Fig. 4.17. In this case we have assumed that the probe is at plasma potential. The current density of charged particles to the probe, in reduced units, is plotted as a function of magnetic field, also in reduced units. The surprising feature of the two reduced curves is that they almost coincide. The curve $r_c/r_w = 1.05$ corresponds to a magnetic shell extending only 5% further than the radius of the wire – in other words, to the case of plane geometry. The curve $r_c/r_w = 100$ corresponds to cylindrical geometry. Thus the momentum probe essentially has only one free variable, the reduced magnetic field A. We also computed six other curves having r_c/r_w between the above extreme values, and all the resultant curves fell between those given in Fig. 4.17.

Curves showing the momentum probe's magnetic analysis, when biased to various electrostatic potentials, are given in Fig. 4.18. Note that when the probe is biased strongly positive (to prevent secondary electron emission, for example), the magnetic field is still able to perform a good analysis. To derive these curves we have made the assumption that both the electric and the magnetic fields act over a distance of only one Debye length. This assumption should be checked both by experiment and perhaps by a more complete, self-consistent theory. However, we feel that the curves in Fig. 4.18 probably do show the general behavior of the momentum probe.

Curves showing the electrostatic analysis of the momentum probe for various constant values of magnetic field are given in Fig. 4.19. Note how the curves approach those of a conventional Langmuir prove as the magnetic field is decreased toward zero.

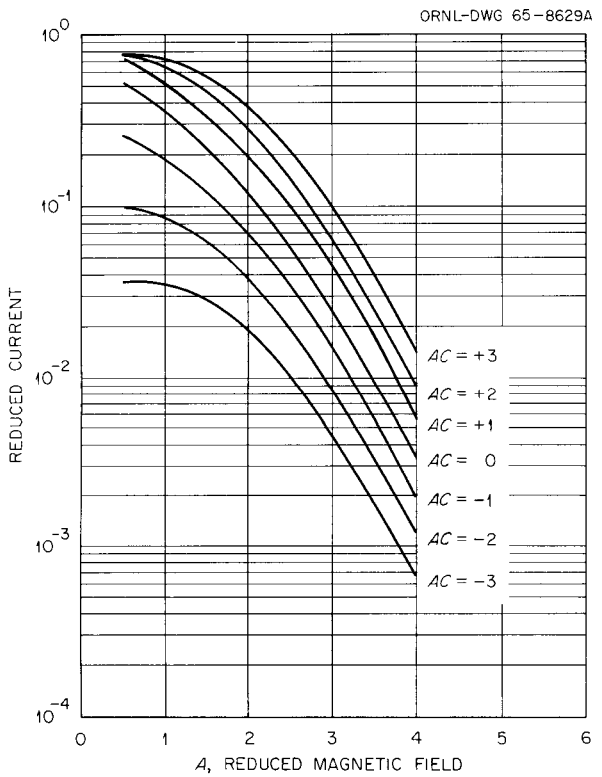

Fig. 4.18. Momentum Analysis Holding the Electrostatic Potential Constant. The reduced variables A,B,C are those used in Eq. (2). Here, $r_c = 1.1r_w$. The reduced current is the integral of Eq. (2) not multiplied by the constant α. $B = 0.21$.

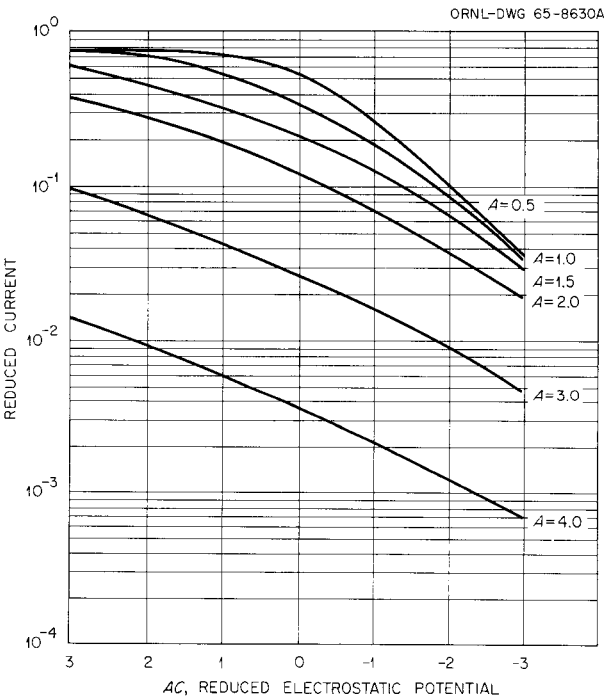

Fig. 4.19. Energy Analysis Holding the Magnetic Field Constant. The reduced variables A,B,C are those used in Eq. (2). Note that as the magnetic field goes toward zero, the curves approach the Langmuir probe form. Here, $r_c = 1.1r_w$. The reduced current is the integral of Eq. (2) not multiplied by the constant α. $B = 0.21$.

4.6.3 Acknowledgments

The authors wish to express their appreciation to C. E. Parker for help in the numerical calculations, and to J. G. Harris for constructing much of the fine experimental apparatus.

4.7 EXPERIMENTS IN LOW-FREQUENCY INSTABILITIES IN COLD PLASMAS

4.7.1 Gas Arc Facility

H. C. Hoy N. H. Lazar
T. H. Rayburn

Studies of the macroscopic cross-field mass motion ("fluting") from the hydrogen arc have continued. As was described previously,[29] probe signals of either ion or electron current or floating potential show nearly exact detailed correlations when probes are displaced axially along a flux line some distance radially from the arc column. When the probes are displaced either radially or azimuthally, the correlation becomes less exact, although a clear time delay is evident which may be related to the velocity of the flute. The inexactness of correlation of detail and the nonreproducibility in the pulse shape from pulse to pulse, as well as between time-related pulses, point to a turbulent nature of the flute rather than to a plasma clump moving in a rigid, coherent manner. Despite this apparent turbulence, the width of the flute, as determined from the time for the pulse to fall and the velocity, is not much different at 5 cm from what it is at 2 cm – in some cases with a variation by factor of 10 in velocity. This behavior is still not understood.

The gas arc facility magnetic field has been modified by the addition of a coil pair inside the usual mirror pair in order to be able to produce a radial minimum in the magnetic field on the axis. Previous results showed such a geometry may produce an apparent stabilizing effect on the flutes.[30] The magnetic field from the coil system was measured (Fig. 4.20) and is in agreement with the calculations carried out for us by Mozelle Rankin. In line with our concepts of the "$\int dl/B$" stabilization of the arc in the earlier experiments, the values of $\int dl\ \nabla B/B^2$ were calculated for the simple mirror and for several values of the booster coil currents. The results for the highest-current case (minimum B) in Fig. 4.20 are shown in Fig. 4.21 for the flux line through the cathode (r = 1 cm). It may be noted that with the booster coils, $\int dl\ \nabla B/B^2$ reaches a value greater than that with a short arc in a simple mirror (although there remain some small negative-gradient regions) and the absolute magnitude, if normalized to the central field value, is considerably larger than that with the simple mirror.

Experiments were carried out on the midplane with the same type of probes used earlier, and fluctuations which can only be interpreted as flutes are seen at nearly all radii.

When the saturation ion current to the probe was examined as a function of radius, the curves shown in Fig. 4.22 were obtained for various booster coil current settings. For each field shape except one, the saturation current fell exponentially with radius over more than a decade. When the field shape (maximum booster coil current configuration) was held constant but the total field was reduced, the data no longer yielded an exponential radial profile (solid triangles). For the other cases, the e-folding length depended on B_0, the midplane field, as $B_0^{-0.67}$. This behavior differs from previous results. In simple mirror geometry an exponential profile was observed but the e-folding length was almost independent of the midplane field magnitude.[29] It may be remarked that the probe current at r = 2 cm falls $1\frac{1}{2}$ orders of magnitude when the midplane field changes by only a factor of 3. A similar behavior, as mentioned previously, is seen when the field shape is held constant but the anode is moved closer to the cathode. It appears that the radial transport rate is strongly affected by the field shape, even though the flutes are not entirely suppressed. Another aspect of this behavior is seen in the radial velocity of the flutes. Figure 4.23 shows the radial velocity from time delay measurements between two probes displaced radially by $\sim$3 mm. It is interesting to note the rapid radial motion of

---

[29] *Thermonuclear Div. Semiann. Progr. Rept. Oct. 31, 1963*, ORNL-3564, p. 63.

[30] *Thermonuclear Div. Semiann. Progr. Rept. Oct. 31, 1964*, ORNL-3760, p. 49.

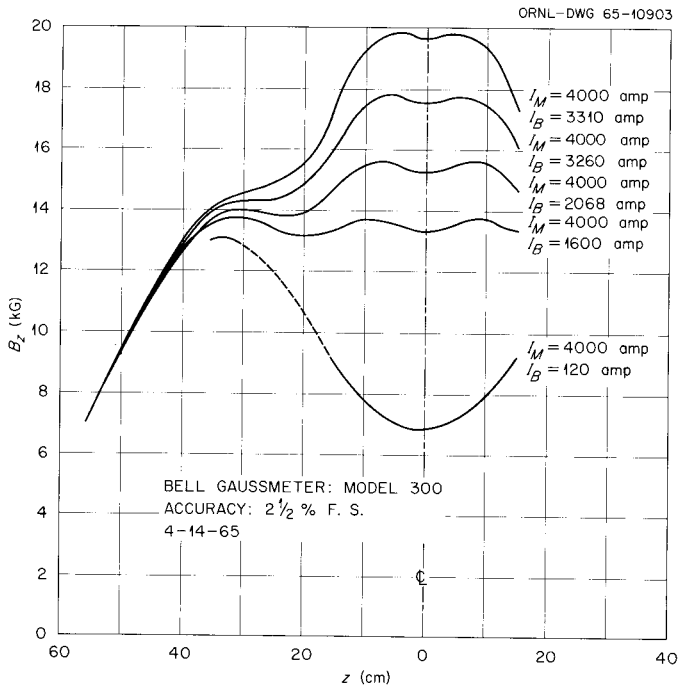

Fig. 4.20. Magnetic Field in Gas Arc Facility as a Function of Axial Position for Different Booster Coil Currents (I_B). I_M is the current in the mirror coils.

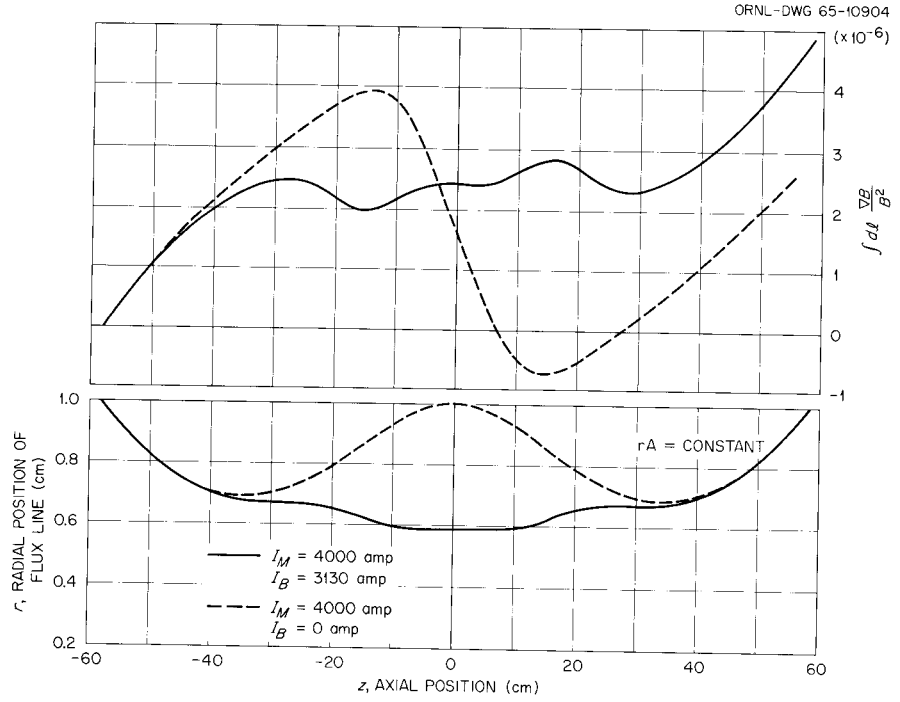

Fig. 4.21. Flux Line and $\int dl\ \nabla B/B^2$ Calculated for Simple Mirror and Machine Booster Coil Current. The solid curve represents the machine current, and the dotted curve represents zero booster coil current.

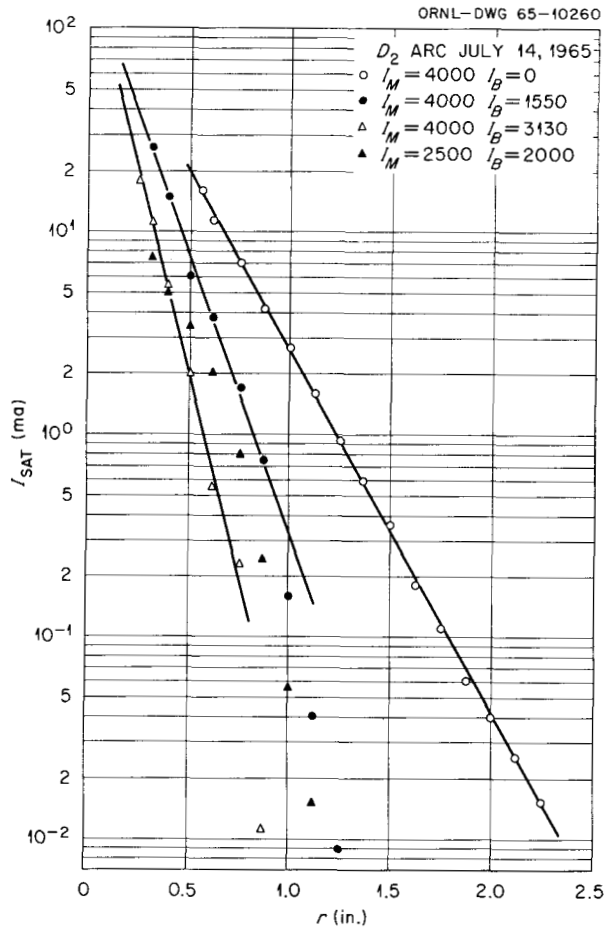

Fig. 4.22. Saturation Ion Current to 0.010-in.-diam by 0.125-in.-long Wire Probe as a Function of Radial Position for Various Booster Coil Current Values.

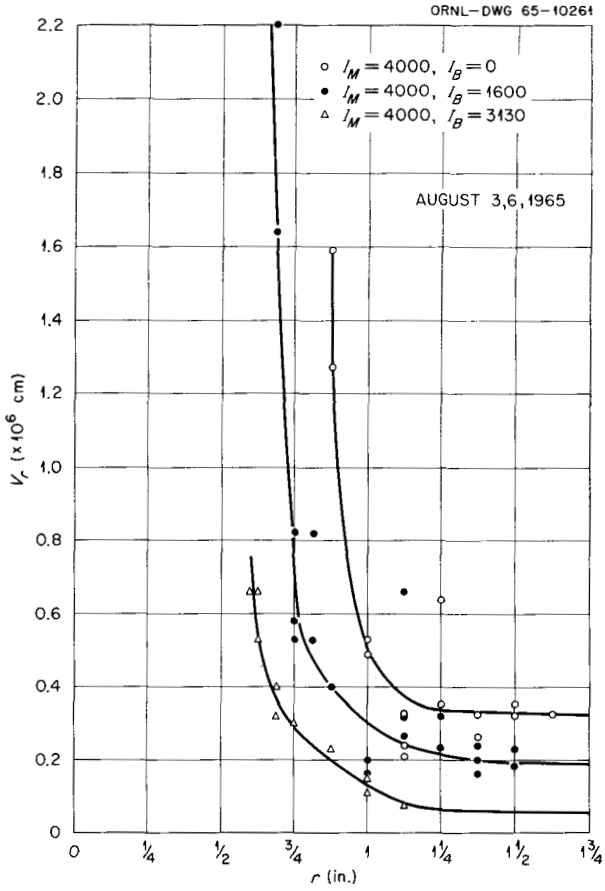

Fig. 4.23. Radial Velocity as a Function of Radial Position. Helium, 3.4 cm^3/sec, 150 amp.

plasma close to the arc core, followed by a slowing down and then nearly constant radial velocity at larger radii. Data in the "minimum-B" geometry (I_B = 3100 amp) could not be analyzed at the larger radii, because a true coherence could not be established. If the extrapolated curve for velocity in this case is proper, the ratio of velocity to that in the simple mirror case is 10, although the field magnitude is only increased by a factor of 3.

4.7.2 PIG Plasma Source in Beta Tank D

C. W. Blue N. H. Lazar

The plasma issuing from the PIG-type plasma source has been examined in further detail in the uniform magnetic field in beta tank D. The energy of the ions has been shown to be quite high in some cases.[31] The ion energy was shown to depend, primarily, on the rate of gas feed into the cathode. The energetic ions, up to several hundred volts at the lowest gas feeds, could not have been generated in the anode region of the source, because their Larmor diameters are too large. The process in which they are produced is considered to be related to a streaming instability of energetic electrons directed axially through the plasma drifting out of the anode aperature – in the fashionable jargon, through "turbulent heating."

The density of plasma has been measured as a function of radius outside the main plasma column.

[31] *Thermonuclear Div. Semiann. Progr. Rept. Apr. 30, 1964*, ORNL-3652, p. 90.

A series of concentric rings were biased negatively to ion saturation, and the charge collected on each of the rings after the discharge was cut off was determined from the integral of the ion current. If it is assumed that half the current flows in the direction of the rings (placed at one end of the tank volume), the average density at each of the radial positions may be estimated. The results are shown in Fig. 4.24. For these experiments, the source was modified to enable easier starting and turnoff by changing the cathode to an electrically heated strip instead of the ion-bombardment-heated cylinder used previously.

In view of the experience in the GAF, where flutes have been identified in the halo of the deuterium arcs, correlation experiments were undertaken to determine whether a similar behavior is seen with this plasma. Data have been taken, so far, with hydrogen gas flows of 0.07 and 0.10 atm-cm^3/sec. Fluctuations, much like those seen in the GAF, are observed. Typical pulses are seen in Fig. 4.25*a*, when the gas flow was 0.07 cm^3/sec. Correlation measurements between probes displaced azimuthally give the radial distribution of the azimuthal velocity, when the pair of probes is moved radially. When the gas flow is increased, the pulses change character at

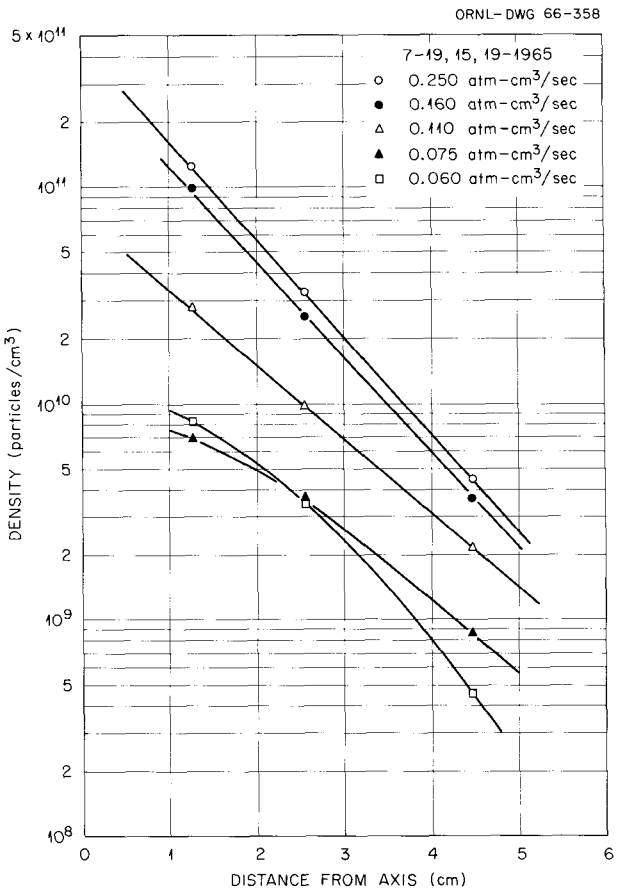

Fig. 4.24. Density vs Radial Position for the Plasma Produced by PIG Geometry in Beta Tank D.

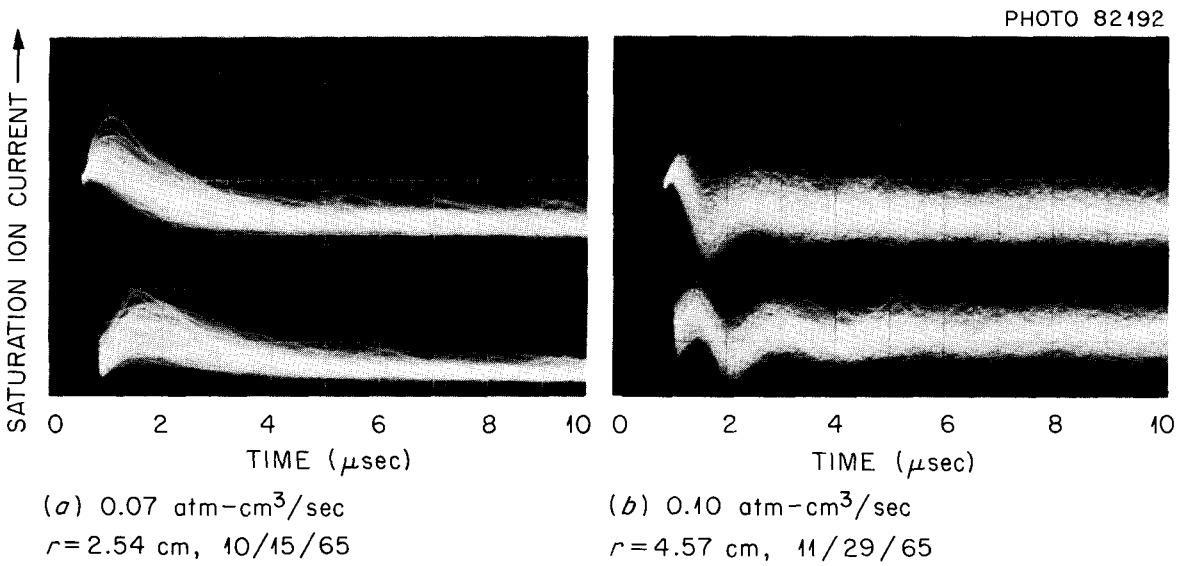

Fig. 4.25. Ion Saturation Current to Two Probes Displaced Azimuthally 3.36 cm. Sweep speed, 1 μsec/cm. (*a*) Radial position (r) = 2.54 cm from the plasma axis. The phase lag is a measure of azimuthal velocity. These are the "long pulses." (*b*) Radial position (r) = 4.57 cm. Again the phase lag is apparent. These are the repetitive pulses of Fig. 4.28.

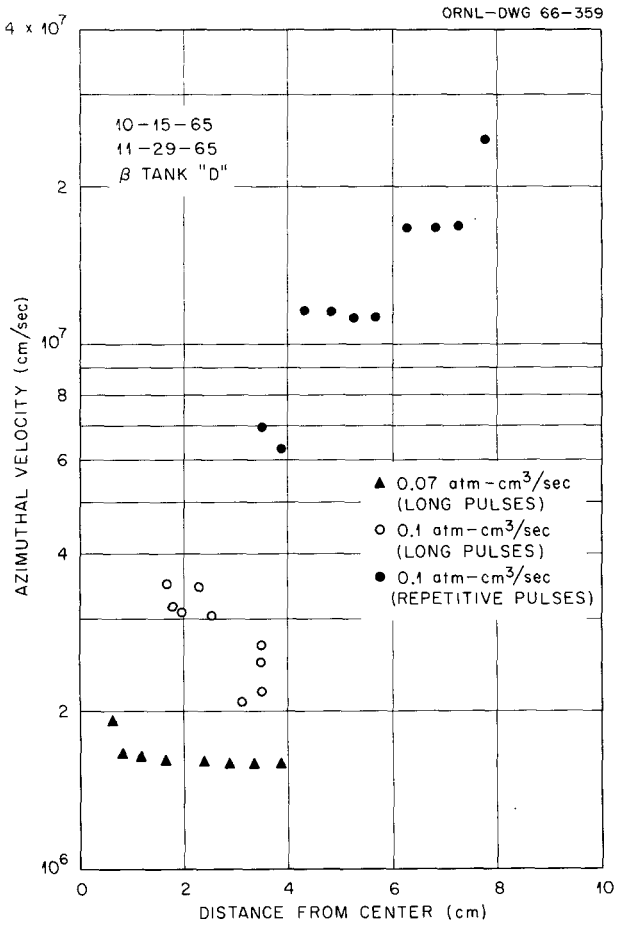

Fig. 4.26. Azimuthal Velocity as a Function of Radial Position of the Probes at Two Different Gas Feeds. The repetitive pulses are typical of the ones seen in Fig. 4.25*b*, while the long pulses are typically indicated in Fig. 4.25*a*.

larger radii. This is illustrated in the pulses shown in Fig. 4.25*b*. The radial distribution shows that these pulses, too, represent plasma rotating but not necessarily fluting. The azimuthal velocity increases almost proportionally to radius; that is, there appears to be a constant angular frequency. Close to the arc column, however, both types of pulses are seen. The azimuthal velocities determined from the average time delay between pulses are plotted in Fig. 4.26. The long pulses are characterized by those shown in Fig. 4.25*a*, while the repetitive pulses are similar to those shown in Fig. 4.25*b*.

4.8 HYDROGEN ARC FLUCTUATIONS

J. E. Francis P. M. Jenkins
P. R. Bell

The strong fluctuations of the ion current to a negatively biased Langmuir probe in the column of a hydrogen vacuum arc have been studied for some time. The fluctuations of the ion current to probes separated radially are considerably less well correlated in time for a long arc operating in a uniform magnetic field than they are for a short arc operating in a 2:1 mirror field geometry.

In an attempt to understand the nature of the fluctuations, the cumulative number of fluctuations vs their pulse amplitude was measured with a linear amplifier and discriminator. Some of the resulting distributions are shown in Fig. 4.27 for several different distances of the short, electrically shielded probe from the arc axis. The distributions are quite good exponentials, with a slow steepening of the slope with increasing distance from the axis. The distributions and the scope traces rather resemble white noise signals as seen through a low-pass filter.

At a given pulse height, the counting rate of pulses larger than this value was found to have also a remarkably rapid increase with arc current, as shown in Fig. 4.28.

Good correlation of the fluctuations along a given magnetic flux line has been reported previously by Gibbons and Lazar[32] for an arc in a 2:1 magnetic mirror system. These have also been seen for a uniform field. The degree of this correlation for probes separated axially by 40 in. in the uniform field is shown by the *x-y* oscillogram of Fig. 4.29. Here the crossing of the central graticule lines marks the point of zero current to both probes. It can be seen that the magnitude of the fluctuation is comparable to the average value of the ion current. While the correlation is quite good, it is clear that it is far from perfect, but correlation is as good for the dips of current as it is for the peaks. When one probe is moved 3 mm away from the correct field line (in azimuth) the correlation deteriorates, as can be seen in Fig.

[32] R. A. Gibbons and N. H. Lazar, *Thermonuclear Div. Semiann. Progr. Rept. Oct. 31, 1964*, ORNL-3760, p. 49; R. A. Gibbons, N. H. Lazar, and W. F. Peed, *Thermonuclear Div. Semiann. Progr. Rept. Apr. 30, 1964*, ORNL-3652, p. 71.

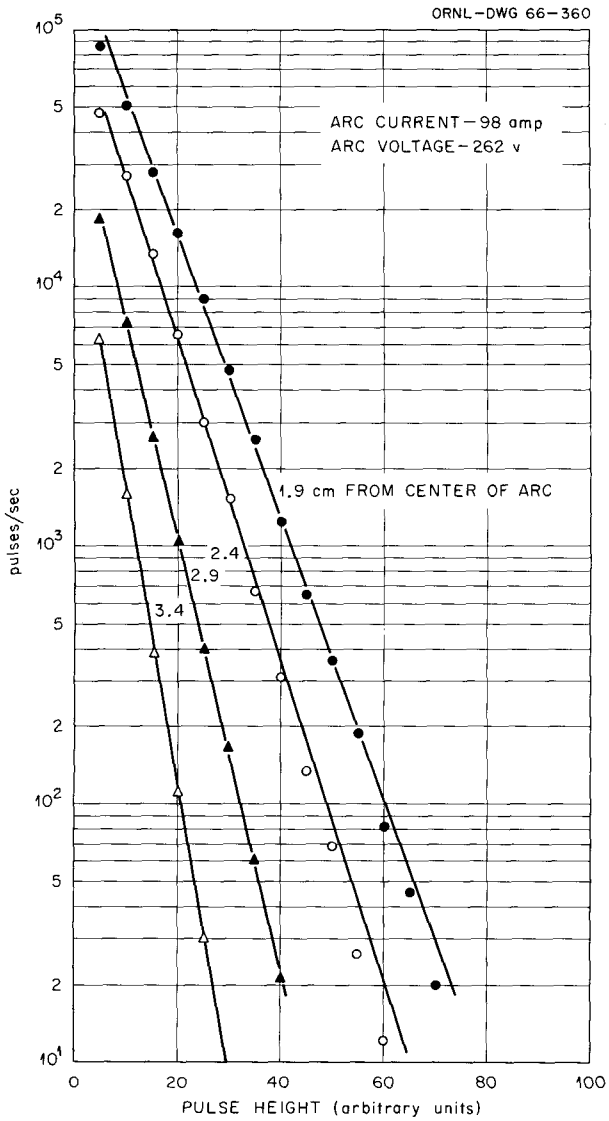

Fig. 4.27. The Number of Current Fluctuations Greater than the Indicated Height vs Height for Several Distances of the Probe from the Arc Axis.

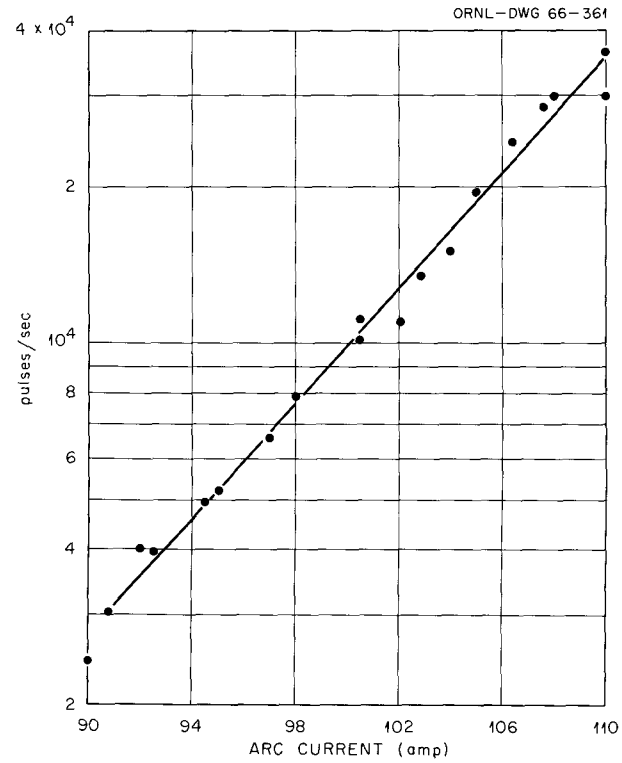

Fig. 4.28. Fluctuation Rate as a Function of Arc Current. Probe 2.9 cm from the arc axis.

4.30. The maximum fluctuation is seen to be rather rarely larger than twice the average value of the ion current. Using the rough value (~3 mm) of the radial correlation distance (see below) we conclude that single fluctuations rarely involve more than ~5% of the ions at a radial distance of about 2 cm.

The radial velocity of the fluctuations was measured by separating two probes radially at an axial spacing of 1 in. The delayed correlation of the fluctuations on the two probes was very hard to see for radial separations of more than 3 mm and even at this spacing was considerably poorer than that seen in the 2:1 mirror geometry. This value of 3 mm could be considered a rough value for the radial correlation distance. From the delayed correlations, radial velocities were found as large as 1.5×10^5 cm/sec at 2.5 cm from the arc axis and as small as 3×10^4 cm/sec at 4 cm radius. These are considerably lower velocities than generally found in the mirror geometry. In the mirror geometry, the disturbances not only moved radially but also rotated around the axis. In the uniform field of the long solenoid, however, the maximum correlation for probes separated a few millimeters is found when the probes lie along the same radius. This implies no rotation of the fluctuations.

These experiments lead to the conclusion that the hydrogen arc in a uniform magnetic field more closely resembles a turbulent rather than a fluting plasma. The exponential pulse height distribution found and the rapid loss of radial correlation much more closely resemble a turbulent behavior rather than hydromagnetic flutes. Also, the rather

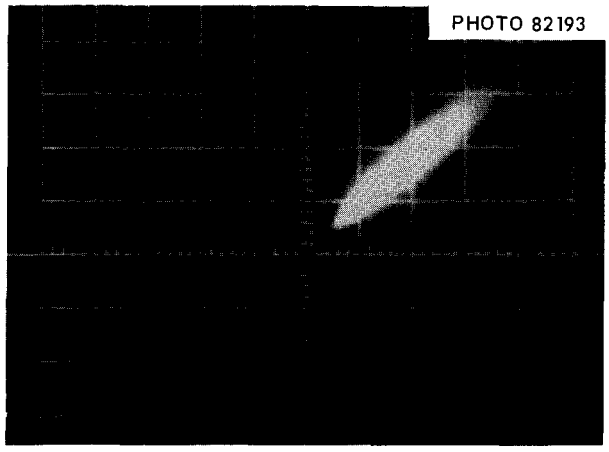

Fig. 4.29. *x-y* Plot of the Response of Two Langmuir Probes on the Same Flux Line Separated by 40 in. in the Hydrogen Arc.

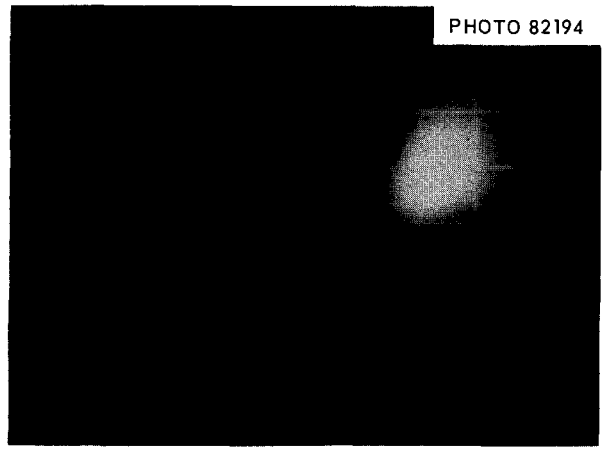

Fig. 4.30. *x-y* Plot of the Response of Two Langmuir Probes Not on the Same Flux Line Separated by 40 in. in the Hydrogen Arc.

small value of ~5% of the ions at a given radius that are involved in one fluctuation would seem more suitable as the size of a turbulence cell than as that of a flute, which often involves $\frac{1}{4}$ or more of the ions in a plasma column.

More accurate correlation distances, both in radius and in azimuth, should be determined for the hydrogen plasma, and the dependence upon plasma density and arc current should give a clearer picture of turbulence in this completely ionized and moderately hot plasma.

4.9 BEAM STABILIZATION IN THE CALUTRON

D. E. Harrison[33] E. D. Shipley
O. C. Yonts

During this period the Ca^+ beam passing through a homogeneous magnetic field has been studied. The experimental arrangement for studying the calutron beam is shown in Figs. 4.26 and 4.27 on p. 56 of the preceding semiannual report.[34] Figure 4.31 shows how the depth of the positive potential well at the 90° point depends on pressure. The minimum depth of 25 v occurs at a pressure of 4×10^{-6} torr. This point is used as a reference in Table 4.6.

Ion loss rate is the current collected by the Faraday cup for zero stopping voltage. Beam imperfection is defined as the ratio of the total beam current to the beam current that enters the collector slit.

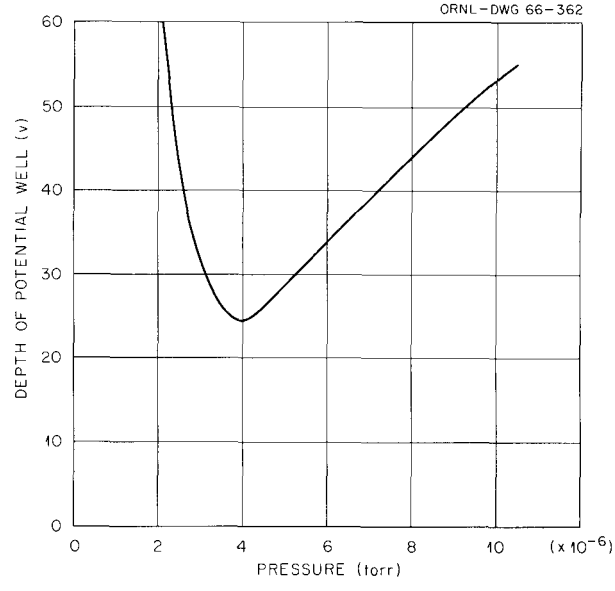

Fig. 4.31. Depth of Potential Well vs Pressure.

[33]Consultant, U.S. Naval Postgraduate School, Monterey, Calif.

[34]O. C. Yonts and E. D. Shipley, *Thermonuclear Div. Semiann. Progr. Rept. Apr. 30, 1965*, ORNL-3836, p. 56.

Table 4.6. Qualitative Comparisons of Observed Operating Conditions

Pressure	Depth of Positive Potential Well	Beam Imperfection	Ion Loss Rate
Higher	Deeper	Larger	Larger
Reference	Reference	Reference	Reference
Lower	Deeper	Larger	Smaller

The disturbance which perturbs the beam and gives rise to a large beam imperfection appears to to be associated with the depth of the positive potential well. The problem posed by this table can be stated in several ways; for example, if, as shown in the top row, the deeper potential well is required to produce the larger ion loss rate, then why is the deeper potential well required in the bottom row?

The development of a computer program has begun which will simulate various individual aspects of the beam-plasma interaction in the calutron. The "foundation" potential distribution has been completed for a lune-shaped charge distribution for various wall configurations and plausible perturbations. Work is in progress on a program which allows electrons to move in the foundation potential well.

4.10 EXCITATION HEATING OF CARBON IONS BY ELECTRONS

J. R. McNally, Jr. J. E. Francis, Jr.
M. R. Skidmore P. M. Jenkins

4.10.1 Introduction

During this report period we have developed further confirmation for the excitation-heating model[35] suggested for heating carbon ions to high temperatures ($T_{+\perp}$ up to 4×10^6 °K) in the presence of cold electrons ($T_- \approx 40{,}000$ °K). The model proposed the excitation of C^{2+} ions to a 6.5-ev metastable state which becomes overpopulated with respect to the ground state. This is followed by electron rearrangement collisions between pairs of metastables, resulting in each ion gaining 6.5 ev on the average *per excitation-heating cycle.*

We have observed an incipient leveling off of the maximum ion temperature at $T_{+\perp} \approx 4.3 \times 10^6$ °K in very long arcs and have applied the adiabatic maximum rule, in terms of an intermediate near-resonance reaction, to predict an energy for the maximum cross section in the heating step. Also, we have obtained an improved understanding of the degree of our ignorance in evaluating electron temperatures. Lastly, an experimental value for "ln λ" of 1.0 has been measured in terms of the resistivity of the carbon arc and gives a crude check with the value of 1.4 predicted from our revised energy transfer rate from hot ions to cold electrons,[35] as compared with the value of 8.6 predicted by the conventional form of ln λ.

4.10.2 Experimental

Figure 4.32 illustrates the brilliant carbon arc core and weaker halo as viewed through one of the observation ports in the long solenoid. The Doppler broadening and slant effects observed in a 5.45-m-long carbon arc in a field of 8300/5500/8300/5500/8300 gauss (double mirror) are illustrated by Fig. 4.33. The halo of Fig. 4.32 is about $\frac{1}{15}$ as bright for C^{2+} λ 4647 A spectra as the arc core but gives $T_{+\perp}$ ~75% as high as the core at 5.25 m from the anode. The average ion orbit (d = 1.2 cm) is almost as large as the central arc core, which is only slightly larger than the cathode ($d \approx 1.9$ cm). Tentatively, we attribute the reduction of average ion energy in the halo to the radial electric field

[35] *Thermonuclear Div. Semiann. Progr. Rept. Apr. 30, 1965*, ORNL-3836, sect. 4.8, pp. 64–66.

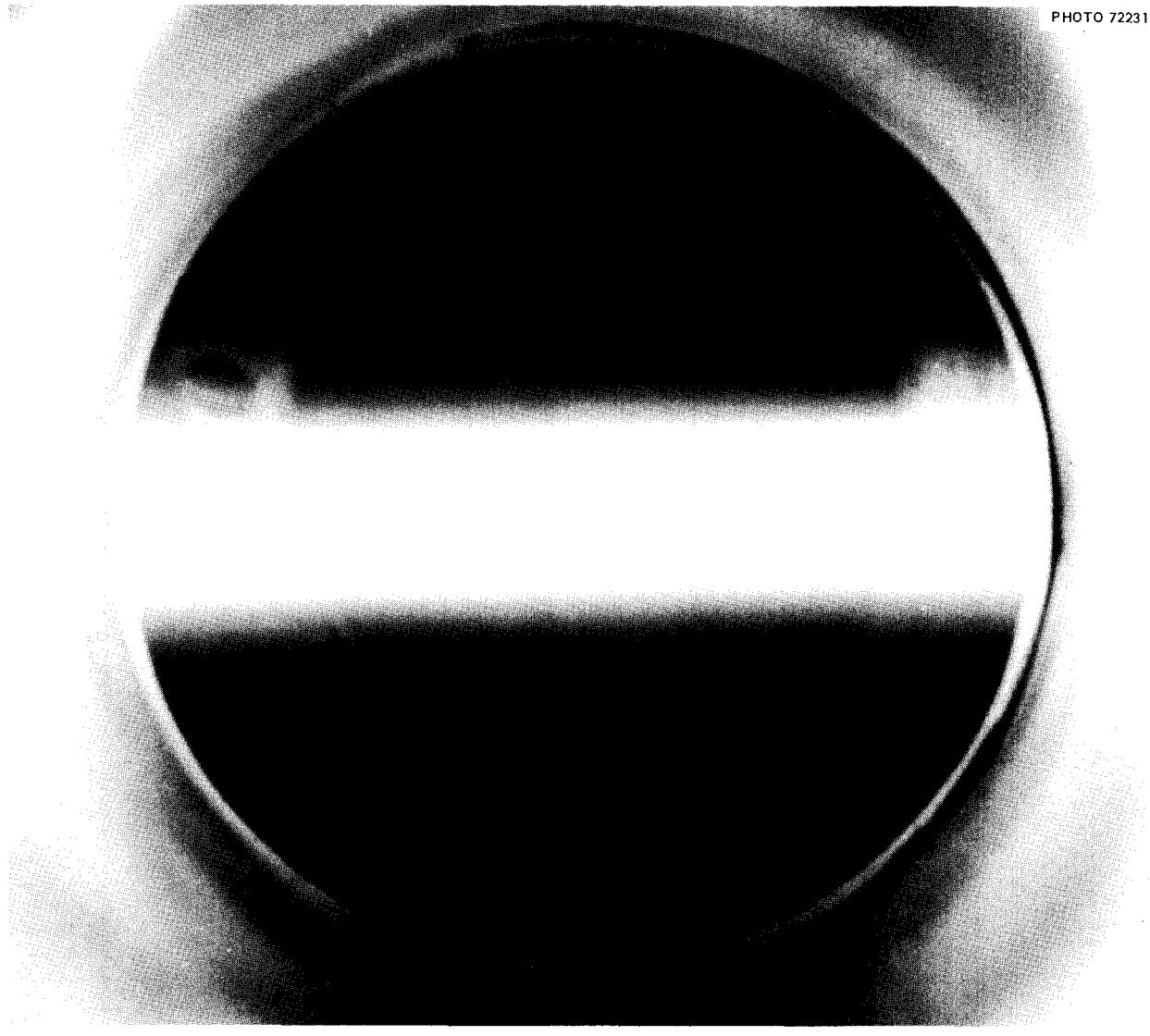

Fig. 4.32. Photograph of Short Section of Energetic Carbon Arc, Showing Halo Outside Main Arc Core.

(~50 to 100 v/cm) usually associated with the arc cores. For C^{2+} this would give a reduction of about 150 ev, a figure in rough agreement with the observations. No attempt was made to compare the reduction in ion "temperature" for C^{+} or C^{3+}, so confirmation of this interpretation awaits further experiments.

Figure 4.34 suggests for the first time an incipient leveling off in the ion temperature at about $T_{+\perp} \approx 4.3 \times 10^{6}$ °K in extremely long arcs. Although other causes (such as size of the cathode and pressure damping) may possibly bring about such a saturation, it will be pointed out in the next section that the excitation-heating process is predicted to attain a limiting rate. The cooling effects of cold electrons eventually produce an equilibrium with $T_{+\perp} \approx 100 T_{-}$. No significant change in ion temperature was obtained with variation in cathode size.

Attempts were made to vary the C^{2+} population relative to C^{3+}. Figure 4.35 illustrates the effect on Doppler half-width and ion temperature as a function of the intensity of the resonance lines of C^{2+} and C^{3+}. The data were obtained by varying

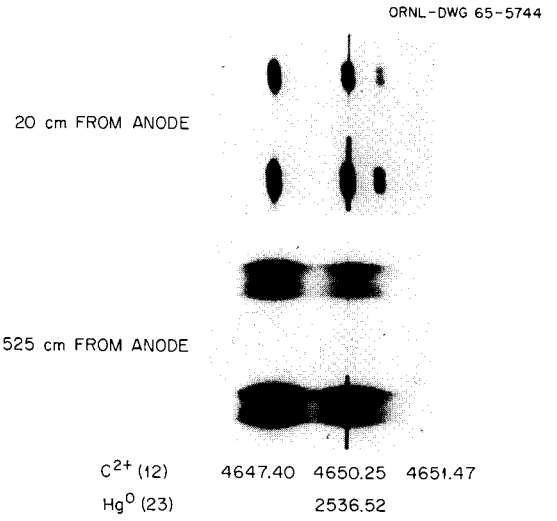

Fig. 4.33. Spectrograms of Blue Triplet of C^{2+} in Twelfth Order of Jaco-Ebert Spectrograph. Note Doppler slant effect in top spectrograms and marked Doppler broadening at great distances from the anode (other experiments have demonstrated that carbon ions do not have to originate at anode). Arc conditions: 135 amp, 170 v, length 545 cm, 4×10^{-6} torr (center manifold), 5500/8300 gauss as a double mirror, carbon electrodes.

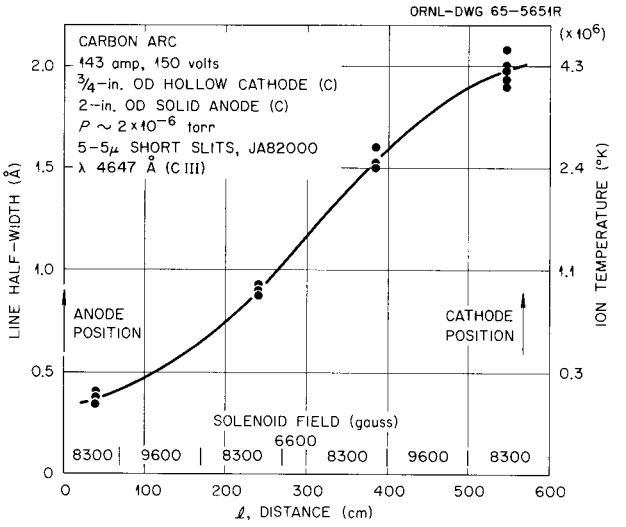

Fig. 4.34. Observed Line Widths and Associated Ion Temperature of C^{2+} Ions in 5.7-m-long Carbon Arc Confined by Magnetic Field. Ion temperature shows incipient saturation at about 4.3×10^6 °K in this arc.

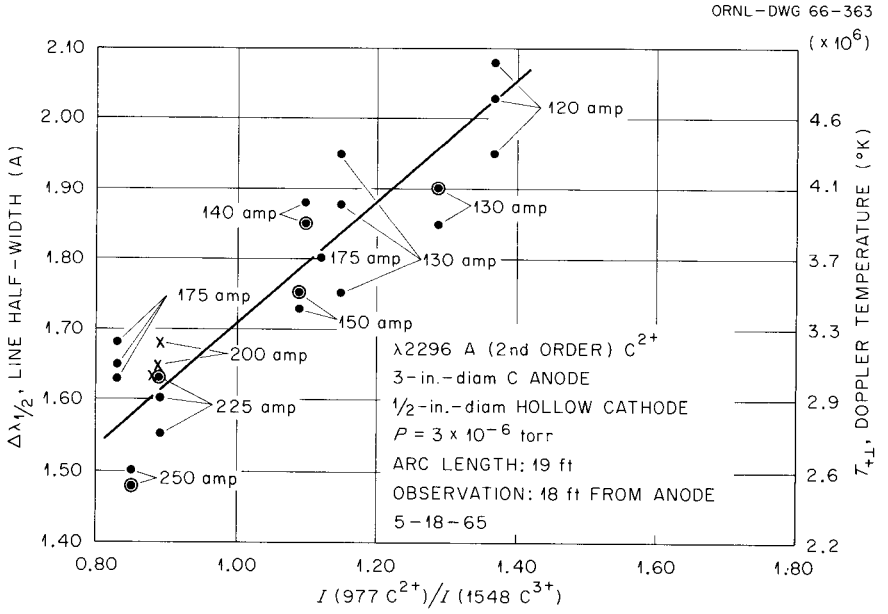

Fig. 4.35. Variation of Doppler Half-Width and Ion Temperature as a Function of the Intensity Ratio of the Resonance Lines of C^{2+} and C^{3+} for Various Arc Currents.

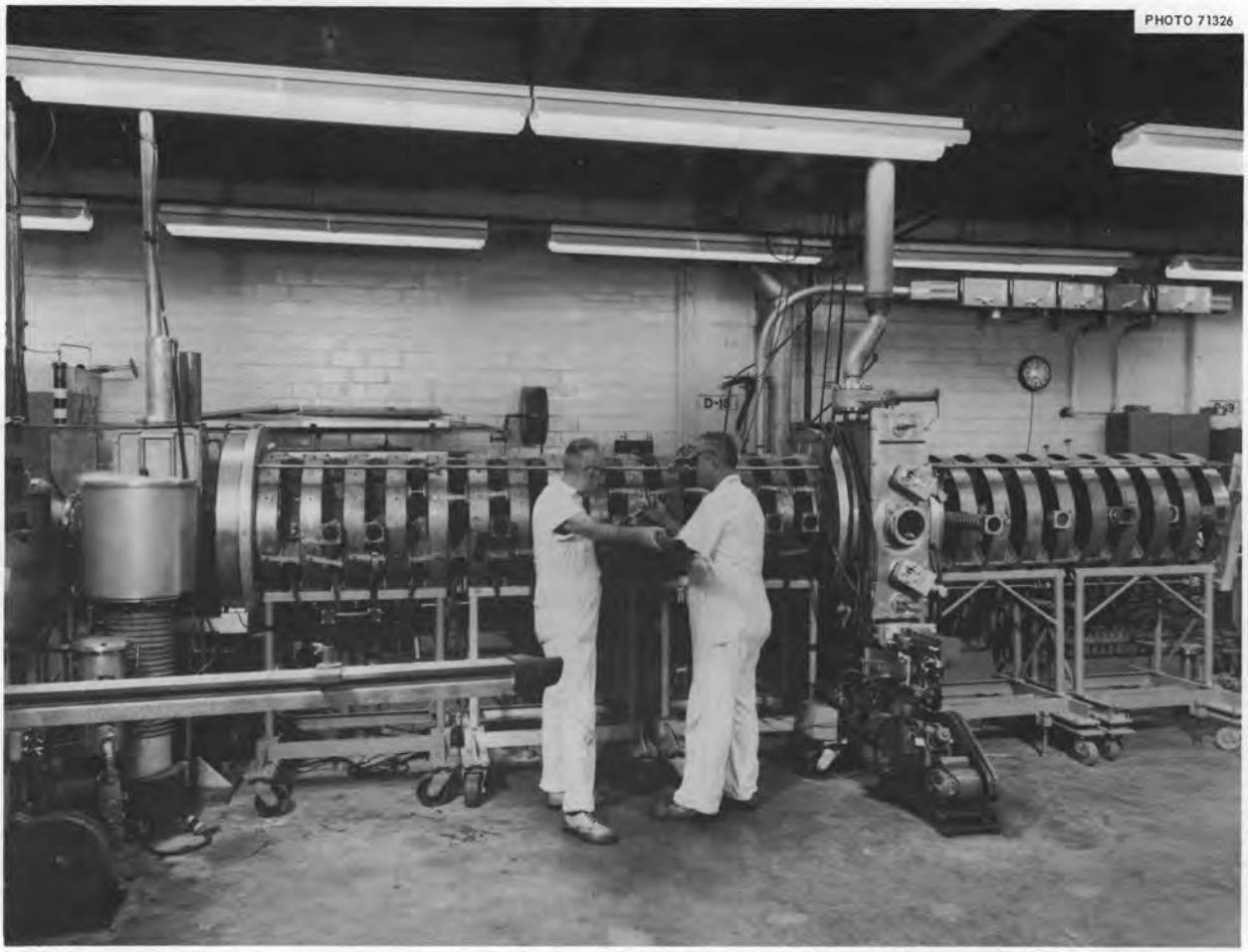

Fig. 4.36. Long Solenoid Facility Used in Study of Magnetically Confined Arcs. Magnetic field of 8300 gauss requires 3000 amp from two 1.75-Mw dc generators.

the arc current from 120 to 250 amp and were taken over a two-day period with various arc restarts. Although the pressure at the central manifold (see Fig. 4.36) was approximately constant ($\sim 3 \times 10^{-6}$ torr) during the series of experiments, it is quite possible that increased outgassing at the higher currents caused some cooling of the ions. [Addition of methane (CH_4) gas at the cathode increased the peak intensity ratio rather significantly (to 1.89) but at the expense of the ion temperature (1.2×10^6 °K). In this experiment the *peak* intensity of C^{2+} λ 2296 A was *doubled*, as was the manifold pressure. The C^{3+} λ 1548 A total line intensity decreased by 30% while the C^{2+} λ 977 A line increased by only 8%; the control line C^{2+} λ 2296 A also increased by only 8% as regards integrated intensity.] Thus, it is not abundantly clear that the short series of experiments giving Fig. 4.35 clarified satisfactorily the importance of the C^{2+} ion to the heating process – it is probable that the doubling of the gage pressure in the methane feed experiments resulted in a drastic cooling of the ions.

A check on the constancy of the doublet intensity ratio of C^{3+} λ 1548–51 A, for the arc currents of Fig. 4.35, gave a ratio of 1.98 (±6%), vs a theoretical ratio of 2.00. We concluded that self-absorption is relatively constant and small with such broad spectrum lines; that is, there is but slight entrapment of resonance radiation in the carbon arc plasma, due primarily to the pronounced Doppler broadening.

In another series of experiments using the standard $\frac{1}{2}$-in.-diam cathode, a crude check of

"ln λ" was made in terms of the electrical resistivity relation of Spitzer.[36] The resistivity, η, of the carbon arc is about 0.001 ohm-cm assuming the arc cross-section area, A, to be defined by the cathode area (the smaller the area the smaller is "ln λ"). Using the spectroscopically determined electron temperature of about 42,000°K, the predicted "ln λ" is 1.0. The uncertainty in A as well as in T_e and η make this estimate rather approximate; however, our revised expression for "ln λ"[37] given elsewhere[35,37] is 1.4, vs the conventional value of 8.6.

4.10.3 Quasi-Resonance Reaction Step

The *excitation-heating* process, previously suggested as a mechanism for generating very energetic ions in the magnetically confined carbon arcs, would be enhanced by an intermediate step which is near-resonance, that is, the excitation exchange step,

$$C^{2+*}(^3P^0) + C^{2+*}(^3P^0) \rightarrow C^{2+}(^1S) + C^{2+}(^1P^0) + 0.28 \text{ ev}, \quad (1)$$

which is then followed by the heating step,

$$C^{2+}(^1S) + C^{2+}(^1P^0) \rightarrow C^{2+}(^1S) + C^{2+}(^1S) + 12.7 \text{ ev}. \quad (2)$$

By analogy with known atomic collision processes,[38] the maximum value of the cross section is expected to occur at $v_{rel} \approx 2b|\Delta E|/h \approx 4.8 \times 10^6$ cm/sec ($E_{max} = 137$ ev or 34 ev per particle for near head-on collisions) for impact parameter (b) ≈ 3.5 A and $|\Delta E| = 0.28$ ev. Inclusion of polarization and partial screening effects for the colliding ions would be expected to change ΔE slightly. A resonance such as (1) can be likened to the resonances observed in the formation of a compound nucleus in nuclear reactions, whereas (2) can be likened to the subsequent decay of a compound nucleus via a different exit channel. Similar resonance-enhanced excitation-heating processes should be expected for the isoelectronic series Be, B^+, C^{2+}, N^{3+}, O^{4+}, etc.; however, (1) the increased Coulomb barrier to the reaction would be expected to inhibit the process for the higher series members in arcs having ions initially at low energy, and (2) the increased $|\Delta E|$ for the higher series members would push the maximum in the cross section to higher energies (e.g., N^{3+} would have a predicted E_{max} of ~430 ev or 108 ev per particle), thus making it more difficult to ignite the excitation-heating process. Thus, the excitation-heating model, though still conjectural, gains further credence as a result of this low-energy resonance.

4.10.4 Metastable Collisions

Previously,[39] we estimated the cross section for the reaction

$$2C^{2+*} \rightarrow 2C^{2+} + 13.0 \text{ ev}$$

to be about 2×10^{-15} cm^2 in order that the overall excitation-heating process offset the strong cooling of ions by the cold electrons. There is some recent experimental evidence regarding collisions between pairs of metastable helium atoms which, although the end products differ, reveals a very large cross section for electron rearrangement.

The ionization of helium in the collision of two mestastable helium atoms has an estimated σv of 5×10^{-8} cm^3/sec according to Tynes,[40] that is, $He^* + He^* \rightarrow He_2^{**} \rightarrow He_2^+ + e$ (or $He + He^+ + e$). The cross section for triplet-triplet deactivation collisions has also been determined[41] as 10^{-14}

---

[36] L. Spitzer, *Physics of Fully Ionized Gases*, Interscience, New York, 1962.

[37] "ln λ" = ln $(1 + x)^2 - 2x/(1 + x)$, where $x^2 = b_{max}\, mv_+^2/2Ze^2$.

[38] J. B. Hasted and A. R. Lee, *Proc. Phys. Soc.* 79, 702 (1962); see also J. B. Hasted, *Physics of Atomic Collisions*, Butterworths, London, 1964. Hasted uses $a = 2b = 7$ A based on many experimental cases.

[39] *Thermonuclear Div. Semiann. Progr. Rept. Apr. 30, 1965*, ORNL-3836, sect. 4.8, pp. 64–66.

[40] A. R. Tynes, thesis, Oregon State University, Corvallis, 1964.

[41] A. V. Phelps and J. P. Molnar, *Phys. Rev.* 89, 1202 (1953).

cm^2 at 300°K. Pakhomov and Fugol[42] report a *rate* one-half as large at 77°K as that of Phelps and Molnar at 300°K, thus indicating the cross section to be essentially the same.

4.10.5 Electron Temperature Considerations

There is some large uncertainty in the experimental choice of T_-, since C^{2+} spectra indicate an excitation temperature of about 30,000°K, whereas C^{3+} spectra give about 60,000°K (see Fig. 4.37). The actual energy transfer rate from hot ions to cold electrons is proportional to Δn_-, which varies as $T_-^{-3/2}$ *for a Maxwellian distribution*; thus, if T_- were 60,000°K the ion cooling rate would drop by about 35%; however, if $T_- = 30{,}000$°K the ion cooling rate would be 66% larger.

[42] P. L. Pakhomov and I. Y. Fugol, *Dokl. Akad. Nauk SSSR* **159**, 59 (1964).

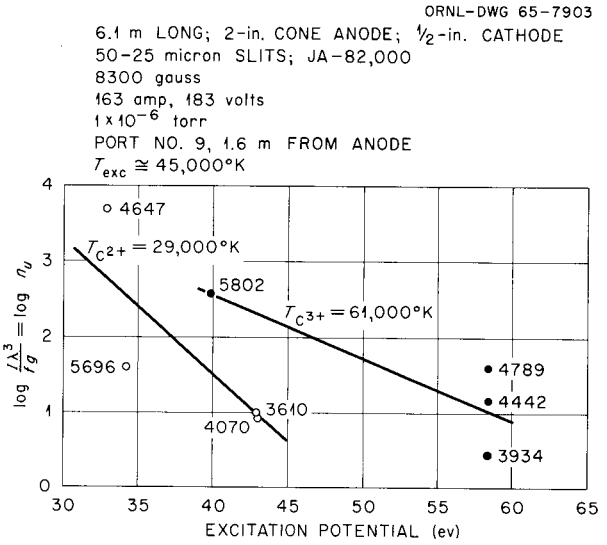

Fig. 4.37. Determination of Electron Excitation Temperature of Energetic Carbon Arc for Spectral Lines of C^{2+} and C^{3+}. Open circles represent C^{2+} lines; black circles represent C^{3+} lines.

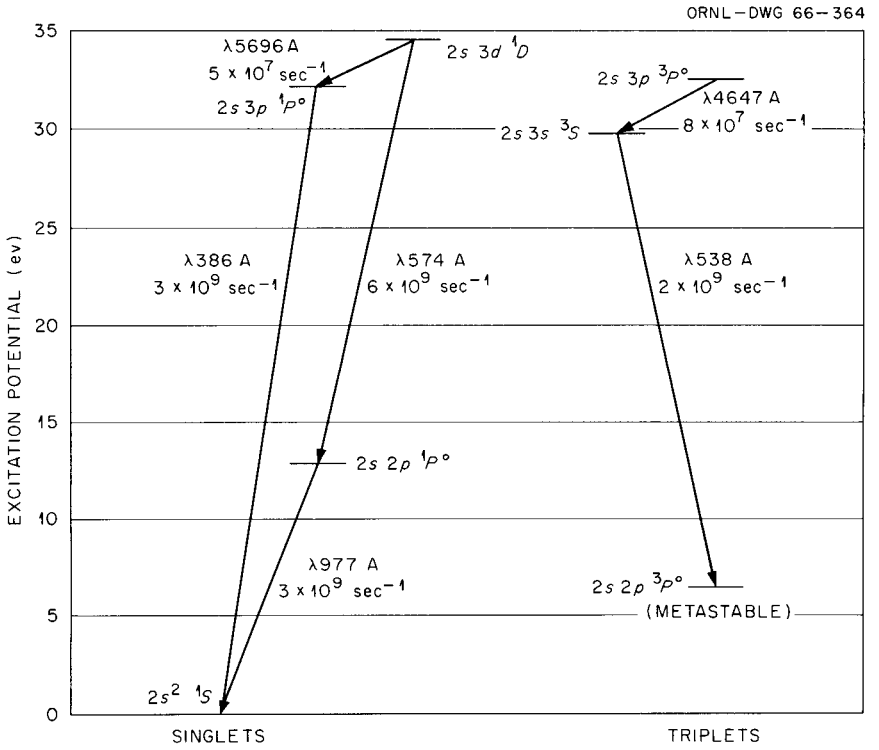

Fig. 4.38. Selected Low Energy Levels of C^{2+} to Illustrate the Effects of Strongly Allowed Transitions in the Preferential Depopulation of Certain Levels in Optically Thin Plasmas.

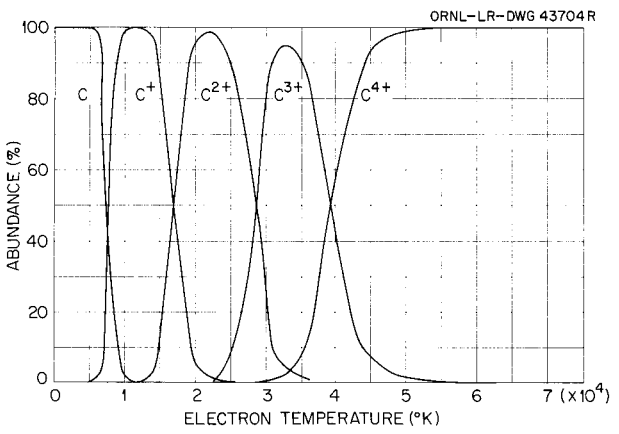

Fig. 4.39. Relative Abundances Predicted by Saha Relation for Carbon Ions as a Function of Electron Temperature for $n_e = 10^{14}$ cm^{-3}.

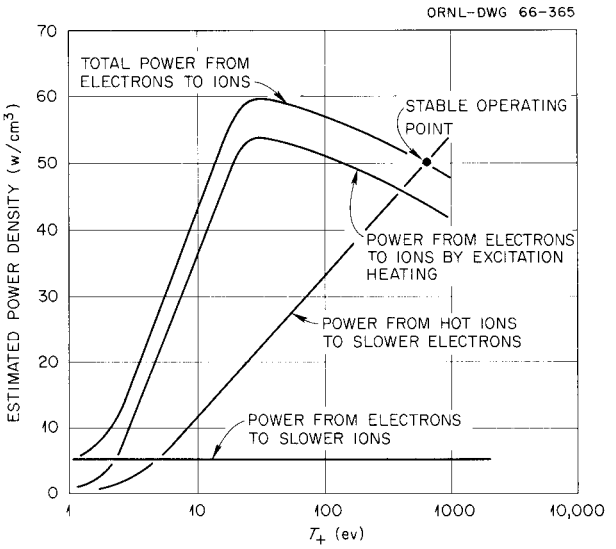

Fig. 4.40. Schema of Power Transfer in Energetic Carbon Arcs. The stable operating point is a function of impurities, history of carbon ions in the arc, scattering losses, etc.

Figure 4.38 illustrates some of the low energy levels of C III (C^{2+}) with pertinent radiative transitions and their computed transition probabilities (A in sec^{-1}). Note that level $2s\ 3d\ ^1D$ is selectively depopulated by λ 574 A at a rate 120 times that of the 5696 A line which was used in the estimation of an electron excitation temperature (see Fig. 4.37). The $2s\ 3p\ ^3P^0$ levels, on the other hand, decay only via the blue triplet group λ 4647–51 A. Similarly, λ 5802 A competes weakly with λ 312 A in depopulating the $3p\ ^2P^0$ levels of C IV (C^{3+}). If the intensities of λ 5696 A and λ 5802 A were increased by appropriate factors (up to 120 and 3000 respectively) to give improved measures of the quasi-equilibrium population density of the upper levels involved, the electron excitation temperature would become only about 18,000°K; however, somewhat smaller upward adjustments should also be made for the intensities of most of the higher transitions as well. In addition, despite the gross Doppler broadening, some compensations should be made for partial imprisonment of the highly allowed transitions. The observed ratio of the resonance line of C^{2+} (λ 977 A, excitation potential = 12.6 ev) to that of C^{3+} (λ 1548 A, excitation potential = 8.0 ev), together with estimated excitation and reflectivity corrections, give $n^{2+} > n^{3+}$ and hence a Saha temperature of the order of 25,000°K (see Fig. 4.39). Obviously, the determination of the electron temperature of optically thin plasmas by the intensities of spectral lines involving very highly excited states merits a more rigorous evaluation than we have attempted here.

Figure 4.38 also illustrates the rapid depopulation of the $2s\ 3s\ ^3S$ level via λ 538 A, which, along with the selective decay of $2s\ 3p\ ^3P^0$ levels via λ 4647–51 A only, may contribute to the lasing properties of the blue triplet.[43]

4.10.6 Conjectures on Ignition of the Excitation-Heating Mode

Figure 4.40 illustrates a schema on the estimated power transfer (per unit volume) between ions and electrons in the energetic carbon arc as a function of ion temperature. The electron temperature is assumed constant at about 40,000°K. The sum of the contributions from the curve for elastic collisions and that for excitation heating ($\frac{1}{2}\ n_+^2 \sigma v$ times 13 ev) for heating ions is selected to intersect the loss curve at 50 w/cm^3 based on estimates given previously ($n^* \approx 3 \times 10^{13}$ cm^{-3} and $\overline{\sigma v} \approx 3 \times 10^{-8}$ cm^3/sec).[39] The maximum in

[43] See R. A. McFarland, *Appl. Phys. Letters* 5, 91 (1964).

the excitation-heating curve is set at about 30 ev (see Sect. 4.10.3), and, since $\overline{\sigma v}$ frequently falls with v, the point (30 ev, 53 w/cm^3) is chosen for this maximum.

Thus, we note that a carbon arc plasma, initially of $T_e \approx T_+ \approx$ (say) 5 ev and having a high density of metastables, will escalate in ion temperature, since the total heating rate for the ions exceeds the loss rate up to quite high ion temperatures. Eventually, an equilibrium will be attained consistent with the average residence time of ions in the arc, the metastable density conditions, the impurity levels, and the exact energy transfer rates.

We further note that, in the example illustrated, the reaction becomes stable at about 500 ev; that is, if the ions heat up too much (1) they are cooled on the cold electrons more efficiently *and* (2) the excitation-heating rate also decreases – and vice versa – thus maintaining a stable operating point for the "burning temperature" of the reaction.

A significant reduction in the density of metastable carbon ions in the arc plasma would lower the excitation-heating rate such that the excitation-heating mode would be insufficient to "ignite" the ion heating process – thus, if n^* drops by a factor of, say, 5, the excitation heating power density drops by 25, and if Fig. 4.40 were valid and not merely schematic in the region $T_+ \approx 5$ to 10 ev, the loss rate to cold electrons would exceed the total heating power and the ions could not escalate to high energy. This interpretation of an "ignition" condition may account for the lack of energetic nitrogen ions in nitrogen arcs (see Sect. 4.10.3).

5. Atomic and Molecular Cross Sections[1]

C. F. Barnett
D. A. Griffin
M. O. Krause
J. A. Ray

5.1 EXCITED ELECTRONIC STATES OF HYDROGEN MOLECULES

In the previous semiannual report we described the existence of highly excited electronic states of H_2 as being analogous to the hydrogen atom. These states are formed by the electron capture of H_2^+ passing through a gaseous medium. A simple picture consists of a single high-quantum orbital electron plus an H_2^+ core. This can be shown theoretically if one solves the Schrödinger equation and neglects the orbital electron interaction with the core electron; then the solution reduces to the hydrogen atom solution, in which the orbital electron radius varies as n^2, the principal quantum number.

This concept led to the prediction that H_3^+, on passing through a gas, would also capture an electron in a similar manner. Previous theoretical investigations have indicated that H_3^+ is a tightly bound molecular ion forming a triangular structure with a binding energy in excess of 5 v. Also, it is well known that the ground electronic state of H_3 is a repulsive state and therefore unstable. Experimentally, the procedure was similar to that used previously. A 50-kev H_3^+ ion beam from the accelerator was passed through a differentially pumped gas cell. Particles emerging from the collision chamber passed through an electrostatic field in which the charged particles were removed. The neutrals were detected by a suitable energy-sensitive detector.

Both dissociative and capture collisions occurred in the gas cell. The H_3^+ particle dissociated in either of two modes,

$$H_3^+ + H_2 \longrightarrow H_2^+ + H^0 + H_2 \qquad (1)$$

or

$$H_3^+ + H_2 \longrightarrow H_2^0 + H^+ + H_2 \,. \qquad (2)$$

The H_3^+ could capture an electron into a stable excited state,

$$H_3^+ + H_2 \longrightarrow H_3^* + H_2^+ \,, \qquad (3)$$

or into a repulsive state with the subsequent dissociation

$$H_3^* \longrightarrow H_2^0 + H^0 \,. \qquad (4)$$

In reactions (1), (2), and (4), internal potential energy is converted into kinetic energy of the reaction fragments, giving rise to a divergence angle in the laboratory frame of reference. Both a proportional counter and a silicon surface-barrier detector were used to measure the neutral components. The entrance aperture of the proportional counter was a vertical slit 0.001 by 1 in. which was used to scan across the beam. The pulse height or energy spectrum contained two groups of particles – the H^0 at one-third of the initial H_3^+ energy (E_0), corresponding to reaction (1), and the H_2 particles of $\frac{2}{3}E_0$, from reaction (2). In addition to these two components of the neutral beam, a small group of particles was found at full energy. This group consisted of any stable excited H_3^* formed from reaction (3) or the sum of H_2^0 and H^0 formed in reaction (4). The H_2^0 and H^0 from repulsive states of H_3 and from scattering either in the vertical direction of the slit or in the forward-backward direction will arrive at the detector in coincidence. Thus, there will be a summing of the H_2^0 and H^0 energy, giving rise to an equivalent pulse of full energy.

The proportional counter was replaced with a silicon surface-barrier detector with a larger areal

[1]AEC activity No. 05 07 04 01 0.

extent such that the fraction of particles found at full energy should increase due to the larger summing coincidences of H_2^0 and H^0 in reaction (4).

The results from these experiments can be summarized as follows: (1) the maximum fraction of H_3^+ that captures an electron into all states was less than 1%; (2) the number of neutral particles with full E_0 was a factor of 10 greater for the silicon detector than for the proportional counter, indicating that most of the capture collisions are into repulsive states; (3) if the assumption was made that H_3^* was one-tenth of the total neutral yield with energy E_0, then the H_3^* beam intensity was too small to measure the population of excited states by ionization in an electric field. The fact that less than 1% of the H_3^+ particles capture an electron was surprising, since both H^+ and H_2^+ readily undergo electron capture collisions at equivalent velocities. The present data seem to indicate that, if any capture collisions take place to stable electronic levels of H_3, then the collision cross section is very small. Further experimental evidence must be accumulated to confirm the hypothesis that stable excited states of H_3 exist.

5.2 ENERGY-DISPERSED ATOMIC HYDROGEN BEAMS

During the past few years evidence has been accumulating to indicate that some of the microinstabilities observed in magnetic-mirror-confined plasmas could be avoided by injecting an energy-dispersed beam.[2] Several techniques are available for producing beams with an energy distribution; however, we chose to investigate the parameters controlling conversion of protons and H_2^+ into energetic H^0 in a decelerating gas cell. Shown in Fig. 5.1 is a schematic diagram of the apparatus. The 50-kev H^+ beam from the accelerator was collimated by an 0.008-in.-diam aperture. The gas cell consisted of an 11-electrode structure, which was used previously as a section of a proton accelerator tube. A linear decelerating field was provided across the gas cell by applying a positive 40-kv potential to the exit electrode with a resistive divider network connecting the other electrodes. Argon gas was admitted to the collision chamber. Ions were deflected from the exit beam by a transverse electric field, and the energy spectrum of the neutral particles was detected by a proportional counter. Since counting techniques were used to measure the energy spectrum, the input current to the gas cell was restricted to less than 10^3 counts/sec, and the minimum proton exit energy was restricted to 10 kev.

The conversion efficiency (the ratio of H^0 to input H^+) is shown in Fig. 5.2 as a function of the cell pressure. The behavior of the retarding-potential cell was similar to a standard conversion cell in that the efficiency increased as the pressure increased. Equilibrium conditions, or a conversion efficiency of 40%, were obtained at a pressure of approximately 10^{-3} torr in a gas cell 74 cm long. The H^0 energy distribution could be changed by varying the gas pressure or shifting the potential distribution across the electrodes. In Fig. 5.3 is plotted the energy distribution of a beam of H^0 obtained from the 50-kev proton beam in argon gas. Plotted is the counting rate per energy interval as a function of the particle energy. Shown also for reference is the energy spectrum obtained for a 50-kev proton beam, with no attempt made to normalize the area under the curves. This near-uniform distribution was obtained for a gas cell pressure less than that required for maximum conversion efficiency. Increasing the gas cell pressure to maximum conversion efficiency redistributed the particle energy, as shown in Fig. 5.4. The peak occurring at 10 kev was due partially to gas streaming out the exit end of the gas cell, which increased the effective path length for the low-energy ions before conversion to neutrals.

The scanning slit of the proportional counter was used to measure the angular divergence of the neutral beam. This divergence (defined as the width of the beam to include more than 99% of the particles) was found to be 3.5 milliradians, or in more practical application terms, a $\frac{1}{2}$-in.-diam beam entering and leaving a similar gas cell would spread to $\frac{3}{4}$ in. diameter at 6 ft from the entrance aperture.

Some preliminary work with 50-kev H_2^+ ions incident on the gas cell aperture indicated a conversion efficiency of 45% at an argon pressure of 2×10^{-4} torr and with the same 40-kv retarding potential. This efficiency was less than expected, but probably results from increased

[2]For a timely example, see sect. 1.3 of this report.

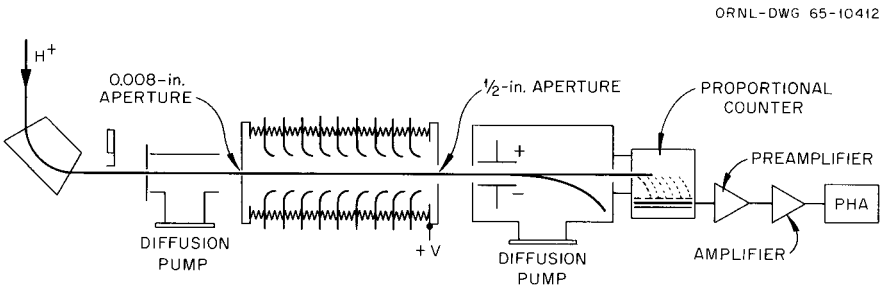

Fig. 5.1. Schematic Diagram of Apparatus Used to Produce an Energy-Dispersed Beam of H^0.

scattering of particles in the low-energy region. Gas cell pressures greater than 2×10^{-4} torr yielded lower conversion efficiency. Shown in Fig. 5.5 is the energy spectrum obtained for a 50-kev H_2^+ beam at a conversion efficiency of 15%. The small fraction of neutrals in the energy region 25 to 50 kev is due in part to the electron-capture formation of H_2 neutrals. Competing processes of electron capture and dissociation result in a filling in of the energy distribution down to thermal energies with an applied 40-kv retarding potential. For energies less than 3 kev the proportional counter resolution was not reliable; however, the pileup of low-energy particles was real and not a result of counter noise. Increasing the gas cell pressure to 2×10^{-4} torr partially depletes the low-energy spectrum due to increased particle scattering at the higher pressures. The divergence of the neutral beam with H_2^+ incident was 8.0 milliradians.

Deceleration of a positive ion beam in a gas cell poses a serious problem, since entrance and exit apertures act as aperture lenses. If the decelerating field is made a function of distance along the beam axis such that the entrance lens focal length is equal to the exit lens focal length, then the focusing effects at the two ends will cancel out. The necessary condition is that

$$\frac{E(x)}{V(x)} = \text{constant} ,$$

where $E(x)$ and $V(x)$ are the axial field and potential, respectively, at a point x on the axis.

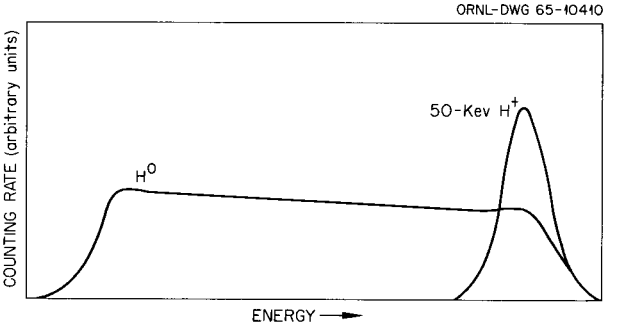

Fig. 5.3. Energy Spectrum of H^0 Produced from Incident 50-kev H^+ in an Argon Gas Cell at Low Pressure.

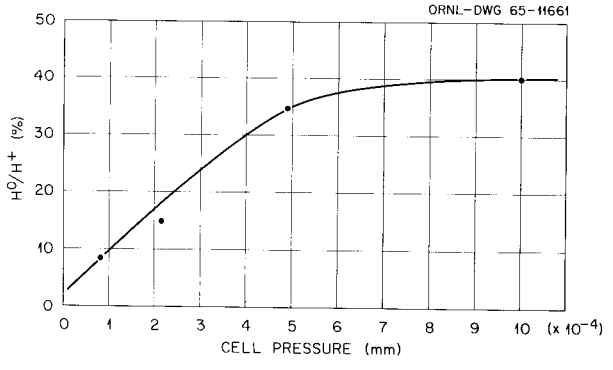

Fig. 5.2. Conversion Efficiency of Argon Gas Cell for 50-kev Protons.

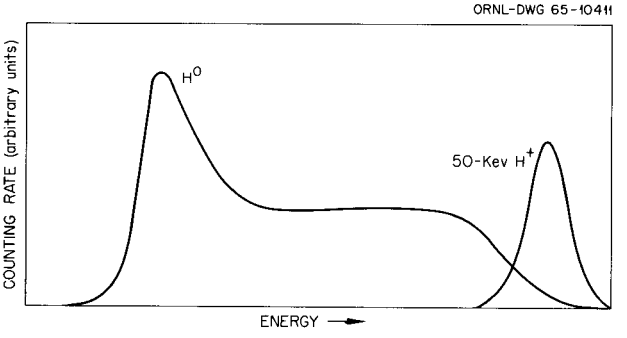

Fig. 5.4. Energy Spectrum of H^0 Produced from Incident 50-kev H^+ in an Argon Gas Cell Operating at a Pressure of 10^{-3} Torr.

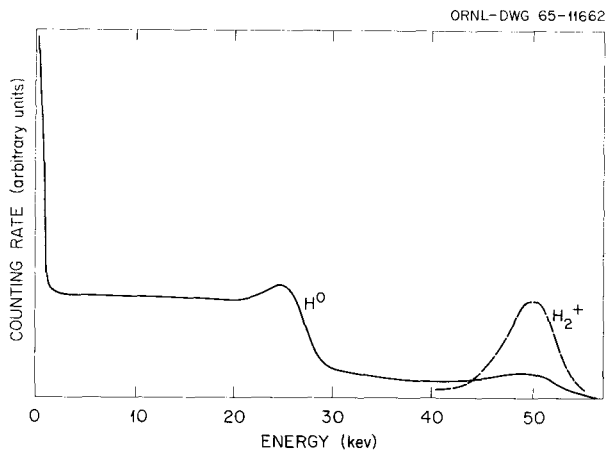

Fig. 5.5. Energy Spectrum of H^0 Produced by H_2^+ in a Retarding-Potential Argon Gas Cell. Between 25 and 50 kev there is a contribution from H_2^0 formed by simple electron capture.

The solution of this simple equation is the well-known exponential, $V(x) = ae^{-bx}$. A potential divider was constructed such that a decreasing exponential potential could be applied across the cell electrodes. With the exponential potential drop the maximum conversion efficiency of 50-kev H^+ decreased to less than 10%. The application of the exponential-type field is valid only for ions entering and leaving a region with two apertures. Neutrals formed in the diverging section of the particle path in the gas cell struck the boundaries of the exit aperture, thereby decreasing the conversion efficiency. We have concluded that linear fields are superior to exponential fields for the electrode geometry used in these experiments.

With proper care in choosing gas cell parameters, it is feasible to produce an energy-dispersed neutral beam for injection into a magnetic configuration. Still unanswered are the effects of large beam currents producing ionization and consequent breakdown in the gas cell.

5.3 MEASUREMENT OF KINETIC ENERGIES OF H^+ AND H^0 FOLLOWING DISSOCIATION OF H_2 BY ELECTRON IMPACT

Several observations[3] indicate that the Franck-Condon principle may sometimes be violated in the dissociation of the H_2 molecule. To test this possible deviation from the Franck-Condon principle, we have designed an apparatus which will allow measurement of the H^+ and H^0 recoil energies and thus the H_2 dissociation energies for the following reactions:

$$H_2 \longrightarrow H^+ + H^+ , \quad (1)$$

$$H_2 \longrightarrow H^+ + H^0 , \quad (2)$$

$$H_2 \longrightarrow H^0 + H^0 . \quad (3)$$

The hydrogen molecule will be excited by electrons of energies up to several kilo-electron volts, and the kinetic energy of the fragments will be determined by their flight time over a 5-cm distance. Following energy analysis, the particles will be identified by mass analysis in a 50-cm-long flight tube. In the case of charged particles the experiment is straightforward; however, for neutral particles a second ionization ($H^0 \rightarrow H^+$ after energy analysis) is necessary to make mass analysis and detection feasible.

For all energies of the primary electrons, except for electrons below about 50 ev, all three reactions take place according to the partial cross sections of reactions (1) to (3). To distinguish the reactions, the combined energy and mass analyzer (Fig. 5.6) is operated in the following modes:

1. Protons detected by electron multiplier PM II in coincidence with protons detected by PM I and with electron gun II off. Only protons of reaction (1) are recorded.
2. PM II in anticoincidence with PM I and gun II off. Protons of reaction (2) are displayed.
3. PM II in anticoincidence with PM I and gun II on. Neutral hydrogen atoms of reaction (3), converted into H^+ by electrons from gun II, are measured.

The expected low count rate for particles from reaction (3) makes it mandatory to operate the system automatically. Briefly, the time interval from 0.8 to 20 μsec after pulsing electron gun I is scanned randomly by triggering electron gun II

[3] R. Caudano *et al.*, *Ann. Soc. Sci. Bruxelles* **76**(III), 127 (1962); F. P. G. Valckx and P. Verveer, *IV Intern. Conf. Phys. Electron. At. Collisions, Quebec, 1965*, 333 (1965).

ORNL-DWG 66-366

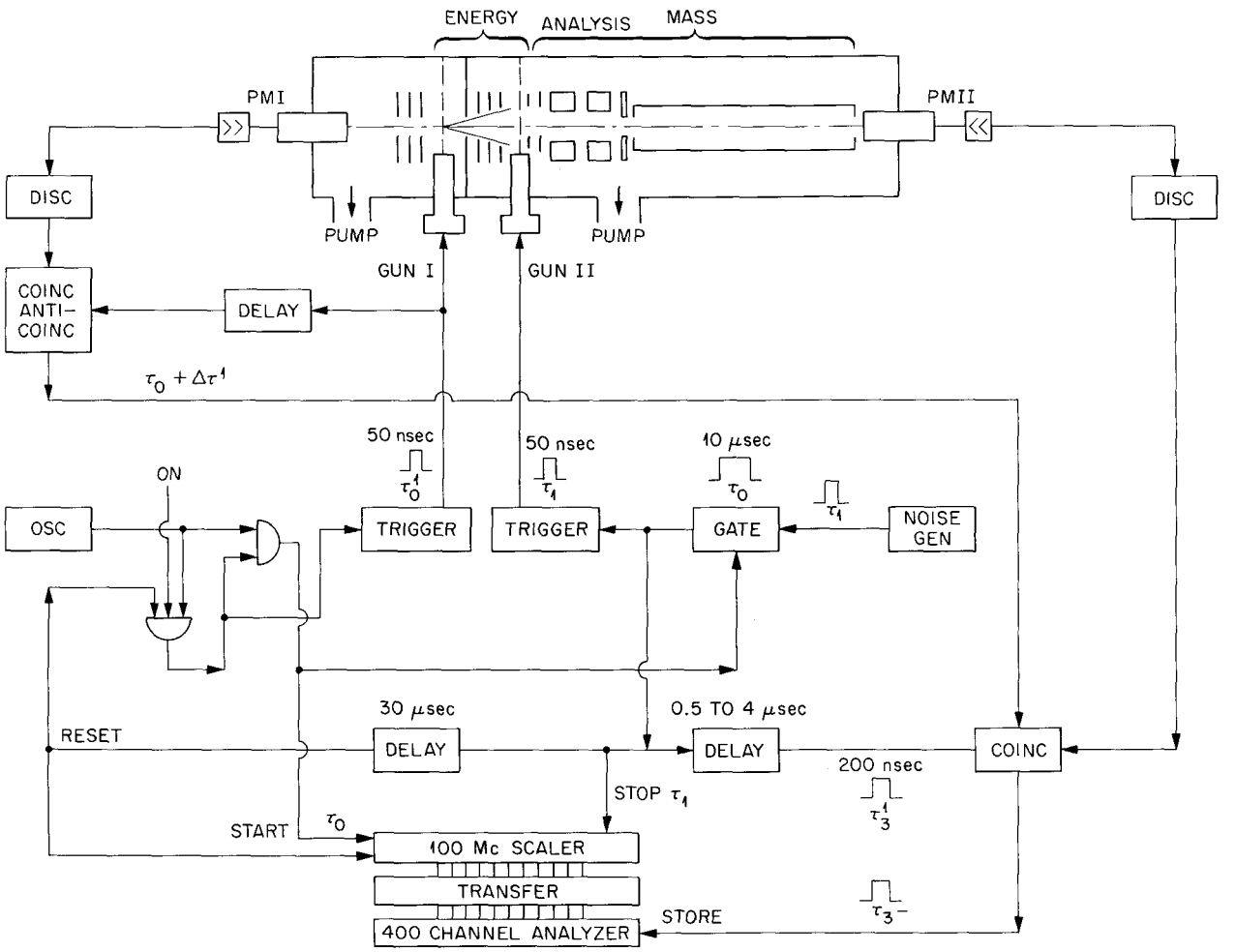

Fig. 5.6. Schematic Diagram of Time-of-Flight Energy and Mass Analyzer.

from a noise generator providing a white spectrum. This time interval corresponds to particles with kinetic energy from 20 to 0.3 ev. At the moment of firing gun II, the channel advance of a pulse-height analyzer's memory core started by gun I is halted and prepared to store a potential event, namely, a signal from PM II, placed in delayed coincidence with the trigger signal of gun II. This procedure is repeated every 50 to 100 μsec, so that fluctuations and drifts in gas pressure and outputs of the electron guns become immaterial. In particular, any protons produced from background gas in the ionization region of gun II will be distributed evenly over all channels of the memory core. The mechanical features have been fabricated and assembled, and the electronic components are being put together.

5.4 SILICON BARRIER DETECTORS FOR LOW-ENERGY PARTICLES

Main emphasis during this period has been placed on reducing the noise level of the silicon surface-barrier detector and associated electronics. The field-effect transistor preamplifier was mounted in close proximity to the silicon detector, and both were cooled with liquid nitrogen. Engineering modifications in the detector and preamplifier mounting have decreased microphonic noise until the noise width at optimum temperatures and zero input capacitance is 1.48 kev in silicon. The detector pulse width (full width at half maximum amplitude) is plotted as a function of the preamplifier temperature in Fig. 5.7. The detector temperature was always within a few degrees of

the preamplifier temperature. Two determinations are plotted, 50- and 40-kev protons. Best resolution was obtained in the temperature range –100 to –130°C.

Shown in Fig. 5.8 are several pulse-height spectra obtained from protons whose energies varied between 10 and 40 kev. For energies less than 10 kev, the pulse spectrum was shifted down into electronic noise with a peak-to-valley ratio of 1 for 7-kev protons. An inflection point was still prominent in the pulse-height spectra for 6-kev protons. By the use of simple noise subtraction techniques, the particle response was easily distinguishable from the electronic noise with the resolution remaining constant throughout the range of proton energies. The optimum peak width for protons was 2.75 kev, obtained when both the preamplifier and detector were at a temperature of approximately –120°C. The output pulse height is shown as a function of proton energy in Fig. 5.9. The reproducibility of the data is about that shown by the scatter of the data at 20, 30, and 40 kev. The best-fitting straight line through the experimental data indicates zero output at a proton energy of 500 ev, suggesting that this value is the energy loss in the dead layer provided by the gold layer and any region between the gold layer and the depletion region in the silicon. The intercept can be shifted a few hundred electron volts by a slight change in the slope of the curve in Fig. 5.9.

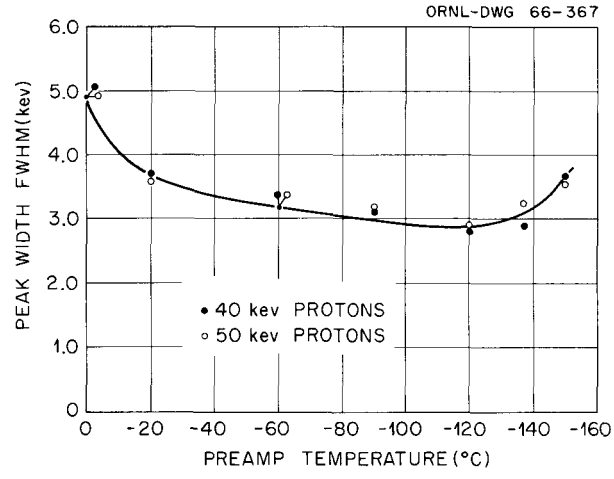

Fig. 5.7. Peak Width of a Silicon Surface-Barrier Detector for Protons as a Function of the Preamplifier Temperature.

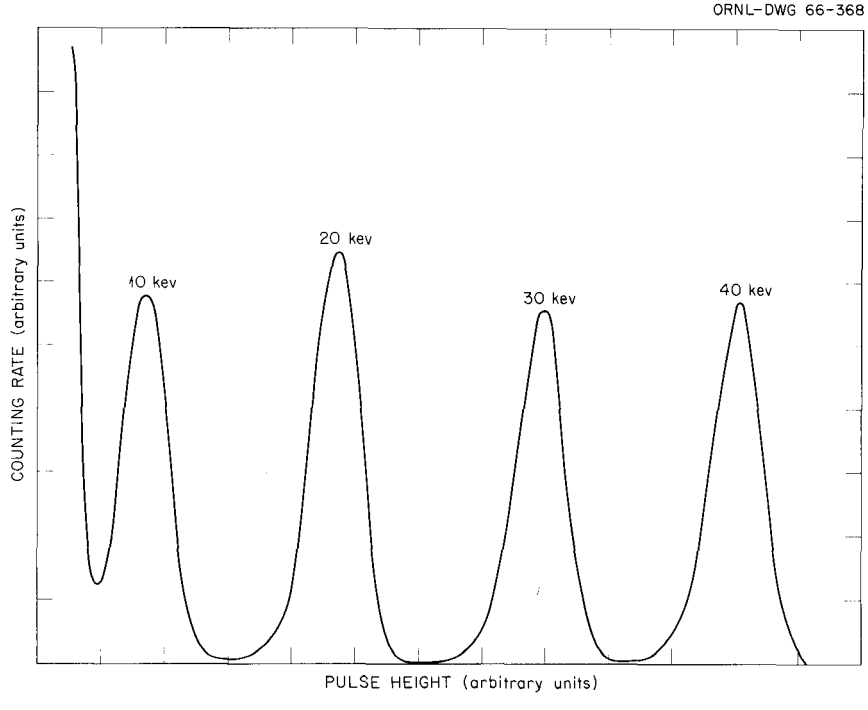

Fig. 5.8. Energy Spectra of Silicon Surface-Barrier Detector for Low-Energy Protons.

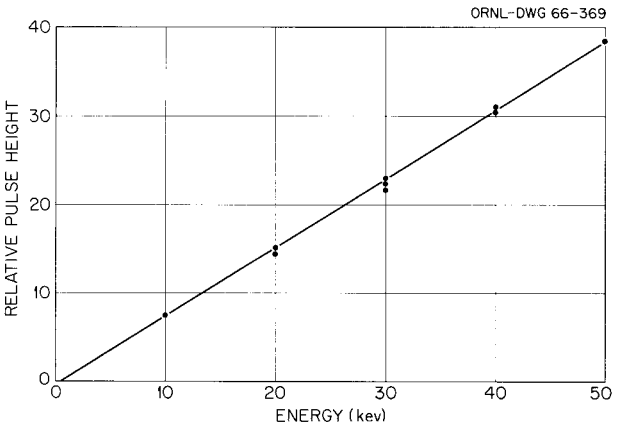

Fig. 5.9. Pulse-Height Linearity of Silicon Surface-Barrier Detector Used in Detecting Protons.

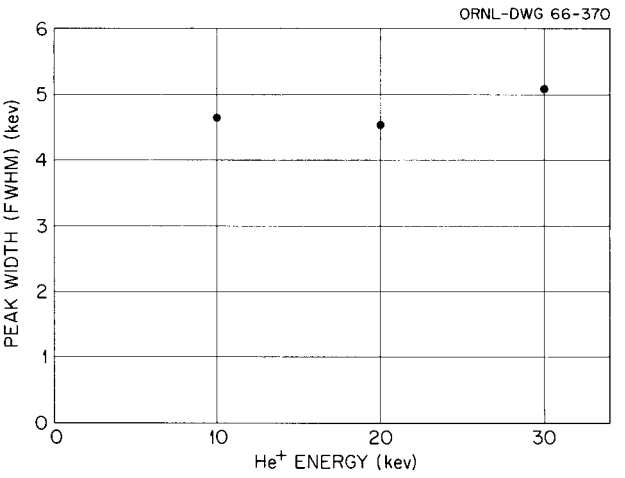

Fig. 5.10. Peak Width of He^+ Ions as a Function of Energy.

To determine if crystal channeling existed as the protons passed through the gold layer, the silicon detector axis was rotated about the direction of the beam. One would expect that a rotation of 1 to 2° would produce a noticeable change in the position of the peak pulse height if channeling was present. No changes were detectable in the peak pulse-height position for 10-kev protons as the detector swept through an angle of ±3°. By rotating the detector through larger angles, the energy loss in the gold foil can be determined by measuring the displacement of the peak pulse height as the effective thickness increases with decreasing angle of incidence. The average energy loss in the 50-$\mu g/cm^2$ gold foil was 190 ev. These results vividly illustrate the small energy loss of low-energy protons passing through metallic foils.

The use of silicon barrier detectors was extended to heavier particles. The peak width of the detector for incident He^+ ions as a function of the ion energy is shown in Fig. 5.10. The resolution is, and remains, approximately constant for helium ion energies between 10 and 30 kev. The output pulse height as a function of energy is shown in Fig. 5.11. Extrapolation to zero output indicates no energy lost by the helium ions passing through the foil, indicating again that the intercept does not accurately determine the energy loss in the dead layer. The valley-to-peak ratio of the pulse spectra for 10-kev He^+ was 0.7. Measurements with N^+ ions resulted in resolution of pulses down to 15 kev, where the valley-to-peak ratio

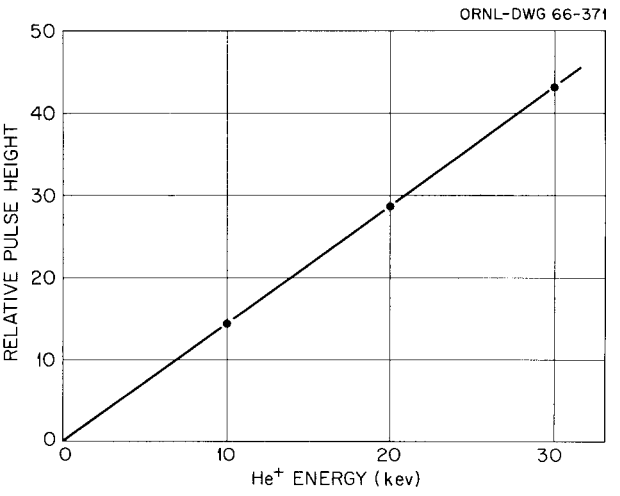

Fig. 5.11. Pulse-Height Linearity of Silicon Surface-Barrier Detector Used in Detecting He^+ Ions.

was 0.9. Evidently, thinner windows are necessary if the silicon barrier detector is to be used as a heavy-particle detector.

5.5 THERMAL DETECTORS

Further work has been done to determine the fast time response of a $BaTiO_3$ crystal to H^0 particles. Barium titanate is in the class of pyroelectric materials which undergo a spontaneous polarization when heat is absorbed on one

face of the crystal. This change in polarization gives rise to a polarization current whose magnitude is directly proportional to the incident radiation. A crystal was placed into DCX-1, and 300-kev H^0 from the plasma impinged on one of its faces. For low input power of the order 10^{-4} w/cm^2, the crystal exhibited a nonlinear response in that the signal was differentiated. Increasing the power or the number of particles striking the face by an order of magnitude eliminated the differentiation, and the output time response of the crystal followed the pulsed beam. The reason for this nonlinear behavior is unknown at present. The measured response time of the crystal, still limited by the amplifier, was approximately 1 msec. Since $BaTiO_3$ is also piezoelectric, the oscilloscope trace exhibits large microphonic noise due to mechanical vibration of the machine.

5.6 ATOMIC AND MOLECULAR PROCESSES INFORMATION CENTER

In August the first Information Center Bibliography was issued as AMPIC-1 (1963). This annotated bibliography contains references and titles for literature searched during the year 1963. In answer to numerous requests for a listing of scientific personnel engaged in the field of electronic and atomic collision physics, an International Directory (AMPIC-2) has been compiled and published. The second bibliography, AMPIC-3 (1964), has been completed and is now being printed.

Final plans are materializing for the first of the the Information Center's evaluation and reviews. The topic will be *Ion-Atom Interchange Reactions* and will be published in the form of a monograph by a commercial publisher. The following have consented to be co-authors of the first monograph: Drs. Earl W. McDaniel, Georgia Institute of Technology; E. Ferguson, NBS Laboratories, Boulder; L. Friedman, Brookhaven National Laboratory; and A. Dalgarno, Queen's University, Belfast. These authors will be under contract to the Information Center to supply the review, after which the Information Center will act as editor and intermediary with the publishers. Present plans are to publish two monographs per year, with the next topics to be *Ionization and Excitation by Heavy Particles* and *Particle Interactions with Electric and Magnetic Fields.*

Our journal search has been extended to include 73 journals and 5 abstract journals. Most of the major journals have now been searched back to 1950 and await further review and classification. Our indexing or classification scheme has now progressed to the point at which we obtain approximately 85% agreement among various members of the technical staff. Our personnel has grown during this report period to include six university scientists under part-time contract and five members of the Health Physics Division, spending 10 to 20% of their time on reviewing and searching the literature. In addition, our own Division now has four members engaged in part-time activities.

A large fraction of our time has been spent on the storage and retrieval problem. Our present conceptual design of the system can best be summarized in two parts: part I, the semiautomatic steps of printing bibliographies directly from a computer in a reproducible form, and part II, the computerized retrieval of information. Shown in Fig. 5.12 is a flowsheet of the various operations involved in the storage and retrieval system. The literature is searched by the technical staff, and the pertinent references are keypunched directly onto computer cards. The cards are sorted and printed out in the form of a working bibliography. This printout is assigned to specialists who read the papers, make preliminary evaluations, index each paper into its proper classification, and note other needed information such as reactants, particle energy regions, etc. This information is punched onto the original reference card, which is printed out in a form suitable for reproduction. Also, the information contained on the cards is transferred to magnetic tape for retrieval by title words or combination of terms, categories, reactants, authors, or any combination of these.

At periodic intervals, the papers will be reassessed or reevaluated. References containing useful data will have the data extracted from the graphs by automatic analog-to-digital conversions. The digital output from this system will be placed on magnetic tape and plotted out in desired units. These graphs and tabulations will be filed in hard copy with the original paper to await the reviewer.

One hundred references were used in a test run to substantiate our ideas on information storage.

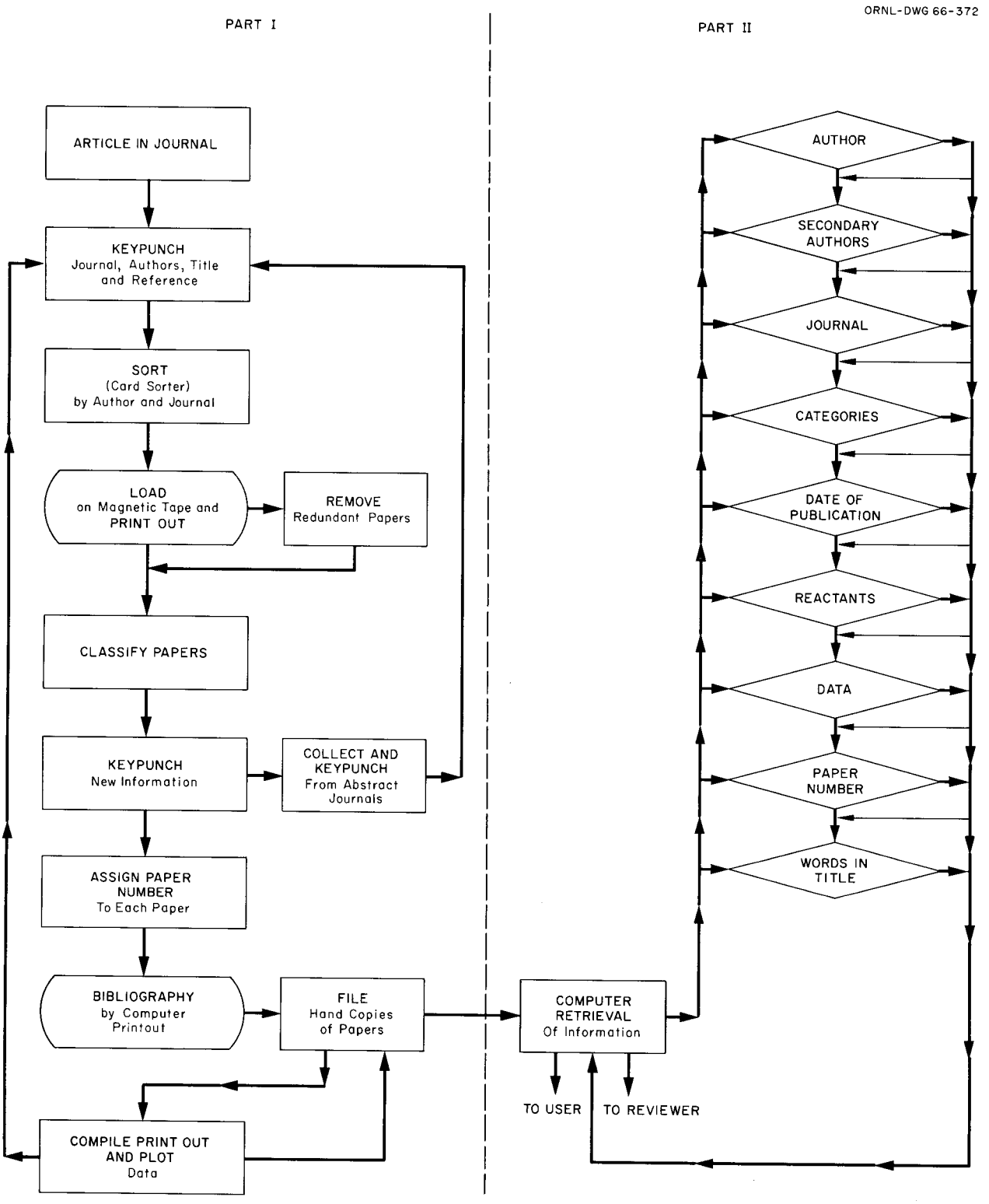

Fig. 5.12. Flowsheet for AMPIC Computer Storage and Retrieval of Information.

All phases of the operations were completed except using the card sorter; this step was replaced by manual methods. Our second tests consist of 7000 punched cards as a data base. Information has been entered on these cards, and we are delayed by the manufacturer in providing an attachment for the card sorter. The data in each journal paper will be contained on many punched cards, with the first card to have a fixed field and the subsequent trailer cards to have an open field. A special brush attachment added to the sorter will allow us to sort by using only the first card. In the meantime, the program for information retrieval is being written.

6. High-Current Ion-Beam Production and Injection

R. C. Davis G. G. Kelley R. F. Stratton
R. R. Hall O. B. Morgan G. M. Babler[1]

The performance of the intense H^+ beam facility developed during the previous report period[2] has been investigated in greater detail. In Fig. 6.1, the beam available (main target current) is indicated as a function of energy for various aperture sizes and total beam currents. The aperture was located 120 cm from the lens, with the beam first passing through a 6-cm aperture located at 30 cm and a 3-cm aperture at 60 cm. The reason for restricting the total beam to less than the maximum available, 900 ma at 70 kev, was thermal problems on the particular targets being used for these dc beam conditions. Better targets could have been built, but for the presently proposed application of this device this information is very adequate. This device is now being installed on DCX-2 for injecting a beam at an angle such that it will just pass through one of the magnetic mirrors. From present DCX-2 data there is evidence of intense electric fields at the proton cyclotron frequency which are perpendicular to the axis. It is hoped that these fields will produce enough energy spread in the injected proton beam to trap a significant fraction of it. The desired injecting energy will be 70 kev or greater, and since the necessary beam collimation will probably be less stringent than that imposed by the 3-cm aperture located at 120 cm in Fig. 6.1, hundreds of milliamperes of H^+ ions should be available for injection.

A new vacuum system has been built and installed on the 100-kv test stand. It was designed to provide a longer beam drift space and to facilitate more detailed beam studies. It has the increased pumping speed needed for a 1-amp beam and neutral beam work. The new facility, Fig. 6.2, allows a beam drift space of ≈240 cm. The vacuum system consists of three PMC-4100 diffusion pumps charged with Silicone 705 oil, Freon-cooled baffles, and a titanium filament evaporation system used to supplement the hydrogen pumping during various experiments. The system is not bakeable and now has a base pressure of $\approx 3 \times 10^{-7}$ torr.

One of the basic problems with the 600-kev DCX-2 injector has been the limitation of the ion source in the production of a large percentage of H_2^+ ions in the beam in the total current range above 100 ma. This is evident from the fact that, although 350 ma of a 600-kev hydrogen beam has been obtained on the test stand, only 96 ma of this beam was H_2^+. The elimination of this restriction has been one of the major efforts of the group during this report period. The goal was an ion source that could be utilized at the 600-kv terminal of our present accelerator, without a major modification, which would produce an intense H_2^+ beam of sufficiently high quality to pass through the DCX-2 duct.[3] It was found that simple scaling of the duoplasmatron ion source did not result in increased molecular ion current. During the period in which the new 100-kv facility was being installed, a temporary ion source experiment was used to pursue this problem. First, multiaperture discharges were operated by using a common

[1]Summer participant, University of Missouri.

[2]*Thermonuclear Div. Semiann. Progr. Rept. April 30, 1965*, ORNL-3836, pp. 74–80.

[3]*Thermonuclear Div. Semiann. Progr. Rept. April 30, 1964*, ORNL-3652, p. 86.

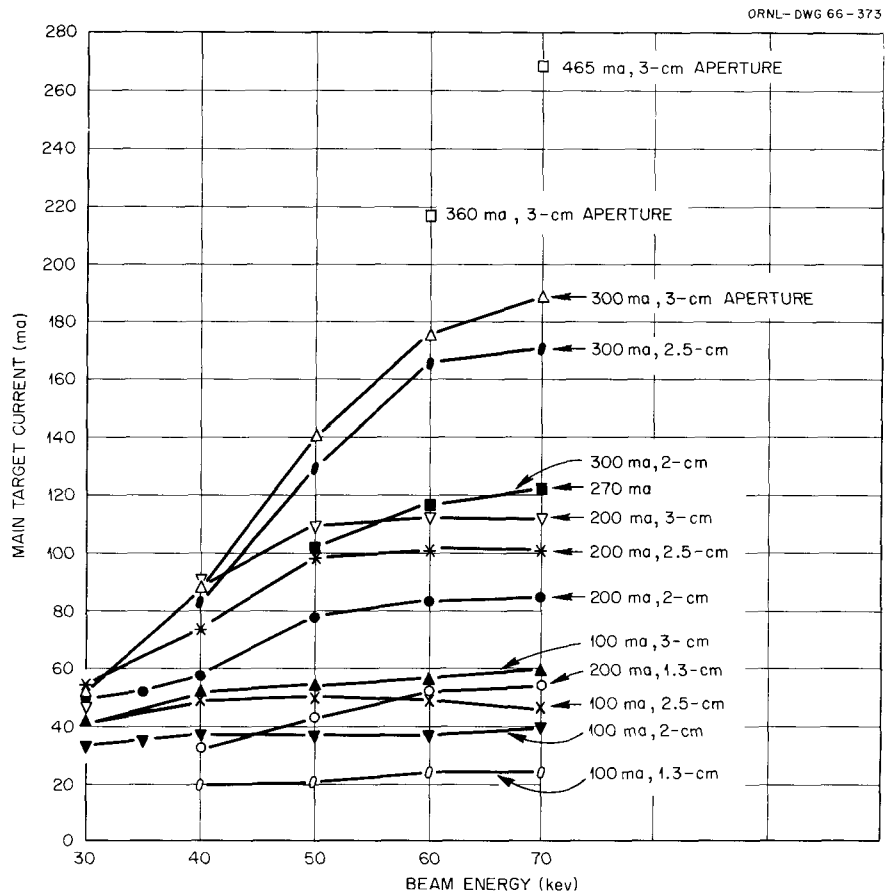

Fig. 6.1. H^+ Ion-Beam Current Available Through Apertures of Various Diameters Located 120 cm from the Lens as a Function of Beam Energy for Various Total Extracted Currents.

filament with individual apertures in the intermediate electrode and anode of a duoplasmatron. Stable operation of up to seven of these discharges was obtained using an all-copper ion source.[4] Later these sources were used on the new 100-kv test stand, where some improvement in H_2^+ production was found (150 ma from a total beam current of 300 ma). The gas efficiency was very poor, and beam extraction from this source in a 600-kv accelerator probably would not be feasible. There remains a good possibility that this source would yield a desirable plasma for a system using an expanded surface area for ion extraction.

The temporary test stand was also utilized in an attempt to evaluate and study the problem of molecular ion production by using a spectroscope to monitor the ratio, R, of the intensities of the H_2^0 4634-A and H^0 4340-A lines in the discharge region as a function of various source parameters. That the variation in the ratio of atomic to molecular neutrals had some correlation to the problem was established by monitoring the change in this ratio while varying some of the source parameters found critical in earlier experiments, where actual ion extraction and analysis were performed. For example, Fig. 6.3 shows the variation of R as a function of the source arc current for the same source pressure and for two intermediate electrode to anode spacings of a standard duoplasmatron. These results agree qualitatively with those actually found by analyzing the beam from this type of source. This system was then used to evaluate attempts to vary the recombination of H^0 atoms by varying the surface material and temperature in the critical region of the source.

[4] *Thermonuclear Div. Semiann. Progr. Rept. April 30, 1965*, ORNL-3836, p. 79.

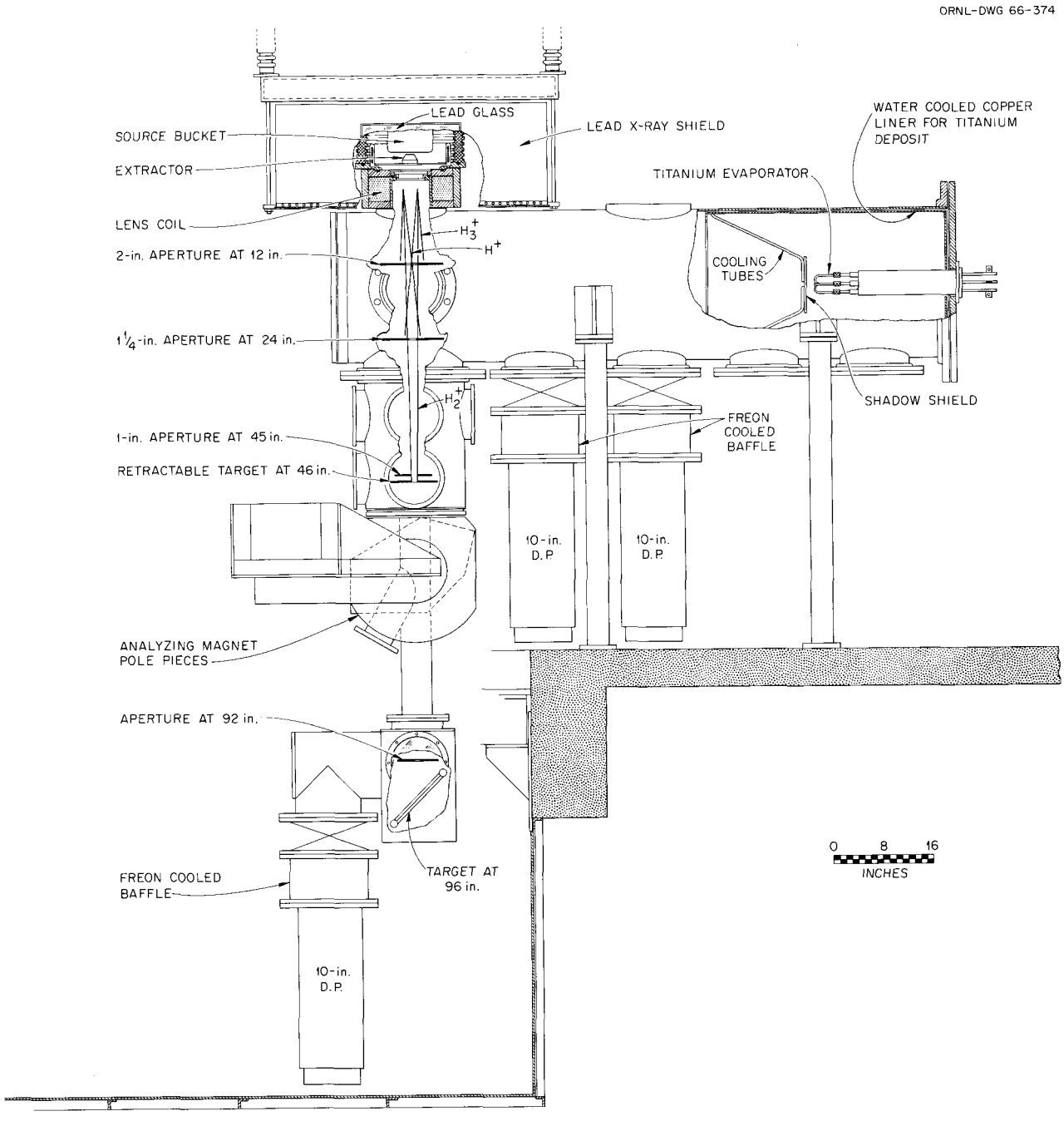

Fig. 6.2. New 100-kv Test Stand with Increased Pumping Speed.

The ratio R was found to depend very weakly on these parameters, and in later checks by beam analysis from two of these same sources the same negative results were discovered.

Variation of the density and energy of the electrons in the source by incorporating a fourth electrode in the duoplasmatron was tried on the new 100-kv test stand. This copper electrode was placed after the anode with plans to vary it from anode to cathode potential. The system was so unstable in the low-pressure region, where molecular ion production would be favored, that it was hard to evaluate. The solution to this low-pressure unstable operation was the incorporation of an

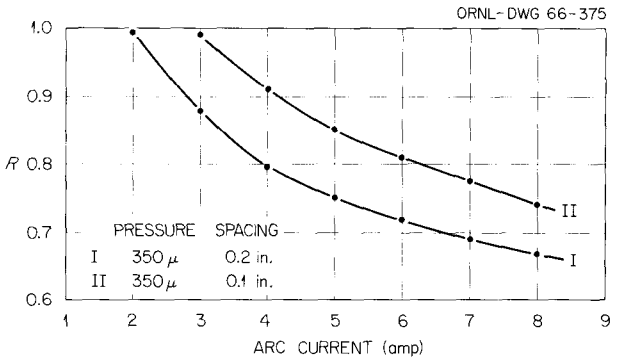

Fig. 6.3. Variation of R, Where R = 4634 A/4340 A Line Intensity Ratio Plotted as a Function of Arc Current for Two Intermediate Electrode to Anode Spacings.

electrode arrangement like that described by Poroshin *et al.*[5] A simplified and scaled-down version of this source, which could possibly be referred to as a plasma-fed PIG source, is shown in Fig. 6.4. The source was simplified and reduced in size primarily to adapt it for use on the 600-kv terminal of the accelerator. It is now ready for testing. A second version of this source, which is incorporated into the beam extraction and focusing system developed earlier for intense 30- to 70-kev H^+ beams, is shown in Fig. 6.5. The ability of this source to produce intense H_2^+ beams is indicated by the following preliminary results with the 100-kv test stand:

Total Beam (ma)	H_2^+ (ma)	Energy (kev)	Percent H_2^+
172	135	60	78.5
252	164	60	65

This source has the electrode aperture cross sections reduced to 40% of those used by Poroshin and Coutant but delivers beams with similar H_2^+ yields as the larger source for total hydrogen ion currents up to 300 ma. From the full-scale source, Poroshin and Coutant obtained ≈450 ma of H_2^+ from a total beam of ≈800 ma. It seems reasonable, therefore, that an ion source of this type can produce the current of H_2^+ ions desired.

[5]O. F. Poroshin and J. J. Coutant, Report No. 600, Physico-Technical Institute, USSR. Translated by Culham Translations Office, July 1964. (Present address of J. J. Coutant: Association Euratom-CEA, Fontenay-aux-Roses, France.)

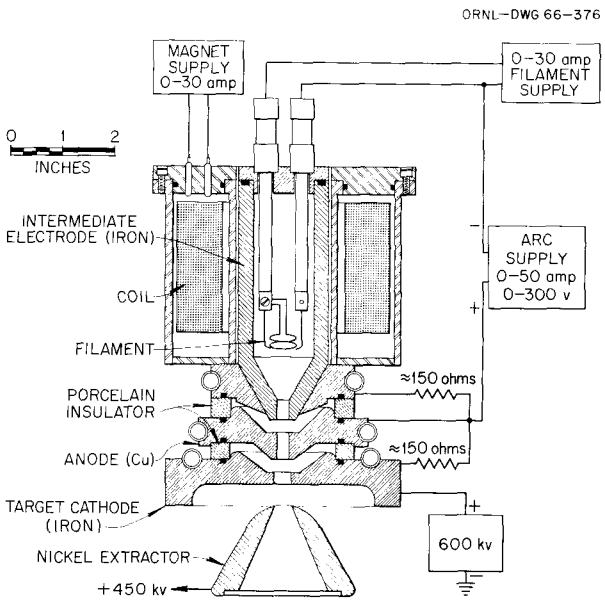

Fig. 6.4. New Ion Source Used for Producing Intense H_2^+ Ion Beams.

However, a very important question that must be answered is how much of this beam can be injected through a DCX-2 type duct with the present accelerator. If this system is not satisfactory, then more elaborate modifications of the present accelerator will be considered.

The 100-kv test stand has also been used to evaluate the system shown in Fig. 6.6, which includes the modified source described above and a beam extraction and focusing system similar to that used at Sukumi.[5] The results indicate that for the energy range of 30 to 70 kev, the system shown in Fig. 6.5 produces an H^+ beam with a higher current density than the H_2^+ beam from the system shown in Fig. 6.6. We are aware, however, that there are many parameter combinations that have not been tried in this preliminary work. In the energy range of 4 to 20 kev the system shown in Fig. 6.6 seems to be superior. For this low-energy range a well-collimated beam can be produced by extracting at elevated energies and then deaccelerating the beam in the vicinity of the auxiliary coil. The most critical parameter is the ampere turns in the auxiliary coil. At these low energies the best results have been obtained using the maximum ampere turns available with the system. The resulting axial magnetic field is also shown in Fig. 6.6. The H_2^+ beam available

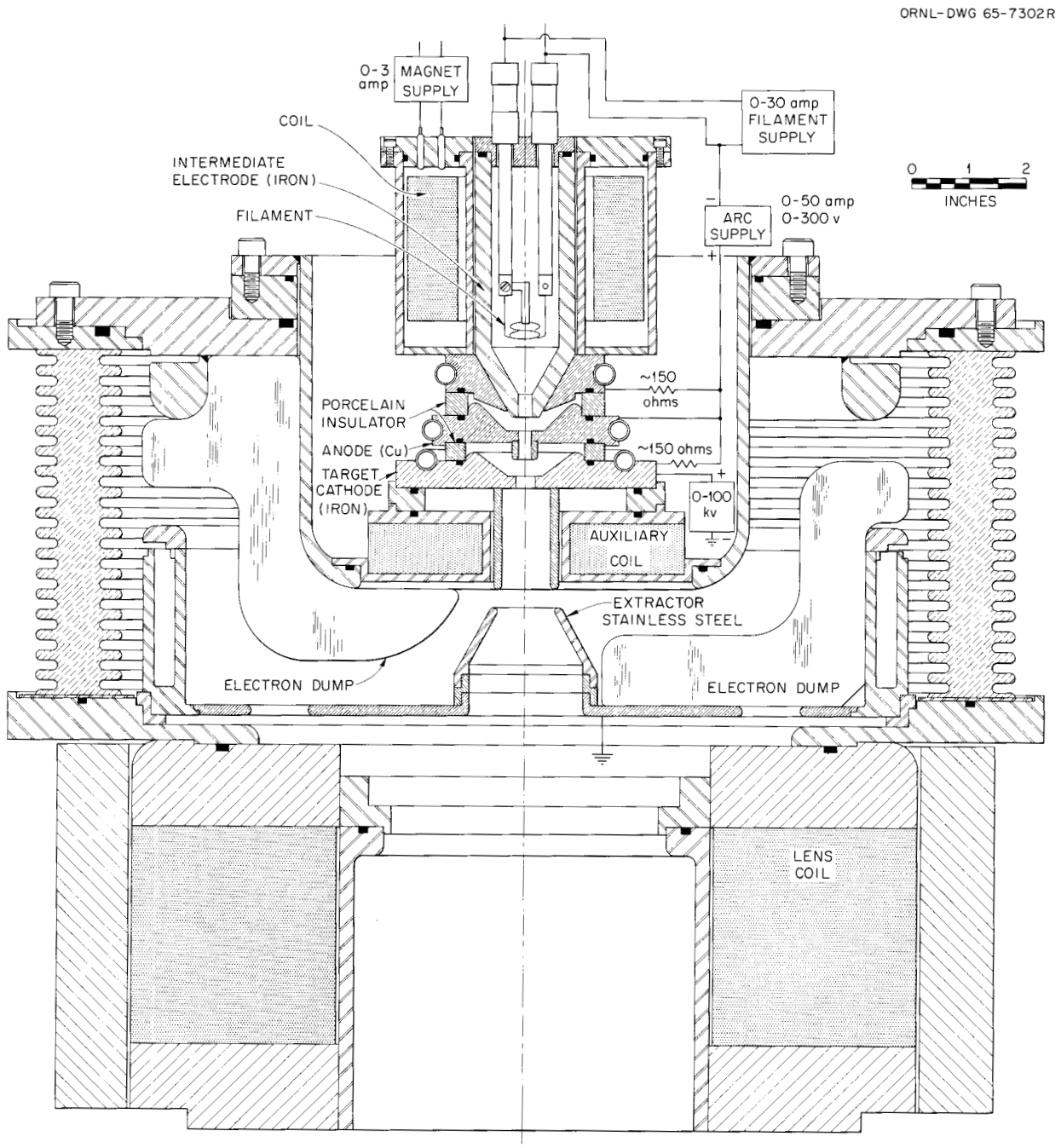

Fig. 6.5. System Used for Producing Intense H_2^+ Ion Beams in the Energy Range of 50 to 70 kev.

from this system through a 2.5-cm aperture located at a distance of 120 cm as a function of energy is shown in Fig. 6.7. This is a well-collimated essentially parallel beam.

A second system built for the generation of ion beams in the energy range of 4 to 20 kev is shown in Fig. 6.8. This system utilizes the all-copper ion source described earlier,[4] with the exception that the base of the anode plasma expansion "cup" is composed of a cooled copper plate with thirty-one 3-mm apertures spaced on 3.5-mm centers. There are two other electrodes composed of water-cooled copper plates with identical sets of 31 apertures. The electrodes are all insulated from

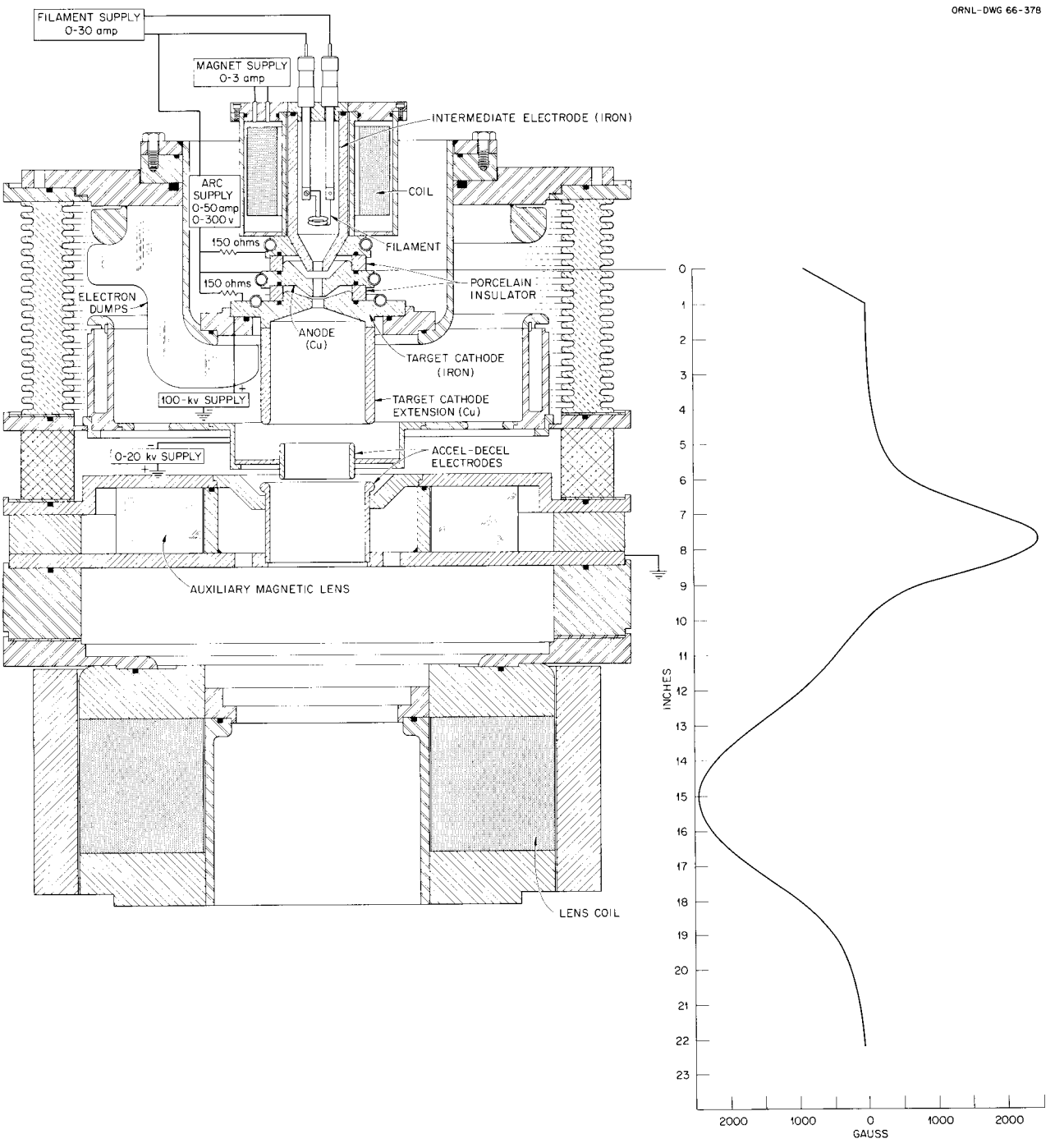

Fig. 6.6. System Used for Producing Intense H_2^+ Ion Beams in the Energy Range of 5 to 16 kev. The axial magnetic field strength is shown at right.

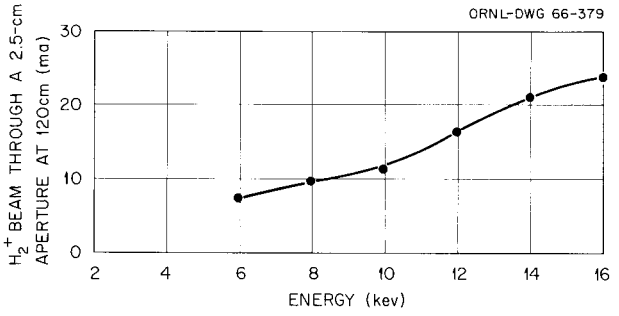

Fig. 6.7. H_2^+ Ion Beam Through a 2.5-cm Aperture Located 120 cm from the Lens as a Function of Beam Energy.

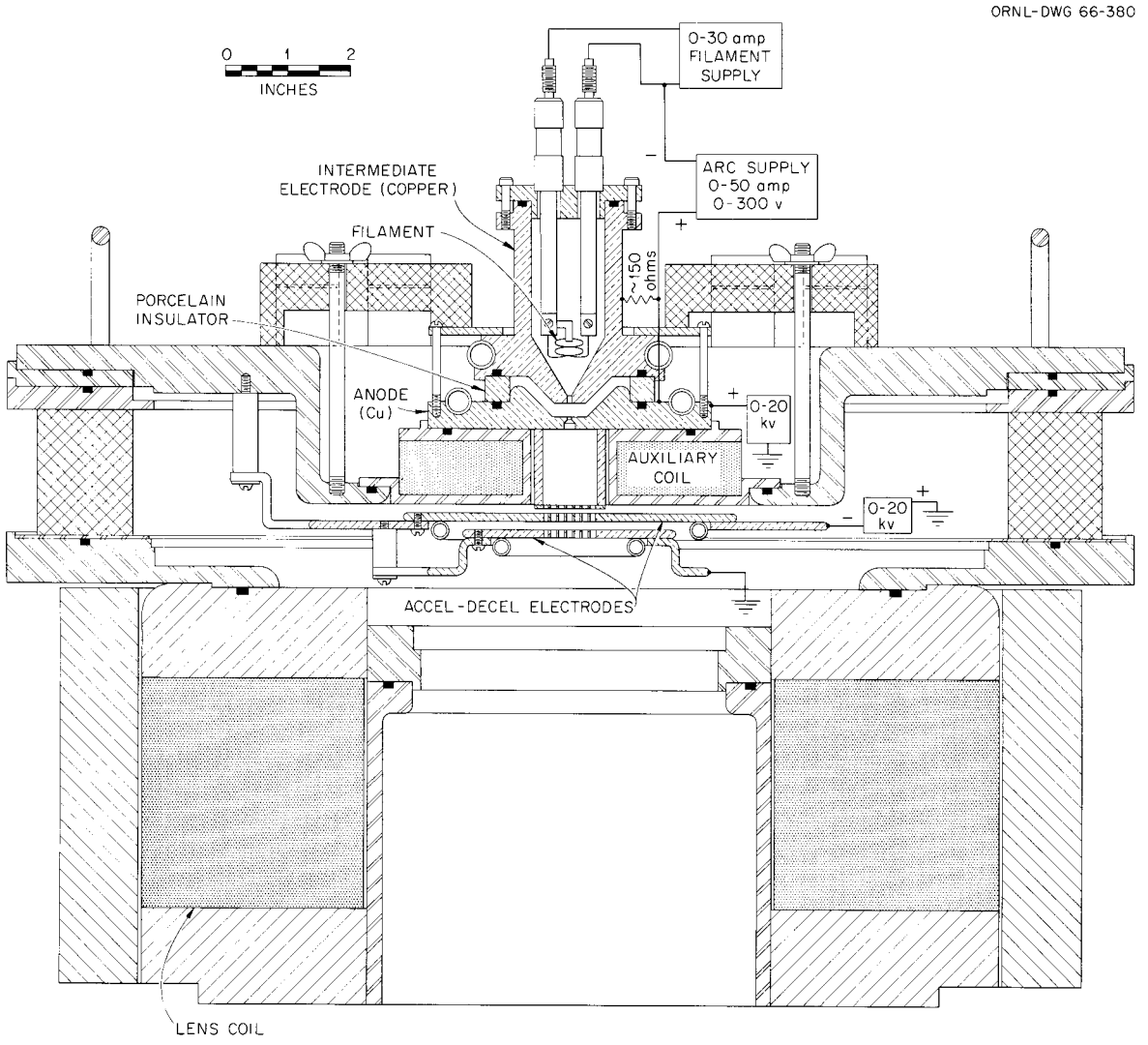

Fig. 6.8. Low-Energy (5 to 16 kev) System for the Production of Intense H^+ Ion Beams.

ground potential and can therefore be operated at a variety of electrical potentials. One of the most obvious, interesting, and fruitful arrangements is to utilize the grids as an accel-decel neutralizing arrangement. For this condition the anode of course is operated at the desired positive potential, the first electrode at a negative potential (to act as a barrier for electrons trying to reach the ion source and increase the initial extraction energy of the ions), and the second electrode is operated at ground potential (which shields the beam region above the lens, where neutralization is desired, from the negative potential of the previous electrode). This system has been operated over the energy range of 4 to 24 kev with a total extracted hydrogen ion beam of 200 ma under dc conditions for several hours with no appreciable erosion of the copper grids. The beam available from this system at a distance of 120 cm through a 5-cm aperture is shown in Fig. 6.9 as a function of beam energy. Both of the low-energy systems described above have only been evaluated for short periods of time. Each system is capable of generating hundreds of milliamperes of beam even at energies of 5 to 20 kev. There are numerous ideas in hand which are likely to produce better results than reported here. These studies will be pursued as time allows and in accordance with need in the thermonuclear program.

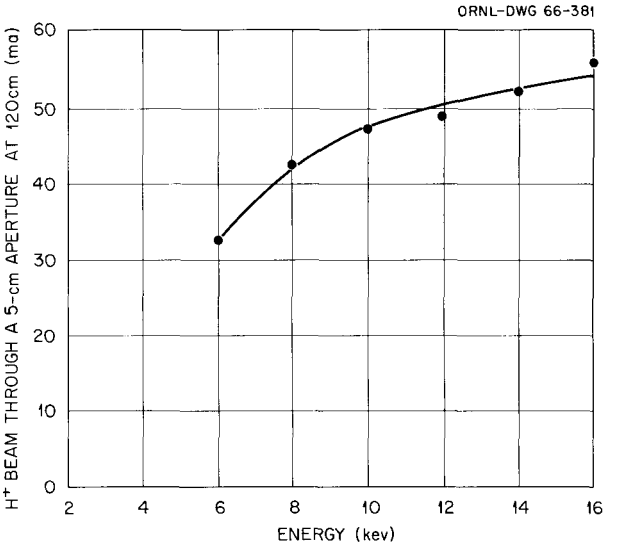

Fig. 6.9. H^+ Ion Beam Through a 5-cm Aperture Located 120 cm from the Lens as a Function of Beam Energy.

7. Plasma Theory and Computation

7.1 NEGATIVE-MASS INSTABILITY IN DCX-1

R. A. Dory

Experiments described in this report[1] have strengthened the suspicion that one of the very potent instabilities in DCX-1 is the negative-mass instability known from the theory of circular accelerators.[2] The following calculations were undertaken in an effort to provide theoretical predictions of certain of the data.[3]

These results are discussed: (1) frequency and growth rates of the unstable mode, (2) proton density at threshold of the instability as a function of the spread in proton energy and of the spread in radial betatron amplitudes. Agreement between theory and experiment is fairly good.

The calculation as it stands does not apply to the case in which the radial betatron amplitudes may be large. As noted in ref. 1, the results are roughly correct in that case, provided one neglects all protons with "large" amplitude. The behavior of the ambient neutralizing background or low-energy protons is neglected in the calculation, as are the dynamics of motion transverse to the beam direction.

The present results are a synthesis of results and ideas from T. K. Fowler, C. E. Nielsen, V. K. Neil, K. R. Symon, and others. Discussions with and preprints from R. W. Landau were especially useful and are gratefully acknowledged.

The negative-mass instability results if particles near a focused orbit (e.g., the concentric circular orbit in the symmetry plane of a mirror machine) experience a decrease in the frequency of traversing the orbit when their energy is increased (as is true for nonrelativistic particles in a mirror machine). The instability will disappear because of damping if the system is given a spread in particle frequencies. Such a spread results from spreading the energy or betatron amplitudes, or from relativistic effects.

We present here a heuristic calculation of the threshold density and oscillation frequency at threshold. Detailed treatments verify the results in cases where they may be carried through.

A monoenergetic group of $2\pi R_0 N$ nonrelativistic protons (energy E_0, mass M, charge e) is put uniformly into a circular orbit (radius R_0, frequency ω_0) in the symmetry plane of a mirror machine [field gradient index $n \equiv -(r/B_z)\cdot(dB_z/dr)|_{r=R_0}$]. A static neutralizing background is assumed. A perturbation at the lth harmonic of the azimuthal angle θ would give electrostatic signals polarized in the azimuthal direction at the gyrofrequency ω_0 of the protons. The signals would grow with characteristic rate[4]

$$\Gamma = \frac{2\pi}{\tau} = \frac{nl}{MR_0}\left[\frac{Ne^2M\gamma_l}{n(1-n)}\right]^{1/2}, \qquad (1)$$

[1] J. L. Dunlap *et al.*, sect. 1, this report.

[2] C. E. Nielsen, A. M. Sessler, and K. R. Symon, *Proc. CERN Symp. High Energy Accelerators, Geneva, 1959.*

[3] These conclusions were presented in paper P13 at the 1965 Annual Meeting of the Division of Plasma Physics, American Physical Society, San Francisco, Calif., Nov. 8–11, 1965.

[4] This paragraph paraphrases unpublished results of T. K. Fowler (ORNL-CF-61-7-1, private communication, 1961) obtained in modifying the theory of ref. 2 to apply to DCX-1. See appendix to ref. 1.

where γ_l (equivalent to g_0 of ref. 2) is given by[5]

$$\gamma_l = l^{-1}\int_0^{2\pi} d\phi \sin\phi \sin l\phi \left(4\sin^2\frac{\phi}{2} + \frac{a^2}{R_0^2}\right)^{-3/2}.$$

This instability is a charge-clustering phenomenon and will not occur if spread is introduced into the angular speeds of the particles so that particles will not remain clustered over a wavelength $2\pi/l$ for as long as a growth time τ of the instability. Thus stability results if $\tau\Delta\dot{\theta} > 2\pi/l$ where we interpret $\Delta\dot{\theta}$ as half-width of the spread. For stability then, one needs $\Delta\dot{\theta} > [Ne^2 n\gamma_l/(1-n)MR_0^2]^{1/2}$. If $\Delta\dot{\theta}$ results only from a spread ΔE in energy, we recover the results of ref. 2. This recovery motivates the choice of numerical factors in our argument, which is, in essence, just dimensional analysis.

We now assume that a further spread in angular speed is introduced by giving the particles a spread in radial betatron amplitude ρ, and calculate a total spread $\Delta\dot{\theta}$ as the sum of $|(\partial\dot{\theta}/\partial E)\Delta E|$ and $|(\partial\dot{\theta}/\partial d^2)\Delta d^2|$, where $d \equiv \rho/R_0$.

Since the calculation is laborious, the details are omitted here. We find in agreement with results of Neil and Landau[6] that the coefficient of Δd^2 is $-\frac{1}{4}(n - n')\omega_0$, where

$$n' = (R_0^2/B_z)(d^2B_z/dr^2)|_{r=R_0}.$$

This results from a perturbation solution of the second-degree nonlinear radial betatron oscillation equation. If one wishes to include the axial betatron oscillations, the spread in $\Delta\dot{\theta}$ should be augmented by $|(\partial\dot{\theta}/\partial\delta^2)\Delta\delta^2|$, where $R_0\delta$ is the axial amplitude. The coefficient of $\Delta\delta^2$ turns out to be $n\omega_0/4$, about half the radial coefficient in DCX-1, where $n' \cong -n$.

For a stability criterion then we take

$$N \lesssim \frac{MR_0^2\omega_0^2}{e^2\gamma_l}\frac{1-n}{n}\left[\left(\frac{1}{4}\frac{n}{1-n}\frac{\Delta E}{E_0}\right) + \left(\frac{1}{4}\frac{n-n'}{2}\Delta d^2\right)\left(\frac{1}{4}\frac{n}{2}\Delta\delta^2\right)\right]^2. \quad (2)$$

The wave frequency at threshold will be the mean angular speed of the beam. We assume that ΔE is even about E_0 so that the wave frequency will be

$$\text{Re }(\omega) = l\omega_0\left[1 - \frac{1}{4}(n - n')\Delta d^2\right], \quad (3)$$

neglecting the contribution of axial oscillations.

In comparing theory with experiment, we consider first the wave frequency at threshold. In experiments[1] where the beam is limited radially so that Δd^2 is small, the relative shift in the $l = 1$ wave frequency $(\omega - \omega_0)/\omega_0$ was found to be negative and very small. The observed shift and the resolution were both about a few tenths of a percent. Applying (3) for the largest $\Delta d^2 = 0.03$ used in the experiment, one finds a predicted shift of -0.2%, in reasonable agreement.

The dependence of N upon ΔE is discussed in detail in ref. 1, where agreement again is found: when the ΔE term of (2) dominates, N should be proportional to $(\Delta E)^2$ except for slight corrections of γ_l.

Figure 7.1 shows an attempt to fit Eq. (2) to the data of Fig. 1.13 of ref. 1. For this fit, reference was made to the detailed data to determine the displacement of the radial limiter, used to define Δd. The energy spread was treated as an adjustable parameter, with ΔE (full width) of 4.5 kev giving the reasonable fit shown. This is in good agreement with the estimated experimental value of 4 kev. The values of γ_l used were those appropriate to the radial beam width at the point in question. The uncertainty in assigning distribution function parameters indicates that the theoretical points could be off at least a factor of 2.

Substantial agreement is seen at the left side of the figure, but the theoretical points seem to fall significantly low at the right side. This may be

---

[5]This is the only place so far where the beam thickness $2a$ must be taken into account. As function of a/R_0, γ_l is only weakly varying in situations of interest; for example, at $4a/R_0 \doteq 10^{-3}, 10^{-2}, 10^{-1}$ numerical quadrature yields $\gamma_l \doteq 15, 11, 6$. The significance of γ_l is that it relates the θ component of the electrostatic field at one azimuth to the perturbed charge density elsewhere in the beam when a density modulation $\propto \exp il\theta$ is introduced. The value is infinite unless a is nonzero.

[6]R. W. Landau and V. K. Neil, UCRL-14406 (Sept. 28, 1965).

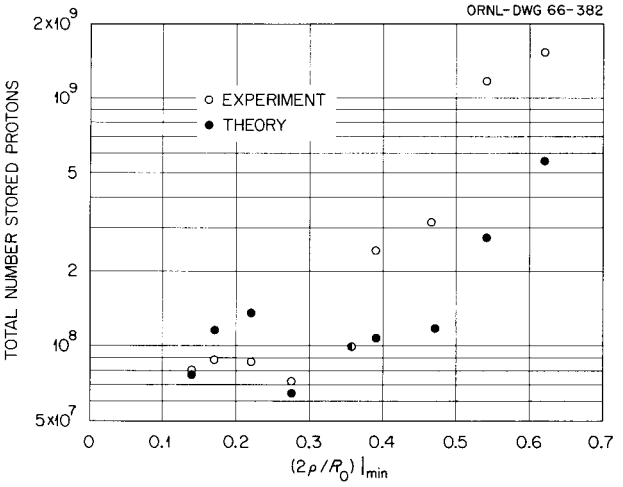

Fig. 7.1. Comparison of Experimental and Theoretical Threshold Proton Number.

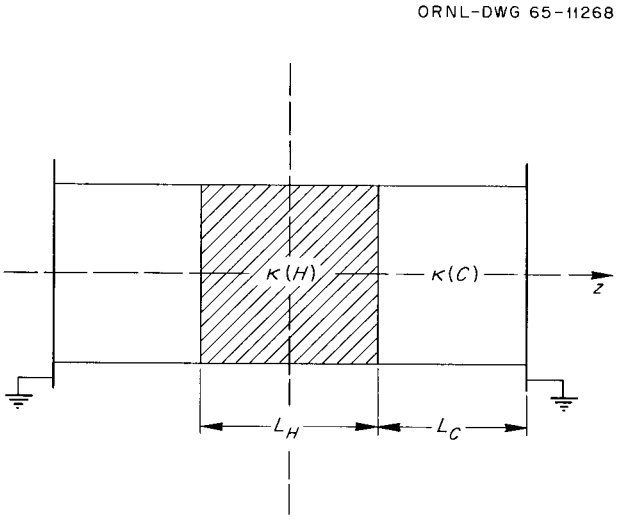

Fig. 7.2. Schematic Indication of the Plasma Model Calculated.

caused by the breakdown of the accuracy of the perturbation calculation of the orbits. The expansion parameter ρ/R_0 is as large as 0.3 at the rightmost point. A numerical test of this possibility should be relatively easy with existing orbit codes.

7.2 COLD-PLASMA STABILIZATION OF DRIFT WAVES IN HOT-ELECTRON PLASMAS

G. E. Guest C. O. Beasley, Jr.

Observations by Ard *et al.*[7] that a cold background plasma can prevent the occurrence of flute-like instabilities in hot-electron plasmas generated by electron cyclotron resonance heating have motivated a calculation of the stability properties of a very simple model of such systems, indicated by Fig. 7.2. The hot-plasma region is assumed to have sharp axial boundaries; the cold plasma extends throughout the length of the conducting cavity, which is situated in a simple magnetic mirror configuration. The very important question of sheath behavior at the end plates is not dealt with here. Rather, we assume that conduction to the walls is large and that the impedance outside the hot-plasma region is dominated by the cold-plasma reactance. The success of stability calculations for hot-ion plasmas in which no axial fields are included[8] suggests that in such cases either (1) the sheath is able to provide a boundary which prevents the plasma from seeing the chamber walls[9] (under these conditions, the present model is obviously inapplicable) or (2) the density of cold plasma is negligibly small.

The dispersive properties of the plasma media for electrostatic waves are described by dielectric tensors, κ(HOT) and κ(COLD); Poisson's equation then becomes

$$\nabla \cdot \kappa \cdot \overrightarrow{\nabla\phi} = 0 , \qquad (1)$$

with solutions of the form

$$\phi_l(r,\ \theta,\ z) \approx J_l(k_\perp r)e^{il\theta}\left(Ae^{k_\perp z\sqrt{\kappa_{11}/\kappa_{33}}} + Be^{-k_\perp z\sqrt{\kappa_{11}/\kappa_{33}}}\right). \qquad (2)$$

Here we have assumed the dielectric tensors to

[7] W. B. Ard, R. A. Dandl, and R. F. Stetson, "Observation of a Mirror-Like Instability in a Hot-Electron Plasma," *Seventh Conference on Ionization Phenomena in Gases, Belgrade, Yugoslavia, August 22–27, 1965* (to be published in the *Proceedings*).

[8] See, for example, L. G. Kuo *et al.*, *Phys. Fluids* **7**, 988 (1964); C. C. Damm *et al.*, *Phys. Fluids* **8**, 1472 (1965).

[9] F. F. Chen, *Phys. Fluids* **8**, 752 (1965).

have the general form

$$\kappa = \begin{pmatrix} \kappa_{11} & \kappa_{12} & 0 \\ -\kappa_{12} & \kappa_{11} & 0 \\ 0 & 0 & \kappa_{33} \end{pmatrix}.$$

The fluctuating potential, ϕ_l, must satisfy the following boundary conditions: (1) $\phi = 0$ at the end walls, (2) ϕ is continuous across the hot-cold interface, (3) $D_Z = -\epsilon_0 \kappa_{33} \dfrac{\partial \phi}{\partial Z}$ is continuous across the hot-cold interface.

In order for nontrivial solutions ϕ to exist, the following dispersion relation must be satisfied:

$$0 = 1 + \sqrt{\frac{\kappa_{11}(H)\,\kappa_{33}(H)}{\kappa_{11}(C)\,\kappa_{33}(C)}} \tanh\left[\frac{k_\perp L_h}{2}\sqrt{\frac{\kappa_{11}(H)}{\kappa_{33}(H)}}\right] \times \tanh\left[k_\perp L_c \sqrt{\frac{\kappa_{11}(C)}{\kappa_{33}(C)}}\right], \tag{3}$$

or, if $k_\perp L \sqrt{\kappa_{11}/\kappa_{33}} \ll 1$, as is generally the case,

$$0 = \kappa_{11}(H) + \frac{2}{k_\perp^2 L_h L_c}\,\kappa_{33}(C)\,. \tag{4}$$

From the usual "finite Larmor radius theory" of a cylindrical plasma with smooth radial density profile in a magnetic field with gentle curvature,[10] one finds

$$\kappa_{11} \cong 1 + \frac{\omega_{pi}^2}{\omega_{ci}^2} - \frac{\omega_{pi}^2}{\omega_{ci}^2}\frac{1}{k_\perp R_p}\left[\frac{e^{-\lambda_i} I_0(\lambda_i)}{\omega - k_\perp v_{gi}} - \frac{e^{-\lambda_e} I_0(\lambda_e)}{\omega - k_\perp v_{ge}}\right] - \frac{\omega_{pi}^2}{\omega_{ci}^2}\sum_{n=1}^{\infty}\frac{1}{n!}\left(\frac{k_\perp \rho_i}{2}\right)^{2(n-1)}\frac{\omega(\omega - n^2/l\omega_{ci})}{\omega^2 - n^2\omega_{ci}^2}. \tag{5}$$

Here $R_p^{-1} = |(1/N_0)\,(dN_0/dr)|$, $\lambda = k_\perp^2 \rho_i^2/2$, ρ_i is the average ion gyroradius; v_{gi} and v_{ge} are the precessional drift speeds of the ions and electrons, respectively, in the inhomogeneous magnetic field. We consider waves such that

$$\lambda = \frac{k_\perp^2 \rho^2}{2} = \frac{l^2}{2}\frac{\rho^2}{R_p^2} \ll 1$$

for ions and electrons. Hence, $e^{-\lambda} I_0(\lambda) \approx 1$, where I_0 is the Bessel function of zeroth order. The cold plasma is taken to be entirely reactive; that is,

$$\kappa_{33}(\mathrm{COLD}) \cong 1 - \frac{\omega_{pe}^2}{\omega^2} \approx -\frac{\omega_{pe}^2}{\omega^2}\,. \tag{6}$$

If the hot-electron precession frequency $\omega_{ge} = v_{ge}/R_p \ll \omega_{ci}$, one can neglect the summation in κ_{11}(HOT) and obtain a simple cubic dispersion relation. The corresponding stability boundary is described by the relation

$$\left(\frac{N_c}{N_h}\right)_{\text{threshold}} \cong \left(\frac{l^2\omega_{ge}}{\omega_{ci}}\frac{L_h L_c}{2R_p^2}\frac{m}{M}\right)\left(\frac{3}{2} + \frac{l^2\omega_{ge}}{\omega_{ci}} \pm \sqrt{\frac{8l^2\omega_{ge}}{\omega_{ci}} - \frac{3}{4}}\right). \tag{7}$$

Here N_c and N_h are the plasma densities in the cold and hot regions respectively. If $l\omega_{ge} \approx \omega_{ci}$, one must retain the ion gyrofrequency resonances, and the dispersion relation becomes a higher-order polynomial equation.

We have obtained numerical solutions for experimental parameters typical of the PTF machine. Stability boundaries are shown in Fig. 7.3, together with curves indicating parameters at which the linear growth rates of the unstable waves have reached 10% of the ion gyrofrequency. Also shown are two straight lines indicating the domain thought to characterize the PTF plasma when it is near threshold for the appearance of the flutelike modes. For $T_e \gtrsim 50$ kev, one sees that the plasma is predicted to be unstable to waves near the fourth (as well as eighth and ninth) harmonic of the precession frequency. From the usual coupled mode approximation, one can derive an approximate

[10] J. D. Jukes, *Phys. Fluids* **7**, 1468 (1964).

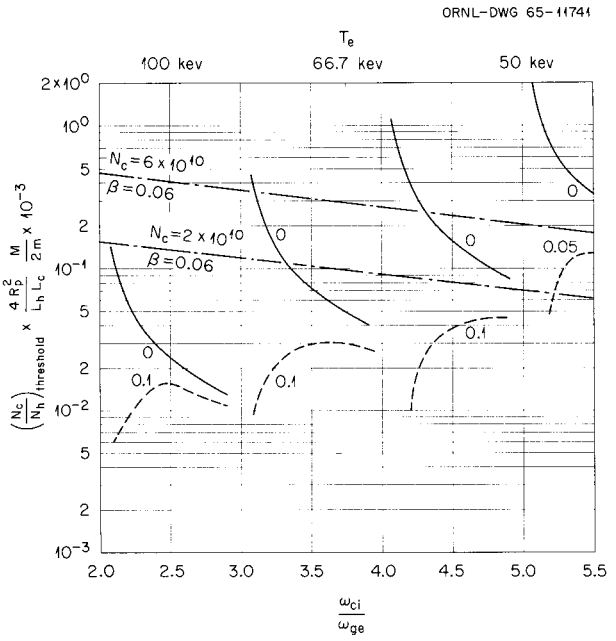

Fig. 7.3. Stability Boundaries for Experimental Parameters Representative of the PTF Machine near Threshold for Appearance of Flutelike Instabilities.

description of the stability boundary shown in Fig. 7.3: if $l\omega_{ge} \lesssim \omega_{ci}$,

$$\left(\frac{N_c}{N_h}\right)_{\text{threshold}} \cong l\left(\frac{L_h L_c}{4R_p^2}\frac{m}{M}\right) \times \left[l - 3 + \frac{l - 1\ (2\omega_{ci}/l\omega_{ge})\ (1 + \sqrt{2\,l - 1})}{(\omega_{ci}/l\omega_{ge}) - 1}\right].$$

The domain of applicability of this model is under continuing study.

7.3 NONLINEAR PLASMA PHENOMENA FROM A QUANTUM-MECHANICAL POINT OF VIEW

E. G. Harris[11]

We claim the following advantages for treating nonlinear phenomena quantum mechanically. (1) It is conceptually simple. One views the plasma as an assembly of weakly interacting particles (electrons and ions) and quasi-particles; that is, collective oscillations such as plasma oscillations (plasmons) and ion sound waves (phonons). (2) The calculations are straightforward. Once one knows the interaction Hamiltonian for a process, then the usual formulas of quantum-mechanical perturbation theory can be applied to calculate transition rates. We have investigated a number of processes by these methods which were previously investigated by classical methods. Our investigation of the wave-vector space instability of Vedenov and Rudakov[12] has led to some new results. In this instability, energy is transferred from plasma oscillations to ion sound waves. A report on this part of our work has been published.[13] We are currently extending our calculations to include nonlinear phenomena in a plasma in a magnetic field.

[11]Consultant from the University of Tennessee.

7.4 DIFFUSION ACROSS A MAGNETIC FIELD

Owen Eldridge[11]

In a previous report[14] the diffusion coefficients of a plasma were calculated from the orbits of test particles in a constant magnetic field and a fluctuating electric field. The coefficients for both velocity and spatial diffusion were calculated in terms of an arbitrary spectrum of electrostatic oscillations in the plasma. The same diffusion equation has now been derived from the more abstract kinetic theory in which one describes the interaction in terms of the correlation function for pairs of particles. The diffusion coefficients are exactly the same as those calculated from the simpler model.

The calculation helps to clarify two questions. First, the spatial diffusion coefficient is divergent and an arbitrary cutoff must be used for one of the integrals. This divergence is related to the absence of Landau damping for electrostatic waves propagating perpendicular to the magnetic field.

[12]A. A. Vedenov and L. I. Rudakov, *Soviet Phys. "Doklady" (English Transl.)* 9, 1073 (1965).

[13]E. G. Harris, ORNL-3871 (November 1965).

[14]E. G. Harris and O. C. Eldridge, *Thermonuclear Div. Semiann. Progr. Rept. Oct. 31, 1964*, ORNL-3760, p. 74.

The kinetic theory model shows that the cutoff distance should be at about the Debye length. Second, the contributions to the diffusion of electrons come from all the species of particles present in the plasma. This is quite different from collisional diffusion, where one finds that only the ions contribute to electron diffusion.

7.5 CODE FOR DCX-2 REOPTIMIZATION

C. E. Parker

Several years ago codes[15,16] were available to optimize a coil system for maximum homogeneity over a given interval. These codes were used extensively in the design work for EPB and DCX-2. However, since both codes were written for the ORACLE (machine language), they are no longer relevant since the ORACLE was dismantled in February 1963.

Recently, interest has arisen in the use of DCX-2 with mirror ratios other than the standard value of 3.3. Since our optimization codes were obsolete, a new FORTRAN code was written. It used the same mathematical method previously described.[17]

The sum of squares of the deviations over a given axial length were minimized, or in equation form

$$\int_0^L (\Delta B)^2 \, dZ \rightarrow \text{minimum} , \qquad (1)$$

where

$$\Delta B = B_z(Z) - B_0 , \qquad (2)$$

$B_z(Z)$ is the actual field at any point produced by the winding, and B_0 is the fixed field desired along the axis.

Equation (1) can be differentiated with respect to the variable current densities, yielding a set of linear equations which can be solved for the desired values.

The code is somewhat versatile in that the integration interval is variable as well as the order of the Gaussian numerical integration. The magnetic field values were calculated using the code described by M. W. Garrett.[18]

7.6 USE OF POLYHOOK AS A SUBROUTINE IN THE DETERMINATION OF COMPLEX ROOTS OF A POLYNOMIAL

C. O. Beasley, Jr.

In an attempt to evaluate numerically the complex roots of a seventh-degree polynomial, in order to determine stability boundaries for flutelike instabilities in a hot-electron plasma,[19] the CO-OP[20] subroutines POLYHOOK or POLYHK at times failed to converge. A more suitable CO-OP program, POLYHOOK, was available as a separate program. However, the usefulness of this as a program was not nearly so great as its usefulness as a subroutine. The program POLYHOOK was then converted into a subroutine POLYHOOK for use on any CDC 1604 computer.

Advantages of the subroutine over other complex polynomial root-finding subroutines are:

1. Variable error bounds to the coefficients of the polynomial may be given.
2. Lower bound on magnitude of the leading coefficient.
3. Starting values may be varied.
4. Choice of single or double precision.
5. Clusters of roots are identified.
6. Many diagnostics are built into the program.

A writeup of the program is available through the Mathematics Division.

---

[15] G. R. North and M. Rankin, *Thermonuclear Div. Semiann. Progr. Rept. July 31, 1960*, ORNL-3011, p. 83.

[16] D. L. Coffey and J. E. Simpkins, *Thermonuclear Div. Semiann. Progr. Rept. Jan. 31, 1961*, ORNL-3104, p. 99.

[17] D. L. Coffey, W. F. Gauster, and J. E. Simpkins, *Thermonuclear Div. Semiann. Progr. Rept. July 31, 1960*, ORNL-3011, p. 80.

[18] M. W. Garrett, *An Elliptic Integral Computer Package for Magnetic Fields, Forces, and Mutual Inductances of Axisymmetric Systems, and a Versatile Line-Tracing Routine*, ORNL-3575 (April 1965).

[19] See sect. 7.2, this report.

[20] CO-OP is the CDC 1604 User's Organization.

8. Magnetics and Superconductivity

8.1 MAGNETIC SYSTEMS GENERATING FIELDS OR AXIAL FIELD GRADIENTS OF HIGH UNIFORMITY. CONTOURS OF CONSTANT VECTOR MAGNITUDE AND OF TOTAL VECTOR ERROR

M. W. Garrett[1]

The following discussion extends previous work[2] on the error contours of axially symmetric systems. The restriction to errors of even order limits its validity to systems with a plane of symmetry or of antisymmetry through the origin. It applies equally to systems for which the axial field component B_z or the axial gradient $\partial B_z/\partial z$ is uniform near the origin, since these two quantities are Laplacian scalars that may be described by two homologous zonal harmonic series. The order of each field series term is incremented by 1 in the gradient series. Polar field coordinates are r, θ; cylindrical coordinates are z, ρ. References to the "D system" and to figures "below" refer to the next following paper.

Uniform-gradient systems do not seem to have been described in detail. Ideally, in such a system $B_z/z = -2B_\rho/\rho$ is independent of the coordinates. That is, B_z is proportional to z and is constant over any transverse plane, B_ρ is proportional to ρ and is constant over any coaxial cylinder, while the tangent of the resultant vector $\boldsymbol{B}$ is everywhere $-\frac{1}{2}$ times the tangent of the polar angle.

For any pair of axially symmetric elements with a geometrical plane of symmetry, there is a unique "Helmholtz" axial spacing for most-uniform field and a "Maxwell" spacing (with opposed currents) for most-uniform axial gradient. The cross section is arbitrary and need not be rectangular. For a pair of field loops of radius a, $z = \pm 0.5a$ ($P_3' = 0$), while for gradient loops $z = \pm 0.5\sqrt{3}\ a$ ($P_4' = 0$). The dominant error for a system of either type is of the fourth order. The B_z or $\partial B_z/\partial z$ contours are mapped in Fig. 3 of ref. 2 and, for 1% only, in Figs. 8.3 and 8.4 of this report. The latter figures include the effect of higher orders, but the difference is scarcely perceptible. The Helmholtz spacing is also correct for a coil pair with opposed currents which is to produce the strongest possible gradient at the origin, regardless of uniformity. The error of such a cusp system is of second order.

When the fourth-order coil pair is pulled apart slightly from the Helmholtz or Maxwell position, the limits for moderate error are extended near the axis and compressed near the midplane. This occurs because the second-order error (dominant near the origin) and the fourth-order error (which takes over at moderate distances) cancel each other partially on the axis but reinforce in the midplane. The reinforcement of errors is more drastic at an intermediate polar angle, especially in the case of small errors, for which separate end regions may actually be pinched off from the central region of tolerable error. In this "prolate" field, two new singular points appear on the axis. These are saddle points, at which the field or gradient error passes through an axial (not an absolute) maximum. Algebraic details appear in ref. 2, where B_z error contours are plotted in Fig. 5. The prolate field has been widely misunderstood[3] and sometimes misused. Use of the D coils to generate such a field would be easy.

---

[1] Consultant, Swarthmore College.

[2] M. W. Garrett, *J. Appl. Phys.* **22**, 1091–1107 (1951). Includes references to earlier literature and shows B_z error plots for five types of field or gradient systems.

[3] See, for example, F. R. Crownfield, Jr., *Rev. Sci. Instr.* **35**, 240 (1964).

The "oblate" field is more interesting, and the D coils will be pushed together initially from the Helmholtz position to produce it. Here the second and fourth orders reinforce each other on the axis, with partial mutual cancellation in the midplane and a severe pinch at large polar angles in the case of small errors. Reference 2 contains an algebraic analysis that will not be repeated here, with a set of B_z contours (Fig. 6) that are nearly identical with those of Fig. 8.5 of this report out to a radius of perhaps 5 in., where sixth and higher orders begin to distort the lines.

In the oblate field the error topology near the axis is quite similar to that of the pure fourth-order case, but a circular singularity appears in the midplane, at which B_z has a maximum value and the two sheets of the B_z contour intersect at right angles. This is indicated in Fig. 8.5 but is seen more clearly in Fig. 6 of ref. 2.

At the singularity $\partial B_z/\partial\rho = 0$, Laplace's equation in B_z reduces to $\partial^2 B_z/\partial z^2 = -\partial^2 B_z/\partial\rho^2$. Thus the circle is the axis of a torus with nearly circular section in which the field is homogeneous to the second order, a property that has been used in a precision measurement of e/m for electrons following a circular orbit.[4]

The singular circle has also the property that if the coil pair is used with opposed currents as the primary of a Rayleigh current balance, the circle defines the best position for the mean turn of the secondary. The condition $\partial B_z/\partial\rho = 0$ holds for each coil separately, while $\partial B_\rho/\partial z = \partial B_z/\partial\rho$, since **curl** $\boldsymbol{B} = 0$. Therefore, with antisymmetric currents B_ρ is insensitive to small z displacements of the secondary. But B_ρ determines the force on the secondary coil.

The following discussion refers explicitly to the errors of field systems. By making three changes, it may be applied in its entirety to gradient systems: read everywhere $\partial B_z/\partial z$ for B_z, $\partial B_z/\partial\rho$ for B_ρ, and **grad** B_z for the field vector $\boldsymbol{B} = -$ **grad** V.

The departure of the vector field $\boldsymbol{B}(z, \rho)$ from an ideal match to the field at the origin (identified by subscript 0) may be defined in several ways. Most often it has been measured, as in ref. 2, by the scalar ratio $\Delta B_z/B_{z0}$. Recently $|\boldsymbol{B}|$, the magnitude of total field, has sometimes been used in place of B_z, as in Figs. 8.1 and 8.5 of this report. Now $\boldsymbol{B}$ differs from B_z only in the addition of B_ρ in quadrature; B_ρ is zero at the origin. Moreover, the term of order e in the zonal harmonic series for the error $\Delta B_z(r, \theta)$ contains $r^e P_e(\theta)$, while that for the error $B_\rho(r, \theta)$ contains $r^e \sin\theta\, P'_e(\theta)/(e+1)$; these two functions of the polar angle θ are multiplied by the same error coefficient ϵ_e. The range of magnitudes of either function is from 0 to (roughly) $\pm\sqrt{e}$. It follows that for all values of r such that the range of magnitudes of $\Delta B_z/B_{z0}$ is small, the range of B_ρ is equally small. Therefore the neglect of B_ρ would cause only a second-order error (cosine error) in $|\boldsymbol{B}|$, which means that in uniform-field systems the error contours of ΔB_z and of $|\Delta\boldsymbol{B}|$ are nearly indistinguishable. As far out as the 10% contour, in a field whose dominant order of error is e, the difference between the polar radii of the two sets is of the order of $(2e)^{-1}$ %. Farther from the origin, as the errors increase, the two sets diverge rapidly and eventually assume totally different forms.

Both the preceding sets of error contours effectively ignore the B_ρ error. They define an experimental working space of complicated shape, with conical extensions in which the unsuspected B_ρ error may cause trouble. It is therefore proposed as more conservative, and for some applications more significant, to measure the inhomogeneity by the magnitude of the "total vector error" $|\boldsymbol{B} - \boldsymbol{B}_0|$, or more simply $|\Delta\boldsymbol{B}|$. Sets of error contours defined in this new way are shown in Figs. 8.2 to 8.4 and 8.6. They are the traces of relatively simple closed surfaces of revolution, replacing the multiple sheets of the B_z contours. Such surfaces are a refinement of the "error spheroids" of ref. 2. Though they require two field components, they are actually easier to calculate, since the forward extrapolation of trial points on the simpler closed curves is more precise.

In a field with the pure order of error e, each B_z contour consists of $2e$ sheets, asymptotic at infinity to $e/2$ double cones of zero error.[2] The minimum polar radius is always on the axis, while the largest of the secondary minima lies in the midplane. The algebraic sign of the error alternates from sheet to sheet. In systems of the most familiar types, the axial sheet carries the minus sign, but there is another general family of uniform-field systems with error signs reversed.[5]

[4] Michael Ference, A. E. Shaw, and R. J. Stephenson, *Rev. Sci. Instr.* 11, 57–62 (1940).

[5] See ref. 2, end of p. 1104, $(P_m)_n$ systems.

As stated above, B_ρ is proportional to

$$r^e \sin\theta\, P_e'(\theta)\ ,$$

while B_z is proportional to $r^e P_e(\theta)$. Each B_ρ contour has again 2e sheets, but one zero-error cone always reduces to the axis (half-angle zero), while another is the midplane (half-angle $\pi/2$). The paraxial error sheet has here the plus sign. Now it can be shown that the contours of ρB_ρ and of B_z, like those of the flux function ρA and the scalar potential V, intersect orthogonally. Also, the polar angles at which $P_e(\theta)$ is zero are those at which $\sin^2\theta\, P_n'(\theta)$ is a maximum, and conversely. Neither statement holds exactly when B_ρ replaces ρB_ρ or when $\sin\theta\, P_e'(\theta)$ replaces $\sin^2\theta\, P_e'(\theta)$. Nevertheless, they are close enough for a rough interpretation of the actual calculated B_z and B_ρ curves, an example of which appears in Fig. 8.3, with its gradient homolog in Fig. 8.4. These are the 1% contours only, with fourth order dominant.

It is not hard to see that the closed surfaces of constant total vector error $|\Delta\boldsymbol{B}|$ must be inscribed in the complete set of B_z and B_ρ contours. As the curve is traced from the axis to the midplane, the error vector $\Delta\boldsymbol{B}$, of constant magnitude, rotates through an angle $\pi e/2$, that is, at an average rate that is e times that of the radius vector and in the opposite sense. This can be seen by considering the position of the error vector at the five points of tangency in Fig. 8.3, with due regard to the signs of the B_z and B_ρ errors, and generalizing the result to order e.

It may be of interest that in the analogous two-dimensional uniform field or gradient systems of order e with general infinite cylindrical geometry, the functions $P_e(\theta)$ and $\sin\theta\, P_e'(\theta)$ are replaced by $\cos e\theta$ and $\sin e\theta$, the B_x and B_y contours are hyperbolic cylinders of identical shape, and the $|\Delta\boldsymbol{B}|$ contours are true circular cylinders.

Figure 8.6 gives essentially the $|\Delta\boldsymbol{B}|$ contours of mixed second and fourth orders (oblate case), since only minor distortion is contributed by the sixth and higher orders. It shows perhaps more clearly than does Fig. 8.5 the pinching off, for small errors, of a separate region above the first singular circle where the error reaches its maximum. It shows also a second singular circle farther out, where the error is zero. Here the nearby contours are almost exact tori, but the field variation is rapid (of first order).

In Fig. 8.7 the radii of the two singular circles are plotted against the mean axial coordinate (upper abscissa) of a single D coil, with origin at the Helmholtz position. The curves are defined by the respective conditions $\partial B_z/\partial\rho = 0$ and $B_z(z, \rho) = B_z(z, 0)$, which hold separately for each coil.

A complete single contour of B_z, B_ρ, $|\Delta\boldsymbol{B}|$, or their gradient homologs, taking account of orders 2 through 32, can be calculated in about 1 sec by a new subroutine of the zonal harmonic computer package that has been described earlier.[6] To compute a single contour of B_z, B_ρ, $|\Delta\boldsymbol{B}|$, or $\partial B_\rho/\partial z$ (here the two remaining types of gradient contour are excluded) requires about 15 sec, using a recent addition to the previously reported elliptic integral package.[7] In this case it may also be elected to write the data on magnetic tape for machine plotting.[8] Agreement between the two methods of calculation is exact. In the case of Fig. 8.3, the contours for $|\Delta\boldsymbol{B}|$ were machine plotted, using elliptic integrals, while those for B_z and B_ρ were added by hand from the zonal harmonic calculation.

8.2 FIELD PROPERTIES OF THE LARGE-VOLUME WATER-COOLED MAGNET COIL SYSTEMS "C" AND "D"

J. N. Luton, Jr.

8.2.1 Progress on the Eighth-Order Field Coil

Two large-volume coils to be installed in the magnet laboratory are presently under construction. The first of these, an eighth-order power-optimized solenoid called C-1, has been described previously.[9] In this design an extremely homogeneous field is generated by a set of adjacent pancake coils whose current density varies with axial position. The actual current distribution differs slightly

---

[6] M. W. Garrett, *Computer Programs Using Zonal Harmonics for Magnetic Properties of Current Systems with Special Reference to the IBM-7090*, ORNL-3318 (November 1962); *Thermonuclear Div. Semiann. Progr. Rept. Oct. 31, 1964*, ORNL-3760, pp. 87–89.

[7] M. W. Garrett, *An Elliptic Integral Computer Package for Magnetic Fields, Forces, and Mutual Inductances of Axisymmetric Systems, and a Versatile Line-Tracing Routine*, ORNL-3575 (April 1965).

[8] We gratefully acknowledge the contribution of A. R. Jenkins of the Mathematics Division of ORNL, who wrote the plotting subroutine for this package.

[9] *Thermonuclear Div. Semiann. Progr. Rept. Oct. 31, 1964*, ORNL-3760, pp. 80–87.

from the ideal because the conductor cross section is not negligibly small compared to the coil cross section and because we restricted the numbers of turns in the pancakes to integral values. Therefore the calculated field (Fig. 8.17 of the cited reference) also varies from the ideal eighth-order case. It has since been found that the field shape may be made almost exactly eighth order by the addition of low-current shunts in parallel with 2 only of the 19 pancakes.

Figure 8.1 is the calculated field that results when 1.3% current shunts are placed across pancakes 2 and 2′. This figure shows contours of $|\boldsymbol{B}|$, that is, at all points on a given contour the magnitude of the flux density $\boldsymbol{B}$ has the same value. Within a sphere of 4 in. radius the field strength magnitude varies less than 0.01% from

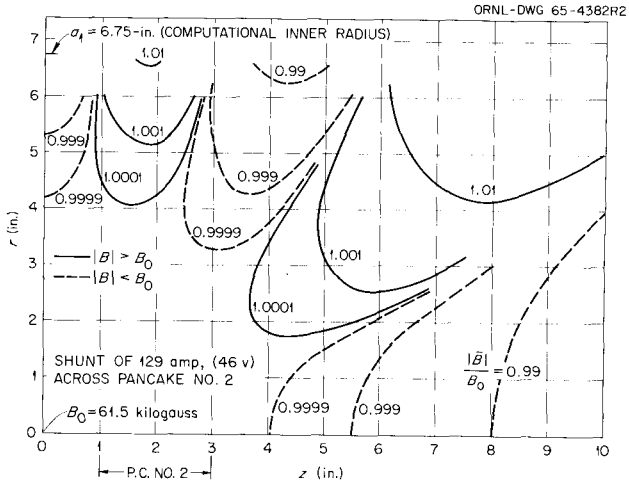

Fig. 8.1. $|B|$ Contours of C-1 with Shunts.

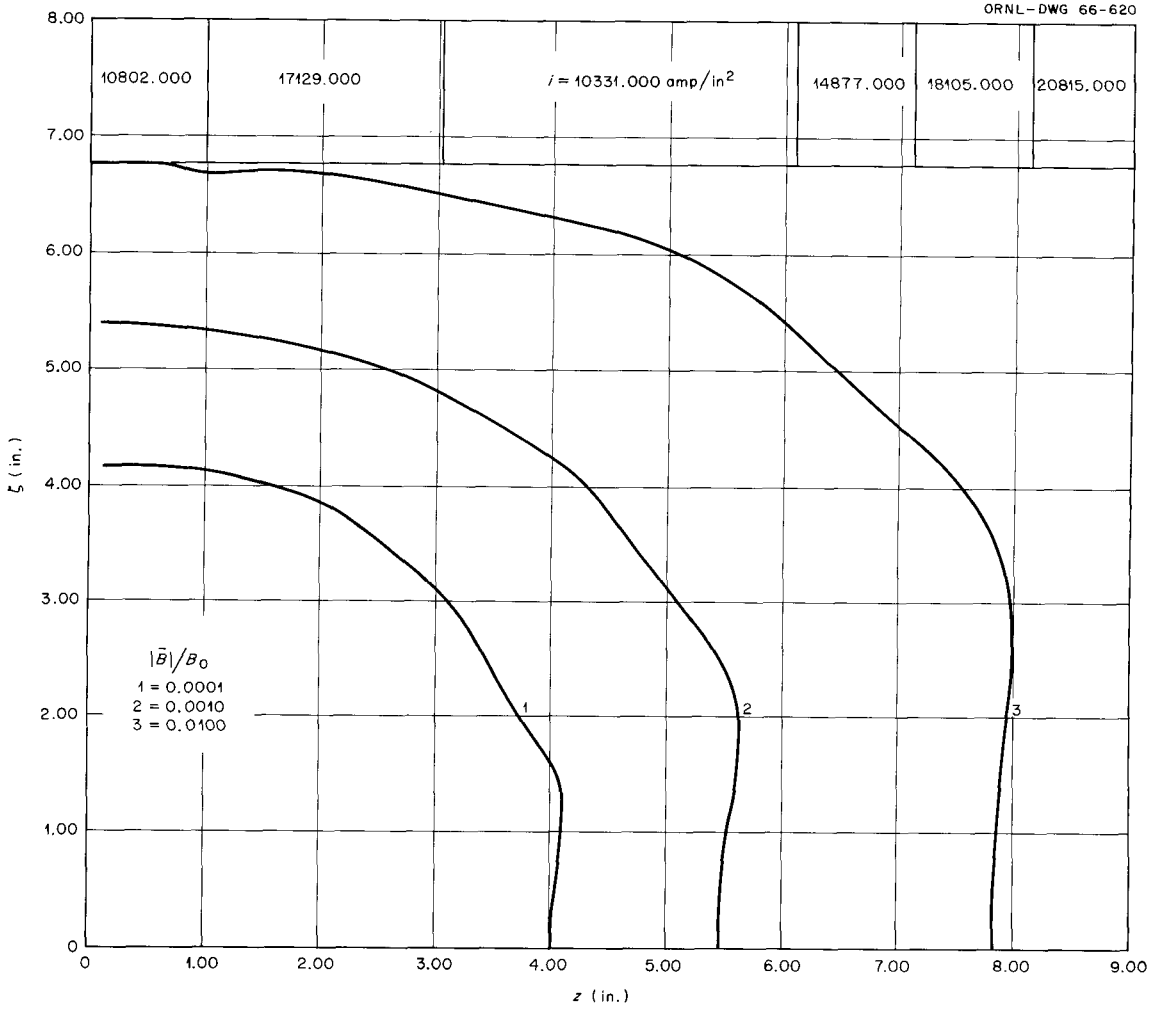

Fig. 8.2. $|\Delta B|$ Contours of C-1 with Shunts.

its value B_0 at the center of the coil. In Fig. 8.2, the quantity that is held constant is $|\Delta \boldsymbol{B}|$, the magnitude of the "total vector error" $\boldsymbol{B} - \boldsymbol{B}_0$, where $\boldsymbol{B}_0$ is the field at the center of the coil system. The concept of total vector error is discussed in Sect. 8.1, and reference should be made to that section for fuller understanding of the figures and data of this section. The contours of Fig. 8.2 are much simpler than those of Fig. 8.1, and for some purposes they may be more significant.

8.2.2 A Versatile, Large-Volume Coil Arrangement

The second large-volume coil assembly under construction for installation in the magnet laboratory consists of a pair of identical ("D") coils having uniform current density, a common vertical axis, and a variable gap between them. The bore will be approximately 26 in. long, and its usable diameter will be about 13 in. for the aiding case, but, because of the necessity of a mechanical support sleeve, only 11 in. for the cusp arrangement. With a power consumption of 6.4 Mw the assembly will generate a homogeneous field of 63.4 kilogauss when the coils are separated by a 1.5-in. gap and are connected to produce mutually aiding fields. However, the electrical leads and mechanical supports are designed to permit operation also with opposing currents. The resulting cusp configuration will provide high field gradients, large radial fields, and, with proper coil spacing, a large region of uniform field gradient, all of which are expected to prove valuable in future service.

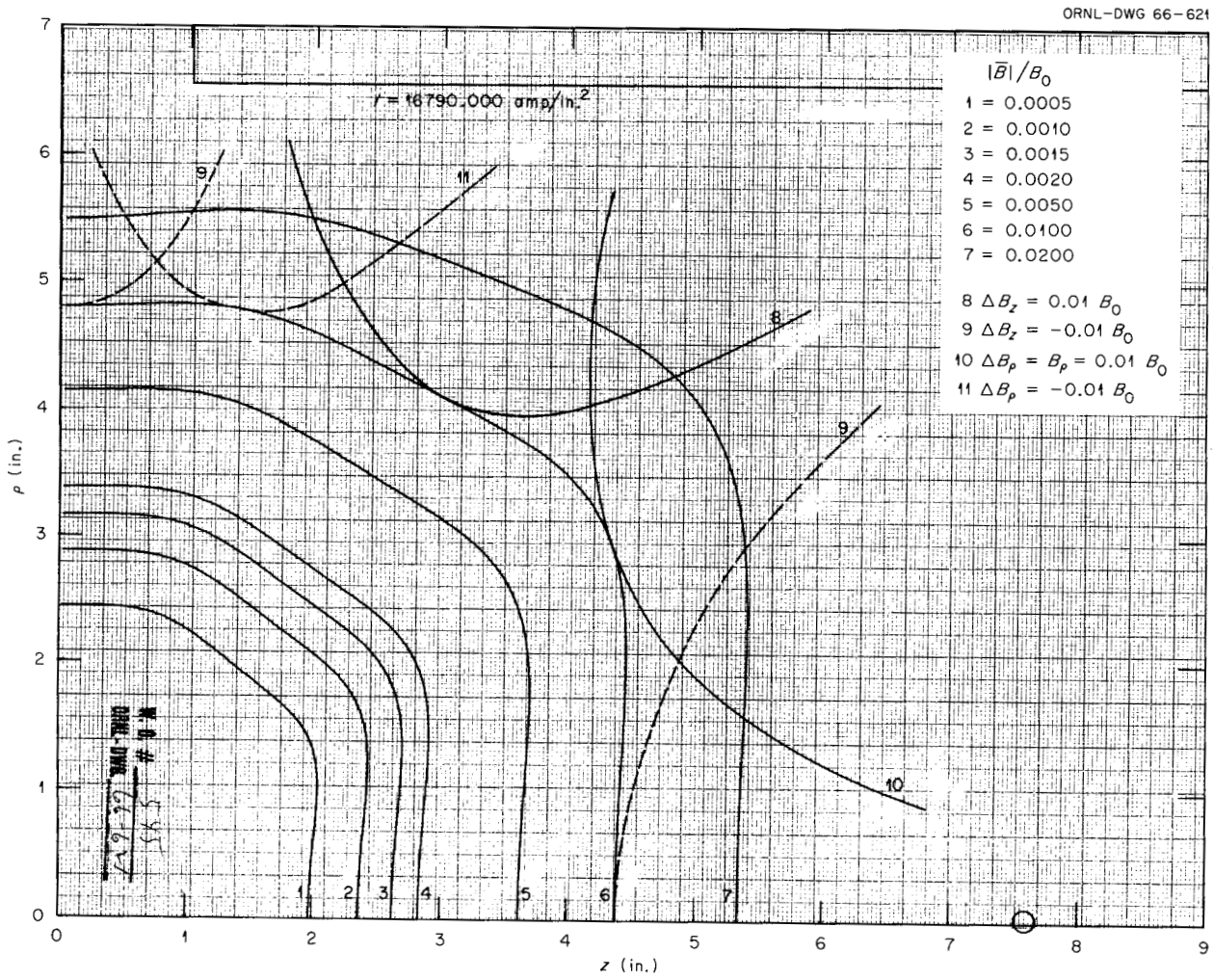

Fig. 8.3. Contours of B_z, B_ρ, and $|\Delta B|$ for the D Coils at Their Helmholtz Spacing.

At their Helmholtz (uniform field) spacing, the D coils produce a field as described by the $|\Delta \boldsymbol{B}|$ contours of Fig. 8.3. The 1% B_z and B_ρ error curves are drawn on the same figure to show more clearly the relationship between the three sets of contours. Figure 8.4 is the analogous figure for the Maxwell (uniform gradient) position. The symbol Δ consistently indicates the value of a function minus its value at the origin.

The coils will be operated initially at a spacing slightly less than the Helmholtz spacing in order to obtain a more uniform field over the cross section of a torus centered in the midplane. Large-diameter superconducting coils of small cross

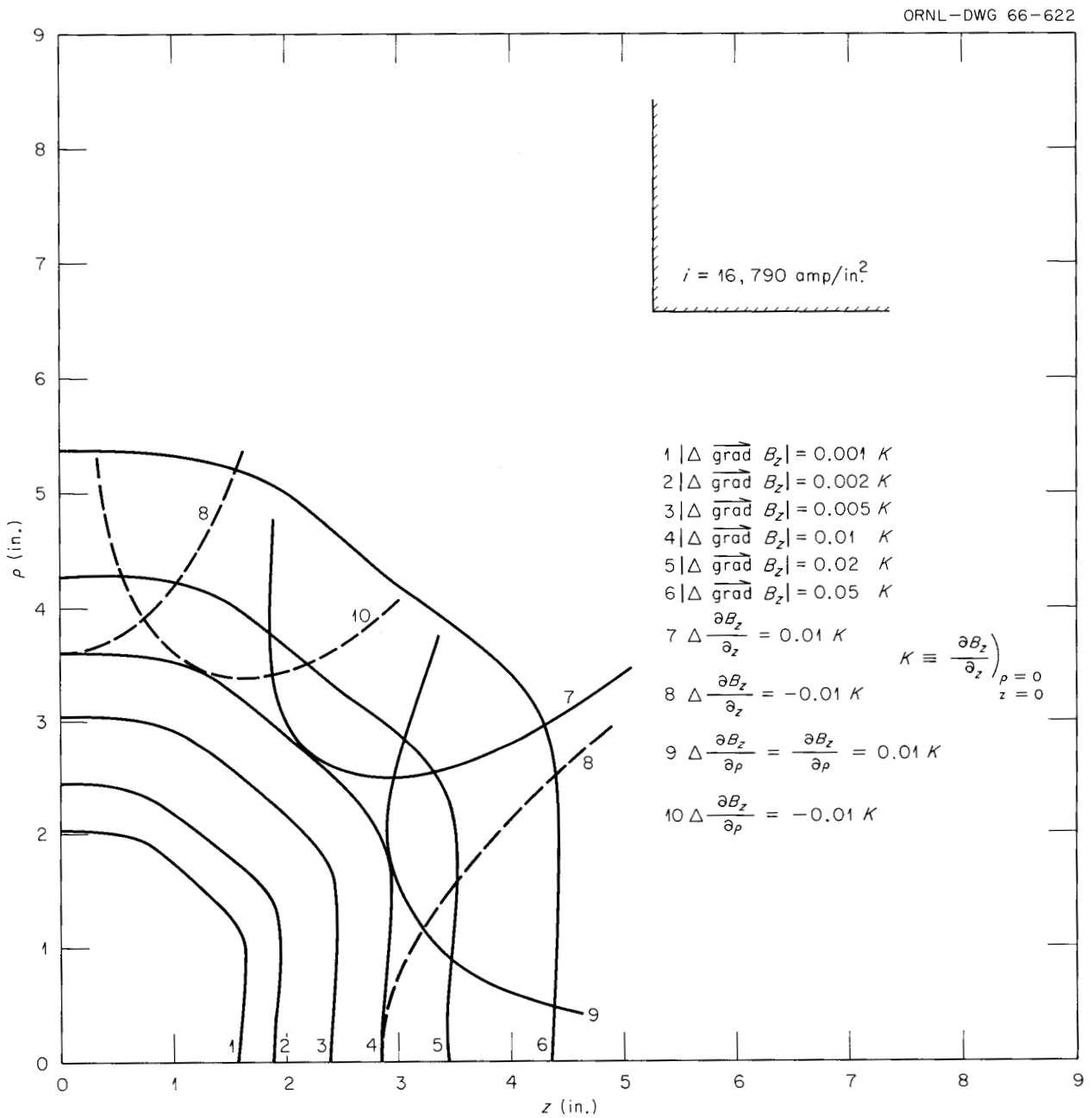

Fig. 8.4. Contours of $\partial B_z/\partial z$, $\partial B_z/\partial \rho$, and $|\Delta \text{ grad } B_z|$ for the D Coils, Maxwell Condition.

section will be tested with their windings in this toroidal region of maximum uniformity. The $|\boldsymbol{B}|$ contours of Fig. 8.5 show, by their increasing separation, midplane regions of greater homogeneity around the point $r \approx 0$ and the circle $r \approx 3.4$ in. Therefore this arrangement of a 1.5-in. gap between the coils would be suitable for producing an extremely uniform field over the windings of a sample coil of only 6.8 in. mean diameter. Figure 8.6 describes the same field configuration by means of $|\Delta\boldsymbol{B}|$ contours and emphasizes not only the singular point at which the field is maximum and the homogeneity is best, but also a singularity at larger radius at which $|\Delta\boldsymbol{B}| = 0$ and the homogeneity is poor. The radius of these two singular circles is shown as a function of the coil spacing in Fig. 8.7. It can be seen that for sample coils with longer radii the appropriate gap is smaller.

When the coils are operated with their fields aiding, the magnetic force tends to pull the coils together, and this force can be withstood by a flat Micarta plate between the coils. At zero gap the total force is 480 tons, but the average pressure is only 1100 psi, well within the compressive strength of Micarta. The thickness of the spacer plate determines the gap length, and provision is made to vary the gap by replacing the plate. Radial access to the magnetic volume can be had through six holes in the spacer plate, except when the gap is small enough to make such holes impractical. When the coils are energized with opposed currents, an axial force of the same magnitude tends

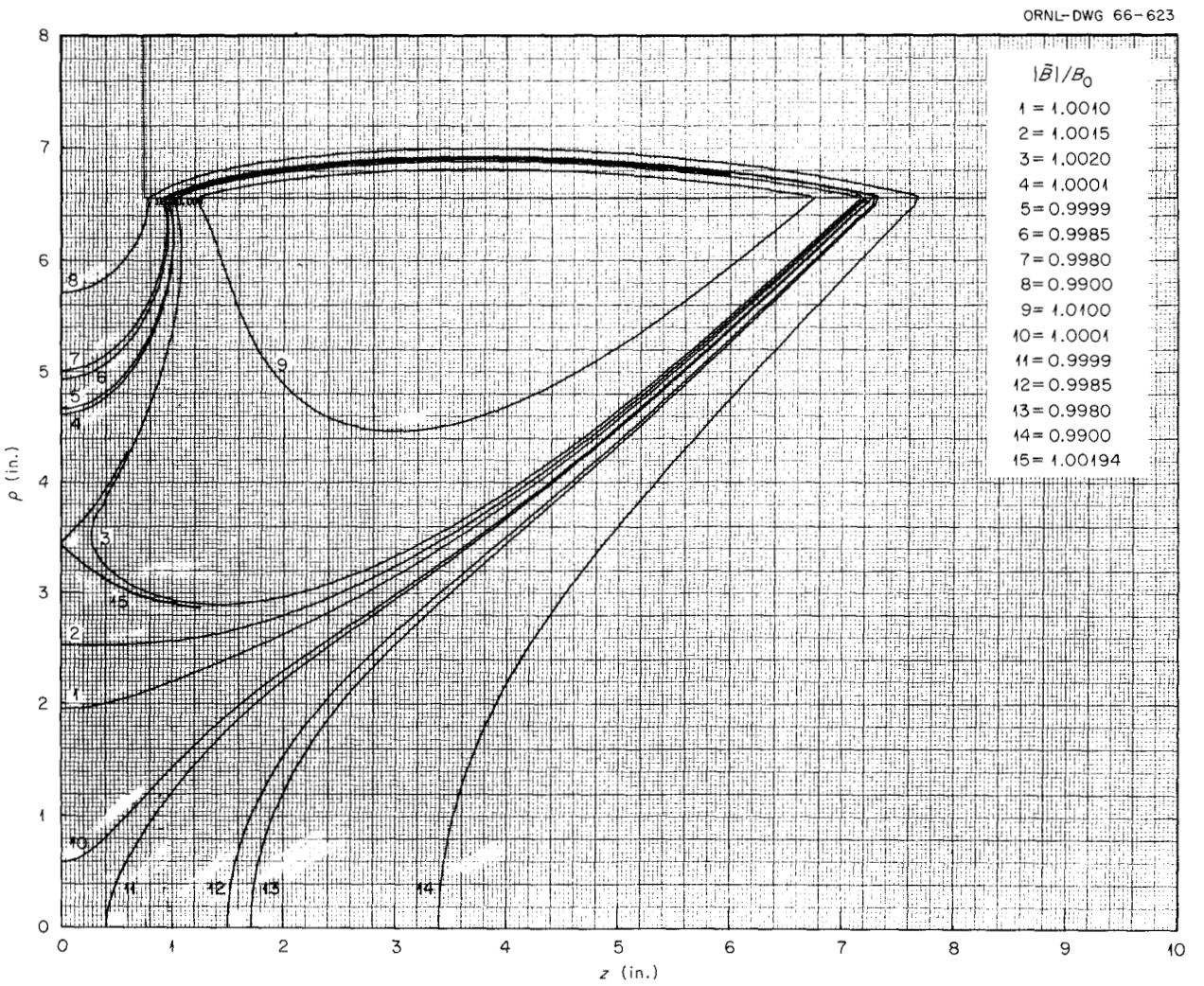

Fig. 8.5. $|B|$ Contours of the D Coils with Central Gap of 1.5 in.

to repel the coils, and the containment of the forces presents a more difficult problem. Strain gages will be mounted to determine the stress and deflection in the structural members and the coil in order to prove the soundness of the mechanical system.

Merely by replacing short electrical leads and inserting a structural sleeve in the bore, the currents in the D coils may be changed from aiding to opposing. The conversion from one gap length to another is only slightly more inconvenient if the desired gap is $2\frac{1}{4}$ in. or less. Although not now contemplated, larger coil spacings, such as the one required for the Maxwell position, would be possible by making certain structural modifications. In view of the versatility of the system, it seems of interest to note briefly its field properties in each of several configurations. For

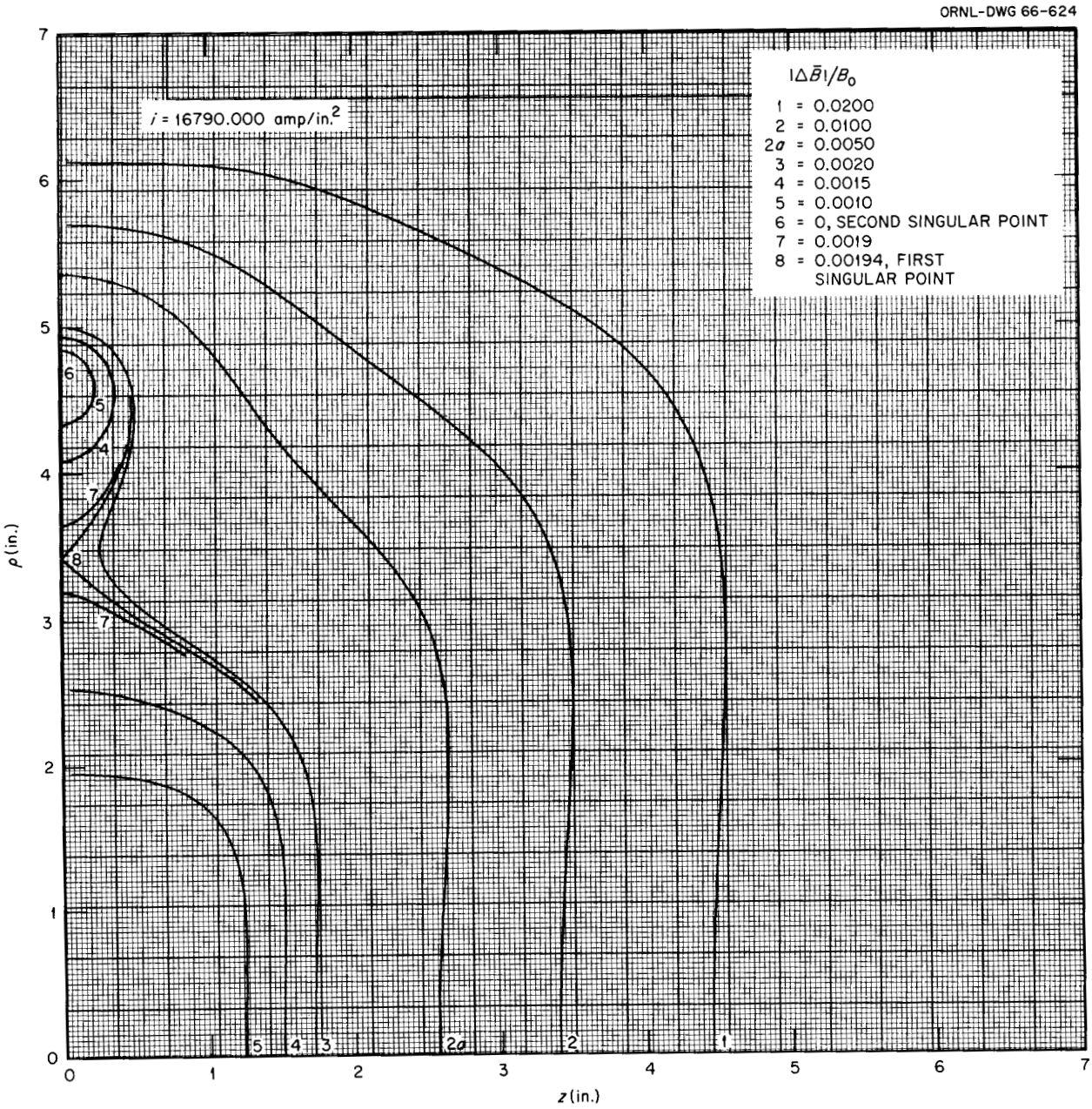

Fig. 8.6. $|\Delta B|$ Contours of the D Coils with Central Gap of 1.5 in.

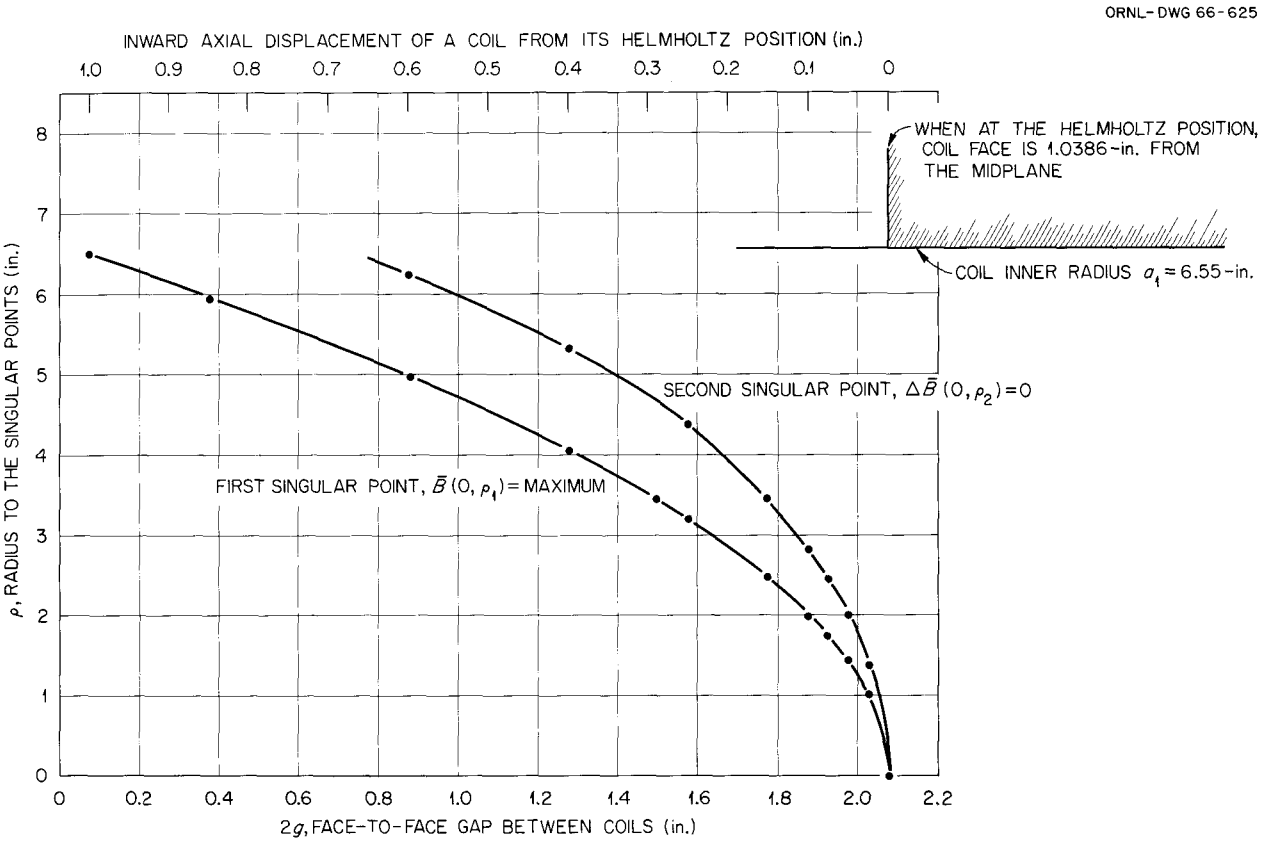

Fig. 8.7. ρ-Coordinate of First and Second Singular Points: $\partial B_z/\partial_\rho = 0$, and $B_z = B_0$.

computational purposes the current density is fixed at 16,790 amp/in.^{2}, and the dimensions of a coil are taken as: inner diameter, $2a_1$ = 13.1 in.; outer diameter, 35.6 in.; and length, 12.7 in. The winding depth is therefore 11.25 in., the mean diameter is 24.35 in., and the volume factor v of the coil pair is 77.8, where the total volume V of coil windings is given by $V = va_1^3$. The data given below and in Table 8.1 are due to M. W. Garrett.[10] When comparisons are made below between the D coils and other coil systems, these systems may have optimal size and (rectangular) shape, but are always considered to have uniform current density and to have the same power and inner radius as the D coils.

Zero Gap. – Moving the coils together gives a system which is almost completely dominated by the second-order term. As shown in Table 8.1 the error limits are small; however, the central field (Fabry factor) is 99% of the maximum obtainable with a second-order coil.

Oblate Position. – This is here considered to be the "normal" position of the coils. The center spacing is 96% of that of the Helmholtz case, making B_0 somewhat (2.9%) greater. The field in the midplane rises to a maximum of $1.00194B_0$ at a radius of 3.427 in. and then falls, reaching B_0 again at ρ = 4.632 in.

Helmholtz Case. – The field strength is down to 90% of the maximum obtainable with a single coil, but the error limits are greatly increased. The maximum field given by any fourth-order coil pair is only 2% greater than that of this case.

Maximum Gradient. – The Helmholtz position with opposing currents gives the maximum on-axis value of the gradient $\partial B_z/\partial z$ that can be obtained with the coils. The value listed in Table 8.1 is 30% more than for the Maxwell case and 89% of that given by coils optimally shaped for the purpose. The axial field reaches a peak of 33.25 kilogauss at 9.38 in. from the midplane.

[10] Private communication.

Table 8.1. Characteristics of Some D-Coil Configurations

Condition	Coil Spacing (in.)		Currents Aiding (+) or Opposing (−)	B_0 (kilogauss)	$\partial B_z/\partial_z$ at the Center of the Midplane (kilogauss/in.)	0.1% Error Limits[a] (in.)		1% Error Limits[a] (in.)	
	Center to Center	Face to Face				Axial	Equatorial	Axial	Equatorial
Zero gap	12.7	0	+	67.9	0	1.36	1.94	4.30	6.14
Oblate	14.2	1.5	+	63.4	0	2.48	3.90	6.80	11.40
Helmholtz	14.777	2.077	+	61.66	0	4.72	5.76	8.77	9.55
Maximum gradient	14.777	2.077	−	0	6.02	0.44	0.60	1.40	2.0
Maxwell	23.214	10.514	−	0	4.59	3.19	4.05	5.72	7.15

[a]In order to more nearly characterize a working volume, the dimensions given are equivalent to "diameters" rather than "radii" and are twice the corresponding values read from Figs. 8.3 to 8.6.

Maxwell Case. – The gradient is only 68% of the maximum obtainable, but is 92% of the maximum possible by means of a fourth-order coil pair. The axial field peaks at 39.88 kilogauss at $z = 12.4$ in.

8.3 SMALL-VOLUME, HIGH-FIELD MAGNET COILS

R. V. Neidigh J. G. Harris
J. N. Luton, Jr.

Plasmas of interest to the thermonuclear program have usually required magnetic volumes of at least a liter. However, some recent interest in collision-dominated plasmas may permit useful experiments in much smaller volumes, perhaps those of a few cubic centimeters. The corresponding reduction in the size of the magnet coils opens new possibilities in their design. For example, direct-current cryogenic coils become economically feasible in a larger number of cases. For both cryogenic and room-temperature coils, the use of much shorter coolant paths and higher coolant velocities makes possible higher power densities and greater magnetic field strengths. Finally, the reduced cost of the smaller coils will permit frequent alteration and rapid replacement of the coils, and the experiment should profit from greater flexibility and less downtime.

As the size of a coil is reduced, the cross-sectional area of its conductor must also be reduced, particularly if the same power supply is to be used. When the conductor size reaches a lower limit, say $^3/_{16}$ by $^3/_{16}$ in. (or the current density reaches an upper limit), it becomes necessary to abandon the often-used scheme[11] of an internally cooled conductor with water flow along the axis of the conductor and to replace it with a cooling scheme more suited to very high current densities and fabrication in the smaller sizes. The following sections describe two such arrangements, with a few preliminary test data obtained from prototypes. Although life tests[12] have not yet been extensively run, nor the coils well perfected, the early data have been sufficiently encouraging to warrant continuation of the work.

[11] *Thermonuclear Div. Semiann. Progr. Rept. Oct. 31, 1963*, ORNL-3564, pp. 121–25.

[12] Because of the occurrence of water-insulator-conductor interfaces, it is felt that coil life may be more limited than with coils wound from hollow tubular conductors.

8.3.1 Solid-Wire Pancake Coil (with Coolant Flow Perpendicular to the Coil Axis)

R. V. Neidigh J. G. Harris

Figure 8.8 shows a winding and cooling scheme especially applicable for small coils with restricted space at the ends. The two-layer pancake is wound from a single length of insulated solid conductor, potted in epoxy, and then machined on both sides to provide better cooling by exposing the bare copper directly to the coolant. Pure copper has a tendency to smear during machining. To prevent this effect from producing turn-to-turn shorts, the path traced by the cutting tool in going from one turn to the other was made relatively long, both by using conductors with generously rounded corners and by moving the cutting tool in circles having the same axis as the pancake. The latter procedure is easily carried out in a lathe and provides for an attack angle of the tool against the turn-to-turn insulation which is as small as

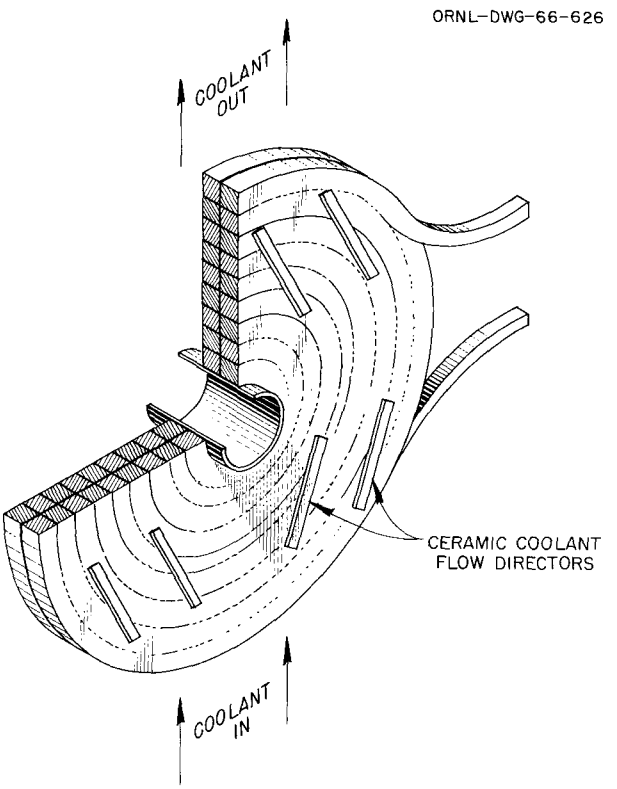

Fig. 8.8. Schematic Diagram of Solid Conductor Pancake.

the pitch angle of the conductor spiral. No difficulties have been experienced with shorts thus far. Figure 8.9 is a photograph of one of the pancakes ready for addition of the flow divertors and installation into a coil.

The test pancake of Figs. 8.8 and 8.9 was operated by R. L. Brown for 11 hr at a copper current density of 107,000 amp/in.^{2} (12 kw/in.^{3}), producing 9.6 kilogauss in a coil throat of $\frac{3}{8}$ in. Assuming the coil design will permit a space factor of 0.5, this would provide 60 ka/in.^{2} over the entire cross section of the coil winding, more than twice the current density of the Burnout V or DCX-1 coils. After the operating characteristics of the pancake were determined, its current was increased until failure occurred. The pancake failed either by shorting to the case or by local overheating and melting of the conductor, not under a ceramic flow director, but at the point where the conductor crosses over from one spiral to the other. As can be seen in Figs. 8.8 and 8.9, the pancake was oriented so that the crossover was downstream from the tube passing through the bore of the pancake. It was thus in the region where vortices would be expected to be continually formed and dissipated, with a resultant lowering of cooling effectiveness.

The conditions at which burnout occurred were, approximately:

Total current, amp	1700
Copper current density, amp/in.^{2}	182,000
Magnetic field in the throat, kilogauss	16.3
Conductor power density, kw/in.^{3}	43.5
Water flow, gpm	10
Water temperature rise, °C	7

An operational coil would be expected to be composed of several pancakes stacked together, with the ceramic flow directors then serving also as separators to maintain the proper gap between adjacent pancakes. A test assembly of two pancakes is now being built to determine what new difficulties might be introduced by the addition and simultaneous operation of other pancakes.

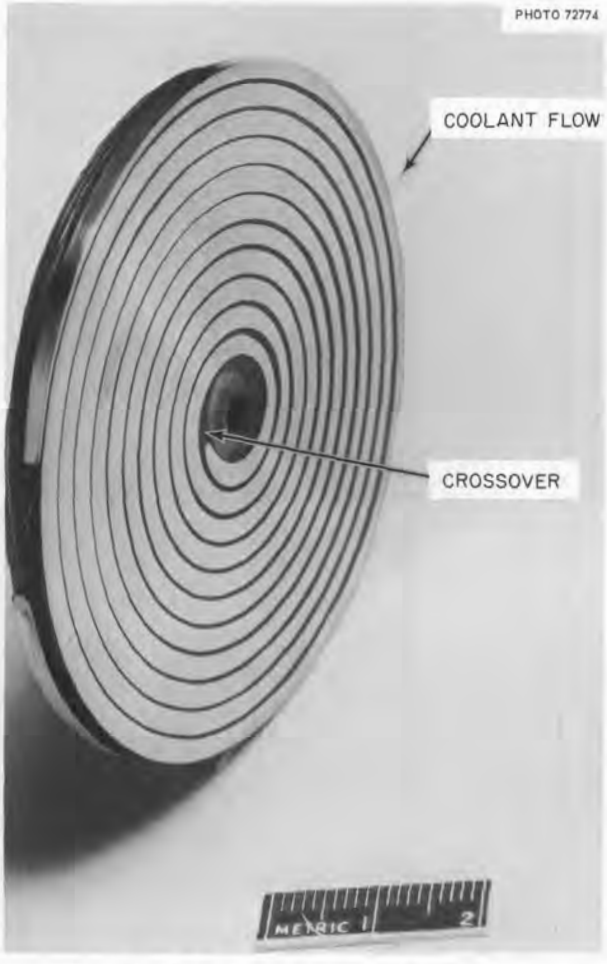

Fig. 8.9. Solid Conductor Pancake.

8.3.2 Ribbon Coil (with Axial Coolant Flow)

J. N. Luton, Jr.

One method of manufacturing magnet coils of moderate power density is to wind an insulated conducting ribbon into a spiral and to cool the conductor only at its edges. The method has been adapted to high current densities by commencing with a bare ribbon and inserting, during the winding, a series of insulated ribs between turns.[13] Cooling water is then forced parallel to the coil axis, through the gaps between the spacer ribs. The ribs themselves are aligned along radii, so that the radial forces can be carried outward to a supporting metal ring. The design requires high-purity cooling water and careful handwork for the inserting of hundreds to thousands of spacer ribs, and has not been much used. The coil described

[13] H. H. Kolm, *Proceedings of Symposium on Magnetic Field Design in Thermonuclear Research*, ORNL-2745, pp. 41–43 (Sept. 23, 1959). See also photograph on the frontispiece of *High Magnetic Fields* (Kolm, Lax, Bitter, Mills), MIT Press and Wiley, 1962.

herein makes axially cooled ribbon coils more practical by eliminating the spacer ribs and making the winding of the coil as simple as in the case of edge-cooled ribbon coils.

The new arrangement is wound from a copper ribbon which is smooth on one side and has small grooves in the other to serve as coolant passages. The "teeth" between the coolant passages are made much wider than the passages themselves, so that they can transmit forces radially outward regardless of their alignment. As a result, the grooves can be equally spaced, and so can be preformed in the ribbon before the winding of the coil is commenced.

Rather than attempt to machine shallow grooves across a thin copper ribbon, we chose to build a machine to form the channels by rolling. The rollers are about 4 in. in diameter and 10 in. long, one having rounded ribs 0.0165 ± 0.0005 in. high and the other being smooth but barrel-shaped to compensate for the bending of the rollers during operation. The rolling machine, designed by H. L. Watts, has been tried out, and produces ribbons of high quality. The water passages are uniform and have extremely smooth walls, their ends are free of burrs and other flow obstructions, and the whole ribbon is stronger as a result of the work hardening. The back side of the ribbon does show some waviness and some surface polishing under the coolant passages, due to the 11% elongation of the ribbon during rolling. Figure 8.10 shows conductor samples rolled from $\frac{1}{2} \times 0.035$ in. copper strip which had previously been annealed and acid cleaned.

Figure 8.11 is an exploded view of the first test coil. Cooling water flows from one of the round tubes into the space between the coil and the Lucite end flange, axially through the coil, and out through the other end header and tube. The water tubes are soldered to the case, as is the outer end of the ribbon, so that they can serve as one electrical terminal. The inner end of the ribbon is soldered to the central rod, which serves as the other terminal. In multicoil systems the coil might require end restraints, and supporting spokes were added to the end flanges to see if

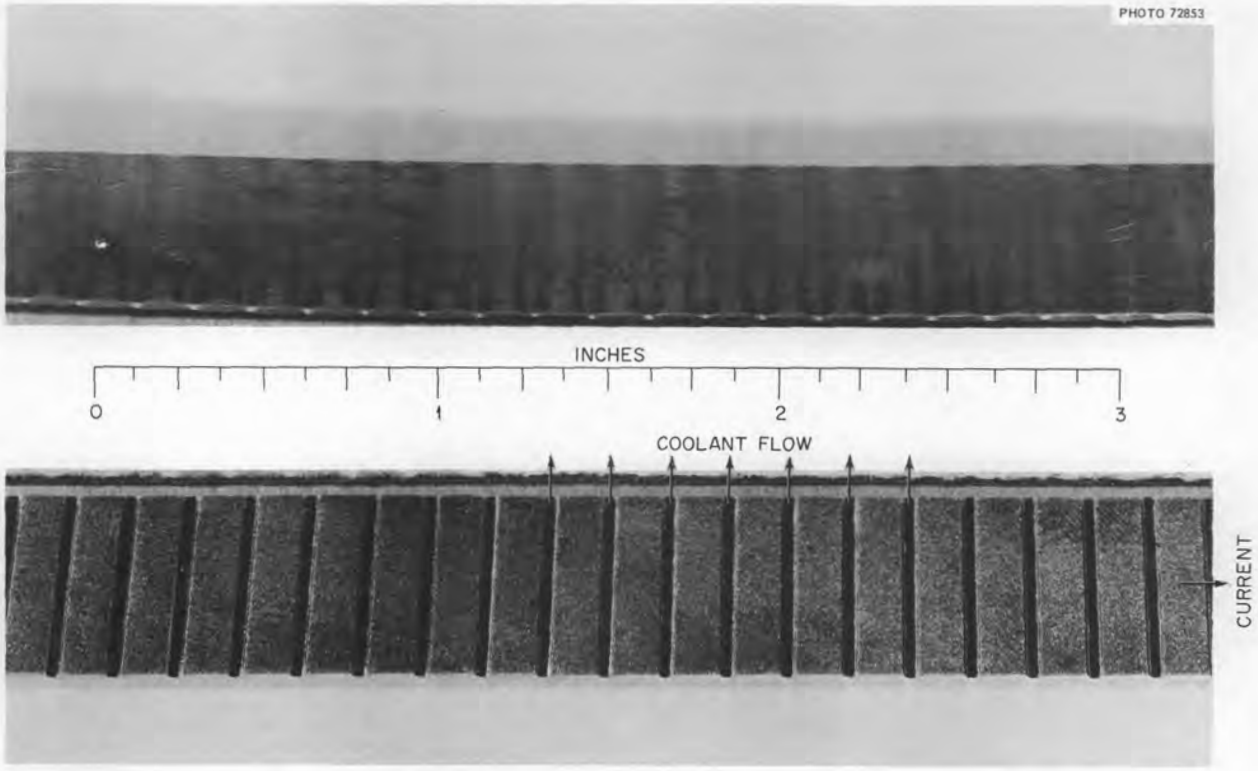

Fig. 8.10. Sample Ribbon Conductor, Showing Coolant Passages.

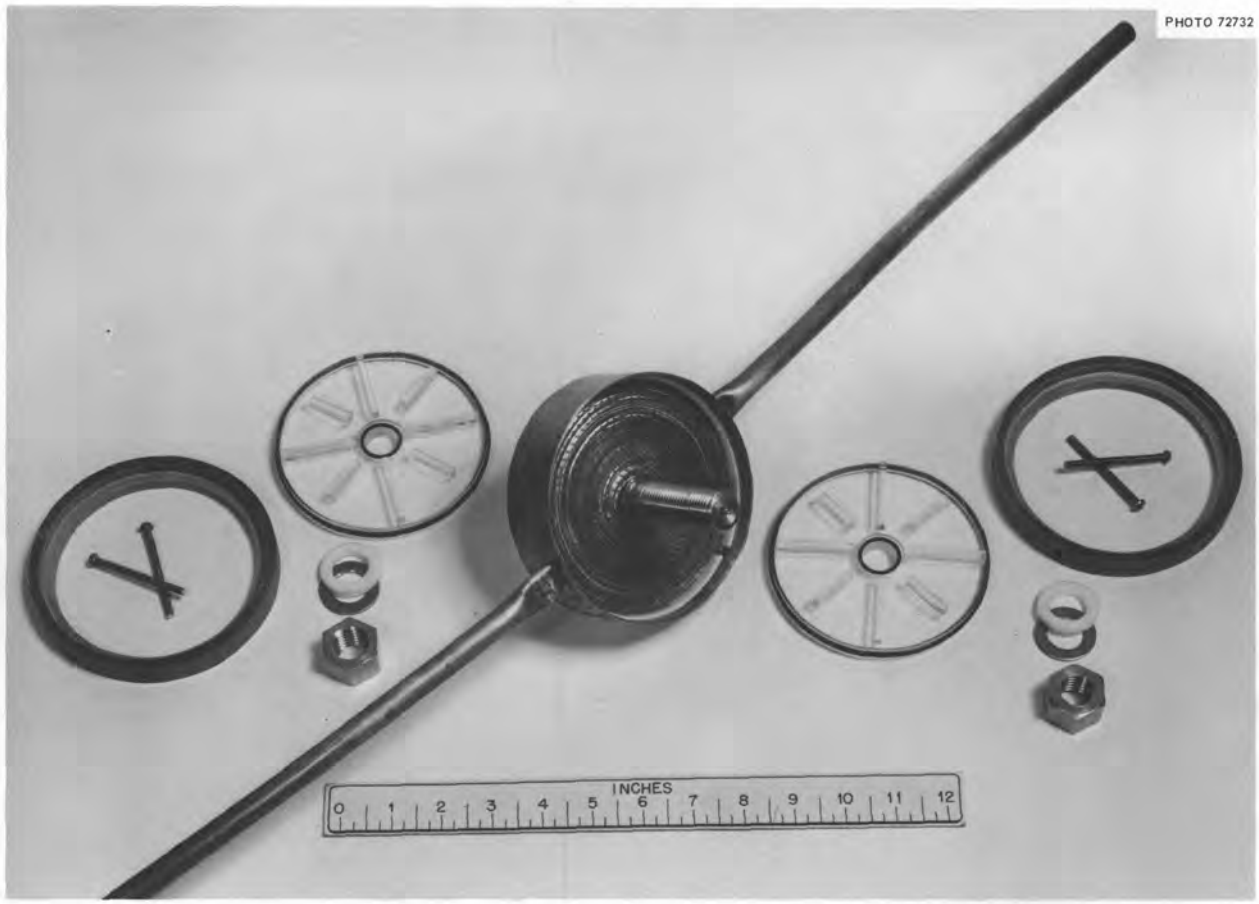

Fig. 8.11. Exploded View of First Ribbon Coil.

they caused unacceptably severe blockage of water paths. Figure 8.12 is an end view of the assembled coil, with a light source behind it to accentuate the coolant channels. Note that the teeth, being $2\frac{1}{2}$ times as wide as the grooves, never tend to collapse a radially adjacent groove by bearing on it only, but rather span the groove and press on adjacent teeth. It can also be seen that the Lucite spokes are not wide enough to block thermally (azimuthally) adjacent water channels.

In order to save radial and axial space, the first test coil had only one entrance and one exit tube, and the Lucite end spokes, which determine the header depth, were only 0.2 in. thick. There was thus reason to believe that the flow distribution would be poor, and qualitative tests confirmed it: When a slug of dye was inserted in the inlet tube, a vortex pattern was easily visible in each sector of the inlet header, except in the sectors traversed by a diameter drawn through the entrance and exit headers; and the dye at the centers of these vortices remained for a relatively long period after other parts of the header were swept clean. The question still remained as to whether the cooling degradation due to the vortices was worse than that due to the blockage of passages by the Lucite spokes. This question was answered, for one flow, by raising the coil current until failure occurred. Overheating, arcing, and conductor melting occurred in the central portion of the sector between the spokes, while the conductor portions directly under the spokes were not damaged. At failure, the current was 1570 amp, the flow was 7.9 gpm, and the bulk water temperature rise was 15°C.

The coil case was then fitted with larger inlet and outlet tubes, four each symmetrically spaced,

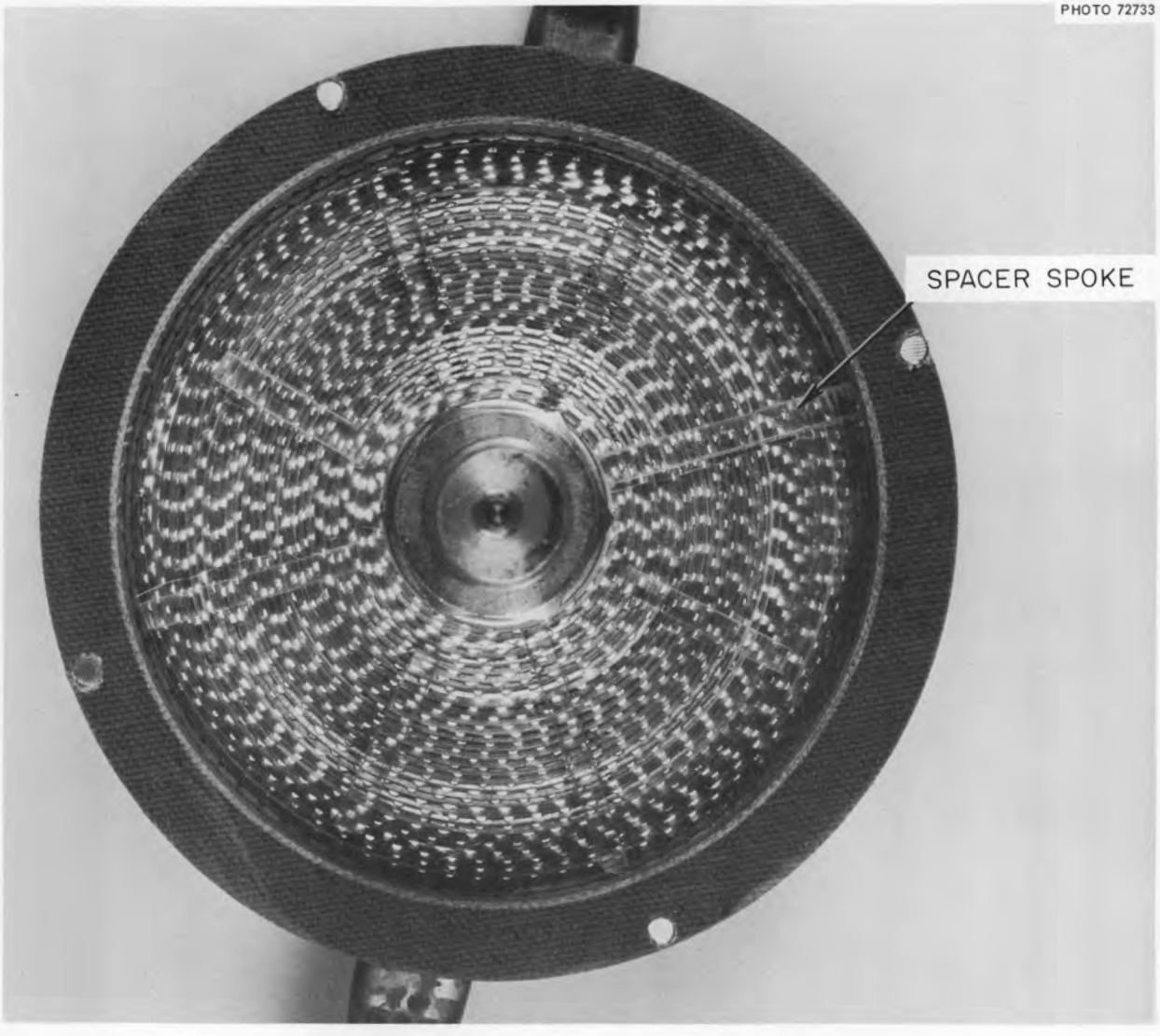

Fig. 8.12. End View of First Ribbon Coil.

and a second ribbon was wound on the central rod. The water flow increased to 55 gpm at the pressures used with the first coil, showing the tubes had been the major flow restriction in the original arrangement. Dye patterns suggested that large vortices were eliminated. The coil was then run for 52 hr at 1000 amp and 50 gpm, without noticeable change in its resistance or appearance. The current was later raised to the limit of the power supply, without damage to the coil. The operating conditions[14] at this point were as listed in Table 8.2. Provision is being made to connect the coil to a larger power supply in the magnet laboratory.

8.4 IRON-CORE ELECTROMAGNET PRODUCING A MAGNETIC WELL WITH NONZERO MINIMUM FOR PLASMA CONFINEMENT

I. Alexeff

Note: This development is discussed in the Magnetics Section of this publication for ease of reference.

[14]We gratefully acknowledge the contributions of O. M. Thomas of the General Engineering and Construction Division of ORNL, who ran the tests on both coils.

Table 8.2. Parameters and Test Conditions of Second Ribbon Coil

Conductor width and length	$\frac{1}{2}$ in. × 26.75 ft
Conductor thickness	0.0435 in. at teeth, 0.0293 in. at web
Coolant channels	0.042 in. wide; 0.0142 in. deep; on 0.165-in. centers
Insulation	$\frac{1}{2}$- by 0.005-in. Mylar ribbon
Total current	2220 amp
Maximum current density in the copper	151,500 amp/in.^{2}
Minimum current density in the copper	102,100 amp/in.^{2}
Overall current density in the winding	91,500 amp/in.^{2}
Coil voltage	29.5 v
Power	65 kw
Water flow	84 gpm
Pressure drop between end headers	22.1 psi
Total pressure drop	90 psi
Surface cooling rate	1277 w/in.^{2}
Inner diameter of winding	0.31 in.
Outer diameter of winding	5.39 in.
Number of turns	43.4
Calculated central field	27.1 kilogauss

A basic problem in the magnetic confinement of a dense plasma for nuclear fusion purposes is the tendency of the plasma to migrate toward regions of lower magnetic field strength. In a conventional "magnetic mirror" system, the magnetic field decreases radially from the axis of the machine, and the result is that "flutes," or projections, from the confined plasma move radially and are lost on the wall.[15] These flutes can lead to serious plasma losses.

One technique for preventing plasma losses via flutes is to place the plasma inside a "magnetic well," in which the absolute value of the magnetic field increases in every direction from the center. However, single-particle orbit theory shows that such a well must have a nonzero minimum in the magnetic field if excessive plasma losses are to be avoided.[16] An experimental demonstration of the effectiveness of such a magnetic well has been given by Gott *et al.*,[17] and theoretical discussions of coil configurations producing such magnetic wells have been given by Furth,[18] Andreoletti,[19] and Larkin.[20]

A difficulty in the design of air-core coils for such magnetic wells is that for strong magnetic fields, very high power densities must be maintained in the coils. The high power densities lead not only to excessive power consumption but also produce difficulties in keeping the coils intact.

One way of avoiding a high power density is to use an iron-core electromagnet. The magnetomotive force is produced in a region far from the plasma by large coils using a more moderate power density and operating at a higher efficiency. The magnetic flux is conveyed to the region of interest

[15] D. J. Rose and M. Clark, Jr., *Plasmas and Controlled Fusion*, p. 264, Wiley, New York, 1961.

[16] *Ibid.*, p. 268.

[17] Yu. V. Gott, M. S. Ioffe, and V. G. Telkovsky, *Nucl. Fusion*, 1962 suppl, Part 3, 1045–47 (1963) (in Russian).

[18] H. P. Furth, *Phys. Rev. Letters* 11, 308 (1963).

[19] J. Andreoletti, *Compt. Rend.* **257**, 1235 (1963) (in French).

[20] F. M. Larkin, CLM-R-37 (June 1964) (unpublished).

via iron flux conductors. The magnetic well is then constructed by means of properly shaped pole pieces.

Initial experiments[21] with magnetic-well-type magnetic fields at ORNL revealed the power difficulties caused by the appropriate electromagnets. Therefore, at the suggestion of R. V. Neidigh, studies of iron-core magnets were undertaken, and a hybrid iron–air-core magnet was developed by P. A. Thompson.[22] In this report is discussed a magnet that is purely an iron-core device.

An experimental model of the iron-core electromagnet that produces a magnetic well with a nonzero minimum is shown in Fig. 8.13, and a sketch of the pole pieces with typical lines of the magnetic field is shown in Fig. 8.14. As shown in Fig. 8.14, this particular pole-piece configuration produces a field corresponding to that of a quadrupole Ioffe machine. However, higher-order multipole systems obviously can be produced in an analogous manner. In high-flux magnets the pole pieces would be fed with iron flux conductors of large cross section.

---

[21] *Thermonuclear Div. Semiann. Progr. Rept. Oct. 31, 1963*, ORNL-3564, p. 44.

[22] *Thermonuclear Div. Semiann. Progr. Rept. Apr. 30, 1964*, ORNL-3652, p. 125.

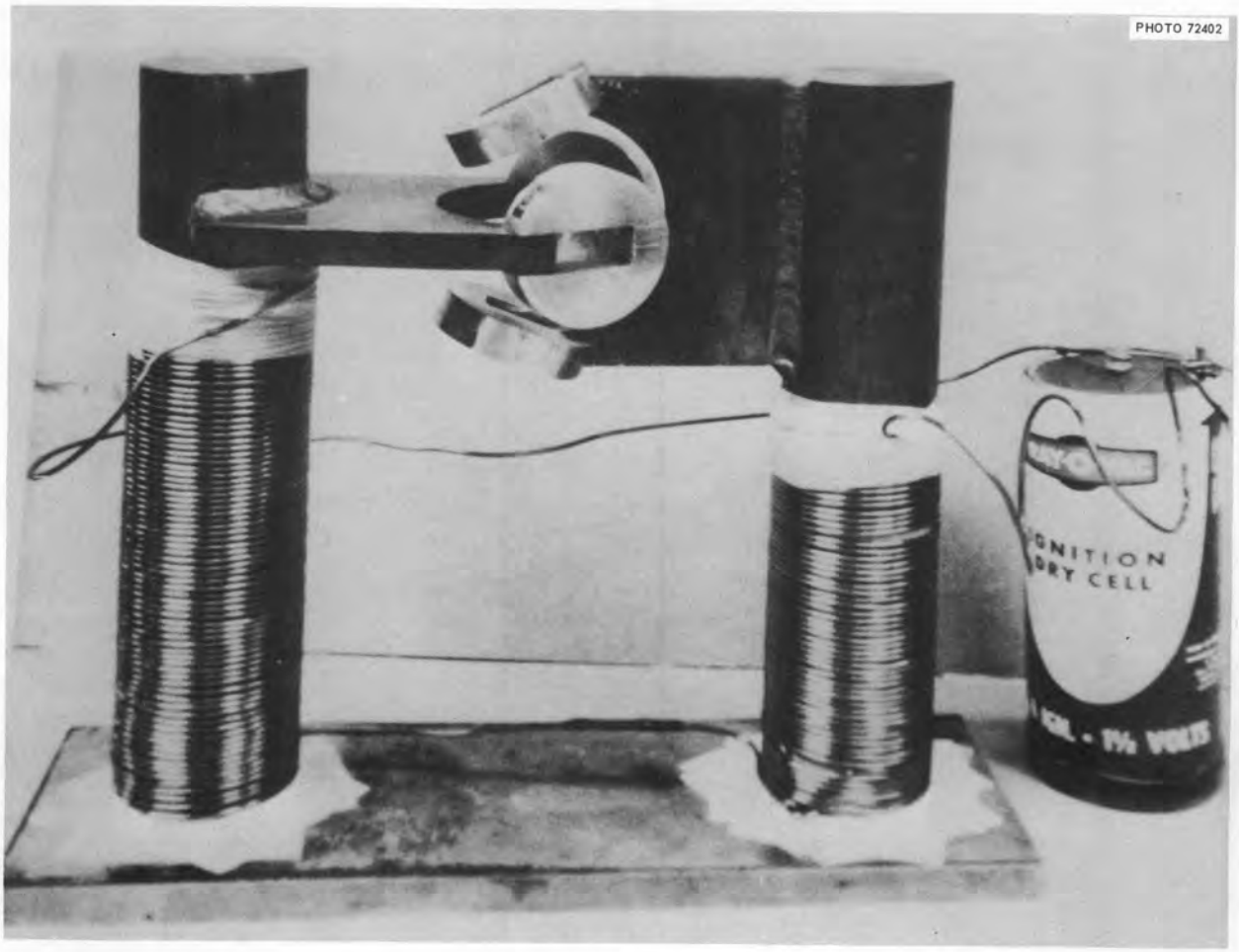

Fig. 8.13. Test Electromagnet. The volume enclosed is 3 in. in diameter. The pole pieces are made of iron 4 in. wide by 1/2 in. thick. Each pole piece has a 3-in. semicircle cut out from its end. The pole pieces are placed at right angles to each other and enclose a spherical volume 3 in. in diameter. Each pole piece is equipped with two circular iron shims 2 in. in diameter by 1/2 in. thick. The shims are slotted to permit adjustment relative to the pole pieces.

ORNL-DWG 66-627

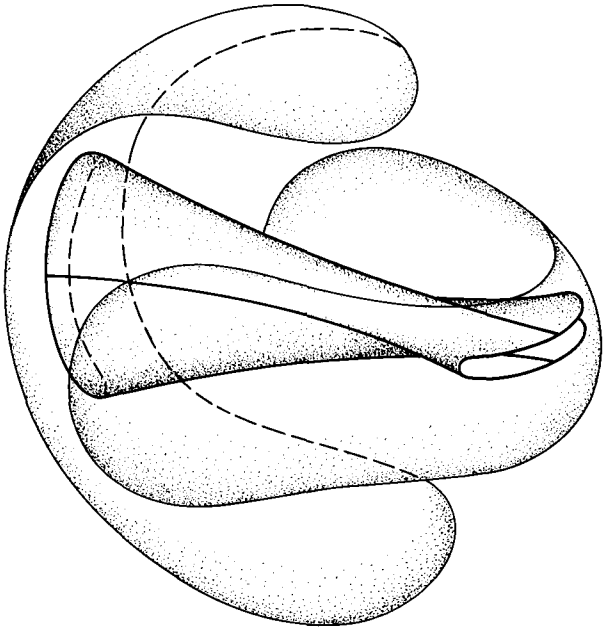

Fig. 8.14. Artist's Conception of an Iron-Core Magnet with Ideal Pole Pieces (Light Lines) and Typical Lines of the Magnetic Field (Dark Lines).

Extensive tests were made on the magnet shown in Fig. 8.13. For one particular setting of the pole-piece shims, systematic magnetic probing showed that a magnetic well was present in the center which increased in all directions by more than a factor of 3.5. By swinging the adjustable shim pieces in or out from this position, the mirror ratio increased or decreased respectively. The region available for coil windings in such a device as the one shown is obviously much larger than that available to an air-core coil producing an equivalent field. The equivalent air-core coil would correspond in size to the gap between the pole pieces at their closest approach, and thus the coil would look like the seam of a tennis ball. Thus this iron-core magnet produces a magnetic field similar to that produced by the air-core coil in ref. 19.

In summary, the advantages of the iron-core magnet over the air-core coil are as follows:

1. The iron-core magnet is much more easily fabricated, due to lower power density in the coils.
2. The iron-core magnet has much less power consumption for a given field over a given volume.
3. The mirror ratio is easily changed by swinging the pole-piece shims in or out.
4. Random access to the plasma volume is available by simply drilling holes through the iron. (Note that the experimental model has large holes in the pole pieces.)

The disadvantages of such an iron-core magnet are the following:

1. The maximum magnetic field at the surface of the pole pieces is limited to about 24 kilogauss, due to saturation of the iron (Permalloy). At the point of minimum B the magnetic field is limited to about 24 kilogauss $\div$ m, where m is the maximum mirror ratio. The value of 24 kilogauss $\div$ m holds only for an ideal magnet and may be lower in practice.
2. The escape route of plasma being lost along lines of magnetic force is blocked by the iron pole pieces.

Since the fabrication of such nonzero magnetic wells using iron-core magnets is not difficult, these iron-core magnets may be of use in test devices designed to study the confinement of plasma.

The author appreciates the help of John M. Lohr in performing the magnetic measurements; of W. F. Gauster, W. D. Jones, and R. V. Neidigh for helpful discussions; and of J. G. Harris, who constructed the experimental apparatus.

8.5 RECENT WORK ON SUPERCONDUCTIVITY AT THE THERMONUCLEAR DIVISION

8.5.1 Guidelines of the Working Program

W. F. Gauster

The research and developmental work in superconductivity at the Thermonuclear Division is motivated by the attempt to produce magnetic fields without ohmic losses for thermonuclear research facilities. This task would become of greatest importance as soon as a breakthrough in research might open the engineering field of controlled thermonuclear power production. Another desirable application of lossless magnetic field production is the proton shielding of space vehicles.

Thus, work on superconductivity in this Division is sponsored by the Thermonuclear Branch of the AEC and by the George C. Marshall Space Flight Center of NASA.

We believe that the development of superconducting, large-volume, high-field magnets, especially for nonaxisymmetric fields (for instance B-minimum fields or noncircular shielding magnets) can be considerably facilitated if the relevant physical properties of the high-field superconductors are better understood. From this unifying point of view, the motivation of the rather greatly diversified working program, which has been under way here during the last few years, can be better understood:

1. Micro Hall probes with high resolution for scanning magnetic fields have been successfully developed.[23]
2. These micro Hall probes are being employed to scan the magnetic fields in gaps of high-field superconductor cylinders in longitudinal fields in order to determine the flux density distribution. Similar measurements are being made in the midplane gap of high-field superconductor solenoids.[24]
3. Magnetic moment measurements on high-field superconductors have been performed here with a ballistic method.[25] Furthermore, we developed vibrating magnetometers,[26] which are working satisfactorily since lock-in amplifiers have been used. However, simpler arrangements for magnetic moment measurements which employ mechanical or electronic flux integration also will be used here in the near future.
4. Flux jump measurements were made on small superconducting coils and on (solid and hollow) cylinders.[27] It is hoped that especially the second group of experiments will eventually greatly contribute to the understanding of the performance of the high-field superconductors. Experiments covering the range of isothermal to adiabatic field change are under way.
5. Theoretical work on the macroscopic theory of superconductors of the second and third kind is being done which represents a most desirable backing of our previously mentioned experimental work.[28]
6. Our magnet laboratory provides an almost unique possibility of making tests on superconducting winding elements in large-volume, high-intensity fields.[29] These tests include the measurement of critical currents under largely diversified experimental conditions and were recently extended to flux creep measurements, which are of great importance for the understanding of the performance of "stabilized" superconducting magnets.[30]

The following sections report on those phases of our superconductivity research program in which noteworthy progress has been achieved recently.

8.5.2 Field Distributions in Hard Superconducting Cylinders with Adiabatic Field Change

W. F. Gauster H. A. Ullmaier

Introduction. – In the previous semiannual report experiments with hollow and solid cold-worked Nb–25% Zr cylinders were described.[31] Subsequently, it was possible to develop the following theoretical approach, which allows an accounting for these experimental results with fair accuracy.

If a longitudinal field around a hard superconducting cylinder is adiabatically raised, flux penetrates. The distance ξ of the flux front [i.e., the surface inside the cylinder which separates the regions with ("wave") and without flux] from the cylinder surface is a time-dependent function $\xi(t)$.

The distance of a point inside the wave from the wave front is x. Of course, $x \leqq \xi$. The distribution of any quantity, say the flux density B, inside the wave is in general a function of x and of the time t,

$$B = B(x,t) .$$

[23] *Thermonuclear Div. Semiann. Progr. Rept. Apr. 30, 1965*, ORNL-3836, p. 97.

[24] See sect. 8.5.3 of this report.

[25] *Thermonuclear Div. Semiann. Progr. Rept. Oct. 31, 1963*, ORNL-3564, p. 118.

[26] *Thermonuclear Div. Semiann. Progr. Rept. Oct. 31, 1964*, ORNL-3760, p. 91.

[27] *Thermonuclear Div. Semiann. Progr. Rept. Apr. 30, 1965*, ORNL-3836, p. 103; and sect. 8.5.2 of this report.

[28] See sect. 8.5.4 of this report.

[29] *Thermonuclear Div. Semiann. Progr. Rept. Oct. 31, 1963*, ORNL-3564, p. 105.

[30] K. R. Efferson, ORNL-TM-1266 (prepared for George C. Marshall Space Flight Center, NASA, Government Order No. H-76798), p. 2 (September 1965).

[31] H. A. Ullmaier, *Thermonuclear Div. Semiann. Progr. Rept. Apr. 30, 1965*, ORNL-3836, p. 103.

The speed of the flux front is[32]

$$v_{ff} = \frac{d\xi}{dt} = \left(\frac{\partial B/\partial t}{\partial B/\partial x} \right)_{x = 0}$$

The change of flux will induce an electromotive force. The electric field strength E on the surface of a cylinder with the radius r is

$$2\pi r E = - \frac{d\phi}{dt} . \qquad (1)$$

Since E has the same direction as the shielding current density J_d,[33] an energy per unit volume of

$$dW = - E J_d \, dt = \frac{J_d}{2\pi r} \, d\phi \qquad (2)$$

is dissipated. This leads to a temperature rise dT. Under adiabatic conditions

$$\frac{J_d}{2\pi r} \, d\phi = c(T, B) \, dT , \qquad (3)$$

where $c(T, B)$ is the specific heat in the superconducting state at the temperature T and the field B.

Another basic relation is Maxwell's equation,

$$\nabla \times \boldsymbol{H} = \boldsymbol{J} + \dot{\boldsymbol{D}} ,$$

which reduces for the one-dimensional cylindrical geometry, and when $\dot{\boldsymbol{D}}$ is neglected, to

$$J = \frac{\partial H}{\partial x} .$$

This current density J can only be identified with the dissipative current density J_d if a definition of the field strength H is used which holds for the "macroscopic" description of superconductors as set forth in Sect. 8.5.4. If we employ the "semi-microscopic" description for not too high[34] flux densities B, we can simply write

$$\boldsymbol{B} = \mu_0 \boldsymbol{H} ,$$

and therefore

$$J = \frac{1}{\mu_0} \frac{\partial B}{\partial x} . \qquad (4)$$

The current density determined in this way is, however, not the dissipative current density J_d as used in Eqs. (2) and (3). To identify J with J_d might lead to appreciable discrepancies, especially for fields near the lower critical field strength H_{c1}. Furthermore, it must be pointed out that in the following calculations the flux density B is supposed to be continuous at the surface of the superconducting cylinder; that is, London surface currents are neglected. An appreciable error might result, especially for low values of the external field. Nevertheless, for the time being, we will disregard these facts in order to be able to develop a simple calculation method which allows checking, with fair approximation, the experimental results. Additional basic experiments are under way, with the goal to understand more fully the performance of hard superconducting cylinders in changing longitudinal fields.

Field Distribution in a Semi-Infinite Slab. – First we consider a hard-superconducting semi-infinite slab ($r \to \infty$) with zero initial conditions (the whole material in "virgin state," i.e., $B = 0$ and $T = T_0$). The following step-by-step method could be used for determining the distributions of B, T, and J. The designations in Fig. 8.15a are self-explanatory. For the wave front

$$\frac{\partial B}{\partial x} = \mu_0 J(T, B) = \mu_0 J(T_0, 0) = \mu_0 J_{b0} \qquad (4a)$$

is constant. Therefore (for sufficiently small s)

$$B_{10} = B_{21} = B_{32} = \ldots = \mu_0 s J_{b0} . \qquad (5)$$

The flux increase per unit length (in the z direction) is

$$\phi_{10} = \phi_{21} = \phi_{32} = \ldots = \tfrac{1}{2} \, s B_{10} . \qquad (6)$$

From Eq. (3)

$$T_{10} = T_{21} = T_{32} = \ldots = T_0 + \frac{J_{b0}}{c(T_0)} \, \phi_{10} , \qquad (7)$$

and therefore

$$J_{21} = J_{32} = J_{43} = \ldots = J(T_{21}, B_{21}) . \qquad (8)$$

---

[32] See also S. L. Wipf and M. S. Lubell, *Phys. Letters* **16**, 103 (1965).

[33] J_d is the dissipative current density (see sect. 8.5.4).

[34] A. M. Clogston *et al.*, *Phys. Rev. Letters* **9**, 262 (1962); A. M. Clogston, *Phys. Rev. Letters* **9**, 266 (1962); and B. S. Chandrasekhar, *Appl. Phys. Letters* **1**, 7 (1962).

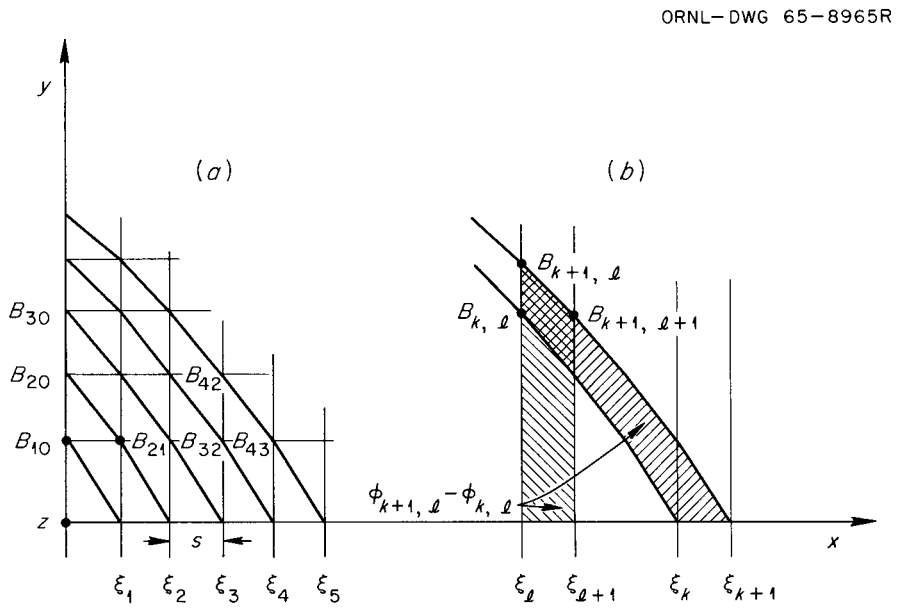

Fig. 8.15. Step-by-Step Calculation of the B Distribution in a Semi-Infinite Slab.

Finally

$$B_{20} = B_{31} = B_{42} = \ldots = B_{21} + \mu_0 s J_{21} . \quad (9)$$

The succeeding values of flux increase to be substituted in Eq. (3) can be easily determined; see Eq. (10). This calculation procedure, which can be continued in a similar way, shows that for the case of a semi-infinite slab the distributions of B, T, and J inside the wave move along with the wave; that is, B, T, and J are functions of x only.

In this calculation it has been assumed that the gradient $\partial B/\partial x$ of the flux density distribution in Eq. (4) does not depend on the rate of rise $\partial B/\partial t$ of the flux density, that is, $J(T, B)$ represents the critical-state current density. A more exact calculation should consider the dynamic behavior of moving fluxoids, which might be appreciably influenced by the temperature gradient too.

It would be possible to write a computer code based on Eqs. (4) to (9). In the special case of a slab the distributions can be expressed in a closed form if we replace the general expression $c(T, B)$ in Eq. (3) by Eq. (14). Then we can proceed as follows:

We consider the wave positions ξ_k, ξ_{k+1}. The flux increase $\phi_{k+1,l} - \phi_{k,l}$ is the difference between the areas bounded by the curve segments $k + 1$ and k. Therefore (see Fig. 8.15b),

$$\phi_{k+1,l} - \phi_{k,l} = \frac{s}{2}(B_{k+1,l} + B_{k+1,l+1}) . \quad (10)$$

Going to the limit $s \to dx$, Eq. (3) (for the case of a semi-infinite slab, $2\pi r$ must be omitted) and Eq. (10) yield

$$J\, d\phi = JB\, dx = \frac{1}{\mu_0}\frac{\partial B}{\partial x} B\, dx$$

$$= \frac{B}{\mu_0} dB = c(T)\, dT . \quad (11)$$

Therefore for any distance x inside the wave the relation

$$\frac{B^2}{2\mu_0} = \int_{T_0}^{T} c(T)\, dT \quad (12)$$

is valid. This equation applied to the surface of the superconducting slab is the flux jump condition given by Wipf and Lubell.[32]

In order to determine the functions $B(x)$, $T(x)$, and $J(x)$, we make the following assumptions:

1. In the range of interest the critical temperature T_c can be approximated by

$$T_c = T_{c0} - bB \ , \qquad (13)$$

where T_{c0} is the critical temperature at $B = 0$.[35]

2. The specific heat c for Nb-Zr will be approximated by

$$c = kT^4 \ . \qquad (14)$$

For Nb–25% Zr, $k = 4.65$ joules m^{-3} $(°K)^{-5}$ (see ref. 36). Equation 14 is a numerical fit of experimental results and seems to contradict the T^3 law of the lattice specific heat. In fact, for superconducting Nb_3Sn, the specific heat follows closely the expression

$$c = KT^3 \ ,$$

where $K = 25.5$ joules m^{-3} $(°K)^{-4}$ (see ref. 37). It must be considered that these measurements have been made in zero fields. There might be an appreciable influence of the flux density.

3. The expression

$$J(T, B) = J_{b0} \frac{T_c - T}{T_c - T_0} f(B) \qquad (15)$$

is considered to be a sufficiently good approximation. In this respect two more basic experiments are needed. It should again be emphasized that $J(T, B)$ represents the critical value of the current density due to flux creep which considers only approximately the actual dynamic performance.

The term $f(B)$ is a constant if the model of C. P. Bean and H. London is used. For Kim's model

$$J = J_{b0} \frac{T_0 - T}{T_c - T_0} \frac{B_0}{B_0 + B} \qquad (16)$$

4. The external field is raised rapidly enough to be almost adiabatic, but slowly compared with the electromagnetic diffusion time.[38]

Considering Eqs. (13) to (15), we obtain

$$dx = \frac{1}{\mu_0 J_{b0}} \frac{T_{c0} - T_0 - bB}{T_{c0} - bB - [(5B^2/2k\mu_0) + T_0^5]^{1/5}} \times \frac{dB}{f(b)} \ . \qquad (17)$$

We integrated this equation for various forms of $f(B)$ and $T_0 = 4.2°K$ (Fig. 8.16). If the external field is very slowly raised, the isothermal wave front (Fig. 8.16, curve a) results. In Fig. 8.17 isothermal (solid lines) and adiabatic (dotted lines) flux distributions are compared.

Equation (12) holds only if the wave front does not hit a boundary before the flux jump condition has been reached. For $T = T_c$, the current density J becomes zero and therefore ξ approaches ∞. Keeping this fact in mind the following condition for the temperature dependence of B_{FJ} (the external flux density where flux jump occurs) is obtained from Eq. (17):

$$bB_{FJ} + \left(\frac{5B_{FJ}^2}{2k\mu_0} + T_0^5 \right)^{1/5} = T_{c0} \ . \qquad (18)$$

This dependence is represented in Fig. 8.18.

Experiments show that the B_{FJ} values calculated by Eq. (18) are about 15% higher than the measured values. A careful theoretical check and some pertinent new basic experiments are under way.

Field Distribution in Cylinders. – For superconducting cylinders the distributions of the quantities B, T, and J are not functions of x alone and therefore do not move undistorted with the flux wave. We have developed a numerical integration method similar to that described previously for the semi-infinite slab. It is based on Eqs. (3) and (13) to (16). By means of a computer program, flux density distributions similar to that shown in Fig. 8.17 have been determined.

If the wave reaches the axis of a solid, or the inner surface of a hollow cylinder, the computation procedure must be modified. Small arbitrary steps of B on the inner boundary are assumed which lead to ϕ, T, and J values in a similar way as described above. It is also possible to consider

---

[35] Equation 13 is in good agreement with the Bardeen-Ginzburg relation $H_{c2} = H_{c2}(0)(1 - T/T_c)(1 + T/T_c)^{-1}$, which has been tested experimentally for several cases; see S. H. Goedemoed *et al.*, *Physica* **30**, 18 (1964) and B. S. Chandrasekhar *et al.*, *Phys. Letters* **5**, 18 (1963).

[36] El Bindari and M. M. Litvak, *J. Appl. Phys.* **34**, 2913 (1963).

[37] L. Vieland and A. W. Wicklund, RCA Technical Report AFML-TR-65-169, p. 17 (June 1965).

[38] Y. B. Kim, C. F. Hempstead, and A. R. Strnad, *Phys. Rev. Letters* **13**, 794 (1964).

initially trapped fields. Figure 8.19 shows the flux distribution in a hollow cylinder with previously isothermally trapped flux. The shaded areas indicate the adiabatic flux changes. Additional computer results compared with experimental data will be published later.

The following final remark seems to be important. If the shape of the magnetic wave penetrating the superconducting cylinder has been calculated, it is possible to verify experimentally these results in various ways: For instance, by measuring the critical external field strength H_{FJ}; by oscillo-

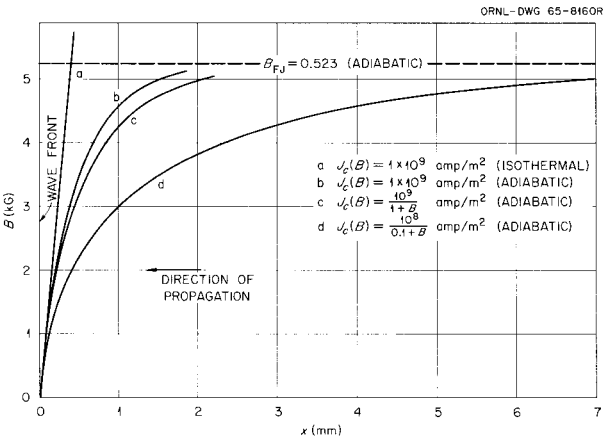

Fig. 8.16. Magnetic Waves in a Slab of Nb–25% Zr.

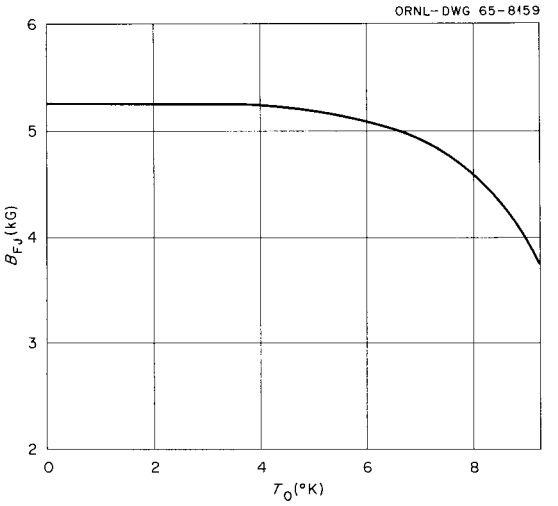

Fig. 8.18. Dependence of B_{FJ} on the Bath Temperature T_0.

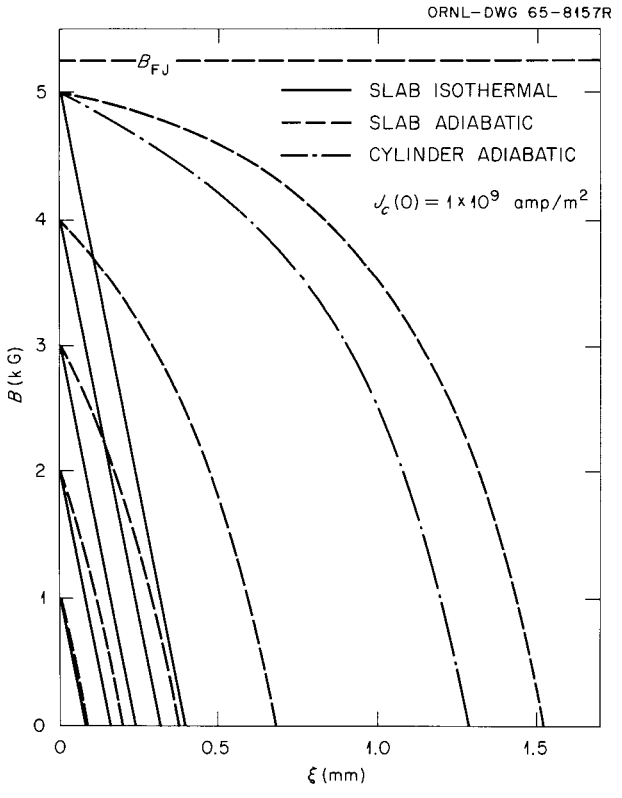

Fig. 8.17. Flux Distribution for Isothermal and Adiabatic Field Changes in Nb–25% Zr.

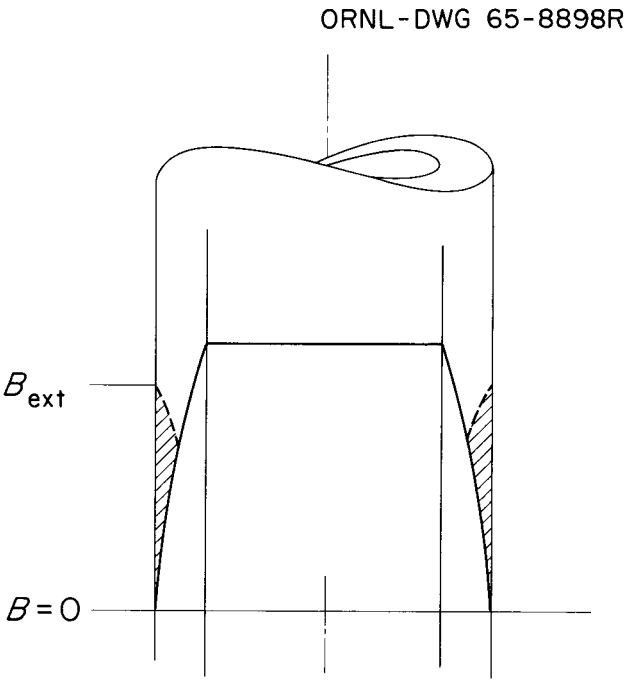

Fig. 8.19. Flux Distribution in a Hollow Cylinder with Initially Trapped Flux.

graphing the voltage induced in a pickup coil; and, in case of a hollow cylinder, by observing the time dependence of the internal field strength $H'(t)$ upon the external field strength $H(t)$. Presently such experiments are being done here.

8.5.3 Micro Hall Probe Measurements on Nb–25% Zr Cylinders and Coils[39]

W. F. Gauster K. R. Efferson
D. L. Coffey J. E. Simpkins

Introduction. – An important diagnostic method is the measurement of the spatial magnetic field distributions around superconductors. For instance, W. Meissner *et al.* used for this purpose ballistic coils 1.5 mm wide, 1 mm thick, and 10 mm long.[40] Recently, H. T. Coffey employed a micro Hall probe consisting of a bismuth Hall cross vacuum deposited onto a mica substrate with an active area of 0.1 mm side length.[41] In our laboratory a new type of micro Hall probe has been developed which has the following significant data:[42]

Material	Indium arsenide
Cover	Silicon monoxide
Substrate	Mica
Sensitive area, mm^2	0.002
Total thickness, mm	0.03
Sensitivity, v/amp-gauss	10^{-3}
Impedance, ohms	2000
Linearity	5% of full scale to 50 kilogauss

Indium arsenide proved to be less temperature sensitive than indium antimonide. Figure 8.20 shows the probe-positioning device. The substrate of the Hall element can be rotated about axis A. The sweep speed is adjustable through a gear arrangement outside the Dewar (range 30 min/sweep to $\frac{1}{2}$ min/sweep).

Magnetic field measurements were made in the gap between the two halves of a cold-worked Nb–25% Zr cylinder in a longitudinal field and in a slit in the midplane of a superconducting magnet coil.

Micro Hall Probe Measurements on a Cylinder. – Field distributions in a cold-worked Nb–25% Zr rod have been investigated in longitudinal magnetic fields at 4.2°K. The sample was a $4\frac{1}{8}$-in.-long, 0.26-in.-diam solid cylinder which had been split into two equal pieces by cutting perpendicular to the longitudinal axis. The cylinder was then mounted in such a way that the gap between the two halves was 0.004 in. The position of the probe is determined electrically so that field magnitude vs position can be plotted on an *X-Y* recorder.

The field in a cylinder without a gap is, of course, different from that measured with our arrangement. Since the ratio of gap width (0.004 in.) to rod diameter (0.26 in.) is very small, a field disturbance can be expected only near the cylinder surface. This zone is, however, of special interest, and calculations and additional experiments are being made to estimate the possible influence of the gap disturbance. The following measurement results have not been corrected for fringe effects.

Some characteristic field measurements are represented in Fig. 8.21. In order to determine exactly the location of the outside surface of the cylinder, two open Nb-Zr single-layer windings (Fig. 8.20, S_1 and S_2) were arranged which produced field spikes at a measured distance from the cylinder surface (spikes S in Fig. 8.21). By means of a bifilar heater winding, the sample was

ORNL-DWG 65-10639R

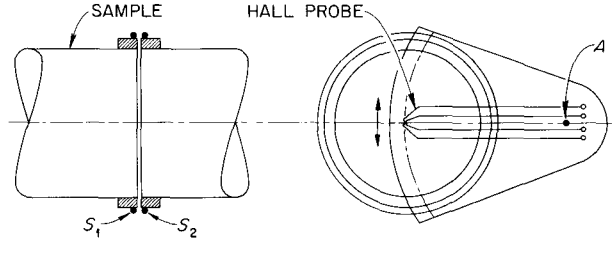

Fig. 8.20. Scanning of Superconducting Cylinder (Experimental Arrangement).

---

[39]Work partly sponsored by the George C. Marshall Space Flight Center, NASA, under Government Orders H-71484 and H-76798. See sects. V-A and -B of ORNL-TM-1266 covering the period June 1 to August 1, 1965.

[40]W. Meissner and Fr. Heidenreich, *Physik. Z.* 37, 449 (1936).

[41]H. T. Coffey, Westinghouse Research Memo 65-1JO-CRYOA-M1 (Apr. 15, 1965).

[42]J. E. Simpkins, *Thermonuclear Div. Semiann. Progr. Rept. Apr. 30, 1965*, ORNL-3836, p. 97.

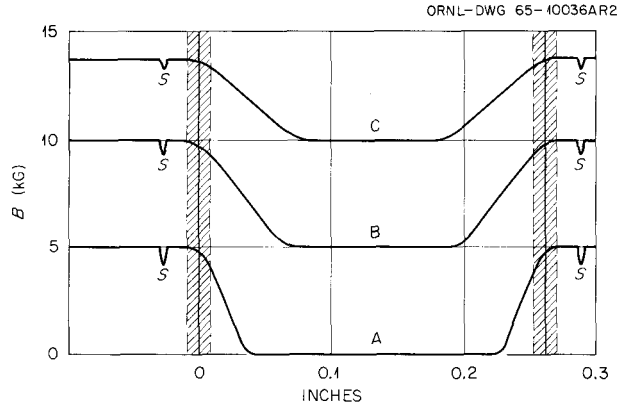

Fig. 8.21. Change in Flux Distribution in the Gap of an Nb–25% Zr Cylinder with External Field. Curve A, with 5-kilogauss external field; B, with 5-kilogauss internal and 10-kilogauss external (see text); C, 10-kilogauss internal and 14-kilogauss external. The dips are introduced for relative location of cylinder and microprobe.

driven normal in zero external field, and after cooling of the sample the external field was was raised to 5 kilogauss (Fig. 8.21*A*). Keeping this external field constant the sample was again heated and cooled so that the field of 5 kilogauss penetrated the entire sample. When increasing the external field to 10 kilogauss, curve B was obtained. Finally, curve C shows the flux distribution with an external field of 14 kilogauss after flux penetration at 10 kilogauss due to heating. Probably due to the intermediate heating, the relatively large final field of 14 kilogauss could be achieved without obvious flux jumping. As to be expected, from Kim's formula,

$$J = \frac{\alpha}{B + B_0} ,$$

the local current density J decreases with increasing B. The numerical values of the current density as calculated from these measurements are in the same order of magnitude found by other authors.

This field scanning method is also convenient for studying flux jumps in hard superconducting cylinders. Figure 8.22 shows the following example: First, the sample was heated and cooled in an external field of −1.5 kilogauss (curve A). After raising the external field to +4 kilogauss, the flux distribution B was obtained. Lowering the external field to zero yielded the distribution curve C. The distribution is far from axisymmetric. Furthermore, when lowering the external field from +4 kilogauss to zero the field distribution inside a certain zone remained unaffected.

The occurrence of flux jumping when raising the field from a negative to positive value might be explained by the concept of the "annihilation instability" suggested by Beasley *et al.*[43] and recently by Wischmeyer.[44]

These flux distribution measurements will be continued.

Micro Hall Probe Measurements on a Sample Coil. – An experimental arrangement permits the sweeping of a micro Hall probe through a small (0.013-in.) slit in the midplane of a superconducting coil. The slit width is approximately one wire diameter. This coil has 0.375 in. inside and 1.375 in. outside diameter and is 1 in. long; the winding consists of 2740 turns of 10-mil Nb–25% Zr wire with copper cladding of 1 mil radial thickness. Field measurements have been made with the Hall probe connected either directly to an *X-Y* recorder or with an amplifier between the probe and the recorder.

Examinations to date have included only the self-fields generated by the superconducting coil. Later experiments will be made with superimposed external fields.

[43] M. R. Beasley *et al.*, *Phys. Rev.* **137**, A1205 (1965).
[44] C. R. Wischmeyer, *Phys. Letters* **18**, 100 (1965).

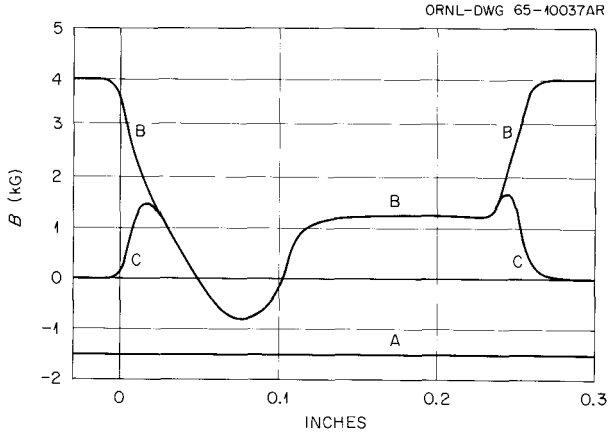

Fig. 8.22. Flux Jumps in an Nb–25% Zr Cylinder Obtained with Low Internal Fields.

The midplane field of a nonsuperconducting (e.g., copper) coil with dimensions and turns equal to that of the superconducting coil is shown in Fig. 8.23, curve A. The effect of a 0.013-in. gap between sections is indicated by curve B. This curve is the starting point for the analysis of the effects of the diamagnetic currents in the superconducting coil.

In a superconducting coil it can be expected that the diamagnetic behavior of the wire will distort the field. As the current is increased, flux penetration of the wire results, and the field distributions approach more closely that of a nonsuperconducting coil. This effect is apparent in Fig. 8.24. The influence of the diamagnetic currents is seen in the shape of the field within the winding and the bore of the coil. In order to study field shape at low currents in more detail, an additional amplifier between the micro Hall probe and the recorder has been used. The field shape recorded is shown in Fig. 8.25. The coil current is 2 amp, and the calculated maximum self-field in a corresponding nonsuperconducting coil is 2084 gauss. An appreciable deviation of the field shape of the superconducting coil from that of the corresponding nonsuperconducting coil can be seen. In an (infinitely) long superconducting coil, the coarse-grained average midplane field is identical with that of a nonsuperconducting coil.[45] For a short superconducting coil, however, the diamagnetic currents cause first a rapid drop in field intensity as one proceeds from the inside toward the outside surface. Thereafter the field gradient is smaller than that in the nonsuperconducting coil (Fig. 8.25). This observation is in accordance with the fact that the self-inductance of a superconducting coil is smaller than that of the same coil in normal state.[46]

In Figs. 8.24 and 8.25, spatial field ripples are clearly evident. Their number is approximately one-half of the number of layers. Visual examination of the winding end planes of a similarly wound coil shows that alternate layers are generally displaced axially one-half of one wire

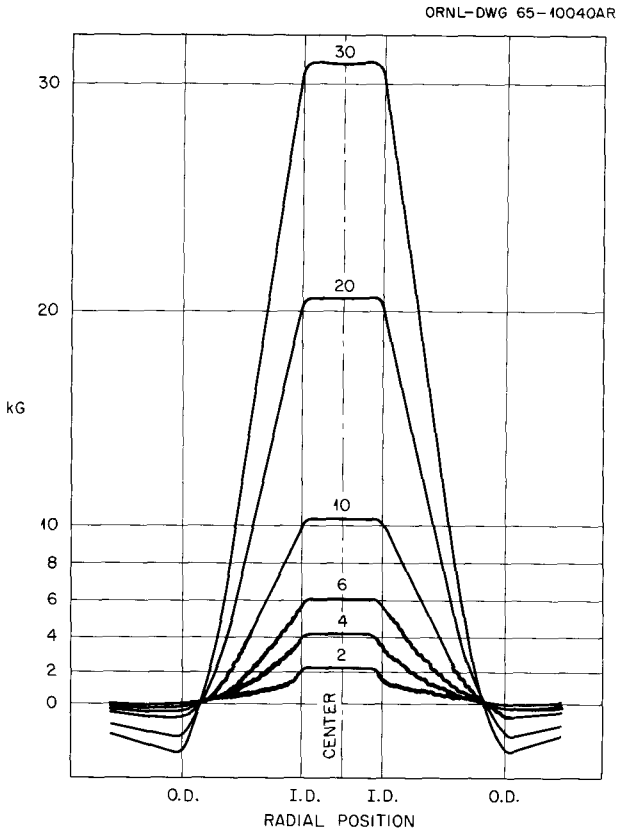

Fig. 8.24. Virgin Coil. Midplane field scan (with transport currents from 2 to 30 amp).

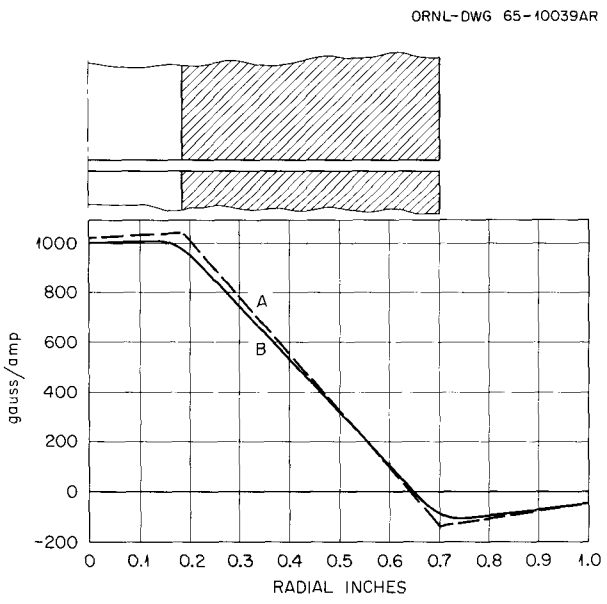

Fig. 8.23. Calculated Midplane Field of a Nonsuperconducting Coil. The coil axis is at the left.

[45] B. S. Chandrasekhar, W. F. Gauster, and J. K. Hulm, *Appl. Phys. Letters* 2(11), 228–29 (1963).

[46] H. T. Coffey *et al.*, *J. Appl. Phys.* 36, 128 (1965), Fig. 8 (p. 135).

diameter. A more thorough investigation of these ripple fields is planned.

Figure 8.26 shows the remanent fields with zero applied current after successively energizing the coil to 2, 4, 6, 10, 20, and 30 amp. Magnetic moment measurements on bundles of 0.010-in. Nb–25% Zr wires[47] showed that a field of about 5 kilogauss is necessary to reach maximum magnetization. This corresponds to the observation on the superconducting coil that for fields of 5 kilogauss or more, the remanent magnetization (i.e., the field after raising and lowering the transport current) reaches maximum values. In accordance with this result, Fig. 8.26 shows that maximum remanent fields are trapped over a radial distance where the maximum transport current field has reached or exceeded about 5 kilogauss. This seems to explain the change of the shape of the remanent field from a nearly triangular form to an almost rectangular shape.

The remanent fields shown in Fig. 8.26 were obtained after reaching a maximum transport current

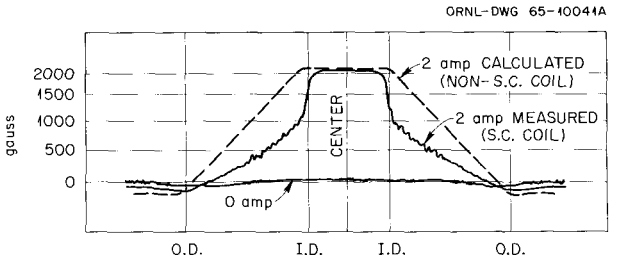

Fig. 8.25. Coil Midplane Self-Field with 2-amp Transport Current, Showing Effect of Diamagnetism in the Superconducting Windings as Compared with the Calculated Field Distribution for a Copper Coil.

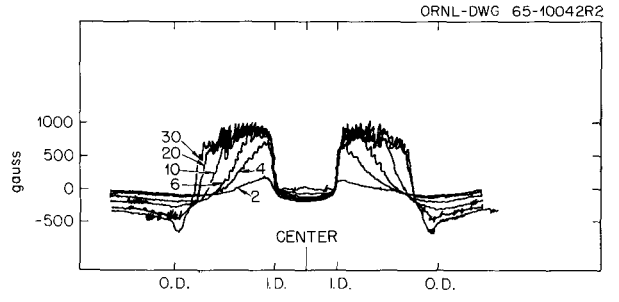

Fig. 8.26. Remanent Fields Without Quenching Transitions.

field without occurrence of a normal transition (quenching). Other measurements were made to investigate the remanent fields after quenching (Fig. 8.27). The quenching currents were between 30 and 44 amp; irregular training effects have been observed. It was, however, not possible to correlate remanent fields preceding or following the quenching process with the numerical values of the quenching currents concerned (see cases A and B, and C and D in Fig. 8.27). The obvious reason for this fact is that the remanent field in the midplane is not sufficient to characterize the overall state of the superconducting coil between successive quenchings. After reaching thermal equilibrium, diamagnetic currents trapped in other parts of the winding might have decisive influence.

These micro Hall probe measurements in the coil midplane complement the investigations of Aron and others, who studied the axial fields of superconducting coils.[48] Attempts to measure the diamagnetic current distribution in the entire winding of a superconducting coil have been made with ballistic methods.[49] However, these results do not fully agree with the micro Hall probe measurements described above.

8.5.4 A Note on the Macroscopic Theory of Superconductors of the Second and Third Kind

H. W. Koppe

Introduction. – It seems that an agreement has been reached that type III superconductors are in general type II superconductors in which the flux lines are prevented, by some "pinning" mechanism, from moving freely. The agreement is, however, at present not complete concerning the formulas which should be used to describe the actual behavior of type III superconductors.

In this paper we shall try to clarify this situation by separating those features of the problem which can be dealt with by thermodynamical considerations from those where special assumptions

---

[47] D. C. Hopkins and W. F. Gauster, *Thermonuclear Div. Semiann. Progr. Rept. Oct. 31, 1963*, ORNL-3564, p. 118.

[48] Paul R. Aron, *Magnetization and a Superconducting Solenoid*, UCRL-10854 (June 5, 1963); see also A. C. Anderson and R. J. Sarwinski, *Rev. Sci. Instr.* 34, 298 (1963).

[49] B. Taquet, *J. Appl. Phys.* 36, 3250 (1965).

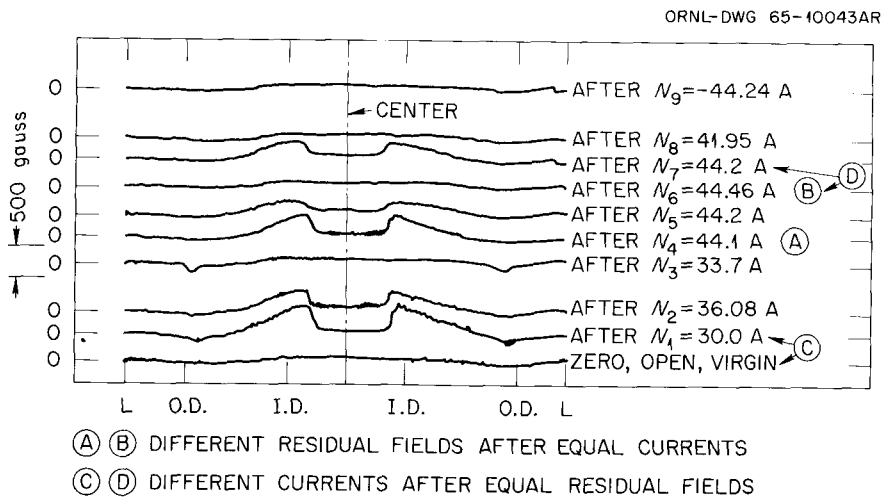

Fig. 8.27. Remanent Fields After Successive Normal Transitions.

about the behavior of the pinning mechanism are necessary. We shall aim at macroscopic description analogous to the description of "thick" superconductors as absolute diamagnetics.[50] This means that we do not take into consideration the special effects which play a role in surface layers of the order of 10^{-3} cm (e.g., mirror forces on flux lines) and that London shielding currents will appear as surface currents. There is already a vast amount of literature on the subject; we should like to refer to the comprehensive list of references given by Lowell.[51]

It turns out that much depends on the definition of the current density $\boldsymbol{J}$ and the magnetic field $\boldsymbol{H}$. Whereas the magnetic induction $\boldsymbol{B}$ is defined in a completely unambiguous way, the definition of $\boldsymbol{J}$ and $\boldsymbol{H}$ is, in electrodynamics, partly a matter of convention (and convenience). We shall find it useful to define $\boldsymbol{H}$ as the derivative of the field energy with respect to B:

$$\boldsymbol{H} = \frac{\partial f}{\partial \boldsymbol{B}} \qquad (1)$$

and

$$\partial \boldsymbol{J}_d = \text{curl } \boldsymbol{H} \, . \qquad (2)$$

One should keep in mind that the various possible definitions of $\boldsymbol{J}$ differ only by the curl of a magnetization and lead to the same value of the total current through a wire. Furthermore, all equations are now really equations for $\boldsymbol{B}$ and are quite independent of any abbreviations one introduces along the way.

In the following we shall first treat the "two-dimensional" case, where the magnetic field and the flux lines are in the z direction and depend only on x and y. In this case we can treat the flux lines as a two-dimensional gas and obtain all results in a quite straightforward way. These results can be generalized; however, as explained later, the general situation might well be much more complex.

Type II Superconductors. – Let us consider a cylindrical superconductor inside a coil. The current through the coil determines the magnetic field H_e outside the superconductor. If we bring one flux line carrying a unit flux $\phi_0 = \hbar/ec = 2 \times 10^{-7}$ gauss/cm^2 into the superconductor, we need a certain amount, Δf, of free energy. Since the flux lines repel each other, Δf will depend on the density n of the flux lines already present. The free energy of unit area is therefore $n\,\Delta f(n)$. Since the average magnetic induction $B = n\phi_0$ is proportional to the density of flux lines, it is convenient to express everything in terms of B instead of n, and to write $n\,\Delta f(n) = f(B)$.

[50] See, e.g., Shoenberg, *Superconductivity*, p. 13, Cambridge, New York, 1960.

[51] J. Lowell, *Cryogenics* 5, 185 (1965).

The equilibrium value of B is determined by the minimum of

$$G = F - \phi H_e = \int f(B)\, dO - H_e \int B\, dO ,$$

and this leads to

$$\frac{\partial f}{\partial B} = H_e . \tag{3}$$

This equation permits the determination of B as a function of H_e, once $f(B)$ is known. On the other hand, one can use (3) to determine $f(B)$ from magnetization curves determined experimentally. If we plot H_e vs B we can integrate (3) and obtain

$$f(B) = \int_0^B H_e(B)\, dB . \tag{4}$$

Figure 8.28 shows a typical plot of H_e vs B. The curve starts horizontally with a value H_{c1} at $B = 0$ and then goes over rather sharply into an almost straight line:[52]

$$H_e = \frac{1}{\alpha} B + H_r \quad \text{(approx)} , \tag{5}$$

$$H_r = \frac{\alpha - 1}{\alpha} H_{c2} ,$$

which cuts the line $H_e = B$ at the upper critical field $H_e = H_{c2}$. For thermodynamical reasons, the shaded area in Fig. 8.28 must be equal to $\frac{1}{2}H_c^2 = f_n - f_s$, the difference of free energy between normal and superconducting material.

From (5) and (4) we obtain

$$f = \frac{B^2}{2\alpha} + H_r |B| + C , \tag{6}$$

where, owing to the fact that (5) does not hold for small values of B, C is, strictly speaking, a function of B, which, however, goes rather quickly to a constant. In many cases it will be a sufficient approximation to use (6) with constant C. One should keep in mind that this leads to incorrect results for very small B.

We shall now reinterpret Eq. (3) by considering the flux lines as a two-dimensional gas of density B, which can distribute itself over the two phases "superconductor" and "vacuum." It is more convenient to consider a situation where the superconducting cylinder is not in a coil, but inside a hole of another superconductor, so that the total flux ϕ is conserved (Fig. 8.29). The term A is the cross section of the superconducting cylinder, and A_0 is the cross section of the vacuum. If one

ORNL-DWG 66-628

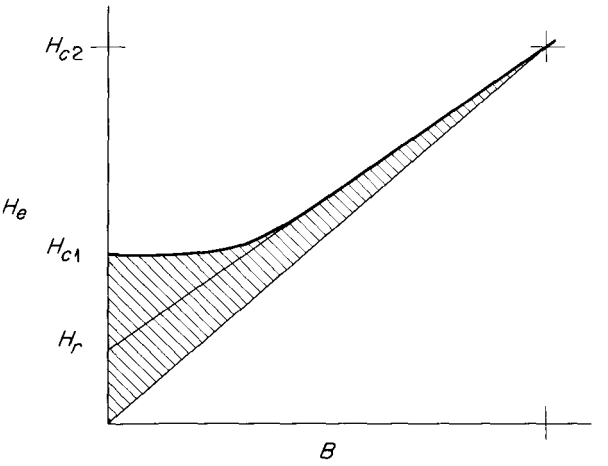

Fig. 8.28. Plot of H_e vs B.

ORNL-DWG 66-629

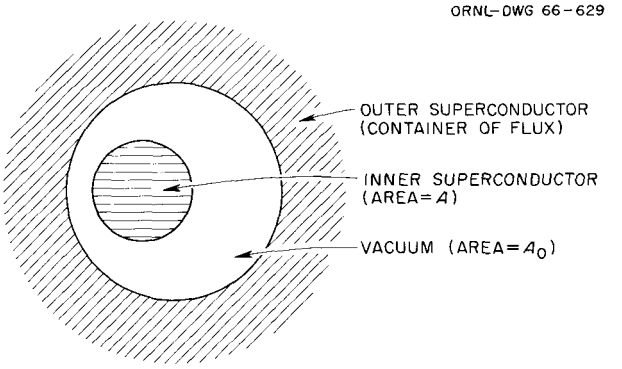

Fig. 8.29. Superconducting Cylinder in a Cavity Within Another Superconductor.

[52] According to the GLAG theory, we would have $\alpha = (2.36\kappa^2 - 0.18)/(2.36\kappa^2 - 1.18)$. It seems to be advisable to introduce some special letter for this frequently occurring constant.

remembers that the free energy of the "B gas" in vacuum is $f_0 = B^2/2$, we have to minimize

$$F = A\, f(B) + A_0\, f_0(B_0) \tag{7a}$$

under the condition

$$\phi = AB + A_0 B_0 = \text{const.} \tag{7b}$$

Introducing a Lagrangian multiplier χ (the chemical potential), we obtain

$$\frac{\partial f(B)}{\partial B} = \chi\,, \tag{8a}$$

$$\frac{\partial f_0}{\partial B_0} = B_0 = H_e = \chi\,. \tag{8b}$$

In (8a) we have made use of the fact that in vacuum $B = H$. If we eliminate χ between (8a) and (8b) we come, of course, back to (3). Nevertheless, there is a considerable conceptual difference between (3) and (8): Whereas in (3) we relate the magnetic induction inside the superconductor to a value H_e of the magnetic field in a quite different place, Eqs. (8) are local in the sense that they state that the chemical potential χ is constant and that we have different "concentrations" in different phases because the relations between the concentration and the chemical potential are different. This shift of emphasis is important since it can be generalized for nonequilibrium states.

From (8b) we see that in vacuo the chemical potential χ is equal to the magnetic field strength. Up to now we did not use the concept of the magnetic field strength H inside the superconducting cylinder. If we define this by

$$H \overset{\text{def}}{=} \frac{\partial f}{\partial B}\,, \tag{9}$$

then the condition for equilibrium becomes simply

$$H = \text{const.} \tag{10}$$

Since superconductors have magnetic permeabilities which are very close to 1, one could, of course, insist that $H = B$, contrary to (9).

However, in this case one had to take into account the rapid variations of B inside the Abrikosov structure, whereas (9) expresses the macroscopic point of view. This difference becomes very important in connection with the definition of the current. If we write the first Maxwell's equation in the form

$$\dot{\boldsymbol{D}} + \boldsymbol{J} = \text{curl}\ \boldsymbol{B}\,, \tag{11}$$

then the current density J defined by this equation is an average of the local currents, and therefore in a certain way the true current density. On the other hand, we can define a current density J_d by

$$\dot{\boldsymbol{D}} + \boldsymbol{J}_d = \text{curl}\ \boldsymbol{H}\,. \tag{12}$$

The difference between (11) and (12) is seen, if we consider the loss for the conservation of free energy in the usual way. Then we obtain from (11):

$$\frac{\partial}{\partial t}\left(\frac{1}{2}\boldsymbol{DE} + \frac{1}{2\mu_0}\boldsymbol{B}^2\right) + \boldsymbol{JE} + \text{div}\,[\boldsymbol{E}\times\boldsymbol{B}] = 0\,,$$

and from (12):

$$\frac{\partial}{\partial t}\left[\frac{1}{2}\boldsymbol{DE} + f(B)\right] + \boldsymbol{J}_d\boldsymbol{E} + \text{div}\,[\boldsymbol{E}\times\boldsymbol{H}] = 0\,. \tag{13}$$

The second equation contains the time derivative of the correct density of free energy, and therefore $J_d E$ can be identified as a dissipated heat. Therefore we call J_d the dissipative current. As far as the macroscopic point of view is concerned, we need only to take into account the dissipative current, since (12) is the natural definition of the current. This has the advantage that all the familiar formulas of electrodynamics remain valid.

We can, however, split J into two parts:

$$J = J_d + J_s\,. \tag{14}$$

Then J_s does not produce any Joule's heat and behaves like an ordinary London current.

There is one point that one should keep in mind: One can treat the flux lines to a large extent as a two-dimensional gas with density B and chemical potential H; but, whereas in an ordinary gas the density c cannot be negative and the chemical potential goes to $-\infty$ for $c \to 0$ (owing to an entropy term of the term c log c in

f), B can be positive or negative and H is undefined for $B = 0$. This does not lead to any difficulties as far as equilibrium is concerned, but this point has to be taken up again when non-equilibrium states are considered.

Forces on Flux Lines. – If we consider the flux lines as a two-dimensional gas with a density B and a density of free energy f, we can derive the pressure p from the well-known formula

$$p = \frac{\partial f}{\partial B} \cdot B - f = HB - f . \tag{15}$$

The force per unit area on the flux lines is therefore[53]

$$k = \text{grad } p = -B \text{ grad } H . \tag{16}$$

The force on a single flux line is obtained by dividing through the density[54]

$$k_s = -\frac{B}{|B|} \text{ grad } H = -\text{grad } |H| . \tag{17}$$

One can derive these formulas in the following way: Suppose the flux line at point $\mathbf{r}$ is displaced by $\delta\mathbf{s}(\mathbf{r})$. Then the conservation of flux lines gives

$$\delta B + \text{div } B \, \delta\mathbf{s} = 0 . \tag{18}$$

On the other hand, the total change in energy is

$$\delta u = \int f \, dO = \int H \, \delta B \, dO = -\int H \text{ div } (B \, \delta\mathbf{s}) \, dO$$

$$= \int \delta\mathbf{s} \, B \text{ grad } H \, dO .$$

But δu must be equal to the work done against the forces:

$$\delta u = -\delta\mathbf{s} \, \mathbf{k} \, dO ,$$

and since this must hold for arbitrary $\delta\mathbf{s}$, we obtain (16), and from (16) our old condition for equilibrium: $H = \text{const}$.

[53]Note that all vector operations are in two dimensions and that B and H are to be treated as scalars.

[54]Since B is in reality only proportional to the density of flux lines, this is really the force per mole. The force per line is obtained by multiplying with $1/\phi_0$, which plays here the role of Loschmidt's number.

The following points should be noted:

1. The relation B grad H = grad p follows from (15) under the assumption that f does not explicitly depend on r, so that, although the chemical potential stays constant over the boundary between the superconductor and the vacuum, the pressure is discontinuous and smaller in the superconductor.
2. As we pointed out above, H and a fortiori grad H is undefined for $H < H_{c1}$. This of course does not matter, since then B is zero, and an arbitrary force acting on a nonexistent flux line does not produce any physical effects.

Pinning in Type III Superconductors. – The properties of hard superconductors can be described, if one assumes that the flux lines are "pinned" and can move only if the force exerted on them exceeds a certain critical value. Since the force per flux line, grad H, has the dimensions of a current, this constant is generally called the critical current J_c, and one has thus the condition

$$|\text{grad } H| \leqq J_c (B, T) . \tag{19}$$

If one remembers that $|\text{grad } H| = |\text{curl } H| = J_d$, this can be read as

$$J_d \leqq J_c . \tag{20}$$

As indicated, J is a function of B and T. Various models proposed so far vary with respect to the functional dependence on B. The simplest assumption (which should be good for small B) is to assume that J_c is constant. The still simpler model of H. London assumes that $H_{c1} = 0$; that is, $df/dB = H = B$. It is, however, to be expected that J_c decreases with increasing B. The simplest *Ansatz* would be

$$J_c = \frac{J_{c0} B_c}{B_c + B} . \tag{21}$$

If one inserts this into (20) one obtains

$$J_c \cdot (B_c + B) = \text{const} ,$$

which is the relation of Anderson and Kim.

This is not quite satisfying, since one should expect that J_c vanishes for $B = H_{c2}$. It is tempting to make the following conjecture: Since the

pinning is probably due to the fact that there are small normally conducting regions in the material and that the flux lines like to thread through these regions, one could assume that the pinning force is approximately proportional to the difference in free energy between normally conducting and superconducting material at a given B:

$$J_c = \text{const} \left[\frac{1}{2} B^2 + \frac{1}{2} H_c^2 - f(B) \right] . \quad (22)$$

Using the approximate formulas (5) and (6), we would obtain

$$J_c = \gamma (H_{c2} - B)^2 = \gamma\alpha (H_{c2} - H)^2 .$$

Here γ and $\gamma\alpha$ should be fairly independent of temperature. For small B this again gives the Anderson-Kim relation with $B_0 = H_{c2}/2$. This, however, is quite wrong, since experimentally B_0 is in general a few percent of H_{c2}, so that J_c decreases much faster with increasing B. A possible explanation might be that at very low densities there are enough pinning centers available so that the pinning force per area is proportional to the density; whereas at high densities only part of the flux lines are pinned, so that finally the pinning force per area is independent of the density. Combining this with the formula above, we would obtain

$$J_c = \gamma \frac{(H_{c2} - B)^2}{B + B_0} , \quad (23)$$

where γ and B_0 are more or less geometrical factors which should not depend on T.

If one wants to calculate the distribution of B inside a hard superconductor, one has of course to know $f(B)$. Then it is generally assumed that the superconductor is in critical state as long as $B \neq 0$. In the case of a half-space $x > 0$, where the field penetrates from the left, (19) would give

$$\frac{dH}{dx} = -J_c(B) \text{ for } B > 0 .$$

This can be integrated by separation:

$$\int_0^B \frac{dH}{J_c(B)} = a - x , \quad (24)$$

The constant of integration has to be obtained from suitable boundary conditions at $x = 0$. The condition generally used is that H is continuous at the surface, which means that B attains the equilibrium value at the boundary. This assumption is, however, not absolutely necessary. From an analogy with the theory of diffusion it would be possible that the surface itself acts as a finite barrier, and that there could be a jump in H on the surface. Another possibility which has to be taken very seriously and which makes all calculations based on simple geometries somewhat doubtful would be that flux lines can only enter the superconductor at certain "activation centers" on the surface. This would of course mean that the actual situation would be much more complicated than the simple overall geometry of the problem would suggest.

If one inserts H as a function of B in Eq. (19), one obtains

$$\text{grad } B = \frac{J_c}{dH/dB} = J_c' , \quad (25)$$

a formulation quite frequently used in current literature. The value J_c differs of course from J_c' by the factor dH/dB, which, for values of B which are not too small, is a constant not too much different from unity. There are, however, two reasons why the use of (25) is somewhat dangerous: (1) As was pointed out above, the heat dissipated is $\boldsymbol{E}$ curl $\boldsymbol{H}$ and not $\boldsymbol{E}$ curl $\boldsymbol{B}$. (2) Since H depends on B and T, Eqs. (19) and (25), respectively, are no longer equivalent in the case of a gradient of temperature. In this case, according to (17), the force on a flux line would be

$$k_s = -\frac{dH}{dx} = -\left(\frac{dH}{dB}\right)_T \frac{dB}{dx} - \left(\frac{dH}{dT}\right)_B \frac{dT}{dx} . \quad (26)$$

It is not necessary that (26) give the correct expression for the force on a flux line in the presence of a gradient of temperature, since there could be a thermodiffusion force proportional to grad T, which would not have been obtained by the argument leading to (17). However, on account of the Onsager relations, such a force should lead to a heat flow at T = const if B varies, and this is rather unlikely.

Since dH/dT is negative, this means that the flux lines tend to move toward places of higher

temperature. (The reason for this is, of course, that by doing so they save on energy needed to produce the normally conducting core.)

Generalization to Three Dimensions. – So far we have only considered situations where all flux lines are parallel to the z direction and all quantities depend only on x and y. Then we could describe the system of flux lines simply by the average magnetic induction B.

In a realistic three-dimensional case we could be faced with different situations:

1. The flux lines are no longer straight, but at least all the lines in the neighborhood of a point have the same direction. In this case the system of flux lines could again be described by an average induction B.
2. Suppose we have a type II superconducting wire and first pass a current I through it and switch it off again. Then we are left with a system of circular flux lines within the wire. Then we switch on a longitudinal magnetic field which presses in flux lines which are parallel to the wire and have therefore a direction which is perpendicular to those already present. It is difficult to say what would happen in this case, but the experiment might well lead to some sort of "flux spaghetti," where the flux lines are highly disordered.

Since a theoretical treatment of case 2 seems to be rather hopeless, we shall only consider case 1 (bearing well in mind that this might render all the following derivations somewhat hypothetical). Then we can describe the situation by giving the magnetic induction $\boldsymbol{B}$. The next thing we need is the dependence of the density of free energy f on B. Since we can assume that the superconductor is isotropic, the free energy can only depend on $|\boldsymbol{B}|$ and must be therefore the same reaction $f(B)$ considered above.

Assuming this, we need the conditions for equilibrium of a soft type II superconductor. An obvious generalization of the condition $H = \text{const}$ would be

$$\operatorname{div} \boldsymbol{B} = 0 , \tag{27a}$$

$$\operatorname{curl} \boldsymbol{H} = 0 . \tag{27b}$$

This means that we simply treat the superconductor as a diamagnetic substance. Equations (27) are known to have a unique solution under adequate boundary conditions. As an example, we can use them to calculate the magnetization of a superconducting sphere (see Sect. 8.6).

Unhappily, this conjecture is not a necessary consequence of the condition that the forces on the flux lines vanish.

It is easily seen that the generalization of (18) is

$$\delta\boldsymbol{B} + \operatorname{curl} [\boldsymbol{B} \times \delta\mathbf{s}] = 0 . \tag{28}$$

[If one assumes that $\boldsymbol{B}$ has only a z component and $\delta\mathbf{s}$ is in the x-y plane, then (18) and (28) become identical.] From this one obtains as the force on the volume element

$$\boldsymbol{K} = -\boldsymbol{B} \times \operatorname{curl} \boldsymbol{H} . \tag{29}$$

This of course is no longer the gradient of a pressure (it is the divergence of the Maxwell tensor). The force on unit length of a single flux line is then

$$\boldsymbol{K}_s = -\boldsymbol{B} \times \operatorname{curl} \boldsymbol{H}/|B| .$$

From (29) we obtain as the conditions for equilibrium

$$\operatorname{div} \boldsymbol{B} = 0 , \tag{30a}$$

$$\boldsymbol{B} \times \operatorname{curl} \boldsymbol{H} = 0 . \tag{30b}$$

It is obvious that any solution of (27) automatically satisfies (30), but it is not immediately obvious that the opposite is true. From (30) we only obtain the condition that curl $\boldsymbol{H}$ is parallel to $\boldsymbol{B}$, and this condition can indeed be satisfied with a nonvanishing curl $\boldsymbol{H}$, as is seen from the following example, where X is an arbitrary function of x:

$$B_x = H_x = 0 ,$$

$$B_y = H_y = \cos [X(x)] ,$$

$$B_z = H_z = \sin [X(x)] .$$

The situation is somewhat puzzling for the following reason: It is well known that Eqs. (27) have a unique solution for any finite superconducting region (e.g., a sphere) if the behavior of

H for $|\mathbf{r}| \to \infty$ is given. This solution is automatically a solution of (30). Does this indicate that the solution of (30) is not unique? One could, for instance, consider a superconductor with rotational symmetry in a magnetic field parallel to the axis of rotation. If one looks for a solution of (30) which has the full symmetry, namely, where the components B_θ and H_θ are zero, one finds that curl $\boldsymbol{H}$ is perpendicular to $\boldsymbol{B}$, and that (30*b*) implies (27*b*). It is, however, known that in nonlinear problems the minimal solution must not necessarily have the maximal possible symmetry (a striking example is the minimal surface inside a cube, which has no cubic symmetry).

Things are still much worse if we turn to type III superconductors. The pinning condition would be

$$|\boldsymbol{B} \times \text{curl } \boldsymbol{H}| \leqq |\boldsymbol{B}| J_c \ . \tag{37}$$

This, and div $\mathbf{B} = 0$ are two equations for the three components of B, so that the problem is underdetermined unless the number of components of B can be reduced by symmetry postulates. That such possibilities are rather dubious is seen from the following example: If one considers a type III superconducting ellipsoid with its axis parallel to the magnetic field, the condition of criticality is sufficient to derive the symmetrical solution. As soon as we tilt this ellipsoid very slightly, we are not only faced with a much more difficult mathematical problem, but we simply have no longer enough equations. However, since the probability that an ellipsoid is not slightly tilted is zero, we have never enough equations, which of course means that even in the case of a well-aligned ellipsoid there was no justification for the assumption that the magnetic field would have cylindrical symmetry.

Since the two-dimensional theory considered in the first part of this paper was based on symmetry arguments, it is subject to the same doubts; strictly speaking there exists no simple static macroscopic theory of type II and type III superconductors, and it is in principle necessary to consider the equations of motion for the flux lines, which shall be treated in a subsequent report.

Appendix 1. Magnetization of a Sphere. – It is easy to calculate the magnetization of a type II sphere, assuming that the Eqs. (27) hold. We merely need to repeat the well-known calculations for the diamagnetic sphere of radius R. We assume that for $r > R$, the field is given by the superposition of a constant field $\boldsymbol{H}_0$ and a dipole field:

$$\boldsymbol{H} = \boldsymbol{B} = \boldsymbol{H}_0 + \frac{mr^2 - 3(\boldsymbol{m}\boldsymbol{r})\boldsymbol{r}}{r^5} \qquad r > R \ , \tag{38}$$

whereas inside the sphere we have constant values $\boldsymbol{B}_i$ and $\boldsymbol{H}_i$ respectively. We have to fulfill the conditions that the normal components of $\boldsymbol{B}$ and the tangential components of $\boldsymbol{H}$ are continuous at $r = R$, and this is the case if

$$-\boldsymbol{B}_i + \boldsymbol{H}_0 = 2\frac{\boldsymbol{m}}{R^3} \ , \tag{39}$$

$$\boldsymbol{H}_i - \boldsymbol{H}_0 = \frac{\boldsymbol{m}}{R^3} \ . \tag{40}$$

Eliminating $\boldsymbol{m}$ from these two equations, we obtain

$$3\boldsymbol{H}_0 = 2\boldsymbol{H}_i + \boldsymbol{B}_i \ . \tag{41}$$

From this we obtain the magnetic induction $\boldsymbol{B}_i$ inside the sphere if we know $\boldsymbol{H}_i$ as a function of $\boldsymbol{B}_i$.[55]

We can use the formulas (39) and (40) to find a simple connection between measurements made with a sphere and measurements made with a cylinder. We first observe that (on account of the continuity of the tangential components of H) H_i is simply the magnetic field on the equator of the sphere, so that the relation between H_i and B_i for a sphere should be the same as between H_e and B_i for a cylinder. Adding (39) to (40) we obtain

$$H_i - B_i = 3\frac{m}{R^3} \ . \tag{42}$$

Experimentally one measures a quantity $D = c \cdot m$, where c is an unknown (or badly known) factor, which depends on the experimental setup. However, for sufficiently small H, H_i is less than H_{c1}, and therefore $B = 0$ and $m/R^3 = H_0/2$. If one therefore plots D vs H_0 in such a way that

[55] As a point of interest, we note that for the relations (39) and (40) to hold, it is not necessary that the four vectors involved are parallel, so that even for an anisotropic material the sphere still has a constant factor of demagnetization.

the initial slope is $D = \frac{3}{2} \cdot H_0$, one has in fact a plot of $H_i - B_i$ vs H_0. From this one obtains according to (40) a plot of $H_i - B$ vs H_i, if one shifts every point to the right by an amount which is one-third of its ordinate, and the curve obtained in this way should be the magnetization curve of a cylinder of the same material. Figure 8.30 shows the results one had to expect if the magnetization curve would consist of two straight lines. Experimental results look rather different, as is shown in Fig. 8.31 by a typical example.[56] One sees that a direct comparison is not possible since with the same material the cylinder is more irreversible than the sphere. An interesting feature which is at present not yet understood is that the curve obtained by the reduction given above does not drop perpendicularly from its maximum as it should. (As long as the magnetization inside the sphere is so small that the flux lines "do not touch," it should behave exactly like a type I sphere in the intermediate state, and the magnetization should be determined by $H_i = H_{c1}$.)

Appendix 2. Freezing In of Flux. – As we have seen above, the relation between H and B is in a good approximation given by

$$H = \frac{1}{\alpha} B + \frac{\alpha - 1}{\alpha} H_{c2} , \qquad (43)$$

where α is generally not too different from 1. If we would (as is frequently done) write the critical condition as

$$\frac{dB}{dx} = J_c' ,$$

then, as long as T is constant, this would be identical with (43) if one puts $J_c' = \alpha J_c$, so that aside from a numerical factor close to 1 the wrong expression for the force on the flux lines would still lead to correct results. The situation is, however, radically different, if T is not constant, since in this case we have to take into account that H depends on T via H_{c2}.

As an illustration we consider a slab, which is originally at a temperature T_1 and a field $H_1 > H_{c2}(T_1)$. It is therefore in the normal state, and $B = H_1$. Now we suppose that it is cooled down homogeneously to a temperature T_2 such that $H_{c2}(T_2) > H_1$. If we assume that the cooling occurs quickly enough so that the flux lines do not move, then the magnetic field strength must change to

$$H_2 = H_1 + \frac{\alpha - 1}{\alpha} [H_{c2}(T_2) - H_1] .$$

This will lead to a certain leakage of flux along the boundary; the flux in the interior, however, shall remain trapped at its original value, since in the interim H = const, and therefore there is no force on the flux lines.

This example does show that it is not necessary that the condition $|dH/dx| = J_c$ is fulfilled everywhere in the superconductor.

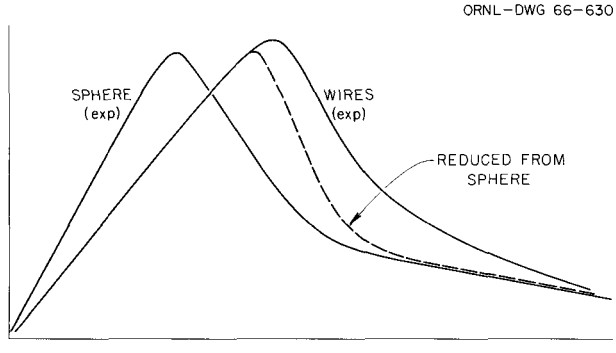

Fig. 8.30. Theoretical Relation Between Magnetization of Sphere and Cylinder (Simplified H–B Relation).

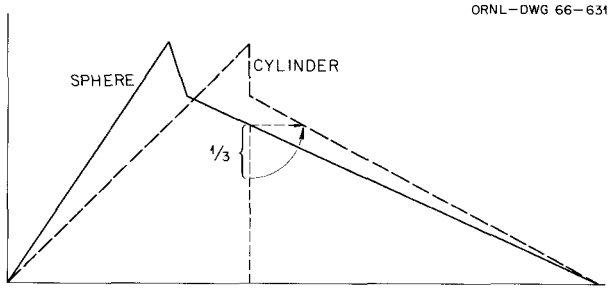

Fig. 8.31. Experimental Magnetization Curves of Sphere and Wires.

[56] From S. Sekula and R. H. Kernohan, to be published.

9. Vacuum Studies, Sputtering, Adsorption, and Diffusion of Gases in Metals

9.1 THE INTERACTION OF TRITIUM WITH THERMONUCLEAR REACTOR MATERIALS – SUMMARY OF A LITERATURE STUDY

S. S. Kirslis[1]

For a thermonuclear reactor to be feasible, the holdup of tritium in the metal of the containment vessel (Mo or W) and of the ion sources (alloys of Ni or Fe) must not exceed amounts which would result in excessive tritium inventory and decay losses. Although the equilibrium solubility of hydrogen at low pressures is low in these metals, the same metals can be cathodically "surcharged" with hydrogen to amounts of the order of 100 cm^3/g at NTP, in some cases causing blistering and cracking of the metal. In order to be able to judge more clearly whether the metal in a reactor under bombardment by energetic tritium atoms might be surcharged with tritium in a somewhat similar way, a literature study of the various surface and interior diffusion processes involved has been made and will be published separately.

The study was organized around a model of the tritium-metal interaction. The 50- to 100-kev tritium atoms may be expected to penetrate the metal to their range depth of 1 to 2×10^{-4} cm. They are then assumed to diffuse inward and also back to the entrance surface according to normal diffusion laws. If there is no appreciable barrier to their egress at the surface, the concentration of tritium atoms just inside the metal will be low or zero. In this case, the steady-state concentration of tritium in the metal will have a peak at the range depth and fall to low values at the bombarded surface and at the far surface of the metal (if a tritium sink is maintained here also). The average concentration in the metal would be about half the peak concentration. In the case of a barrier for tritium egress from the bombarded surface, the whole steady-state curve would correspondingly rise to higher tritium concentrations. The factors determining the peak concentration of tritium are the atom flux to the metal, the diffusion constant of tritium in the metal, and the boundary condition for the degassing of the bombarded metal surface.

Information on hydrogen diffusion in the metals of interest was derived mainly from published permeability and solubility studies. For information on the degassing boundary condition, the literature relevant to the metals of interest was searched in the fields of chemisorption and desorption, catalysis, hydrogen electrode behavior, and hydrogen atom recombination. Other pertinent information, derived from the field of ion bombardment, concerned sputtering of metal surfaces and saturation of metals by proton or deuteron bombardment.

The conclusions of the literature study are as follows:

1. Hydrogen is easily degassed at low pressures and moderate temperatures even from metals (such as W) on which the chemisorption heats are high.
2. Cathodic surcharging depends on a poisoning of the metal surface for hydrogen atom recombination. In a gaseous environment on clean metals, hydrogen atom recombination is rapid.
3. Diffusion rates for hydrogen in Mo at 600 to 800°C are sufficiently rapid to deliver injected atoms rapidly back to the bombarded surface, thus maintaining a very low (and from a practical viewpoint negligible) concentration of hy-

[1]Reactor Chemistry Division.

drogen in the metal. The same is expected to be true for tritium. If the hydrogen concentration will indeed be as low as estimated from the simple diffusion model, it should cause no hydrogen embrittlement problems. Since the diffusion constants for Ni and Fe are much higher than those of Mo, high internal H concentrations are not expected even at much lower temperatures.

4. Some recent work on deuteron bombardment of metals indicates higher concentrations of deuterium just inside the metal surface than predicted by the simple model. Some evidence indicates that this may be the effect of surface contamination on the metal.

9.2 HYDROGEN SURCHARGING OF MOLYBDENUM IN A GLOW DISCHARGE

D. M. Richardson[1] R. A. Strehlow[1]

A study of hydrogen occlusion by a molybdenum cathode in a glow discharge has been conducted. The principal objective of this work was to assess the significance of hydrogen surcharging to design considerations for thermonuclear reactors. Initial studies had indicated a possible hydrogen content of one or more atmospheric cubic centimeters per cubic centimeter of metal after bombardment in a discharge. Even though this concentration of hydrogen is less than 0.1 at. %, it could present serious problems to the reactor designer if this concentration of tritium were present in a large part of a reactor assembly. The work described here and the literature study summarized in Sect. 9.1, however, have led to the conclusion that at elevated temperatures occlusion of hydrogen is not large. At lower temperatures it appears that surface contamination can markedly impede the recombination of hydrogen during even low-energy bombardment and thus yield very high hydrogen concentrations.

For these studies, a 45-cm length of molybdenum wire, 1 mm in diameter, was used as a cathode in a cylindrical tank with a volume of 200 liters. The ends of the tank were electrically shielded with sheet Teflon. The center of the tank was connected to a vacuum system through a 6-in. isolation gate valve and a gate valve with a small orifice which had a speed of 2×10^{-4} the speed of the vacuum system manifold. This allowed a steady introduction of hydrogen gas through a palladium leak to the glow discharge chamber at a pressure of 10^{-2} to 1 torr with continuous mass analysis of the effluent gas from this chamber. The gas during the usual discharge contained not more than one part per thousand non-hydrogen impurity.

For the usual low-temperature discharge, the conditions were as follows:

Wire volume, cm^3	0.35
Wire area (apparent), cm^2	14
Pressure, torrs	0.25
Discharge current, ma	10
Discharge time, min	20
Applied voltage to cathode, v	500

The total bombardment was 12 amp-sec, or about 1 to 3 atm-cm^3 of hydrogen gas. After we had opened the orifice valve and pumped down to a pressure about 1×10^{-7} torr, the wire was heated to redness. Mass spectrometric and ion-gage observations were made of the hydrogen evolved by the degassing process. Pressure rises of as much as 6×10^{-4} torr were observed during the 4-sec degassing procedure. Since the system pumping speed for hydrogen was about 1000 liters/sec, this pressure rise corresponded to about 2 atm-cm^3 of hydrogen.

Stringent cleaning of the wire and ion bombardment of the chamber walls for several hours followed by a repetition of the discharge led to a value of only 0.017 atm-cm^3. Continued repetitions of the discharge-degas cycle led to increasing amounts of hydrogen being occluded. Since the wire was not heated past 1000°C, a gradual increase in surface contamination could have been responsible for the very high values.

Several attempts were made to use this technique at higher current densities (and consequent higher temperatures). Several attempts were made, during which the wire was independently heated, to determine the hydrogen occluded during a usual discharge. None of these attempts led to detectable hydrogen being subsequently evolved.

It appears that clean molybdenum surfaces or hot surfaces during low-energy bombardment do not occlude large amounts of hydrogen.

9.3 PERIODIC PRESSURE BURSTS IN A HIGH-VACUUM SYSTEM

D. M. Richardson[1] R. A. Strehlow[1]

One of the confusing phenomena common to many high-vacuum systems is that of a blip or small

pressure burst which may be of a magnitude from several tens of microtorrs down to fluctuations of a few nanotorrs. The period of these blips may vary by less than a few percent for many hours and might have a frequency ranging from one per second to one in 5 min. The fact that these bursts are rarely seen in metal-gasketed systems leads one to suspect elastomer gaskets. In the particular system used in this study a mass spectrometer correlation was made between various mass peaks and the ionization gage bursts. The magnitude of the blip was about 2×10^{-7} with a frequency of about 30 sec with no liquid-nitrogen cooling. After study of several mass peaks, we found that almost all of the pressure burst was water with perhaps 5% being carbon monoxide. No air (oxygen or nitrogen) appeared to be present as part of the pressure burst. This was surprising, since it was fairly easy to imagine little air bubbles tortuously squeezing around and under a rubber gasket.

By selective heating of the various flanges the pump flange was found to be the principal culprit. (The frequency increases markedly for only a few degrees temperature increase.) The presence of oil is the distinguishing feature of this flange.

It seemed that the gas constituting the burst either was background gas which dissolved in the oil or had evolved from the elastomer O-ring. Several changes of background gas composition were made with no effect on the blip composition. Helium was then used around the O-ring. Within a few hours helium was present in the bursts to an extent of about 10%. It appears that permeation through the O-ring is indeed the dominant gas load for the pressure bursts.

Similar conclusions have been reported recently in the literature.[2]

9.4 MASS-SPECTROMETRIC STUDIES OF THE EFFECT OF LONG-TERM COLD TRAP OPERATION ON BASE PRESSURE COMPOSITION

J. D. Redman[1] R. A. Strehlow[1]

Using the Bendix time-of-flight spectrometer, a study was made of the long-term cleanup of water vapor and the various large mass species to 264 mass units. Of particular interest was the behavior observed for mass number 240, which is presumed to be a principal peak from the DC-705 pump oil (a pentaphenyl-trimethyl-trisiloxane) used in the spectrometer. Within six days after cooling the trap, the magnitude of this peak decreased from a partial pressure of about 5×10^{-10} torr to a value of about 6×10^{-11} torr (uncorrected). The pressure indicated by ion gage fell from 4.6 to 2.2×10^{-7} torr during this period. After the test was concluded, the trap was allowed to warm and the mass 240 peak increased quite rapidly to very near the original value. Water vapor shows a distinctly different performance in that after the trap was warmed the water partial pressure (always the dominant species) did not return to as high a value as it had initially.

A vapor transport mechanism of this oil might be responsible for the apparent speed of transport, contrary to the findings for the mixed hydrocarbon oil studied previously. The water behavior is commonly observed and presents no unusual aspects.

9.5 ANALYSIS OF DCX-2 LINER MATERIAL AND COMPARISON WITH UNUSED PANEL SECTIONS

R. A. Strehlow[1] C. F. Harrison[3]

Samples of the DCX-2 liner, after several years of use, were obtained and submitted for gas analysis, metallographic study, and spectrochemical study. Standards for the gas analysis and metallographic study were obtained from a section of unused panel material. Results from the gas analysis indicated no great difference in gas content between the liner and unused panel material. The oxygen content of three standard samples ranged from 14 to 24 ppm and of four liner samples from 12 to 16 ppm. Hydrogen and nitrogen analyses were for all samples reported as less than 1 and less than 5 ppm respectively. Spectrochemical analysis of material which had been exposed to the plasma and some which had not showed slight differences principally in that the former had a larger amount of iron, chromium, and manganese than the latter. Metallographic results showed no marked differences in the internal structure of the liner sample compared with a sample of a new panel.

[2]U. R. Bance and E. H. Harden, *Vacuum* 15, 437 (1965).

[3]Analytical Chemistry Division.

9.6 ABSOLUTE PRESSURE MEASUREMENTS WITH THE McLEOD GAGE

H. B. Gilbody[4]

In the course of making absolute atomic cross-section measurements it is frequently necessary to measure the absolute pressure of gases in the range 10^{-4} to 10^{-2} torr. In the past extensive use has been made of the McLeod gage as a pressure standard. Several workers[5] have recently called attention to large errors associated with the normal use of McLeod gages. In the McLeod gage a steady stream of mercury flows between the gage and the cold trap used to isolate the mercury gage from the vacuum system. With this vapor flow through the connecting tubing, the gage acts as a pump and the pressure is reduced in the gage. The magnitude of the pressure difference depends on the diffusion coefficient of the gas in Hg vapor, ambient temperature, tubing diameter, and the gas pressure. The correction formula given in the literature[5] is as follows:

$$\ln \frac{p(\text{real})}{p(\text{McLeod})} = 0.905R\,P(\text{Hg})\,\frac{T}{D_{12}}\,,$$

where R is tube radius, P is vapor pressure of Hg at T, T is absolute temperature, D_{12} is diffusion coefficient. One of the simplest methods of eliminating this difficulty is to decrease the temperature of the mercury until its vapor pressure is negligible. To provide us with a pressure standard we have conducted a series of measurements by placing the McLeod gage in a household deep-freeze unit in which the ambient temperature was −15°C. The McLeod gage reading was then compared to a capacitive differential manometer marketed under the trade name Baratron. This gage presumably is calibrated absolutely and suffers from none of the ill effects of the McLeod. In addition, the Baratron would be useful as a pressure-measuring standard for some of the hydrocarbon gases and water vapor in which we are measuring the electron capture cross section by protons.

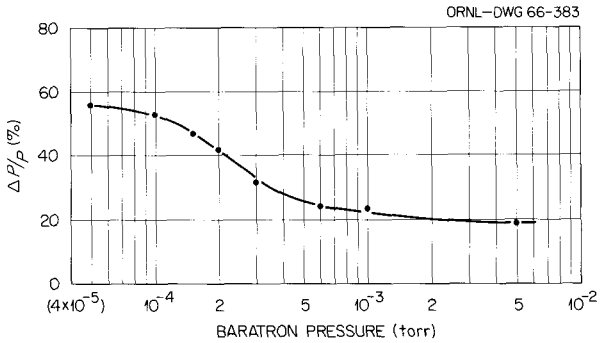

Fig. 9.1. Pressure Corrections Applied to a McLeod Gage as a Function of the System Pressure – Argon Gas at 25°C.

Typical corrections applied to the McLeod gage are shown in Fig. 9.1, in which $\Delta P/P$ is plotted as a function of the pressure reading of the Baratron gage. The ratio $\Delta P/P$ is defined as the difference in McLeod gage pressure readings at 25°C and −15°C divided by the pressure reading at −15°C. The correction is greatest at low pressure, and for argon it is 56%, falling to less than 20% for pressures greater than 10^{-3} torr. As the atomic mass of the gas increases, the corrections become larger; whereas for light gases such as hydrogen, the corrections become negligible, being only 2%, which is within the reading accuracy of the gage. For pressures less than 10^{-3} torr, the Baratron is nonlinear, and investigations are under way to determine the source of this nonlinearity.

9.7 SPUTTERING YIELDS WITH 30-kev D^+ IONS

O. C. Yonts J. P. Wood H. L. Huff[6]

Some sputtering determinations with D^+ ions were made during this report period. These were made

[4]Summer visitor. Present address: University of London.

[5]H. Ishii and K. Nakayama, *Trans. Natl. Vacuum Symp., 8th, 1961*, vol. I, 519 (1962); Ch. Meinke and G. Reich, *Vacuum-Technik* 11, 86 (1962).

[6]Y-12.

under the same conditions and restrictions as those reported previously.[7] Bombardments were carried out with 30-kev ions at current density of 15 ma/cm^2. This is sufficient current density to keep surface layers removed at the operating pressure of 2×10^{-5} mm.[8] Table 9.1 shows the results of this series.

[7]O. C. Yonts, C. E. Normand, and D. E. Harrison, *J. Appl. Phys.* 31, 447 (1960).

[8]O. C. Yonts and D. E. Harrison, *J. Appl. Phys.* 31, 1583 (1960).

Table 9.1. Sputtering Yields with 30-kev D^+ Ions

Target	Ion Energy (kev)	Sputtering Ratio, Atoms Out / Ions In	Yield (mg/amp-hr)
W	28	0.0080	60
Mo	30	0.010	37
Cu	30	0.029	69
316 stainless steel	30	0.0071	18

10. Design and Engineering: Service Report

J. F. Potts, Jr.

The results of the Engineering Services Group are generally reported incidentally with those of the research groups of the Thermonuclear Division. The Group executes or coordinates engineering design, shop fabrication, building operations, and maintenance for the Division.

Design activities for this reporting period are summarized as follows:

Jobs on hand 5-1-65 on which work had not started	9
New jobs received	155
Total jobs	164
Jobs completed	152
Jobs in progress	8
Backlog of jobs 10-31-65	4
Total drawings completed for period (does not include drawings for slides, reports, etc.)	262

Shop fabrication for this reporting period is summarized as follows:

Machine Shops

Completed jobs requiring 16 man-hours or less	205
Completed jobs requiring 17 to 1200 man-hours	236
Completed jobs requiring over 1200 man-hours	5
Completed jobs of miscellaneous character (in plating, carpenter, electrical, glass, lead, etc., shops)	21
Outside contractors	0
Number of jobs in progress	39
Average manpower per week	20.8

Electromagnet Fabrication

Completed jobs	5
Number of jobs in progress	6
Average manpower (per week)	6.5

Publications, ORNL Reports, and Papers

PUBLICATIONS

Open Literature

Author(s)	Title of Article	Journal (or Book)
I. Alexeff and W. D. Jones	Collisionless Ion-Wave Propagation and the Determination of the Compression Coefficient of Plasma Electrons	*Phys. Rev. Letters* **15**, 286 (1965)
W. B. Ard, M. C. Becker, R. A. Dandl, H. O. Eason, A. C. England, and G. M. Haas	Experiments on a Large Volume Electron-Cyclotron Heated Plasma	Pp. 38–44 in *Colloque International sur l'Interaction des Champs H-F Associes a un Champ Magnetique Statique Avec un Plasma, Saclay 16 et 17 septembre 1964*, vol. 1, Presses Universitaires de France, 1965
P. R. Bell and J. H. Neiler	The Scintillation Method	Pp. 245–302 in *Alpha, Beta and Gamma Ray Spectroscopy*, vol. 1, ed. by Kai Siegbahn, North-Holland, Amsterdam, 1965
P. Bletzinger,[1] A. Garscadden,[1] I. Alexeff, and W. D. Jones	A Sampling Oscilloscope as a Coherent Wide-Band Detector	*J. Sci. Instr.* **42**, 358–59 (1965)
J. L. Dunlap, G. R. Haste, H. Postma, and L. H. Reber	Energetic Plasma Losses Due to Microinstabilities	*Phys. Rev. Letters* **14**, 937–39 (1965)
T. K. Fowler[2]	Effect of Plasma Potential on Minimum-B Stability	*Phys. Fluids* **8**, 544–46 (1965)
G. E. Guest and R. A. Dory	Microinstability of a Mirror-Confined Plasma	*Phys. Fluids* **8**, 1853 (1965)
G. R. Haste, J. L. Dunlap, H. Postma, and L. H. Reber	Lorentz Dissociation of H_3^+	*Nucl. Fusion* **5**, 164 (1965)

[1]Wright-Patterson Air Force Base, Ohio.

[2]Now at General Atomic, San Diego.

Author(s)	Title of Article	Journal (or Book)
G. G. Kelley and O. B. Morgan	Ion Source and Column Performance at ORNL	Pp. 456–64 in *Proc. 1964 Linear Accelerator Conf.*, Midwestern Universities Research Association, July 20–24, 1964
M. O. Krause	Relative Intensities of Prominent LMM Auger Transitions in Krypton	*Phys. Letters* **19**, 14–15 (1965)
N. H. Lazar, C. W. Blue, R. A. Gibbons, and O. D. Matlock	Studies in the Halo of the Deuterium Arc and a PIG-Type Discharge	P. 37 in *Proc. Intern. Symposium on Diffusion Across a Magnetic Field*, Feldafing/Starnberger See, Germany, June 29–July 3, 1964, published in December 1964 as IPP 2/36 (IPP is Institute of Plasma Physics)
J. Rand McNally, Jr.	On an Unusual Dynamic Equilibrium in Magnetically Confined Arc-Plasmas	P. 95 in *Condensed Papers, Third International Meeting, Society of Applied Spectroscopy, Cleveland, Ohio, Sept. 28–Oct. 2, 1964*
D. A. Ross, C. C. Harris, M. M. Satterfield, and P. R. Bell	New Challenges in Clinical Counting	*Japan. J. Nucl. Med.* **2**, 81–88 (1965)
D. A. Ross, C. C. Harris, M. M. Satterfield, P. R. Bell, and J. C. Jordan	Low-Energy Gamma Emitters in Scanning and Other Clinical Applications	Pp. 108–25 in *Radioaktive Isotope in Klinik und Forschung*, vol. VI, ed. by K. Fellinger and R. Höfer, Verlag von Urban und Schwarzenberg, München, 1965
Y. Shima and L. S. Hall[3]	Electrostatic Instabilities in a Plasma with Anisotropic Velocity Distribution	*Phys. Rev.* **139**, A1115 (1965)
A. H. Snell	The Atomic and Molecular Consequences of Radioactive Decay	Pp. 1545–55 in *Alpha, Beta and Gamma Ray Spectroscopy*, vol. 2, ed. by Kai Siegbahn, North-Holland, Amsterdam, 1965

[3]Lawrence Radiation Laboratory, Livermore, Calif.

Author(s)	Title of Article	Journal (or Book)
G. K. Soper[4] and E. G. Harris[5]	The Effect of Finite Ion and Electron Temperatures on the Ion-Cyclotron Resonance Instability	*Phys. Fluids* 8, 984 (1965)

[4]Air Force Institute of Technology, Dayton, Ohio.
[5]Consultant, The University of Tennessee.

ORNL Reports

Author(s)	Title	Number	Date
I. Alexeff and W. D. Jones	Report on an Informal Striation Meeting Held at the Seventh International Conference on Phenomena in Ionized Gases, Belgrade, Yugoslavia, Aug. 22–27, 1965	ORNL-TM-1307	October 1965
I. Alexeff, W. Getty,[1] A. Malein,[2] and M. Seidl[3]	Report on a Meeting Held in the Old Lecture Room at Christ Church College, Oxford, at 9 P.M. on Thursday, September 9, 1965	ORNL-TM-1306	October 1965
C. F. Barnett	Directory of International Workers in the Field of Atomic and Molecular Collisions	ORNL-AMPIC-2	September 1965
C. F. Barnett, J. A. Ray, J. C. Thompson, and E. W. McDaniel[4]	Bibliography of Atomic and Molecular Processes for 1963	ORNL-AMPIC-1	July 1965
E. G. Harris[5]	The Electron-Phonon, Electron-Plasmon, Plasmon-Phonon, and Plasmon-Plasmon Interactions and Some Instabilities That They Lead To	ORNL-3871	November 1965
Mozelle Rankin	Magnetic Field Storage Codes and Orbit Calculations	ORNL-TM-1172	June 1965
A. H. Snell	Thermonuclear Division Semiannual Progress Report for Period Ending April 30, 1965	ORNL-3836	September 1965
R. E. Clausing[6]	Exploratory Experiments Concerning the Desorption of Gases by Bombardment with Electrons	ORNL-TM-1166	November 1965

[1]Research Laboratory of Electronics, MIT, Cambridge, Mass.
[2]Culham Laboratory, UK Atomic Energy Authority, Culham, Abingdon, Berkshire, England.
[3]Institute of Plasma Physics, Nademlynska, Prague 9, Czechoslovakia.
[4]Consultant, Georgia Institute of Technology, Atlanta.
[5]Consultant, The University of Tennessee, Knoxville.
[6]Metals and Ceramics Division.

PAPERS PRESENTED AT SCIENTIFIC AND TECHNICAL MEETINGS

1965 Symposium on Engineering Problems of Controlled Thermonuclear Research, University of California, Lawrence Radiation Laboratory, Livermore, California, May 4–7, 1965

P. R. Bell, R. L. Brown, and J. S. Culver, "DCX-2 Beam Injection Duct."

D. L. Coffey and W. F. Gauster, "Developmental Work for Large, Superconducting Magnet Coils."

J. S. Culver, "The DCX-2 Scanning Energy Spectrometer."

S. M. DeCamp, "Operating and Repair Experiences on DCX-2 Coils."

R. S. Edwards, "The Production of 'Excited State' H_2^+ for Lorentz Dissociation in DCX-1."

J. N. Luton, Jr., "Some Problems in the Design of an Eighth-Order, Power-Optimized Solenoid."

O. D. Matlock, "A New, Versatile Vacuum Quick-Seal and Vacuum Lock."

J. F. Potts, Jr., "Engineering Activities at Oak Ridge National Laboratory in Support of Controlled Thermonuclear Research – Summary."

J. A. Ray, R. A. Dandl, and C. F. Barnett, "Particle Detection with Semi-Conductor Detectors."

J. A. Ray and C. F. Barnett, "An Unconventional Ultra-High Vacuum Facility."

E. R. Wells, "The Production of 10^{-9} Torr Within a Large Plasma Container (DCX-1)."

W. L. Wright, "Dissipation of Heat from Large-Scale CTR Apparatus at ORNL."

Symposium on Fundamental Problems in Scanning, Chicago, Illinois, May 8–9, 1965

C. C. Harris, P. R. Bell, D. A. Ross, and M. M. Satterfield, "Rectilinear vs. Stationary Scanners."

12th Annual Meeting, Society of Nuclear Medicine, Miami, Florida, June 16–19, 1965

C. C. Harris, M. M. Satterfield, G. Uchiyama,[1] and H. E. Kimble,[2] "A Rescanner with Photographic Color Readout."

American Physical Society Topical Conference on "Research Problems in the Physics of X-Ray Spectra," Cornell University, Ithaca, New York, June 22–24, 1965

M. O. Krause and Thomas A. Carlson,[3] "Two Electron Emission in Auger and Photoabsorption Processes."

American Physical Society, Division of Plasma Physics, New York, New York, June 23–25, 1965

H. Postma, J. L. Dunlap, and G. R. Haste, "Partial Suppression of Microinstability Driven Losses."

Fourth International Conference on Atomic and Molecular Collisions, Quebec, Canada, August 3–7, 1965

C. F. Barnett and J. A. Ray, "Highly Excited States of H_2^+."

C. F. Barnett, "Atomic and Molecular Processes Information Center at ORNL" (invited paper).

---

[1]ORINS Fellow.

[2]ORINS.

[3]Physics Division.

Seventh International Conference on Phenomena in Ionized Gases, Belgrade, Yugoslavia, August 22–27, 1965

W. B. Ard and R. A. Dandl, "Observation of a Mirror-Like Instability in a Hot-Electron Plasma."

I. Alexeff, W. D. Jones, D. Montgomery,[4] and M. Rankin, "Simple Momentum Probe for Plasma Studies."

P. R. Bell, G. G. Kelley, N. H. Lazar, and R. F. Stratton, "Ion Cyclotron Harmonic Spectrum Generated in an Energetic Ion Plasma."

W. D. Jones and I. Alexeff, "A Study of the Properties of Ionic Sound Waves."

IAEA Second Conference on Plasma Physics and Controlled Nuclear Fusion Research, Abingdon, Berkshire, England, September 6–10, 1965

I. Alexeff, W. D. Jones, R. V. Neidigh, W. F. Peed, and W. L. Stirling, "Plasma Heating and Burnout in Beam-Plasma Interaction."

P. R. Bell, R. A. Gibbons, G. G. Kelley, N. H. Lazar, J. F. Lyon, and R. F. Stratton, "The Oak Ridge Multiple-Pass Injection Experiment, DCX-2."

R. A. Dandl, W. B. Ard, A. C. England, G. M. Haas, and N. H. Lazar, "Energetic Neutral Injection into an Electron-Cyclotron Plasma."

J. L. Dunlap, H. Postma, G. R. Haste, and L. H. Reber, "Severe Microinstability-Driven Losses in an Energetic Plasma."

T. K. Fowler[5] and G. E. Guest, "Anomalous Plasma Diffusion in Magnetic Wells."

First International Conference on Medical Physics, Harrogate, England, September 8–10, 1965

R. H. Rohrer[6] and E. M. Smith,[7] "Internal Dose Calculations for Tc-99m – An Illustrative Example of Current Problems in Internal Dose Calculations."

Southeastern Section, Society of Nuclear Medicine, Memphis, Tennessee, October 22–23, 1965

D. A. Ross, "Calibration and Standardization of Thyroid Uptake Measurements."

M. M. Satterfield, P. R. Bell, and C. C. Harris, "A 'Sliding-Average' Count-Rate-Indicator."

East Tennessee Section, Institute of Electrical and Electronics Engineers, Knoxville, Tennessee, October 26, 1965

J. F. Potts, Jr., "Power from Fusion – Progress and Problems."

---

[4]Consultant, State University of Iowa, Ames.

[5]Now at General Atomic, San Diego.

[6]Consultant, Emory University, Atlanta, Ga.

[7]Cornell Medical Center.

ORNL-3908
UC-20 – Controlled Thermonuclear Processes

INTERNAL DISTRIBUTION

1. I. Alexeff
2. W. B. Ard
3. C. F. Barnett
4. C. O. Beasley
5. M. C. Becker
6–11. P. R. Bell
12. D. S. Billington
13. E. P. Blizard
14. C. W. Blue
15. C. J. Borkowski
16. G. E. Boyd
17. R. L. Brown
18. E. H. Christy, Jr.
19. D. L. Coffey
20. F. L. Culler
21. J. S. Culver
22. R. A. Dandl
23. R. C. Davis
24. S. M. DeCamp
25. R. A. Dory
26. J. L. Dunlap
27. H. O. Eason, Jr.
28. R. S. Edwards
29. K. R. Efferson
30. A. C. England
31. J. C. Ezell
32. J. L. Fowler
33. J. E. Francis, Jr.
34. J. H. Frye, Jr.
35. W. F. Gauster
36. D. A. Griffin
37. W. R. Grimes
38. G. E. Guest
39. E. Guth
40. G. M. Haas
41. W. Halchin
42. C. C. Harris
43. G. R. Haste
44. R. E. Hill
45. J. L. Horton
46. H. C. Hoy
47. R. P. Jernigan, Jr.
48. W. D. Jones
49. G. G. Kelley
50. R. L. Knight
51. H. W. Koppe
52. M. O. Krause
53. C. E. Larson
54. N. H. Lazar
55. G. F. Leichsenring
56. W. J. Leonard
57. J. Lewin
58. R. S. Livingston
59. J. N. Luton, Jr.
60. J. F. Lyon
61. H. G. MacPherson
62. J. R. McNally, Jr.
63. O. D. Matlock
64. O. B. Morgan
65. R. V. Neidigh
66. J. Neufeld
67. C. E. Parker
68–69. R. B. Parker
70. W. F. Peed
71. H. Postma
72. J. F. Potts
73. F. M. Rankin
74. J. A. Ray
75. R. G. Reinhardt
76. D. M. Richardson
77. D. A. Ross
78. P. W. Reuff
79. W. K. Russell
80. H. E. Seagren
81. Y. Shima
82. E. D. Shipley
83. J. E. Simpkins
84. M. R. Skidmore
85. M. J. Skinner
86–106. A. H. Snell
107. W. L. Stirling
108. R. F. Stratton, Jr.
109. R. A. Strehlow
110. E. H. Taylor
111. H. A. Ullmaier
112. H. L. Watts
113. A. M. Weinberg
114. E. R. Wells
115. G. C. Williams
116. W. L. Wright
117. A. J. Wyrick
118. O. C. Yonts

119. Gale Young
120. Owen Eldridge (consultant)
121. J. W. Flowers (consultant)
122. D. C. Freeman, Jr. (consultant)
123. M. W. Garrett (consultant)
124. H. Grad (consultant)
125. E. G. Harris (consultant)
126. D. E. Harrison (consultant)
127. W. Heckrotte (consultant)
128. R. Hefferlin (consultant)
129. G. W. Hoffman (consultant)
130. J. W. Hooper (consultant)
131. V. W. Hughes (consultant)
132. D. W. Martin (consultant)
133. E. W. McDaniel (consultant)
134. D. R. Montgomery (consultant)
135. S. H. Neff (consultant)
136. C. E. Nielsen (consultant)
137. W. B. Pardo (consultant)
138. J. M. Reynolds (consultant)
139. H. S. Robertson (consultant)
140. H. E. Rorschach (consultant)
141. D. J. Rose (consultant)
142. L. P. Smith (consultant)
143. P. M. Stier (consultant)
144. T. H. Stix (consultant)
145. E. W. Thomas (consultant)
146. M. E. Williams (consultant)
147–167. Thermonuclear Division Library
168. Reactor Division Library
169. Biology Division Library
170–171. Central Research Library
172. Laboratory Shift Supervisor
173–248. Laboratory Records Department
249. Laboratory Records, ORNL RC
250–251. ORNL – Y-12 Technical Library Document Reference Section

EXTERNAL DISTRIBUTION

252. S. C. Brown, Massachusetts Institute of Technology
253. O. Buneman, Stanford Electronics Laboratories
254. Director, Technical Library, Defense Atomic Support Agency, Sandia Base, Albuquerque, New Mexico
255. F. W. Crawford, Stanford Electronics Laboratories
256. M. B. Gottlieb, Princeton University
257. D. W. Kerst, University of Wisconsin
258. A. C. Kolb, Naval Research Laboratory
259. Morton A. Levine, Air Force Cambridge Research Laboratories
260. J. A. Phillips, Los Alamos Scientific Laboratory
261. R. F. Post, University of California, Lawrence Radiation Laboratory
262. John R. Roth, NASA Lewis Research Center (Mail Stop 301-1), 21000 Brookpark Road, Cleveland, Ohio, 44135
263. Russell Shelton, Chief, Nuclear and Plasma Physics Branch, Marshall Space Flight Center, Huntsville, Alabama 35812
264. L. D. Smullin, Massachusetts Institute of Technology
265. L. Spitzer, Princeton University
266. A. W. Trivelpiece, University of California, Berkeley, California
267. C. M. Van Atta, University of California, Lawrence Radiation Laboratory
268. J. A. Swartout, 270 Park Avenue, New York 17, New York
269–270. Research and Development Division, AEC, ORO (1 copy each to H. M. Roth and R. B. Martin)
271–275. Controlled Thermonuclear Research Branch, AEC, Washington (A. E. Ruark)
276–286. USAEC, Division of Research, Controlled Thermonuclear Research Program (Stephen O. Dean)
287–609. Given distribution as shown in TID-4500 under Controlled Thermonuclear Processes category (75 copies – CFSTI)